Optodynamical Measurement and Coupling of Atomic Motion and Spin

by

Jonathan Lynn Kohler

A dissertation submitted in partial satisfaction of the

requirements for the degree of

Doctor of Philosophy

in

Physics

in the

Graduate Division

of the

University of California, Berkeley

Committee in charge:

Professor Dan M. Stamper-Kurn, Chair
Professor Holger Müller
Professor Karl van Bibber

Summer 2018

Optodynamical Measurement and Coupling of Atomic Motion and Spin

Abstract

Optodynamical Measurement and Coupling of Atomic Motion and Spin

by

Jonathan Lynn Kohler

Doctor of Philosophy in Physics

University of California, Berkeley

Professor Dan M. Stamper-Kurn, Chair

The quantum nature of light makes it a basic component for models of quantum measurement and information exchange between disparate quantum modes, pioneered in the field of cavity quantum electrodynamics. The interaction of atomic ensembles with the mode of an optical cavity provides a flexible platform for exploring the coherent interaction of light with diverse macroscopic dynamics, such as collective motion and spin. This dissertation presents experimental results and theoretical models for continuous measurement and control of the center of mass motion and collective spin precession of an atomic ensemble, mediated by coupling to a high-finesse optical cavity. First, the theory of dispersive coupling between the cavity mode and the collective motion and spin of an atomic ensemble is derived, and then a general time-domain formalism is developed for theoretical analysis of multi-mode optodynamical systems. Single-mode optodynamical effects are introduced through experimental demonstrations of measurement and control of the collective atomic spin, providing a close analogy to cavity optomechanics.

Next, multiple collective atomic modes are considered within a single cavity, in order to assemble optically mediated interactions within multi-mode optodynamical systems. A demonstration of optodynamical interactions between the center of mass motion of two atomic ensembles is presented, coupled through an optical spring mediated by the cavity mode. Then simultaneous coupling of the center of mass motion and total spin precession of a single ensemble of atoms is described, yielding an experimental realization of a negative-mass instability, facilitated by the novel resource of the spin ensembles inverted state. A theoretical analysis of the negative-mass instability is presented, which indicates the possibility of generating two-mode squeezed states in the absence of excess incoherent noise. Finally, linear state retrodiction from the optodynamical signals is discussed, providing background and supplemental material for a forthcoming manuscript.

The Real Work

It may be that when we no longer know what to do
   we have come to our real work,
and that when we no longer know which way to go
   we have come to our real journey.
The mind that is not baffled is not employed.
The impeded stream is the one that sings.

Wendell Berry (1934–)

Contents

List of Figures

List of Tables

Acknowledgments

One of the benefits of studying in Berkeley has been being constantly surrounded by fellow students and colleagues who were more gifted and experienced, yet were willing to teach and learn from each other. I was fortunate to join an active experiment, with Sydney and Nicolas charting research goals while patiently teaching me the ropes and Lukas contributing theory insight. In later years, Justin and Emma brought new life and energy to the lab, and their eagerness and persistence were essential to pulling off the most complicated experiments on the apparatus yet. In the past year, this venerable experiment has received a new lease on life with Julian joining the group, giving hope for a bright future of results ahead.

I have learned the most during my graduate career through working alongside these and all other members of the ultracold labs – Ed, Ryan, Andrew, Tom, Claire, Fang, Shun, Zephy, Masayuki, Vicky, Thomas, and Aaron – who patiently answered countless questions, provided valuable feedback during group meetings, and contributed to lively journal club discussions. Between practice talks, bike rides, and coffee runs the group provided feedback and support through the grit of grad school and has been my most consistent community in Berkeley. We've worked beside each other through the highs and lows of a challenging period of life, and I could not have chosen a better group of colleagues.

For my scientific development, I owe particular thanks to my advisor, Dan, who's inimitable scientific intuition has motivated seeking deeper insight, provided direction through confusion, and inspired confidence in work that gained his approval. Prior to graduate school, I was fortunate to learn from many excellent research mentors and teachers, but here will only have space to specifically name a few. Dr. Jonathan Jarvis instilled good lab practices and patiently guided my undergraduate research in the group of Prof. Charles Brau. Sonia Utermann inspired a spirit of adventure and collaboration during my first research experience in the group of Dr. Matthias Schröter at the Max Planck Institute for Dynamics and Self-organisation, sponsored through the DAAD RISE internship. Dr. Core exemplified the value of scholarship and introduced me to the field of physics. Finally, Mr. Reagan provided a college-level education in Algebra I, sparking an interest in mathematics which provided a foundation for my study of physics.

Outside the lab, I have been fortunate to find many good friends along this journey – in particular, my 1044 housemates, friends from Christ Church community groups, and fellow students at the Berkeley Institute. I have been challenged to learn and motivated to grow by close friends and value the time spent together. I am also thankful for the peace and encouragement I received through the community at Berkeley Covenant Church.

Finally, I owe my greatest acknowledgment to my mother and first teacher, who spent decades homeschooling myself and my siblings. From working with me through understanding negative numbers and fractions to putting my DAMOP conference poster on the refrigerator and asking for a presentation, she has continued to exemplify an insatiable curiosity and willingness to learn. More importantly, her life of selfless love, unflinching loyalty, and constant faith in God has been an example of the true priorities and purpose of life.

Chapter 1

Introduction

Light has served as an essential subject and tool of research throughout the history of physics. It has been alternately considered either as a particle, as in Newton's corpuscular theory of ray optics, or as a wave, elegantly arising from Maxwell's equations for electromagnetism. With the advent of quantum mechanics, the apparent wave and particle natures of light have been unified in the theory of quantum electrodynamics (QED), which describes light in terms of photons, discrete excitations of a quantum field. Although the quantization of optical emission played a significant role in the development of quantum mechanics [1], only within the past 50 years has the quantum nature of light been conclusively observed [2, 3], confirming its place among prototypical quantum elements such as atoms and sub-atomic particles.

Coherent optical beams, such as lasers, also facilitate the most sensitive measurements performed, to date the detection of gravitation waves by the Laser Interferometer Gravitational-wave Observatory (LIGO) [4]. Such optical measurements define basic models for the theory of quantum measurement, with sensitivity fundamentally limited by measurement uncertainty due to the quantum fluctuations of photons arriving at the detector, known as photon shot noise, in addition to measurement backaction, incoherent perturbations of the measured system driven by these shot noise fluctuations. This backaction is a necessary consequence of measurement, imparting the requisite uncertainty to the measured system to satisfy the Heisenberg uncertainty bound.

The quantum nature of light is significant because it also allows coherent interaction between light and matter, which can be expressed in terms of a Hamiltonian operator that generates unitary evolution of the hybrid quantum system. As the fundamental excitations of the electromagnetic field, photons are the virtual quantum particles that carry the Coulomb force, mediating long-range interactions between charged quantum objects, such as the nucleus and electrons in an atom. Similarly, long-range interactions between quantum objects can be engineered through the coherent exchange of real photons, which can also be measured to gain information about dynamics of the interacting systems.

Broadly considered, the subject of this dissertation is the observation of backaction-driven dynamics from optical measurements of atomic motion and spin, and the engineering of

optically mediated interactions between disparate modes of atomic motion through coherent optical backaction.

Optically probed atomic ensembles

Considering atoms as test particles for exploring the quantum effects of measurement backaction leverages the advantage of well-developed techniques of trapping and cooling atoms to prepare pure quantum states of the atomic motion and spin [5]. Probing the collective dynamics of an ensemble of N_a atoms enhances the optical coupling strength, which, for instance, provides improved sensitivity to external forces or magnetic fields for applications as an atomic sensor. However, collective dynamics of large ensembles tend to become increasingly classical in nature, with the associated zero-point motion or quantum projection noise decreasing as the mass or number of particles participating in the collective mode increases.

Although this shrinking scale for the 'quantumness' of the collective mode makes it increasingly challenging to prepare and observe distinctly quantum mechanical effects, there is fundamental interest to understand and exploit the consequences of quantum mechanics for increasingly large systems. For instance, non-classical collective states can provide quantum enhancement for measurement sensitivity beyond the standard quantum limit (SQL) and probe the transition of quantum mechanics from the microscopic world of atoms to the macroscopic world dominated by classical dynamics [6, 7].

Cold atomic ensembles present a path toward preparing increasingly large systems in pure quantum states, which can be probed and manipulated through their interaction with light. Placing the atoms in a high-quality optical resonator, the measurement can be further enhanced to achieve sensitivity below the scale of quantum fluctuations and engineer coherent optical interactions.

Cavity QED

In free space, an atom can emit photons into a continuum of optical modes, which carry information in every direction. While the Hamiltonian description can be extended to sum over all of these modes, tracking and measuring their evolution becomes practically impossible, and quantum information is lost to the environment of unobserved optical modes. Achieving a useful degree of control over the light-atom interaction requires isolation of selected optical modes that interact with the atoms, which are decoupled from the environment of other modes into which information would be lost.

This feat is accomplished in the field of cavity QED by engineering optical resonators which geometrically alter the structure of available modes into which an atom can emit a photon. For sufficiently high-quality resonators, the coupling to the cavity mode g_0 can be made to exceed all losses into the continuum of free-space modes in the environment, enabling a rich array of cavity-enhanced quantum light-matter dynamics [8–10]. This condition defines
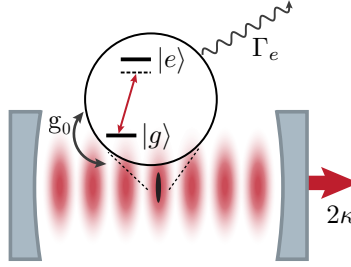
Figure 1.1: Sketch of the basic cavity QED model, illustrating optical coupling to an ensemble of two-level atoms, with interaction strength g_0 and incoherent loss due to free-space atomic spontaneous emission at rate Γ_e and cavity photon loss rate 2κ.

the single-atom strong-coupling regime of cavity QED, quantified by the cooperativity

$$C_{\mathrm{QED}} = \frac{g_0^2}{\kappa \Gamma_e} \gg 1,$$

in terms of the the atomic spontaneous emission rate Γ_e and the cavity photon loss rate 2κ, represented in Fig. 1.1. In this regime, excitations are coherently exchanged between the cavity mode and atomic excited states more rapidly then they are lost to the environment.

Dispersive cavity coupling

Although the cavity used in our experiment falls well within the strong-coupling regime, the work reported in this dissertation was performed in the dispersive coupling limit, where the cavity mode is far detuned from the atomic transition. This detuning reduces the probability of optical transitions into the atomic excited state, suppressing Rayleigh scattering into free-space modes and extending the coherence of the atom-cavity dynamics. In this regime, the atomic excited states can be adiabatically eliminated from the system dynamics.

The detuned cavity mode drives second-order Raman transitions between states within the electronic ground-state manifold, imparting dispersive frequency shifts to the cavity resonance and ac Stark shifts to the atomic ground states. The dispersive shift of the cavity resonance facilitates weak continuous measurement of the atomic ensemble, while negligibly perturbing the nature of the atomic eigenstates. The ac Stark shift of the atomic eigenstates represents a spin- and position-dependent potential, proportional to the optical intensity, which introduces optical backaction from coherent and quantum fluctuations of the cavity photon number. Assuming negligible absorption and scattering from the mirrors, photons escaping from the cavity are transmitted into well-defined output modes and can readily be collected and measured, recovering information about the system dynamics.

The effective dispersive coupling strength $g_c = g_0^2/\Delta_{\mathrm{ca}}$ is reduced for large detuning $\Delta_{\mathrm{ca}} = \omega_c - \omega_a$ between the atomic transition frequency ω_a and the cavity resonance frequency ω_c. However, by trapping ensembles of a few thousand ^{87}Rb atoms within the cavity mode,

optical coupling to the collective atomic dynamics is enhanced by the atom number N_a, entering a regime of collective dispersive strong coupling when $N_a g_c \gg \kappa, \Gamma_e$ [11]. In this regime, the cavity field performs sensitive measurements of the collective atomic dynamics, with sensitivities limited by quantum backaction from shot noise fluctuations of the intra-cavity photon number. Furthermore, the finite lifetime of photons circulating within the cavity allows coherent feedback of the optical measurement onto the subsequent atomic dynamics, conditioning autonomous feedback through coherent optical backaction.

Cavity Optodynamics

Optical measurement and control of the motion of macroscopic objects has been pioneered in the field of cavity optomechanics [12, 13]. In this field, highly engineered mechanical and optical resonators have recently achieved performance in the quantum regime, with demonstrations of squeezed states of a single oscillator [14, 15] and entanglement between the motion of two oscillators [16, 17]. However, the well-developed techniques for cooling and preparing pure states of atomic ensembles enabled early atomic demonstrations of optomechanics in the quantum regime, such as observation of sideband asymmetry of a near-ground-state oscillator [18], ponderomotive squeezing of the optical field [19], and force measurement sensitivity near the SQL [20].

Atomic ensembles also have a long history for optical measurement of collective spin dynamics, such as quantum-limited dispersive measurements [21] used for atomic magnetometry [22]. Within an optical cavity, the collective spin experiences enhanced coupling and optical feedback, allowing measurement and control of its Larmor precession, providing an exact analogy to cavity optomechanics [23]. As with cavity optomechanics, experiments performed with cold atomic ensembles in our optical cavity have provided early demonstrations of quantum spin optodynamical effects, such as backaction-limited dynamics and ground-state cooling [24], presented in Chap. 3. This work provides insight to the emerging field of cavity optomagnonics [25–28], which studies optodynamical effects of collective spin ensembles in solid-state materials which have favorable microwave and optical properties, such as yttrium iron-garnet.

Optical coupling to these two distinct degrees of freedom defines a broader class of cavity optodynamics, defined by coupling between the mode of an optical cavity and dynamic variables of macroscopic systems. The inherent flexibility provided by an atomic ensemble in our optical cavity also allows simultaneous optical coupling to the atomic motion and spin, facilitating hybrid optodynamical interactions with spin and motion [29], discussed in Chap. 5. Such hybrid systems could facilitate novel quantum measurement schemes, such as coherent quantum noise cancellation [30, 31].
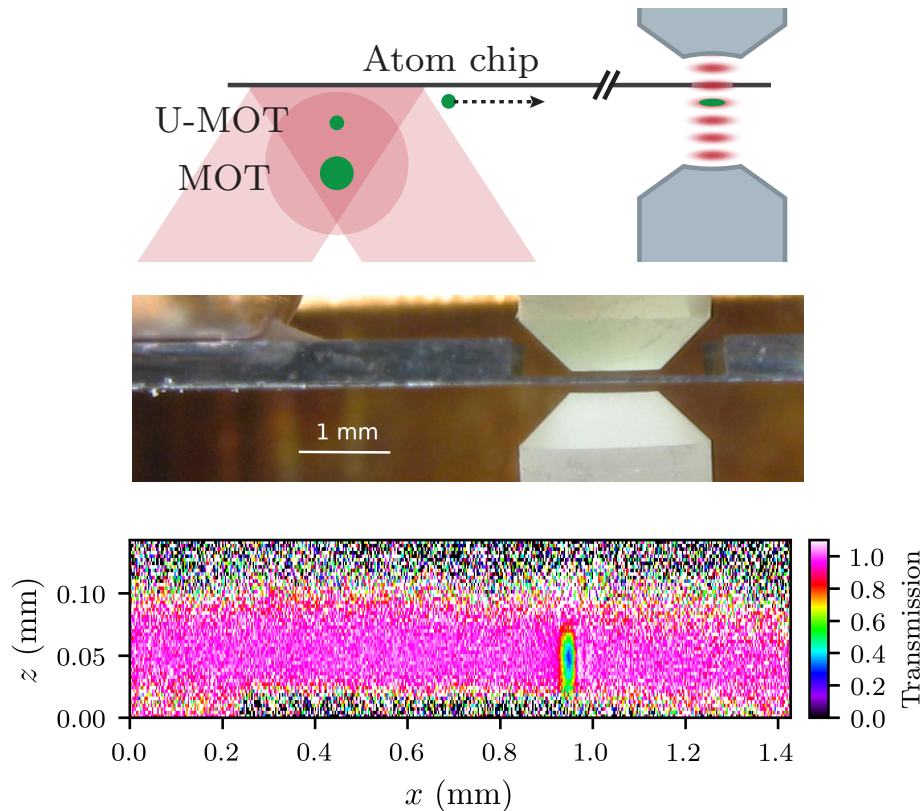
Figure 1.2: (top) An abbreviated diagram of the magneto-optical trap (MOT) and atom chip used for cooling and transport of atoms into the cavity mode. (middle) Side view of the cavity and chip assembly (Photograph by Tom Purdy). (bottom) Absorption image of an ensemble of ~ 2000 atoms inside the cavity, after 0.5 ms time of flight.

1.1 Experimental apparatus

A sketch of the atom-chip, cavity QED apparatus affectionately called 'E3' is sketched in Fig. 1.2, along with a picture of the assembled chip and mirrors and an absorption image of atoms inside the cavity. These images are about as much as I have seen of the most important research tools supporting my work in the past five years. For nearly a decade, this compact assembly has been carefully isolated in a steel chamber under ultra-high vacuum, at about 10^{-11} torr. All the following experiments and results were obtained by carefully injecting electrical currents into atom chip wires and shining laser beams through vacuum chamber windows to tickle the atoms with light reflecting within the optical cavity. A few picowatts of light leaking out of the cavity is measured with an optical heterodyne detector, telling a rich story about the behavior of the hybrid atom-photon cloud suspended between the two highly reflective cavity mirrors.

This vacuum chamber is surrounded by electromagnetic bias coils (illustrated in Fig. C.1),

several tables of optics, and racks of electronics used to generate the optical and magnetic fields necessary to trap, cool, and transport the atoms into the optical cavity and hold them in a standing wave of light. This process requires about 30 seconds to prepare an ensemble of a few thousand cold atoms inside the cavity for each experiment. Then with a brief flash of light, the actual experiment and measurement sequence is performed in a few tens of milliseconds, and the entire process starts over to repeat the next 'shot.'

E3 has a significant scientific legacy left by the graduate students and post-docs who built the apparatus and developed the concepts and techniques that support the following work. In addition to their substantial scientific results [18–20, 32–35], a vast amount of technical innovation has supported the success of this project, most of which is well-documented in the theses of former group members. I give a brief summary of the experimental apparatus and atom transport sequence, however, for details about the construction of the atom chip, cavity, and science chamber, see Tom Purdy's dissertation [36], for details of the cavity laser locking scheme and optical heterodyne detection, see Thierry Botter's dissertation [37], and for details of the optical superlattice trap potential and the phase-insensitive heterodyne probe frequency locking scheme, see Sydney Schreppler's dissertation [38].

A typical experimental sequence

The experimental sequence begins by loading a MOT of ^{87}Rb atoms from a background vapor produced by a rubidium dispenser. The MOT captures only the slow tail of the thermal velocity distribution, loading on order 10^7 atoms within 12 s. This initial MOT is formed at the zero of a quadrupole magnetic field generated by an in vacuum MOT coil and external bias fields, about a centimeter below the atom chip. The MOT is then quickly compressed by detuning the beams further from the atomic cycling transition. The atoms are then released and subsequently captured and re-cooled in the 'U-MOT' stage, named after the 'U'-shaped atom chip wire producing the magnetic quadrapole field. After allowing any residual atomic motion from the transfer to damp, the U-MOT is also compressed closer to the atom chip then switched off, and the magnetic fields are quickly nulled. The atoms then undergo optical molasses and sub-Doppler polarization gradient cooling, resulting in up to 10^7 atoms at a temperature of about $T = 12$ μK. Next, the atoms are optically pumping by resonant, circularly polarized light to prepare them in the magnetically trappable $|f = 2, m_f = 2\rangle$ state, and then they are caught in a magnetic trap formed by the atom chip waveguide and 'U' wires. The magnetically trapped gas undergoes an initial stage of forced rf evaporation, and then the trap is further compressed and shuttled through 36 "links" of a magnetic conveyor belt, transporting them into the cavity mode.

One of E3's most unique capabilities is precise positioning of a cloud of a few thousand atoms within a single lattice site of the cavity optical dipole trap (ODT), realizing a tunable, symmetric coupling of each atom to the cavity field [32]. The cavity is a near-planar Fabry-Pérot resonator formed between two highly reflective mirrors with radius of curvature $R_c = 5$ cm separated by $L_c = 250$ μm. After a final stage of rf evaporation, the atoms are transferred into an ODT of wavelength 842 nm, resonant with a TEM$_{00}$ mode of the cavity,

and all chip wires are subsequently ramped off. The tight confinement of the chip-generated magnetic traps allows the gas to be compressed to sub-wavelength size in all dimensions, such that atoms are primarily loaded into a single well of the cavity ODT, resulting in up to 4000 atoms at temperatures around 3 μK, as revealed by time-of-flight absorption images such as shown in Fig. 1.2.

The standing-wave ODT holding the atoms provides tight confinement in the axial dimension, defining trap frequencies up to $\omega_m = \sqrt{2k_t^2 U_t/m} = 2\pi \times 150$ kHz, in terms of the trap potential depth U_t and wavevector $k_t = 2\pi/842$ nm. The transverse confinement from the cavity mode waist $w_0 = 25$ μm defines much weaker radial confinement, with a corresponding radial trap frequency up to $\omega_r = \sqrt{4U_t/w_0^2 m} = 2\pi \times 1.2$ kHz, resulting in a high aspect-ratio cloud. For the low temperature gas, the confinement is approximately harmonic, with a mean thermal occupation along the axial direction of about 0.5 phonons, but about 50 phonons in the radial directions.

The atoms are probed through their influence on another TEM$_{00}$ cavity mode, which is detuned by Δ_{ca} from the atomic D$_2$ transition at wavelength 780 nm. The cavity half-linewidth at this wavelength is $\kappa = 2\pi \times 1.82$ MHz, corresponding to a finesse of $\mathcal{F} = 1.6 \times 10^5$ and yielding an on-resonance cooperativity of $C_{QED} = 16$, sufficient to access the single-atom strong-coupling regime of cavity QED.

In most experiments, information about the atomic dynamics is measured by driving this mode of the optical cavity with a probe laser, at a fixed detuning Δ from the cavity resonance. The atomic dynamics modulate the amplitude and phase of the intracavity field through the dispersive interaction, and light transmitted through the cavity output mirror carries a record of these dynamics. The amplitude and phase modulations of the transmitted probe light are measured using a balanced heterodyne detector, by beating the output field with a 1 mW local oscillator (LO) derived from the same laser, but offset in frequency by $\omega_0 = 2\pi \times 10$ MHz. Balanced heterodyne detection readily provides shot noise limited measurement of both quadratures of optical modulation, which contain the full optical record of the atomic dynamics. Performing heterodyne detection, with a detuned LO, provides greater flexibility than a homodyne configuration, since it is equally sensitive to both field quadratures, at the cost of reduced detection efficiency for each individual quadrature.

1.2 My time on E3

I joined the ultracold group at Berkeley during summer 2013 and began working with the E3 team. From the start, I benefited by learning from Sydney Schreppler and Nicolas Spethmann, an experienced graduate student and postdoc team, later joined by our resident theorist, Lukas Buchmann. I was fortunate to join a mature, functioning experiment, which enabled me to immediately participate in running experiments, learn the scientific goals and capabilities of the apparatus, and gain experience in designing experimental sequences and interpreting the rich heterodyne data signal.

The first significant project I contributed to was optomechanical coupling of the motion of two atomic ensembles, with results published in Ref. [35] and additional details and analysis presented in Chap. 4. In addition to lending a hand in daily lab operation, I also implemented an automated digital analysis and feedback tool, which helped stabilize the frequency of the atomic oscillators during overnight data taking sessions, by estimating the frequencies observed in the recorded heterodyne signal, and feeding this information back to the computer control software for subsequent experimental repetitions, as described in Sec. 4.1 and Appendix F.

Following some unsuccessful attempts toward generating motional squeezed states through optomechanical parametric amplification, Sydney and I directed our lab efforts in January 2015 toward measuring and controlling the atomic spin through optodynamical coupling. This work quickly yielded strong signals and qualitative demonstrations of the spin analog of cavity optomechanics [23]. However, achieving an accurate quantitative description of the dynamics required lengthy technical improvements, calibrations, and theoretical understanding, assisted by Nicolas, with results published in Ref. [24] and further details described in Chap. 3.

After completing experiments on spin optodynamics, I was joined by graduate students Justin Gerber and Emma Dowd, and we set out to use the effective negative-mass oscillator provided by the atomic spin together with its (positive-mass) motion to demonstrate coherent quantum noise cancellation [39]. However, simultaneous optodynamical coupling to the motion and spin of a single atomic ensemble proved to be more complicated system than anticipated. After realizing the intrinsic obstacle of incoherent energy transfer between positive- and negative-temperature objects, described in Chap. 5, we became interested instead in the coherent dynamics of the coupled positive- and negative-mass oscillators. Achieving control and understanding of this system was an arduous cycle of performing experimental measurements, developing new analysis methods, and forming theoretical models. This work was ultimately very fruitful, producing a demonstration of the negative-mass instability published in Ref. [29] and described further in Chap. 5, as well as a deeper understanding of the matched-filter analysis used for state estimation, introduced in Chap. 6.

While I have been working to complete analysis and writing for the results coming out of the work with Justin and Emma, they have moved on to building the new cavity-microscope experiment named E6. This year, E3 has received new life from grad student Julian Wolf, who has been pioneering a novel regime of spin optodynamics, with the goal of using cavity feedback to stabilize a non-equilibrium state.

After operation under vacuum for most of the past decade, E3 has been functioning better than ever. Many key problem points in the electronic or optical systems have been identified, through accumulated day-to-day experience in the lab, and resolved. In addition to enabling unattended, round-the-clock operation – sparing many overnight lab shifts – this stability has enabled the increasingly ambitious projects outlined above. This improved stability, consequently, allowed us to produce increasingly large, multi-terabyte datasets of digitally sampled heterodyne signals. Handling this scale of data required development of more efficient and flexible analysis methods, implemented through a redesigned analysis code

library, described in Appendix E and available at Ref. [40].

1.3   This work

This dissertation is organized around the assembly of interacting multi-mode optodynamical systems, with the central chapters focused on experimental demonstrations of optodynamical interactions and coupling between collective modes of atomic ensembles. The primary results of this experimental work are reported in Refs. [24, 29, 35] and are summarized in the corresponding chapters, but not replicated. My primary goals in the following chapters are to develop a general theoretical framework for describing multi-mode optodynamical interactions, to position each experiment in context of the related literature, to explain experimental details and challenges overcome in obtaining the published results, and finally to outline open questions and directions of interest for future work. Within this theme, the following chapters fall into three main topics: single-mode optodynamical measurement and control via autonomous feedback, cavity-mediated interactions in multi-mode optodynamical systems, and quantum-limited multi-mode state retrodiction.

Beginning in Chap. 2, I describe how optical coupling to the atomic center of mass motion and collective spin precession is approximated by the canonical optodynamical Hamiltonian, then develop a general formalism for time-domain treatment of optodynamical interactions in multi-mode systems. This chapter ends with a description of optodynamical measurement via heterodyne detection of the output field, resulting in a theoretical model for analyzing and interpreting the signals recorded in experiments. Having introduced these theoretical tools, Chap. 3 gives examples of basic optodynamical effects in the context of spin optodynamics, extending optomechanical concepts to describe autonomous optical feedback to collective spin precession of an atomic ensemble, conditioned by the cavity spectrum. This chapter highlights unique features of the inverted spin "ground" state, as well as effects of the nonlinear equations of motion arising from the spin commutation relations, and finally considers the effect of cavity birefringence on the optodynamical behavior.

Chap. 4 moves beyond single-mode optodynamics, describing our demonstration of a cavity-mediated coupling between the motion of two separate atomic ensembles. This interaction between positive-mass harmonic oscillators results in familiar dynamics of coherent state exchange, but is limited by correlated quantum backaction noise due to the open nature of the mediating cavity mode, which proscribes necessary conditions to realize fully coherent state exchange interactions. Next, in Chap. 5 the familiar picture of coupled oscillators is up-ended by substituting a high-energy spin ensemble as one of the oscillators, providing an approximation of an oscillator with negative effective mass. The optical spring coupling drives resonant pair-creation interactions in this two-mode system and was observed to amplify a correlated mode of the oscillator's motion. Applications of this negative-mass instability to generate two-mode squeezed states of the hybrid system or drive quantum-limited amplification are theoretically considered, suggesting they are achievable within experimentally feasible parameters, though obscured by additional intrinsic incoherent dynamics in

our experimental demonstration.

In Chap. 6, I address the challenge of simultaneous multi-mode state readout through the single-mode cavity output channel. I consider the statistics of linear matched filters used for retrodiction of multi-mode states in Chaps. 4 and 5, calculating optimal filters and quantifying conditions for state estimation approaching the standard quantum limit, for single-mode and multi-mode optodynamical systems under simultaneous measurement by the transmitted cavity field. I describe stochastic, numerical simulations used to simulate the optodynamical measurement record and verify the use of matched filters for inferring moments of multi-mode states, such as two-mode squeezed states.

Finally, a series of appendices provide a derivation of the spin-dependent Hamiltonian referenced in the main chapters (Appendix A), describe detection (Appendix B) and magnetic field calibrations (Appendix C), discus estimation of the probe detuning from phase-modulation sidebands (Appendix D), give a high-level summary of the analysis code library developed to facilitate efficient (re)analysis of the multi-terabyte datasets generated in running these experiments (Appendix E), and outline the use of this automated analysis to feedback to control parameters and extend the experimental stability, which rendered feasible many of the preceding experiments (Appendix F).

1.4 Definitions and conventions

For notational consistency, I adhere to a few typographic conventions throughout. Vector-valued variables are typeset in boldface (e.g. $\boldsymbol{v}$), and matrices in roman typeface (e.g. M). Quantum mechanical operators, as usual, are indicated with a caret (e.g. $\hat{n}$).

The operators $\hat{a}_i$ and $\hat{c}$ are used to describe unitless bosonic modes, satisfying the canonical commutation $[\hat{a}_i, \hat{a}_j^\dagger] = \delta_{ij}$ and likewise for $\hat{c}$. The operators $\hat{a}_i$ always refer to various *atomic* modes, whether referencing motion or approximating collective Larmor precession, while $\hat{c}$ always describes the *cavity* field amplitude. When defining quadratures of such non-Hermitian operators, I always use the unitary normalization convention

$$\hat{X}_i = \frac{1}{\sqrt{2}}\big(\hat{a}_i^\dagger + \hat{a}_i\big) \qquad\qquad \hat{P}_i = \frac{i}{\sqrt{2}}\big(\hat{a}_i^\dagger - \hat{a}_i\big) \tag{1.1a}$$

for atomic modes, with commutator $[\hat{X}_i, \hat{P}_i] = i$, and

$$\hat{c}^{\mathrm{AM}} = \frac{1}{\sqrt{2}}\big(\hat{c}^\dagger + \hat{c}\big) \qquad\qquad \hat{c}^{\mathrm{PM}} = \frac{i}{\sqrt{2}}\big(\hat{c}^\dagger - \hat{c}\big) \tag{1.1b}$$

for optical modes, with commutator $[\hat{c}^{\mathrm{AM}}, \hat{c}^{\mathrm{PM}}] = i$. Corresponding definitions are assumed for the quadratures of the optical vacuum and thermal bath inputs, $\hat{\xi}$ and $\hat{\eta}_i$ respectively, which are assumed to be itinerant bosonic fields that satisfy $[\hat{\xi}(t), \hat{\xi}^\dagger(t')] = \delta(t - t')$ and $[\hat{\eta}_i(t), \hat{\eta}_i^\dagger(t')] = \nu_i \delta(t - t')$, for a equilibrium thermal bath occupation ν_i.

Functions represented in Fourier space are typeset with the frequency parameter in square brackets $f[\omega]$. I follow the unitary convention for normalization of the angular-frequency
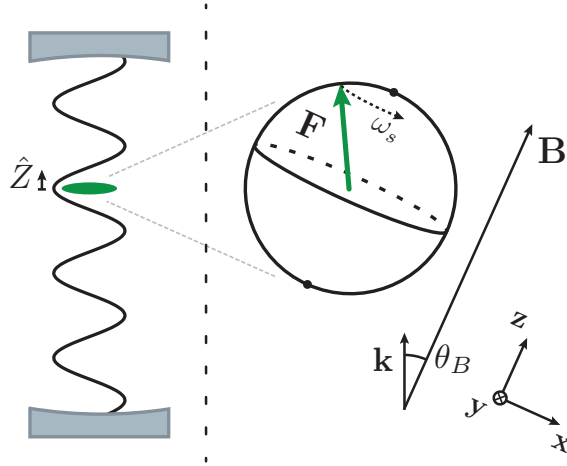
Figure 1.3: Definition of independent coordinate systems for the axial atomic position and the atomic spin components. The axial center-of-mass position is always described by the operator $\hat{Z}$, while the components of the atomic spin are defined relative to the orientation of the applied magnetic field.

Fourier transform and its inverse

$$f[\omega] = \frac{1}{\sqrt{2\pi}} \int_{-\infty}^{\infty} dt \, e^{i\omega t} f(t) \qquad \text{and} \qquad f(t) = \frac{1}{\sqrt{2\pi}} \int_{-\infty}^{\infty} d\omega \, e^{-i\omega t} f[\omega], \qquad (1.2a)$$

respectively.

I adopt a convention in this work, unique from the related publications, to always designate the atomic spin quantization axis as $\mathbf{z}$, which is defined by the orientation of a large, applied magnetic bias field as displayed in Fig. 1.3. Although the lab-frame orientation of this field is actually changed to realize different experimental dynamics, it is more intuitive to work in a reference frame defined by the good atomic eigenstates, with the longitudinal spin component conventionally labeled as $\hat{F}_z$. As a consequence, the cavity axis unit vector $\mathbf{k} = \cos\theta_B \mathbf{z} + \sin\theta_B \mathbf{x}$ changes in this coordinate system as the magnetic field is rotated.

Upper case operators (e.g. $\hat{Z}$ and $\hat{F}_z$) are used to describe collective atomic degrees of freedom, while lower case operators (e.g. $\hat{z}_i$ and $\hat{f}_z^{(i)}$) act on the states of single atoms. Because this work primarily considers one-dimensional, axial atomic motion, for simplicity of notation I always use $\hat{Z}$ and $\hat{z}_i$ to refer to the axial position, independent of the coordinate system used to describe the spin components, defined by the magnetic field. These position operators carry units of length and are to be distinguished from the *unitless* quadrature operators $\hat{X}_i$ defined above, which are related according to

$$\hat{Z}_i = Z_{\text{HO}}\left(\hat{a}_i^\dagger + \hat{a}_i\right) = \sqrt{2} Z_{\text{HO}} \hat{X}_i \qquad (1.3)$$

by the corresponding collective harmonic oscillator length

$$Z_{\text{HO}} = z_{\text{HO}}/\sqrt{N_a} = \sqrt{\hbar/2N_a m_a \omega_i} \qquad (1.4)$$

Table 1.1: Parameter definitions and values

Symbol		Definition	(Typical) Value
L_c	:	Cavity mirror separation	250 μm
R_c	:	Cavity mirror radius of curvature	5 cm
w_0	:	Cavity mode waist (radius)	25 μm
κ	:	Cavity half-linewidth	$2\pi \times 1.82$ MHz
m_a	:	Atomic mass of ^{87}Rb	1.44×10^{-25} kg
ω_{a}	:	^{87}Rb D$_2$ $f = 2 \to f' = 3$ transition frequency	$2\pi \times 384.228$ THz
Γ_e	:	Excited state decay rate	$2\pi \times 6$ MHz
g_0	:	QED coupling strength	$2\pi \times 13$ MHz
C_{QED}	:	Resonant cavity QED cooperativity	16
Δ_{ca}	:	Cavity-atom detuning	$(2\pi \times -42$ GHz$)$
g_{c}	:	Dispersive coupling strength	$(2\pi \times -4$ kHz$)$
α_0	:	Relative D$_2$ scalar coupling strength	2/3
α_1	:	Relative D$_2$ vector coupling strength	1/6
α_2	:	Relative D$_2$ tensor coupling strength	0
N_a	:	Atom number	(1000–4000)
$\bar{n}$	:	Intra-cavity photon number	(0–10)
Δ	:	Cavity-probe detuning	$2\pi \times (-2$–2 MHz$)$
ω_{m}	:	Axial trap frequency	$2\pi \times (90$–150 kHz$)$
ω_{s}	:	Larmor frequency	$2\pi \times (100$ kHz–2 MHz$)$
ϵ	:	Total cavity photon detection efficiency	(10–15%)

defined in terms of the single-atom harmonic oscillator length z_{HO}, the total atom number N_a, the atomic mass m_a, and the axial trap frequency ω_i.

Additional parameters and typical values are summarized in Table 1.1.

Chapter 2

Cavity optodynamics with atoms

In this chapter, I develop a general theoretical framework for cavity optodynamics with atomic ensembles. Starting from a microscopic atomic model, I derive an effective Hamiltonian for optodynamical coupling to collective atomic motion and spin. Then I develop a time-domain formalism for analyzing linearized dynamics of a multi-mode optodynamical system. Finally, I describe a model for optodynamical measurements obtained from the optical field transmitted through the cavity. Although the individual theoretical results derived here are not fundamentally new, my goal is to present a novel, unified framework for treating interactions in multi-mode optodynamical systems.

This chapter begins in Sec. 2.1 with a brief review of dispersive coupling between the field of a single-mode optical cavity and an ensemble of two-level atoms. Spatially dependent coupling gives rise to optomechanical interactions between the cavity field and the atomic center of mass motion [41], which has been thoroughly analyzed in previous dissertations [11, 36] and used to demonstrate quantum effects in atomic optomechanical systems [18–20, 32, 34, 35]. In Sec. 2.2, I expand this derivation to consider spin-dependent dispersive coupling within the full ground-state hyperfine manifold. The resulting effective Hamiltonian describes scalar, vector, and tensor components of the ac Stark shift acting on each atom and a corresponding spin-dependent optical phase shift imprinted on the light, which together facilitate measurement of the total atomic spin and autonomous feedback to modify its precession [23].

By controlling the trap position and applied magnetic fields, this interaction can be tuned to realize first-order coupling to the atomic position or spin, either independently or simultaneously. By linearizing the effective Hamiltonian for small amplitude oscillations of the atomic motion and spin, each of these various configurations can be generally described by a canonical multi-mode optodynamical Hamiltonian, defined in Sec. 2.4. The cavity and oscillator equations of motion and their steady-state solutions are readily obtained from this Hamiltonian, following standard frequency-domain methods [13]. Alternatively, to better facilitate analysis of pulsed, transient, or non-stationary dynamics of interacting multi-mode systems, in Sec. 2.5 I develop a reduced time-domain formalism by eliminating the cavity

field, providing a unified description across the unresolved- to resolved-sideband regimes.

Finally, in Sec. 2.6 I consider detection of the optical field transmitted through the cavity mirror, which carries information about a linear combination of oscillator quadratures. I derive a general model for heterodyne or homodyne detection that facilitates analysis of the optodynamical response and measurement noise captured in the recorded signal. As an example, I apply this model to consider the cycle-averaged mean-squared displacement, which can be derived from the recorded optodynamical signal and is useful to reveal correlated dynamics in multi-mode optodynamical systems, as demonstrated in Chap. 5. A much more detailed analysis of linear state estimation from optodynamical signals is explored in Chap. 6.

2.1   Dispersive optomechanics with two-level atoms

The interaction between an ensemble of two-level atoms and a single-mode cavity is well-described by the Tavis-Cummings Hamiltonian [42]. This familiar model for light-matter interaction is obtained after making the electric-dipole approximation, which assumes a uniform electromagnetic field across the electron wave function, and the rotating-wave approximation (RWA), which neglects the off-resonance effect of the counter-rotating component of the optical field. The resulting Hamiltonian can be written as

$$\mathcal{H}_{\mathrm{TC}} = \hbar\omega_{\mathrm{c}}\hat{c}^\dagger\hat{c} + \hbar\omega_{\mathrm{a}}\sum_i \hat{\sigma}_{e;e}^{(i)} + \hbar\sum_i\Big[g(\hat{\boldsymbol{r}}_i)\,\hat{c}\,\hat{\sigma}_{e;g}^{(i)} + g^*(\hat{\boldsymbol{r}}_i)\,\hat{c}^\dagger\hat{\sigma}_{g;e}^{(i)}\Big],\qquad(2.1)$$

in terms of the cavity photon annihilation operator $\hat{c}$ and density operators $\hat{\sigma}_{\alpha;\beta}^{(i)} = |\alpha\rangle_i\langle\beta|_i$ for each atom i, with $\alpha, \beta \in \{g, e\}$ indexing the atomic ground and excited states, respectively. Here, $g(\hat{\boldsymbol{r}})$ parametrizes the position-dependent coupling strength between the atomic dipole and the cavity mode, which quantifies the rate that excitations are exchanged between an atom and the cavity field.

The eigenstates of an atom are generally more complicated than such a two-level system. Even for relatively simple alkali atoms, with only a single valance electron, fine-structure from electronic spin-orbit coupling distinguishes the D_1 and D_2 dipole transitions according to the total electronic angular momentum $j' = \{1/2, 3/2\}$ of the excited states, respectively. Coupling between the electron and nuclear spin further induces hyperfine splitting that distinguishes ground- and excited-state manifolds, according to the total atomic spin f. The work reported in this dissertation was performed using ^{87}Rb atoms, initially polarized in the $|f = 2, m = 2\rangle$ sublevel of the $5S_{1/2}$ electronic ground state, and optically driven on the D_2 transition to the $5P_{3/2}$ excited state at wavelength 780.24 nm, with hyperfine structure sketched in Fig. 2.1a. Pumping the cavity with σ^+ polarized light, the atoms are driven on the cycling transition $|f = 2, m = 2\rangle \leftrightarrow |f' = 3, m' = 3\rangle$, and the population dynamics are constrained to the Hilbert space of this effective two-level system, as illustrated in Fig. 2.1b.

The coupling strength can be written as $g(\hat{\boldsymbol{r}}) = g_0 U(\hat{\boldsymbol{r}})$, a product of the maximum cavity-enhanced coupling strength g_0 and the relative cavity mode amplitude at position $\hat{\boldsymbol{r}}$.
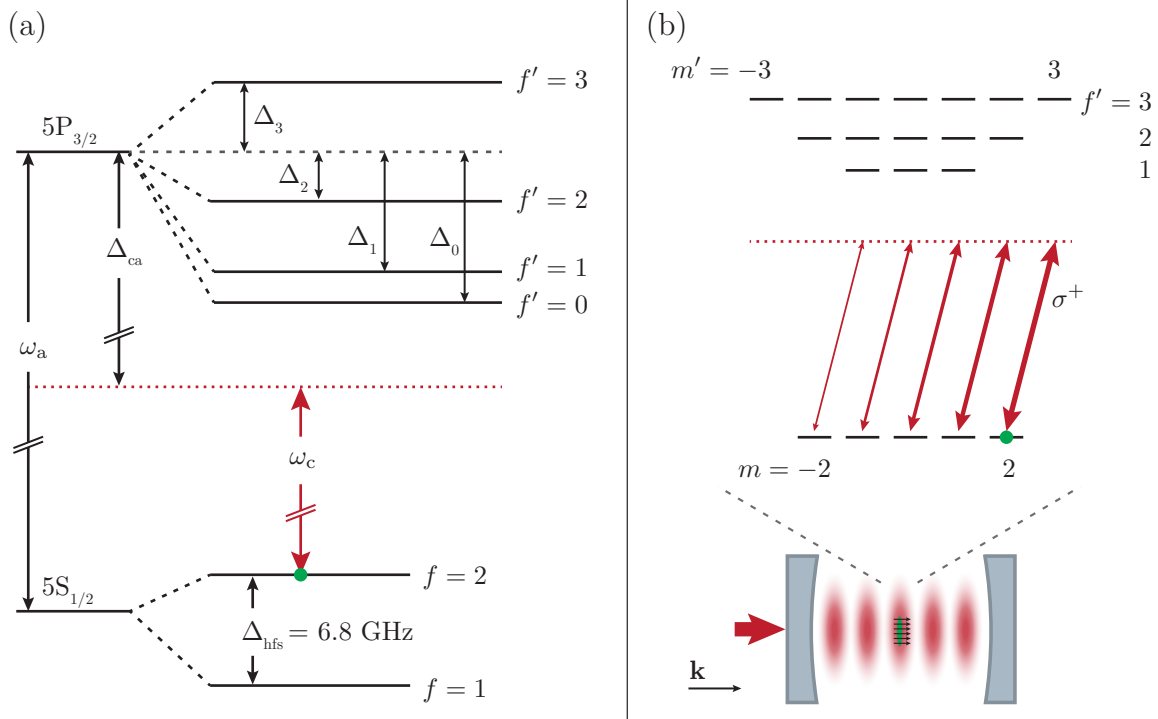
Figure 2.1: (a) Energy level diagram for the hyperfine structure of the ^{87}Rb D$_2$ transition. The cavity mode is far-detuned by $\Delta_{\mathrm{ca}} = 2\pi \times -42$ GHz from the D$_2$ line, relative to the hyperfine splittings $\Delta_{f'} = \{-302, -230, -73, 194\}$ MHz for $f' = \{0, 1, 2, 3\}$, resulting in a spin-dependent dispersive coupling that produces a scalar and vector Stark shift of the ground-state sublevels. (b) For atoms initially polarized in the $|f = 2, m = 2\rangle$ ground state, a σ^+ polarized cavity mode drives an atomic cycling transition, isolating an effective two-level system. In the dispersive coupling regime, the relative coupling strength for each spin state $\alpha_0 + \alpha_1 m$ is determined by the sum of Clebsch-Gordon coefficients for all accessible transitions, summarized by the scalar and vector coupling strengths, $\alpha_0 = 2/3$ and $\alpha_1 = 1/6$, respectively.

For a TEM$_{00}$ mode of our near-planar cavity, with the mirror spacing much less than their radius of curvature $L_c \ll R_c$ (values indicated in Table 1.1), the mode function $U(\hat{\boldsymbol{r}})$ can be approximated by a standing-wave, Gaussian wavefunction

$$U(\hat{\boldsymbol{r}}_i) \approx e^{-\hat{r}_i^2/w_0^2} \sin k_p \hat{z}_i, \tag{2.2}$$

in terms of the atomic axial and radial coordinates $\hat{z}_i$ and $\hat{r}_i$, respectively. This mode function is parameterized by the Gaussian mode waist $w_0 = 25$ μm and probe wave vector $k_p = 2\pi/(780$ nm$)$, with the mode divergence and Gouy phase neglected since the cavity length is much smaller than the Rayleigh range $z_R = 2.5$ mm.

The maximum cavity-enhanced coupling strength g_0, for an atom at an anti-node of the cavity field, is given by [8]

$$g_0 = \sqrt{\frac{\omega_{\mathrm{a}}}{2\hbar\epsilon_0 V_m}}\, d = 2\pi \times 13 \text{ MHz}, \tag{2.3}$$

in terms of the cavity mode volume $V_m = \int |U(\hat{\boldsymbol{r}})|^2 d^3x \approx \pi w_0^2 L_c/4$ and the dipole strength $d = 2.989 e a_0$ for the cycling transition [43].

Dispersive optical coupling

The nature of the optical interaction can be controlled by the detuning between the cavity frequency and the atomic transition $\Delta_{\mathrm{ca}} = \omega_{\mathrm{a}} - \omega_{\mathrm{c}}$. If this detuning is large, the probability of exciting an atom into the excited state can be made vanishingly small, while off-resonant coupling to the excited state induces a second-order correction to the ground state energies and imparts an optical phase shift. This phase shift can be described by an effective atomic index of refraction, which, like any other dispersive medium inserted into the cavity, changes the optical path length and the cavity resonance frequency.

This 'dispersive' coupling regime is realized for $|\Delta_{\mathrm{ca}}| \gg \sqrt{N_a} g_0$, with a detuning much larger than the vacuum Rabi splitting for a cavity coupled to an ensemble N_a atoms [44]. In this limit, the electronic excited state can be adiabatically eliminated from the equations of motion by assuming that the population of the excited state is negligible $\hat{\sigma}_{e;e}^{(i)} \approx 0$ and and by approximately solving for the ground-state–excited-state coherences $\hat{\sigma}_{e;g}^{(i)}$, assuming they adiabatically follow the cavity field in a rotating frame.

After eliminating the electronic excited state in this way, the resulting equations of motion are described by the effective interaction Hamiltonian

$$\mathcal{H}_{\mathrm{D}} = \hbar g_c \hat{c}^\dagger \hat{c} \sum_i e^{-2\hat{r}_i^2/w_0^2} \sin^2 k_p \hat{z}_i, \tag{2.4}$$

in terms of the dispersive coupling strength $g_c = g_0^2/\Delta_{\mathrm{ca}}$. This interaction reflects a frequency shift of the cavity resonance, determined by the spatial distribution of atoms inside the cavity mode, as well as an optical dipole force acting back on the atomic motion due to the spatially dependent optical potential.
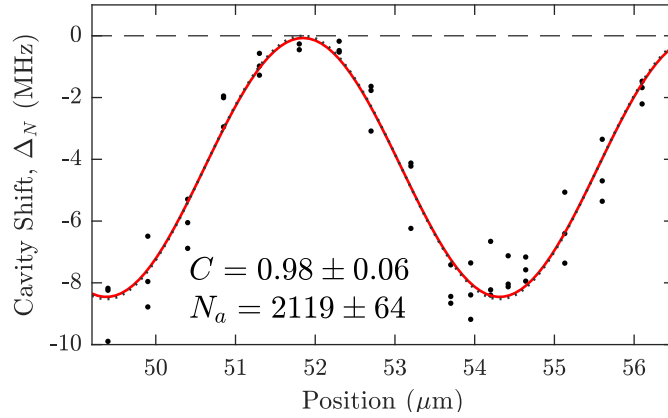
Figure 2.2: Measured cavity frequency shift from $N_a \sim 2000$ atoms, trapped at different positions z_0 across one beatnote period of the relative phase between the ODT, with wavelength $\lambda_t = 842.97560$ nm, and probe, with wavelength $\lambda_p = 780.33298$ nm. The observed contrast C and average atom number N_a are recovered from the mean and amplitude of a sinusoidal fit to $\Delta_N = g_c N_a \big[1 + C \sin(k z_0 + \phi) \big]/2$.

If the ensemble of atoms is confined to a region much smaller than the probe wavelength, achieved by loading in a single well of the ODT introduced in Sec. 1.1, then each atom experiences approximately equal coupling to the cavity mode, such that the light interacts only with fully symmetric modes of the atomic ensemble. For an ensemble trapped at an equilibrium position z_0 with probe phase $\phi_p = k_p z_0$, Eq. 2.4 can be expanded to second order in the axial center-of-mass displacement $\hat{Z} = \sum_i (\hat{z}_i - z_0)/N_a$, assuming independent axial and radial motion, yielding

$$\mathcal{H}_{\mathrm{mech}} = \hbar g_c N_a \hat{c}^\dagger \hat{c}\, e^{-2\sigma_r^2/w_0^2} \left[\sin^2(\phi_p) + k_p \hat{Z} \sin(2\phi_p) + k_p^2 (\hat{Z}^2 + \sigma_z^2) \cos(2\phi_p) \right] \qquad (2.5)$$

where σ_r and σ_z are the root-mean-square (RMS) radial and axial width of the ensemble, respectively.

The first term of this interaction describes the static cavity frequency shift due to the presence of N_a atoms at position z_0. In practice, the atom number N_a and distribution of the atomic ensemble is estimated by measuring the amplitude and contrast of this relative cavity shift as a function of loading position, as shown in Fig. 2.2. The observed contrast reflects both the width of the atomic cloud σ_r as well as the distribution of atoms into multiple neighboring wells of the incommensurate ODT, each of which experience a slightly different probe coupling phase, reducing the degree of observable contrast.

The second and third terms represent the tunable linear or quadratic optomechanical coupling to the collective motion [32], which has been explored in most work previously performed on this apparatus, covered in detail in Refs. [36–38]. The linear coupling, realized at $\phi_p = \pi/4$, has been used to demonstrate quantum optomechanical effects such as ponderomotive squeezing of light [19] and sideband thermometry of a near-ground-state oscillator

[18]. In addition, another cavity mode driven by a second trap laser at 860 nm can be used to create an optical super-lattice potential, with distinct oscillator frequencies at each trap site. This has been used to observe an array of mechanical oscillators [34] and to apply precisely calibrated forces for demonstrating optomechanical force measurement near the SQL [20]. More recently, we demonstrated cavity-mediated optomechanical coupling between two mechanical oscillators [35], defined by two neighboring wells of the hybrid optical super-lattice, which is discussed in Chap. 4.

2.2   Spin-dependent dispersive interaction

The two-level model assumed above in Eq. 2.1 is realized for an atomic ensemble polarized along a magnetic field parallel to the cavity axis and driven on the cycling transition by a σ^+ polarized cavity mode. To include more general, spin-dependent atom-light interactions, the Tavis-Cummings model in Eq. 2.1 must be generalized to describe a degenerate $f = 2$ ground state manifold dispersively coupled to multiple nearly-degenerate excited state manifolds, as sketched in Fig. 2.1. Optical transitions between particular Zeeman sublevels are polarization dependent, therefore it is also necessary to consider both orthogonal, circularly polarized cavity modes. In the following derivation, I closely follow the procedure detailed in Ref. [45].

The generalized Tavis-Cummings model can be written as sums of cavity, atom, and interaction terms

$$\mathcal{H} = \mathcal{H}_C + \sum_i \mathcal{H}_A^{(i)} + \sum_i \mathcal{H}_I^{(i)}. \tag{2.6a}$$

The cavity supports modes of two orthogonal polarizations. Assuming no intrinsic cavity birefringence (a condition that is reconsidered in Sec. 3.5), the cavity polarization modes are degenerate and can be written in terms of photon number operators $\hat{n}_\pm = \hat{c}_\pm^\dagger \hat{c}_\pm$ for circularly polarized photon operators $\hat{c}_\pm$

$$\mathcal{H}_C = \hbar\omega_c(\hat{n}_+ + \hat{n}_-). \tag{2.6b}$$

The atomic contribution represents the energy from the total population of each excited-state hyperfine manifold, with hyperfine splitting $\Delta_{f'}$, summed over all the (approximately degenerate) Zeeman sublevels

$$\mathcal{H}_A^{(i)} = \sum_e \hbar(\omega_a + \Delta_{f'})\hat{\sigma}_{e;e}^{(i)}. \tag{2.6c}$$

where the summation runs over all accessible excited state sublevels $e = |f', m'\rangle$, where $f' \in \{f - 1, f, f + 1\}$. Although I have not yet included the effect of applied magnetic fields, in the weak-field regime considered in this work, the linear Zeeman splitting is a small perturbation, which is negligible for the following derivation.

Finally, the atom-cavity interaction term can be written as

$$\mathcal{H}_I^{(i)} = \sum_{g,e} \hbar \Big[g_{g;e}^+(\hat{\boldsymbol{r}}_i)\hat{c}_+\hat{\sigma}_{e;g}^{(i)}\delta_{m+1,m'} + g_{g;e}^-(\hat{\boldsymbol{r}}_i)\hat{c}_-\hat{\sigma}_{e;g}^{(i)}\delta_{m-1,m'} + \text{h.c.} \Big] \qquad (2.6\text{d})$$

Here the summation runs over all possible transitions from the degenerate ground-state manifold $g = |f = 2, m\rangle$ to the excited states, with polarization-dependent coupling strength defined as $g_{g;e}^\pm$. Each term represents absorption or emission of circularly polarized photons in the cavity mode, driving spin-changing transitions that add or remove units of angular momentum along the cavity axis $\mathbf{k}$, which defines the quantization axis for the spin state basis. The Zeeman sublevels are labeled by the spin projection m along the cavity axis, defined by $\hat{\boldsymbol{f}} \cdot \mathbf{k}\,|f, m\rangle = m\,|f, m\rangle$, such that the transitions must satisfy the selection rule $\Delta m = \pm 1$.

As above, when the cavity detuning Δ_{ca} is large, now also with respect to the excited state hyperfine splittings Δ'_f, the excited states can be eliminated from the equations of motion by performing a similar, but much more tedious, adiabatic elimination, detailed in Appendix A. This approximation results in a spin-dependent dispersive interaction Hamiltonian, describing dynamics within the ground-state manifold

$$\mathcal{H}_I^{(i)} \approx \hbar g_c |U(\hat{\boldsymbol{r}}_i)|^2 \Big[\alpha_0(\hat{n}_+ + \hat{n}_-) + \alpha_1(\hat{n}_+ - \hat{n}_-)\hat{f}_k^{(i)}$$
$$+ \alpha_2 \Big\{ (\hat{n}_+ + \hat{n}_-)\big(\hat{f}_k^{(i)}\big)^2 - \hat{c}_-^\dagger\hat{c}_+\big(\hat{f}_+^{(i)}\big)^2 - \hat{c}_+^\dagger\hat{c}_-\big(\hat{f}_-^{(i)}\big)^2 \Big\} \Big], \quad (2.7)$$

in terms of scalar, vector, and tensor interactions with the total ensemble spin, with coupling coefficients for ^{87}Rb $F = 2$ atoms on the D$_2$ transition described by

$$\alpha_0 = \frac{1}{60}\left(\frac{24}{1 + \Delta_3/\Delta_{\text{ca}}} + \frac{15}{1 + \Delta_2/\Delta_{\text{ca}}} + \frac{1}{1 + \Delta_1/\Delta_{\text{ca}}} \right) \to \frac{2}{3}, \qquad (2.8\text{a})$$

$$\alpha_1 = \frac{1}{120}\left(\frac{28}{1 + \Delta_3/\Delta_{\text{ca}}} - \frac{5}{1 + \Delta_2/\Delta_{\text{ca}}} - \frac{3}{1 + \Delta_1/\Delta_{\text{ca}}} \right) \to \frac{1}{6}, \text{ and} \qquad (2.8\text{b})$$

$$\alpha_2 = \frac{1}{120}\left(\frac{4}{1 + \Delta_3/\Delta_{\text{ca}}} - \frac{5}{1 + \Delta_2/\Delta_{\text{ca}}} + \frac{1}{1 + \Delta_1/\Delta_{\text{ca}}} \right) \to 0, \qquad (2.8\text{c})$$

respectively, with limiting values for large Δ_{ca} indicated.

The spin coupling coefficients are displayed in Fig. 2.3 as a function of the atom-cavity detuning, which shows that for the large detuning $\Delta_{\text{ca}} = 2\pi \times -42$ GHz used throughout this work the tensor interactions are suppressed by nearly 10^{-4} and can be safely neglected. These expressions, however, are only valid so long as the detuning is much smaller than the spin-orbit splitting between the D$_1$ and D$_2$ lines $\Delta_{\text{so}} \gg \Delta_{\text{ca}}$, such that the influence of the $5\,^2\text{P}_{1/2}$ excited state can be neglected.

The scalar interaction in Eq. 2.7 couples only to the total intensity of both polarization modes. The atomic spins, however, are inherently polarization-dependent, coupling differently to each polarization of the cavity field. The two orthogonal optical modes can be
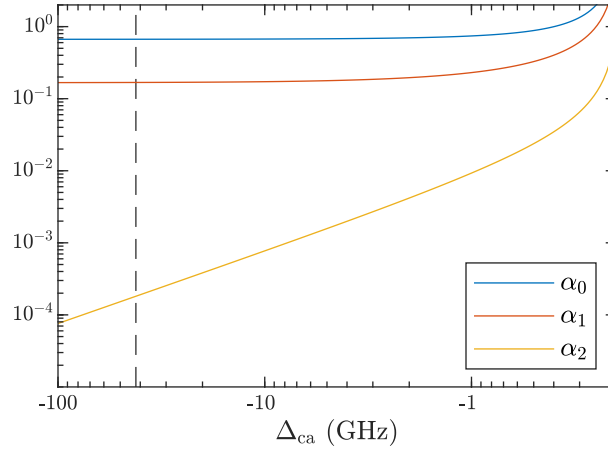
Figure 2.3: Cavity QED spin coupling coefficients for ^{87}Rb in the $f = 2$ ground-state, as a function of detuning from the D_2 transition. The atom-cavity detuning $\Delta_{\mathrm{ca}} = 2\pi \times -42$ GHz used for work reported in this thesis is indicated by a dashed line.

represented in terms of Stokes polarization operators

$$\hat{P}_x = -\frac{1}{2}\left(\hat{c}_+^\dagger \hat{c}_- + \hat{c}_-^\dagger \hat{c}_+\right) \qquad\qquad \hat{P}_y = \frac{i}{2}\left(\hat{c}_+^\dagger \hat{c}_- - \hat{c}_-^\dagger \hat{c}_+\right)$$
$$\hat{P}_z = \frac{1}{2}\left(\hat{c}_+^\dagger \hat{c}_+ - \hat{c}_-^\dagger \hat{c}_-\right) \qquad\qquad \hat{P}_0 = \left(\hat{c}_+^\dagger \hat{c}_+ + \hat{c}_-^\dagger \hat{c}_-\right), \qquad (2.9)$$

which obey the standard SU(2) commutations

$$\left[\hat{P}_i, \hat{P}_j\right] = i\epsilon_{ijk}\hat{P}_k, \quad \left[\hat{P}_0, \hat{P}_i\right] = 0. \qquad (2.10)$$

In terms of these, the interaction Hamiltonian can be recast in a suggestive form, as an interaction between the atomic spins and the polarization 'spin' of the optical field

$$\mathcal{H}_I^{(i)} \approx \hbar g_{\mathrm{c}}|U(\hat{\boldsymbol{r}}_i)|^2 \left[\alpha_0 \hat{P}_0 + 2\alpha_1 \hat{P}_z \hat{f}_k^{(i)} + \alpha_2 \left\{\hat{P}_0\left(\hat{f}_k^{(i)}\right)^2 + \hat{P}_+\left(\hat{f}_-^{(i)}\right)^2 + \hat{P}_-\left(\hat{f}_+^{(i)}\right)^2\right\}\right], \quad (2.11)$$

having defined polarization raising and lowering operators $\hat{P}_\pm = \hat{P}_x \pm i\hat{P}_y$, which convert photons between polarization modes through $\Delta m = \pm 2$ spin flips mediated by the tensor interaction.

2.3   Collective atomic optodynamics

Having derived the effective interaction Hamiltonian for an ensemble of atoms individually coupled to the cavity mode, in this section I outline the conditions under which optodynamical coupling to either or both their collective motion and spin emerges. These specific

configurations are discussed in greater detail in later chapters, indicated below, and the remaining sections of this chapter consider analytic solutions to a generalized, multi-mode optodynamical Hamiltonian which approximates small amplitude dynamics for each config-uration of the atom-cavity system described here.

Substituting the effective single-atom interaction from Eq. 2.7 into the total Hamiltonian of Eq. 2.6 and neglecting the tensor interaction terms, the total effective Hamiltonian for an ensemble of N_a atoms is

$$\mathcal{H} = \hbar\omega_\mathrm{c}\left(\hat{n}_+ + \hat{n}_-\right) + \mathcal{H}_a + \hbar g_\mathrm{c}\sum_i^{N_a}\left[\alpha_0\left(\hat{n}_+ + \hat{n}_-\right) + \alpha_1\left(\hat{n}_+ - \hat{n}_-\right)\hat{f}_k^{(i)}\right]\sin^2 k_p\hat{z}_i, \quad (2.12)$$

where $\mathcal{H}_a$ includes any external potentials or magnetic fields applied to the atoms.

This Hamiltonian describes all experiments considered in the following chapters, yet it is still a formidable model to solve, with $3N_a$ motional degrees of freedom and N_a individ-ual spins. However, for atoms symmetrically coupled to the cavity mode, the optical field interacts only with the fully symmetric, 'bright' collective modes, such as the atomic center of mass motion and total spin. The remaining order $\mathcal{O}(N_a) - 1$ degrees of freedom do not dynamically couple to the cavity mode and form an effective bath which thermalizes the collective modes.

The nature of the collective interactions can be controlled through the atomic part of the Hamiltonian $\mathcal{H}_a$ in Eqs. 2.6, determining the atomic eigenstates which are probed and coupled by the optical interaction. As introduced in Sec. 2.1, the relative phase $\phi_p = k_p z_0$ of coupling to the cavity mode $U(\hat{r})$ can be controlled by choosing the position of the trapping potential z_0. In addition, an external magnetic field $\boldsymbol{B} \parallel \mathbf{z}$ applied at a chosen angle θ_B from the cavity axis, illustrated in Fig. 1.3, defines the eigenstates of the atomic spin and allows tuning of the optical coupling between the longitudinal or transverse spin components. These two experimental knobs, the position and magnetic field angle, define four particular configurations of interest, illustrated in Fig. 2.4 and described below.

For simplicity in the following examples, I consider only the σ^+ circularly polarized cavity mode, which is a good approximation when the cavity is driven with a circularly polarized laser. Only the tensor interaction terms in the preceding section mediate exchange of photons between modes of different circular polarization, which is negligible for $\Delta \gg \Delta_f'$ in the dispersive limit where this work was performed. This can be intuitively understood by recognizing that the cavity's optical field couples primarily to the electronic state of the atom. The total electron angular momentum is $j = 1/2$ in the ground state, so transitions between electronic configurations only support at most $\Delta m = 1$ changes in the total atomic spin. Therefore the nuclear spin must be involved to drive $\Delta m = \pm 2$ atomic transitions, associated with stimulated absorption and emission of photons with opposite circular polarization. Optical coupling to the nuclear spin $I = 3/2$ is mediated through the hyperfine interaction in the electronic excited states, and the electron must spend sufficient time $t \sim |\Delta_\mathrm{ca}|^{-1} \gg |\Delta_f'|$ in the excited states to resolve the hyperfine structure. The effective time an electron spends in the excited states is suppressed for large detuning $|\Delta_\mathrm{ca}| \gg |\Delta_f'|$, resulting in approximate
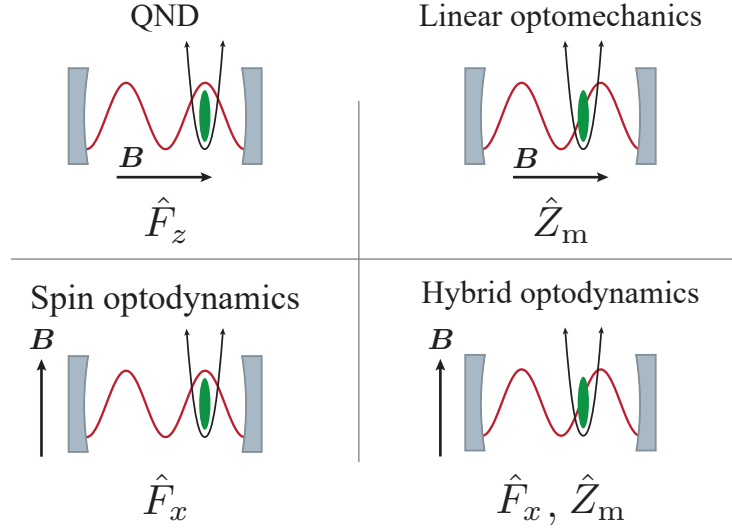
Figure 2.4: Chart of four primary atom-cavity configurations considered in this work. Each configuration is a combination of trap position, either at a probe anti-node or at the maximum intensity gradient, and orientation of the applied magnetic field, either along the cavity axis or transverse to it. In each combination, the collective atomic operators primarily sensed by the cavity are indicated.

conservation of the photon number in each circularly polarized. Conservation of photon helicity, however, is broken if the cavity has a linear birefringence, which introduces an intrinsic rotation between circular polarization states, a complication considered in Sec. 3.5.

QND measurement

If the atoms are confined at an anti-node of the probe field, where the intensity and therefore coupling strength is greatest, there is no spatial variation of the probe intensity to first order, suppressing optical sensitivity to the atomic motion. Additionally, a magnetic field applied parallel to the cavity axis $\mathbf{k} = \mathbf{z}$ fixes the quantization axis, and the atomic Hamiltonian can be written

$$\mathcal{H}_a = \hbar\omega_\mathrm{s}\hat{F}_z, \tag{2.13}$$

assuming a linear Zeeman splitting, in the weak-field limit, with Larmor frequency $\omega_\mathrm{s} = \mu_B|g_f\mathbf{B}|/\hbar$. The total Hamiltonian can then be written entirely in terms of a scalar cavity shift proportional to the atom number and a vector cavity shift proportional to the total longitudinal spin $\hat{F}_z = \sum_i \hat{f}_z^{(i)}$.

$$\mathcal{H} = \hbar\omega_\mathrm{c}\hat{n}_+ + \hbar\omega_\mathrm{s}\hat{F}_z + \hbar g_\mathrm{c}\hat{n}_+\left[\alpha_0 N_a + \alpha_1\hat{F}_z\right]. \tag{2.14}$$

The interaction term commutes with the total Hamiltonian, realizing a quantum non-demolition (QND) measurement of the atom number and longitudinal spin through the shifted

cavity resonance frequency. This longitudinal spin measurement is used in Sec. 3.4 to calibrate rf pulses and measure the spin relaxation and dephasing rates. I have neglected the quadratic optomechanical coupling term $\propto \hat{Z}_{\mathrm{m}}^2$ which appears in Eq. 2.5, because it is second-order in the collective Lamb-Dicke parameter $\eta = k_p z_{\mathrm{HO}} \approx 0.17$ and is therefore negligible for small phonon occupation numbers.

Linear Optomechanics

In the optomechanical configuration, described in Sec. 2.1, the atoms are trapped at the maximum linear gradient of the probe intensity in an applied magnetic field parallel to the cavity axis. The total Hamiltonian therefore commutes with $\hat{F}_z$, conserving the total longitudinal spin component such that only optomechanical dynamics are observed. If the atomic spins begin fully polarized in the high-energy state, the total Hamiltonian can then be approximated to first order as

$$\mathcal{H} = \hbar\omega_{\mathrm{c}}\hat{n}_+ + \hbar\omega_{\mathrm{m}}\hat{F}_z\hat{n}_m + \hbar N_a g_{\mathrm{c}} k_p \hat{n}_+ \hat{Z}, \tag{2.15}$$

in terms of the atomic center-of-mass position $\hat{Z}$. This optomechanical model is extended in Chap. 4 to describe the motion of two atomic ensembles, trapped in neighboring sites of a super-lattice potential formed by two ODTs, which gives each ensemble a distinguishable axial mechanical frequency.

Spin Optodynamics

If the atoms are trapped at the probe anti-node, again suppressing coupling to their motion, but the magnetic field is oriented transverse to the cavity axis $\mathbf{k} = \mathbf{x}$, then the cavity is sensitive to one of the oscillating components of the transverse spin. The Hamiltonian can be written in terms of components of the total spin

$$\mathcal{H} = \hbar\omega_{\mathrm{c}}\hat{n}_+ + \hbar\omega_{\mathrm{s}}\hat{F}_z + \hbar g_{\mathrm{c}}\hat{n}_+ \left[\alpha_0 N_a + \alpha_1 \hat{F}_x\right], \tag{2.16}$$

where the interaction with the optical field appears like an effective magnetic field along the cavity axis, mediating an exchange of energy between the spin and optical mode. This configuration for cavity spin optodynamics is considered in Chap. 3.

Hybrid spin & mechanical optodynamics

Finally, the remaining configuration realizes simultaneous coupling to the collective spin and motion by both placing the atoms at the linear gradient of the probe intensity and orienting the magnetic field transverse to the cavity axis. A full derivation for this configuration is presented in Chap. 5. The resulting Hamiltonian that describes dynamics of the collective atomic modes is

$$\mathcal{H} = \hbar\omega_{\mathrm{c}}\hat{n}_+ + \hbar\omega_{\mathrm{m}}\hat{n}_m + \hbar\omega_{\mathrm{s}}\hat{F}_z + \hbar g_{\mathrm{c}}\hat{n}_+ \left(\alpha_0 N_a + \alpha_1 \hat{F}_x\right)\left(\frac{1}{2} + k_{\mathrm{p}}\hat{Z}_{\mathrm{m}}\right), \tag{2.17}$$

which contains optical interactions with both the center-of-mass position as well as the total spin. In addition, a cross term proportional to $\hat{F}_x \hat{Z}_{\mathrm{m}}$ arises from the spatial variation of the vector ac Stark shift of the atomic states, which directly mediates an interaction between the atomic motion and spin, independent of the optical dynamics. This term is like an effective static magnetic-field gradient, and is also associated with a spin-orbit coupling of each individual atom, which drives incoherent coupling between the total spin and the bath of residual mechanical modes in the center of mass frame, described in Sec. 5.2.

2.4 Canonical optodynamical Hamiltonian

For small amplitude excitations, the optodynamical interactions with the collective motion and spin outlined above can be described with a unified model. In particular, for small deflections away from the applied magnetic field, the motion of a large collective spin precessing on a sphere can be approximately mapped to the rotation of a harmonic oscillator in phase space. This approximation is more rigorously defined in Sec. 3.1, but the essential result here is that the transverse collective spin can be written in terms of a unit-less spin 'displacement' quadrature $\hat{X}_s = \sqrt{2/F}\hat{F}_x = (\hat{a}_s^\dagger + \hat{a}_s)/\sqrt{2}$ for a bosonic spin excitation operator $\hat{a}_s$, as illustrated in Fig. 2.5. In this approximation, the torque produced by the optical interaction becomes a generalized 'force' acting on this spin oscillator.

This approximation allows each of the three different optodynamical Hamiltonians, in Eqs. 2.15, 2.16, and 2.17, to be generalized to a canonical multi-mode optodynamical Hamil-
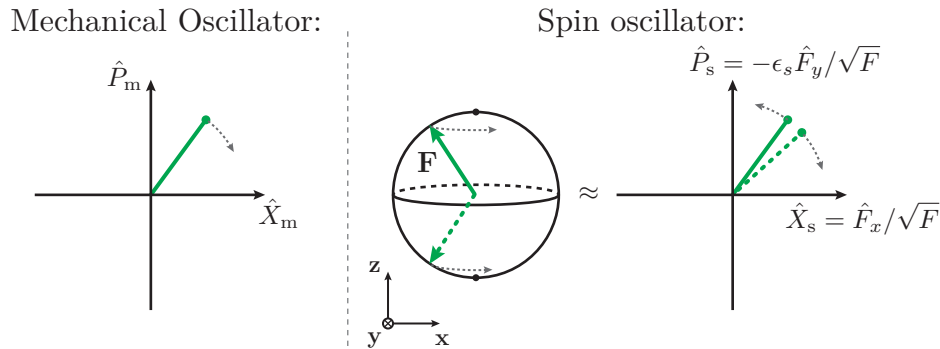
Figure 2.5: Phase space representation of a mechanical harmonic oscillator and an analogous approximation for Larmor precession of the collective spin as a spin oscillator. For small excitations of the collective spin away from the magnetic pole, the spin phase space represents a 2-D projection of the Bloch sphere, viewed from outside toward the center. Near the high-energy pole, the collective spin quadratures rotate in the opposite direction, like an effective negative mass oscillator.

tonian

$$\mathcal{H}_{\mathrm{OD}} = \hbar\omega_{\mathrm{c}}\hat{c}^\dagger\hat{c} + \hbar\sum_i \epsilon_i\omega_i\hat{a}_i^\dagger\hat{a}_i + \hbar\hat{c}^\dagger\hat{c}\sum_i g_i(\hat{a}_i^\dagger + \hat{a}_i), \tag{2.18}$$

for bosonic modes $\hat{a}_i$, generalized to describe arbitrary positive and negative effective masses $\epsilon_i = \pm 1$ respectively, with corresponding optodynamical coupling strengths g_i. The cavity frequency ω_{c} has also been redefined to include the appropriate static frequency shift induced by the presence of the atoms.

The interaction term in Eq. 2.18 contains products of three amplitudes, which give rise to non-linear equations of motion analogous to an optical Kerr non-linearity [46]. Considering a steady-state cavity photon number $\bar{n} = \langle \hat{c}^\dagger\hat{c} \rangle$, the interaction term describes an average radiation-pressure force on the oscillator, displacing its equilibrium position by order $\bar{n}g_i/\omega_i$. This displacement also shifts the cavity resonance frequency by order $\bar{n}g_i^2/\omega_i$, which causes a change in the intracavity photon number $\bar{n}$ if this shift is significant on the scale of the cavity half-linewidth κ. The full non-linear equations describing the intra-cavity intensity and equilibrium position can be numerically solved self-consistently, and describe effects such as optodynamical bistability [23, 32].

However, in the present work I consider the linear regime defined by $\bar{n}g_i^2/\omega_i \ll \kappa$, where the optical backaction provides only a weak perturbation of the oscillator potential. The interaction term can then be linearized by expanding the cavity field operator to describe fluctuations around the mean amplitude $\hat{c} \to e^{-i\omega_{\mathrm{p}}t}(\sqrt{\bar{n}} + \hat{c})$, illustrated in Fig. 2.6, having transformed into a frame rotating at the frequency of the cavity probe laser ω_{p}. This transformation assumes a coherent cavity drive laser with sufficient amplitude to maintain the intra-cavity photon number $\bar{n}$, which is determined by measuring the light transmitted through the cavity, described in Appendix B.1. Further assuming a small modulation depth of the cavity field $\hat{c} \ll \bar{n}$, satisfied for sufficiently small amplitude motion of the oscillators $\hat{X}_i \ll \kappa/g_i$, the optodynamical interaction in Eq. 2.18 can be approximated to first order in the field fluctuations, described by the linearized optodynamical Hamiltonian

$$\mathcal{H}_{\mathrm{OD}} = -\hbar\Delta\hat{c}^\dagger\hat{c} + \hbar\sum_i \epsilon_i\omega_i\hat{a}_i^\dagger\hat{a}_i + \hbar\sqrt{\bar{n}}(\hat{c}^\dagger + \hat{c})\sum_i g_i(\hat{a}_i^\dagger + \hat{a}_i), \tag{2.19}$$

having defined the cavity-probe detuning $\Delta = \omega_{\mathrm{c}} - \omega_{\mathrm{p}}$.

Input-output theory and equations of motion

Because the cavity is an open system, exchanging information with the environment in addition to the coherent dynamics described by the system Hamiltonian, a full dynamical description requires including non-Hermitian input and output dynamics. This can be treated rigorously by deriving a master equation, resulting in the Lindblad equation for a system weakly coupled to a Markovian reservoir. The open quantum dynamics can equivalently be formulated as Heisenberg-Langevin equations of motion by including the appropriate input and output terms to describe the exchange of information with the environment.
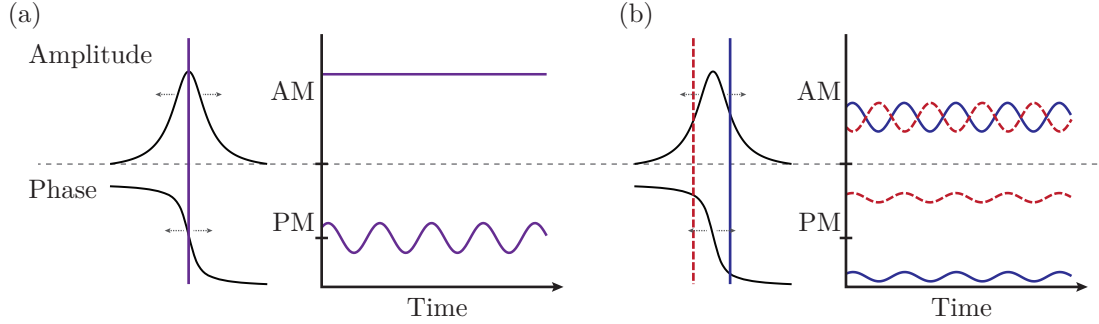
Figure 2.6: Optodynamical modulation of an optical cavity probe (a) The phase of an on-resonance probe laser is modulated by the optodynamical cavity resonance shift, with no amplitude modulation to first order. (b) At a moderate probe detuning, the atomic dynamics predominately modulate the intracavity amplitude, with opposite phase for detuning above vs. below cavity resonance (solid blue vs. dashed red).

For a bosonic mode such as the cavity field $\hat{c}$, coupled to an approximate white-noise bath of bosonic modes, the equation of motion is determined by the system Hamiltonian, in addition to damping and diffusion driven by input bath noise $\hat{\xi}$ [47–49]

$$\dot{\hat{c}} = [\mathcal{H}, \hat{c}] - \kappa\hat{c} + \sqrt{2\kappa}\hat{\xi}. \tag{2.20}$$

Here, κ is the optical cavity's *half*-linewidth, representing the exponential decay of the field amplitude leaking out of the cavity. For a cavity driven by coherent laser light, the input noise is purely vacuum fluctuations of the cavity probe, with two-time correlation $\langle\hat{\xi}(t)\hat{\xi}^\dagger(t')\rangle = \delta(t - t')$. The resulting equation of motion for the cavity field is therefore

$$\dot{\hat{c}} = (i\Delta - \kappa)\hat{c} - i\sqrt{\bar{n}}\sum_i g_i(\hat{a}_i^\dagger + \hat{a}_i) + \sqrt{2\kappa}\hat{\xi} \tag{2.21}$$

The oscillator equations of motion can be similarly obtained. Consider an independent thermal bath $\hat{\eta}_i$ for each oscillator mode, with *energy* relaxation rate Γ_i (which corresponds to the oscillator's full spectral linewidth) and bath temperature parametrized in terms of the oscillators equilibrium thermal occupation ν_i, with two-time correlation $\langle\hat{\eta}_i^\dagger(t)\hat{\eta}_i(t')\rangle = \nu_i\delta(t - t')$. The resulting oscillator equations of motion are

$$\dot{\hat{a}}_i = \left(-i\epsilon_i\omega_i - \frac{\Gamma_i}{2}\right)\hat{a}_i - i\sqrt{\bar{n}}g_i(\hat{c}^\dagger + \hat{c}) + \sqrt{\Gamma_i}\hat{\eta}_i \tag{2.22}$$

It is helpful to also write these equations in terms of the Hermitian quadratures of the optical field

$$\dot{\hat{c}}_{\mathrm{AM}} = -\kappa\hat{c}^{\mathrm{AM}} - \Delta\hat{c}^{\mathrm{PM}} + \sqrt{2\kappa}\hat{\xi}^{\mathrm{AM}} \tag{2.23a}$$

$$\dot{\hat{c}}_{\mathrm{PM}} = \Delta\hat{c}^{\mathrm{AM}} - \kappa\hat{c}^{\mathrm{PM}} - 2\sqrt{\bar{n}}\sum_i g_i\hat{Z}_i + \sqrt{2\kappa}\hat{\xi}^{\mathrm{PM}} \tag{2.23b}$$

and oscillators

$$\dot{\hat{X}}_i = -\frac{\Gamma_i}{2}\hat{X}_i + \epsilon_i\omega_i\hat{P}_i + \sqrt{\Gamma_i}\hat{\eta}_i^{\mathrm{AM}} \tag{2.23c}$$

$$\dot{\hat{P}}_i = -\epsilon_i\omega_i\hat{X}_i - \frac{\Gamma_i}{2}\hat{P}_i - 2\sqrt{\bar{n}}g_i\hat{c}^{\mathrm{AM}} + \sqrt{\Gamma_i}\hat{\eta}_i^{\mathrm{PM}}, \tag{2.23d}$$

as defined in Sec. 1.4.

Care must be taken to heed the definition of κ as the cavity *half*-linewidth and Γ_i as the oscillator *full*-linewidth, which, though perhaps an odd choice that creates an easily overlooked factor of 2, this convention has been used in much of our previous work.

Single-oscillator optodynamical susceptibility

Most linear optomechanical effects are best described in frequency space, in terms of complex spectral susceptibilities and input noise power spectral densities. Frequency-domain optomechanical solutions are well-described in standard references [13], where the linear equations of motion can be transformed into simple algebraic equations in Fourier space. This is particularly powerful for multi-mode systems, which can be manipulated and solved efficiently as matrix equations [50], allowing efficient derivation of optomechanical effects such as damping and amplification [51–54], ponderomotive squeezing [19, 55], optomechanically induced transparency (OMIT) [56–58], standard quantum limits of measurement [20, 59], and multi-mode optomechanical coupling [35, 60].

The equations of motion for the linearized system defined by Eqs. 2.23 can be represented compactly in matrix notation as

$$\frac{\partial}{\partial t}\hat{\boldsymbol{X}} = \mathrm{M}\hat{\boldsymbol{X}} + \hat{\boldsymbol{v}}, \tag{2.24}$$

with the system's state represented by a vector of quadrature operators

$$\hat{\boldsymbol{X}} = \begin{pmatrix} \hat{c}^{\mathrm{AM}}, & \hat{c}^{\mathrm{PM}}, & \hat{X}_1, & \hat{P}_1, & \dots \end{pmatrix}^{\mathsf{T}}. \tag{2.25}$$

The homogeneous part of the system of equations defines a response matrix M and the inhomogeneous part an input vector $\boldsymbol{v}$ of stochastic or coherent drives.

For a single-mode optomechanical system, this dynamical matrix and input noise vector are

$$\mathrm{M} = \begin{pmatrix} -\kappa & -\Delta & 0 & 0 \\ \Delta & -\kappa & -2\sqrt{\bar{n}}g_1 & 0 \\ 0 & 0 & -\Gamma_1/2 & \epsilon_1\omega_1 \\ -2\sqrt{\bar{n}}g_1 & 0 & -\epsilon_1\omega_1 & -\Gamma_1/2 \end{pmatrix} \quad \text{and} \quad \hat{\boldsymbol{v}} = \begin{pmatrix} \sqrt{2\kappa}\hat{\xi}^{\mathrm{AM}} \\ \sqrt{2\kappa}\hat{\xi}^{\mathrm{PM}} \\ \sqrt{\Gamma_1}\hat{\eta}^{\mathrm{AM}} \\ \sqrt{\Gamma_1}\hat{\eta}^{\mathrm{PM}} \end{pmatrix}, \tag{2.26}$$

respectively. The equations of motion are then readily solved in Fourier space, with the quadrature response to input components at frequency ω given by

$$\hat{\boldsymbol{X}}[\omega] = -(\mathrm{M} + i\omega\mathbb{I})^{-1}\hat{\boldsymbol{v}}[\omega]. \tag{2.27}$$

This result reflects that, for linear systems, the inputs are mapped onto the system response according to a susceptibility matrix $\Xi[\omega] = -(\mathrm{M} + i\omega\mathbb{I})^{-1}$, with element $\Xi_{ij}[\omega]$ describing the response of quadrature i to inputs on quadrature j [50]. The analytic form of the general susceptibility matrix is cumbersome, however particular elements can be investigated to form some intuition about what it represents.

The oscillator susceptibility $\chi_i[\omega] = \langle \hat{X}_i[\omega] \rangle / F[\omega]$ is defined as the linear response of the oscillator position to a fictitious test 'force' $F(t) = F_0 \cos\omega t$ at frequency ω, which drives the oscillator's momentum quadrature according to $\partial \hat{P}_1 / \partial t = \cdots + \epsilon_i F(t)$. The optically modified oscillator susceptibility can be obtained from the full susceptibility matrix $\Xi[\omega]$, as the element describing transduction of an applied force to the oscillator's position $\chi_1[\omega] = \epsilon_1 \Xi_{34}[\omega]$. The inverse of this susceptibility is given by [13]

$$\chi_i^{-1}[\omega] = \chi_0^{-1}[\omega] + \Sigma_i[\omega], \tag{2.28}$$

which is modified by the optodynamical interaction according to

$$\Sigma_i[\omega] = \frac{4\epsilon_i \bar{n} g_i^2 \Delta}{\Delta^2 + (\kappa + i\omega)^2}. \tag{2.29}$$

For weak coupling, this optodynamical interaction represents a small perturbation of the oscillator's response and the optodynamical modification $\Sigma_i[\omega]$ can be evaluated in the vicinity of the natural response frequency $\omega \approx \omega_i$. By comparison to the bare oscillator's susceptibility $\chi_0^{-1}[\omega] = (\omega_i^2 - \omega^2 - i\Gamma_i\omega)/\omega_i$, assuming $\Gamma_i \ll \omega_i$, this modification can then be summarized as an optodynamical frequency shift and damping rate,

$$\delta\omega_{\mathrm{opt}} = \mathrm{Re}\{\Sigma_1[\omega_1]\}/2 \qquad \text{and} \qquad \Gamma_{\mathrm{opt}} = -\,\mathrm{Im}\{\Sigma_1[\omega_1]\} \tag{2.30}$$

respectively. The sign of these optodynamical effects depends on that of the effective mass of the oscillator ϵ_i, such that the frequency shift and damping rate are inverted for a negative mass oscillator. This damping rate is the exponential decay rate of the oscillator's occupation, which for a negative-mass oscillator corresponds to an increase in energy.

2.5   Time-domain optodynamical formalism

This optically dressed oscillator susceptibility together with the spectra of cavity probe shot noise and the oscillators' thermal baths are sufficient to describe most steady-state dynamics of single-mode optomechanical systems, such as the collective atomic spin optodynamics explored in Chap. 3. However, frequency-domain solutions are less suitable for non-equilibrium dynamics and time-resolved dynamics, such as pulsed measurements and interactions, or unstable systems with positive gain. To model such situations, it is helpful to develop a time-domain formalism for optomechanical systems.

Analytic solution of general linear systems

Systems of linear equations, in principle, yield straight-forward analytic solutions. Although linear systems might be seen as theoretically trivial, they can provide tractable models that approximate non-linear systems, by expanding around a steady-state condition such as performed in Eq. 2.19. To begin analyzing such a Hamiltonian, here I derive a general solution for the multi-mode covariance matrix C for an arbitrary set of linear equations of motion, assuming Markovian baths, which will be useful for numerical calculations.

Given a linear system fully described by the state vector of quadrature operators $\hat{\boldsymbol{X}}$ and equations of motion summarized by Eq. 2.24 in terms of the dynamical matrix M, the general solution for this linear system can be directly written

$$\hat{\boldsymbol{X}}(t) = e^{\mathrm{M}t}\hat{\boldsymbol{X}}(0) + \int_0^t d\tau e^{\mathrm{M}(t-\tau)}\hat{\boldsymbol{v}}(\tau) \tag{2.31}$$

Time propagation of the quadratures is described by the matrix exponential $e^{\mathrm{M}t}$, which represents the coherent impulse response of the entire system.

In the absence of any coherent drives, the input vector $\hat{\boldsymbol{v}}$ is purely stochastic with zero mean, and time evolution of the coherent amplitude is simply given by propagation of the initial state

$$\langle \hat{\boldsymbol{X}}(t) \rangle = e^{\mathrm{M}t}\langle \hat{\boldsymbol{X}}(0) \rangle. \tag{2.32}$$

The covariance of the state vector also evolves through diffusion driven by the stochastic inputs. If all system baths are Markovian, with no memory, then the input vector defined in 2.26 represents temporally uncorrelated white noise, with two-time correlation function

$$\langle \hat{v}_i(t)\hat{v}_j^\dagger(t') \rangle = \mathrm{N}_{ij}\delta(t-t') \tag{2.33}$$

defining the noise covariance matrix N.

Time evolution of the 2nd-moment matrix $\mathrm{C}(t) = \langle \hat{\boldsymbol{X}}(t)\hat{\boldsymbol{X}}^\dagger(t) \rangle$ is then given by

$$\mathrm{C}(t) = e^{\mathrm{M}t}\mathrm{C}(0)e^{\mathrm{M}^\dagger t} + \int_0^t d\tau e^{\mathrm{M}\tau}\mathrm{N}e^{\mathrm{M}^\dagger \tau} \tag{2.34}$$

Assuming the matrix M is not singular, then there exists an eigen-decomposition M = EDE^{-1}, where D is a diagonal matrix of eigenvalues λ_i, and E is a matrix formed by columns of the corresponding eigenvectors, which transforms the single-oscillator quadratures into a new set of normal modes. For systems of more than two modes, diagonalizing the dynamics might be complicated analytically, but a simple numerical solution of the eigensystem allows calculation of the time evolution with no further approximations.

Writing the covariance matrix and noise input matrix in the normal mode basis, according to $\mathrm{C}' = \mathrm{E}^{-1}\mathrm{C}(\mathrm{E}^{-1})^\dagger$ and $\mathrm{N}' = \mathrm{E}^{-1}\mathrm{N}(\mathrm{E}^{-1})^\dagger$, time evolution of the 2nd-moments is given by

$$\mathrm{C}'(t) = e^{\mathrm{D}t}\mathrm{C}'(0)e^{\mathrm{D}^\dagger t} + \int_0^t d\tau e^{\mathrm{D}\tau}\mathrm{N}'e^{\mathrm{D}^\dagger \tau} \tag{2.35}$$

Because the exponentials are now diagonal, this can easily be evaluated for each component of the matrix, resulting in

$$\mathrm{C}'_{ij}(t) = (\mathrm{C}'_{ij}(0) - \bar{\mathrm{C}}'_{ij})e^{(\lambda_i + \lambda_j^*)t} + \bar{\mathrm{C}}'_{ij} \qquad \text{where} \qquad \bar{\mathrm{C}}'_{ij} = -\frac{\mathrm{N}'_{ij}}{\lambda_i + \lambda_j^*}. \qquad (2.36)$$

For a system with a stable kernel (M is negative definite, such that $\mathrm{Re}[\lambda_i] < 0$), this solution describes transient decay of the initial correlations, saturating to the steady-state matrix $\bar{\mathrm{C}}'$ for $t \to \infty$. For an unstable system, the first, coherent term dominates, resulting in exponential growth of the unstable modes, with relative correlations at long time reduced by the added noise from N_{ij}. The 2nd-moment matrix can be transformed back to the single-mode basis using the eigenvector matrix E according to

$$\mathrm{C}(t) = \mathrm{E}\mathrm{C}'(t)\mathrm{E}^\dagger. \qquad (2.37)$$

If M is a normal matrix, satisfying $[\mathrm{M}, \mathrm{M}^\dagger] = 0$, then this eigenvector transformation is unitary, with $\mathrm{E}^{-1} = \mathrm{E}^\dagger$, and the interacting system can be diagonalized in terms of canonical normal modes by a Bogoliubov transformation. However, if the approximate system Hamiltonian is not positive definite, then the resulting linearized equations of motion might not be diagonalizable in terms of a canonical Bogoliubov transformation, and require a more general treatment [61]. Assuming the dynamics can be diagonalized in terms of non-interacting modes $\mathcal{H} = \hbar \sum_i \omega_i \bar{b}_i b_i$, the corresponding normal-mode operators need not satisfy the canonical bosonic commutation relation, such that $[b_i, \bar{b}_j] \neq \delta_{ij}$ and $b_i^\dagger \neq \bar{b}_i$. For the case of the negative-mass instability, explored in Chapter 5, this allows the realization of a "quantum-mechanics-free" normal mode, facilitating two-mode squeezing and quantum-limited amplification of the initial oscillator states.

Eliminating the optical field

The canonical optodynamical Hamiltonian in Eq. 2.18, extended to include N mechanical or spin modes, represents a system of $N+1$ coupled harmonic oscillators, with an all-to-one coupling of each individual oscillator to the cavity field. In this model, the optical field serves as a shared communication bus, with cavity photons mediating interactions between all oscillators coupled to the cavity, independent of their physical location in the cavity mode. Symmetric coupling of each ensemble to the single-mode cavity restricts the interaction to collective atomic modes, facilitating collectively enhanced dynamics, such as the negative-mass instability presented in Chap. 5.

It is useful, then, to eliminate the cavity degree of freedom from the equations of motion, effectively tracing over the cavity states to obtain a reduced set of equations describing the effective interactions induced between each mode of motion [62]. The response of the cavity field to modulations of the dispersive interaction is determined by the cavity amplitude decay rate κ. If this rate is much faster than the oscillator motion, then the cavity field adiabatically follows their motion, such that the cavity field can be solved in terms of

the instantaneous state of the oscillators. For the multi-mode optodynamical experiments considered in Chaps. 4 and 5, the oscillator frequencies are limited to below 150 kHz by the axial trap frequency, placing the system well-within this fast cavity or 'unresolved-sideband' regime ($\kappa \gg \omega_i$ for all oscillator frequencies ω_i).

A first-order approximation of the cavity field can be obtained through an adiabatic approximation, assuming $\dot{\hat{c}} = 0$ and solving for the state of the cavity field from Eq. 2.21. This approximation captures the optical spring effect, reproducing the optodynamical frequency shift for a single oscillator in the unresolved-sideband limit. However, it neglects the non-adiabatic optodynamical damping effect, which quantifies the exchange of energy between the oscillator and optical field. This effect arises from a viscous force, proportional to the oscillator momentum, caused by a delay between the oscillator motion and the cavity field response. This delay depends on the finite cavity lifetime, which is neglected in the simple adiabatic approximation above, effectively taking $\kappa \to \infty$.

High-Q oscillator approximation

To obtain a more general solution, I begin by solving for the cavity's amplitude spectrum

$$\hat{c}[\omega] = \frac{-i\sqrt{\bar{n}}}{\kappa - i(\Delta + \omega)} \sum_j g_j \left(\hat{a}_j^\dagger[\omega] + \hat{a}_j[\omega] \right) + \frac{\sqrt{2\kappa}}{\kappa - i(\Delta + \omega)} \hat{\xi}[\omega] \tag{2.38}$$

obtained from the Fourier transform of Eq. 2.21. Transforming this solution back into the time domain is not trivial, due to the frequency dependent coefficient of the optodynamical interaction, complicating evaluation of the inverse Fourier transform.

This transformation can be greatly simplified by making a simple assumption of a high-Q oscillator, with $\omega_j \gg \Gamma_i$. The position spectrum $\hat{Z}_j[\omega]$ for such an oscillator is sharply peaked at sideband frequencies $\pm\omega_j$ and negligible elsewhere. This position spectrum can be approximated by Dirac delta functions, and then the coefficients in Eq. 2.38 need only be evaluated at the sideband frequencies, assuming the cavity susceptibility is approximately uniform across the peak width Γ_i (satisfied if either $\kappa \gg \Gamma_i$ or $\Delta \gg \Gamma_i$). Making this approximation, noting the identity $\hat{a}_j^\dagger[\omega] = (\hat{a}_j[-\omega])^\dagger$, and performing the inverse Fourier transform gives

$$\hat{c}(t) \cong -i\sqrt{\bar{n}} \sum_j g_j \left(\frac{1}{\kappa - i(\Delta - \epsilon_i\omega_j)} \hat{a}_j^\dagger(t) + \frac{1}{\kappa - i(\Delta + \epsilon_i\omega_j)} \hat{a}_j(t) \right) + \sqrt{\frac{2}{\kappa}} \hat{\xi}_\Delta(t), \tag{2.39}$$

with the intracavity shot noise fluctuations given by

$$\hat{\xi}_\Delta(t) = \frac{1}{\sqrt{2\pi}} \int_{-\infty}^{\infty} d\omega \frac{\kappa}{\kappa - i(\Delta + \omega)} e^{-i\omega t} \hat{\xi}[\omega]. \tag{2.40}$$

It is noteworthy that $\hat{\xi}_\Delta(t)$ is not a unitary transformation of the shot noise entering the cavity, with the cavity's susceptibility shaping the spectrum of quantum noise. The commutator

and two-time correlation are

$$\langle\hat{\xi}_\Delta(t)\hat{\xi}_\Delta^\dagger(t')\rangle = [\hat{\xi}_\Delta(t),\hat{\xi}_\Delta^\dagger(t')] = \frac{\kappa}{2}e^{i\Delta(t-t')-\kappa|t-t'|}, \tag{2.41}$$

which can be approximated as delta-correlated white noise

$$\langle\hat{\xi}_\Delta(t)\hat{\xi}_\Delta^\dagger(t')\rangle \approx \frac{\kappa^2}{\kappa^2+\Delta^2}\delta(t-t') \tag{2.42}$$

for frequency components ω in the unresolved-sideband limit $\kappa \gg \omega$, when the cavity noise correlation time $1/\kappa$ is much shorter than all other timescales of interest.

This solution of the cavity field can be expressed in terms of optical quadratures

$$\hat{c}^{\mathrm{AM}}(t) = \sqrt{\bar{n}}\sum_j g_j\left(\mathrm{Re}\{\alpha[\epsilon_i\omega_j]\}\hat{X}_j(t) + \mathrm{Im}\{\alpha[\epsilon_i\omega_j]\}\hat{P}_j(t)\right) + \sqrt{\frac{2}{\kappa}}\hat{\xi}_\Delta^{\mathrm{AM}}(t) \tag{2.43a}$$

$$\hat{c}^{\mathrm{PM}}(t) = \sqrt{\bar{n}}\sum_j g_j\left(\mathrm{Re}\{\beta[\epsilon_i\omega_j]\}\hat{X}_j(t) + \mathrm{Im}\{\beta[\epsilon_i\omega_j]\}\hat{P}_j(t)\right) + \sqrt{\frac{2}{\kappa}}\hat{\xi}_\Delta^{\mathrm{PM}}(t) \tag{2.43b}$$

defining complex optical transduction coefficients

$$\alpha[\omega] = \frac{i}{\kappa+i(\Delta+\omega)} - \frac{i}{\kappa-i(\Delta-\omega)} = \frac{2\Delta}{\Delta^2+(\kappa+i\omega)^2} \tag{2.44a}$$

$$\beta[\omega] = -\frac{1}{\kappa+i(\Delta+\omega)} - \frac{1}{\kappa-i(\Delta-\omega)} = \frac{-2(\kappa+i\omega)}{\Delta^2+(\kappa+i\omega)^2}. \tag{2.44b}$$

These coefficients summarize the quadrature susceptibility to modulation of the dispersive cavity frequency shift by the oscillator's motion at frequency ω.

Reduced oscillator equations of motion

Substituting this solution for the cavity field's amplitude fluctuations into Eq. 2.22, each oscillator's evolution is described by the coupled system of equations

$$\dot{\hat{a}}_i = -i\epsilon_i\omega_i\hat{a}_i - \frac{\Gamma_i}{2}\hat{a}_i - \frac{i}{2}\sum_j\left[(k_{ij}-i\gamma_{ij})\hat{a}_j + (k_{ij}+i\gamma_{ij})\hat{a}_j^\dagger\right]$$
$$- i\,\mathrm{sgn}(g_i)\sqrt{B_i}\hat{\xi}_\Delta^{\mathrm{AM}}(t) + \sqrt{\Gamma_i}\hat{\eta}_i, \quad (2.45)$$

defining the backaction diffusion rate $B_i = 4\bar{n}g_i^2/\kappa$ from coupling to cavity shot noise fluctuations. It is enlightening once again to write these equations in terms of the oscillator quadratures

$$\dot{\hat{X}}_i = -\frac{\Gamma_i}{2}\hat{X}_i + \epsilon_i\omega_i\hat{P}_i + \sqrt{\Gamma_i}\hat{\eta}_i^{\mathrm{AM}} \tag{2.46a}$$

$$\dot{\hat{P}}_i = -\epsilon_i\omega_i\hat{X}_i - \frac{\Gamma_i}{2}\hat{P}_i - \sum_j\left[k_{ij}\hat{X}_j + \gamma_{ij}\hat{P}_j\right] - \mathrm{sgn}(g_i)\sqrt{2B_i}\hat{\xi}_\Delta^{\mathrm{AM}}(t) + \sqrt{\Gamma_i}\hat{\eta}_i^{\mathrm{PM}}. \tag{2.46b}$$

Here it is clear that the optical field mediates a spring-like coupling with strength

$$k_{ij} = 2\bar{n}g_ig_j \operatorname{Re}\{\alpha[\epsilon_j\omega_j]\} = \frac{4\bar{n}g_ig_j\Delta(\Delta^2 + \kappa^2 - \omega_j^2)}{(\Delta^2 + \kappa^2 + \omega_j^2)^2 - 4\Delta^2\omega_j^2} \tag{2.47}$$

in addition to 'viscous' interactions described by

$$\gamma_{ij} = 2\bar{n}g_ig_j \operatorname{Im}\{\alpha[\epsilon_j\omega_j]\} = -\frac{8\bar{n}g_ig_j\epsilon_j\omega_j\Delta\kappa}{(\Delta^2 + \kappa^2 + \omega_j^2)^2 - 4\Delta^2\omega_j^2}, \tag{2.48}$$

arising from the finite cavity lifetime. Here, the single-oscillator frequency shift $\delta\omega_{\mathrm{opt}} = \epsilon_i k_{ii}/2$ and damping rate $\Gamma_{\mathrm{opt}} = \gamma_{ii}$ from Eqs. 2.30 are reproduced by each individual oscillator's optodynamical self-interaction.

It is noteworthy that the general form of these coupling strengths are not reciprocal, which is to say $k_{ij} \neq k_{ji}$. This arises because of the frequency selectivity of the cavity, such that a narrow cavity can be tuned to respond only to the motion of oscillators at frequencies within the cavity linewidth, yet the optical force produced by the resulting modulation of the cavity field will be applied equally, if off-resonant, to all other oscillators, regardless of frequency.

In defining the backaction rate B_i induced by coupling to the optical noise $\hat{\xi}_\Delta^{\mathrm{AM}}(t)$, I have taken care to indicate the sign of optodynamical coupling, which is defined according to the chosen coordinate system in the expansions described in Sec. 2.3. For a single oscillator, this sign is rarely of consequence, influencing only the absolute phase of the observed optodynamical signals. However, with multiple oscillators, the sign of optodynamical coupling determines the relative phase of correlations induced by the common backaction noise, and therefore must be considered in predicting the multi-mode evolution. However, to simplify the discussion in following chapters, this cumbersome sign can always be absorbed into a corresponding redefinition of each oscillator's individual coordinate system, such that the effective coupling is always positive $\operatorname{sgn}(g_i) = +1$. The physical consequence of the coupling phase for a particular experimental geometry is then significant only in translating the absolute motion of the oscillators into the lab frame.

Coherent vs. incoherent cavity dynamics

The coupling strengths k_{ij} and γ_{ij} describe the coherent interactions mediated by the cavity mode, however the oscillators also experience measurement backaction from shot noise fluctuations of the light. These fluctuations are described by the photon number power spectral density (PSD)

$$\begin{aligned} S_{nn}[\omega] &= \bar{n}\langle\hat{\xi}_\Delta[\omega]\hat{\xi}_\Delta^\dagger[-\omega]\rangle \\ &= \frac{2\bar{n}\kappa}{\kappa^2 + (\Delta + \omega)^2}. \end{aligned} \tag{2.49}$$

These fluctuations drive absorption or emission of excitations (i.e. phonons) through optical scattering, with transition rates derived from Fermi's golden rule according to the noise spectral density at the excitation frequencies $\pm\omega_i$ [48]

$$\Gamma_{\uparrow,i} = g_i^2 S_{nn}[-\epsilon_i\omega_i] \qquad \text{and} \qquad \Gamma_{\downarrow,i} = g_i^2 S_{nn}[\epsilon_i\omega_i]. \qquad (2.50)$$

The difference between these rates gives the net energy exchange rate, reproducing the optodynamical damping rate $\gamma_{ii} = \Gamma_{\downarrow,i} - \Gamma_{\uparrow,i}$. The sum of these rates represents the total amount of optical scattering, which quantifies the net diffusion of each oscillator's state. This diffusion can be minimized by reducing the shot noise PSD driving the relevant oscillator transitions, which can be accomplished by increasing one of ω_i or Δ, defining two limits in which the optodynamical interaction is coherent.

Resolved-sideband limit

The limit $\omega_i \gg \kappa$ is the well-known resolved-sideband limit, where the relatively narrow cavity linewidth suppresses quantum fluctuations of the field and facilitates sideband-selective coherent interactions driving optodynamical state-exchange [63] or pair-creation [64] interactions between the optical field and individual oscillators. However, in this regime, the relatively long cavity lifetime suppresses sensitivity to real-time oscillator dynamics, and the narrow linewidth restricts simultaneous measurement or coupling of multiple oscillators. Since E3's cavity linewidth and mechanical trap frequencies place the optomechanics far from this regime, I will not explore it further here. However, the results described in Ch. 3 use the widely tunable Larmor frequency to explore the transition between the unresolved and resolved-sideband regime for spin optodynamics,

Unresolved-sideband limit

Considering instead the unresolved-sideband limit, were $\kappa \gg \omega_i$, the form of Eq. 2.49 suggests that incoherent backaction can still be suppressed, by exploring the off-resonant coupling limit $\Delta \gg \kappa$. However, the coherent coupling strengths must also be considered, to ensure they survive in this limit.

In the unresolved-sideband limit, the coupling strengths given by Eq. 2.47 and 2.48 can be simplified by expanding to first order in ω_i/κ

$$k_{ij} \approx \frac{4\bar{n}g_ig_j\Delta}{\Delta^2 + \kappa^2} \qquad (2.51)$$

$$\gamma_{ij} = -\frac{2k_{ij}\kappa\epsilon_j\omega_j}{\Delta^2 + \kappa^2}. \qquad (2.52)$$

Within this approximation, the optical spring strength is reciprocal, resulting in normal spring-like coupling in the equations of motion, instead of the non-reciprocal exchange interactions realized in the resolved-sideband regime.
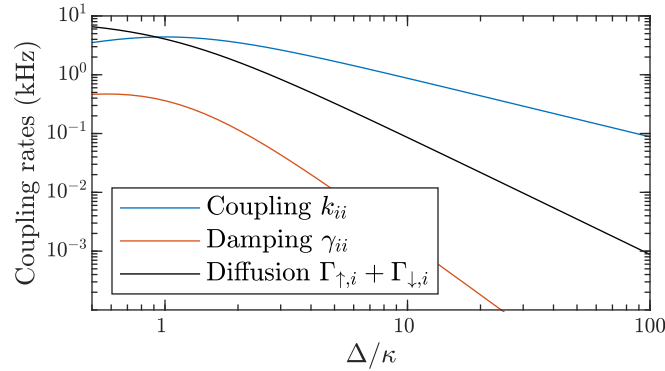
Figure 2.7: Coherent vs. incoherent optodynamical rates in the unresolved-sideband regime, for typical parameter values $g_i = 2\pi \times 20$ kHz, $\omega_i = 2\pi \times 150$ kHz, and $\bar{n} = 10$.

The optical spring strength scales as $\bar{n}/\Delta$, while the shot noise driven diffusion rate

$$\Gamma_{\uparrow,i} + \Gamma_{\downarrow,i} \approx \frac{4\bar{n}g_i^2}{\kappa}\frac{\kappa^2}{\kappa^2 + \Delta^2} \tag{2.53}$$

is proportional to $\bar{n}/\Delta^2$. Therefore, as illustrated in Fig. 2.7, by driving the cavity sufficiently far off resonance, the incoherent effects of backaction can be suppressed while maintaining the same optical spring strength, provided the intra-cavity intensity $\bar{n}$ is increased proportionally. The viscous coupling term γ_{ij}, however, rapidly vanishing in this limit, resulting in a purely 'real', conservative optical spring interaction.

2.6   Cavity output field and detection

In addition to coupling the dynamics of the oscillators and providing an input field to drive them, the cavity field also leaks out of the cavity mode, carrying useful information about the motion of the atomic modes imprinted on its amplitude and phase. We measure the output field with an optical heterodyne detector, to record both the amplitude and phase fluctuations of the light. The cavity output field is given by the boundary condition $\hat{c}_{\text{out}} = \hat{c}_{\text{in}} - \sqrt{2\kappa_{\text{out}}}\hat{c}$ [47–49]. For a one-sided cavity, assuming negligible loss, the output coupling is simply the total cavity decay rate $\kappa_{\text{out}} = \kappa$, and the input field $\hat{c}_{\text{in}} = \hat{\xi}$ is merely the vacuum fluctuations from the steady-state coherent drive represented in Eq. 2.21.

However, for our 2-sided cavity, only a fraction ϵ_{cav} of photons are transmitted through the output mirror, defining $\kappa_{\text{out}} = \epsilon_{\text{cav}}\kappa$. We assume the incident field at the output mirror is quantum vacuum $\hat{c}_{\text{in}} = \hat{\xi}_2$, which forms only part of the total cavity input noise

$$\hat{\xi} = \sqrt{\epsilon_{\text{cav}}}\hat{\xi}_2 + \sqrt{1 - \epsilon_{\text{cav}}}\hat{\xi}_1, \tag{2.54}$$

where $\hat{\xi}_1$ is uncorrelated vacuum input from the input mirror or cavity loss. The total transmitted field from the output mirror is then fully determined in terms of the intracavity

field

$$\hat{c}_{\text{out}} = \hat{\xi}_2 - \sqrt{2\epsilon_{\text{cav}}\kappa}(\sqrt{\bar{n}} + \hat{c}), \tag{2.55}$$

in the rotating frame of the cavity drive. Substituting in the solution for the cavity field from Eq. 2.39, the output amplitude can be written

$$\hat{c}_{\text{out}} = -\sqrt{\frac{2\bar{n}\epsilon_{\text{cav}}}{\kappa}}\left[\kappa - i\hat{d}\right] + \hat{\xi}_{\text{out}} \tag{2.56}$$

identifying the total optodynamical 'measurement' operator

$$\hat{d} = \sum_j g_j \left(\frac{\kappa}{\kappa - i(\Delta - \epsilon_j\omega_j)}\hat{a}_j^\dagger + \frac{\kappa}{\kappa - i(\Delta + \epsilon_j\omega_j)}\hat{a}_j\right). \tag{2.57}$$

This operator is Hermitian for a cavity probed on resonance $\Delta = 0$, corresponding to a real-valued measurable imprinted on the phase of the optical field. Furthermore, in the unresolved-sideband limit $\omega_j/\kappa \to 0$, this measurement corresponds to the total cavity frequency shift from the interaction term of the Hamiltonian in Eq. 2.18.

The optical fluctuations of the output field $\hat{\xi}_{\text{out}}$ are the sum of the reflected vacuum noise at the output $\hat{\xi}_2$ and the transmitted cavity field fluctuations $\hat{\xi}_\Delta(t)$

$$\hat{\xi}_{\text{out}} = \hat{\xi}_2 - 2\sqrt{\epsilon_{\text{cav}}}\hat{\xi}_\Delta(t). \tag{2.58}$$

Together with Eq. 2.40 it can be shown that $\hat{\xi}_{\text{out}}$ is a unitary transformation of the two input noise sources $\hat{\xi}_1$ and $\hat{\xi}_2$, satisfying $\langle\hat{\xi}_{\text{out}}(t)\hat{\xi}_{\text{out}}^\dagger(t')\rangle = \delta(t - t')$. The cavity amplitude fluctuations $\hat{\xi}_\Delta^{\text{AM}}(t)$ also drive the oscillator's motion, generating correlations with the optodynamical response $\hat{d}(t)$. These correlations give rise to effects such as sideband asymmetry [18, 65] and ponderomotive squeezing [19, 55], and must be accounted for when computing the spectrum of the output field [66].

Optical heterodyne detection

We detect this field using a balanced optical heterodyne detector, as shown in Fig. 2.8. By beating the output probe field with a strong LO derived from the same laser, we close an interferometer loop, which gives access to measurements of the probe's phase quadrature, relative to the LO reference [67, 68]. The use of a balanced photodetector gives fundamental and technical advantages, making the output immune to amplitude fluctuations of the LO [69, 70] and canceling the large dc photocurrent before transimpedance conversion, facilitating high-gain amplification without saturation. We perform measurements in heterodyne configuration, where the LO frequency is offset by $\omega_0 = \omega_{\text{p}} - \omega_{LO} = 2\pi \times 10$ MHz from the probe. Their relative phase evolves rapidly, such that the detector splits its time between measuring both amplitude (AM) and phase (PM) modulations of the field, at the expense
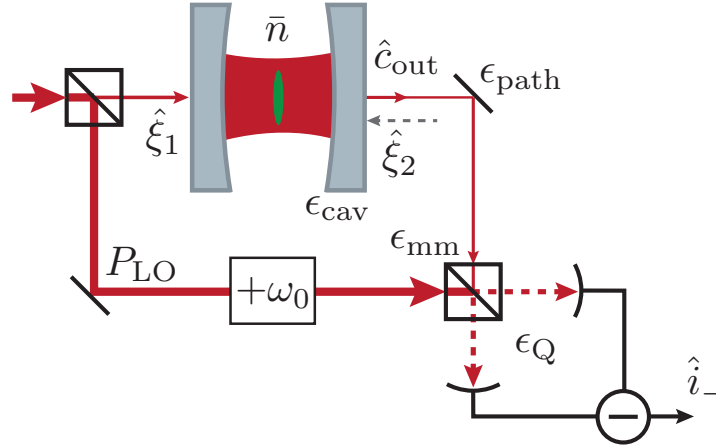
Figure 2.8: The cavity output field $\hat{c}_{\mathrm{out}}$ is interfered with a phase-coherent local oscillator beam with total power $P_{\mathrm{LO}} = 1.0$ mW, derived from the same source and frequency shifted by $\omega_0 = 2\pi \times 10$ MHz. The resulting interference beatnote is recorded with a balanced photodetector (Newport 1807-FS), then electrically amplified and digitized. The total efficiency of detecting intracavity photons is given by the product of the cavity output efficiency ϵ_{cav}, the path efficiency ϵ_{path}, the mode-matching efficiency with the LO ϵ_{mm}, and finally the quantum efficiency of the balanced photodetectors ϵ_{Q}.

of corresponding loss in the signal to noise of each quadrature, relative to a corresponding homodyne measurement.

The output of the balanced heterodyne detector is the difference between the photocurrents from the two ports. The balanced photocurrent operator, derived in Appendix B assuming a strong, shot noise limited LO $(P_{LO} \gg P_p)$, is

$$\hat{i}_-(t) = i e\, \epsilon_{\mathrm{Q}} \sqrt{\epsilon_{\mathrm{path}}\epsilon_{\mathrm{mm}}} |\alpha_L| \left[\hat{c}_{\mathrm{out}}^\dagger(t) e^{i(\omega_0 t + \phi_{\mathrm{L}})} - \hat{c}_{\mathrm{out}}(t) e^{-i(\omega_0 t + \phi_{\mathrm{L}})} \right]$$
$$- e\sqrt{\epsilon_{\mathrm{Q}}(1 - \epsilon_{\mathrm{path}}\epsilon_{\mathrm{mm}}\epsilon_{\mathrm{Q}})}|\alpha_L| \left[\hat{\xi}_{\mathrm{loss}}^\dagger(t) + \hat{\xi}_{\mathrm{loss}}(t) \right] \quad (2.59)$$

where $\alpha_L = \sqrt{P_{\mathrm{LO}}/\hbar\omega_{\mathrm{p}}} e^{i\phi_{\mathrm{L}}}$ is the coherent amplitude of the LO field.

Rewriting this in terms of the solution for the cavity field

$$\hat{i}_-(t) = A_r \sqrt{\frac{2\bar{n}\epsilon S_{\mathrm{sn}}}{\kappa}} \left[\hat{d}\, e^{-i(\omega_0 t + \phi_{\mathrm{L}})} + \hat{d}^\dagger e^{i(\omega_0 t + \phi_{\mathrm{L}})} + 2\kappa \sin(\omega_0 t + \phi_{\mathrm{L}}) \right]$$
$$+ A_r \sqrt{S_{\mathrm{sn}}} \left[\hat{\xi}_d^\dagger(t) + \hat{\xi}_d(t) \right] \quad (2.60)$$

defining the total cavity photon detection efficiency $\epsilon = \epsilon_{\mathrm{cav}}\epsilon_{\mathrm{path}}\epsilon_{\mathrm{mm}}\epsilon_{\mathrm{Q}}$, and the detector's responsivity $A_r = e\epsilon_{\mathrm{Q}}/\hbar\omega_{\mathrm{p}}$. The optical shot noise PSD $S_{\mathrm{sn}} = P_{LO}\hbar\omega_{\mathrm{p}}/\epsilon_{\mathrm{Q}}$ (in cyclic frequency units W^2/Hz) represents the optical gain of the heterodyne detector, reflecting the detected

heterodyne power per unit of the probe vacuum noise. Finally, the vacuum fluctuations reaching the detector are given by the unitary transformation

$$\hat{\xi}_d(t) = \sqrt{1 - \epsilon_{\text{path}}\epsilon_{\text{mm}}\epsilon_{\text{Q}}}\,\hat{\xi}_{\text{loss}} + i\sqrt{\epsilon_{\text{path}}\epsilon_{\text{mm}}\epsilon_{\text{Q}}}\,\hat{\xi}_{\text{out}}e^{-i(\omega_0 t + \phi_{\text{L}})}. \tag{2.61}$$

where $\hat{\xi}_{\text{loss}}$ is additional vacuum noise mixed in due to losses from finite path efficiency ϵ_{path}, mode-matching efficiency ϵ_{mm}, and detector quantum efficiency ϵ_{Q}

The photocurrent is converted to a voltage by a transimpedance Z_{TI} then amplified along the electronic signal path with gain G, detailed in Appendix B. We record a trace $V_{\text{GS}}(t)$ of the heterodyne beatnote with a computer based oscilliscope (GageScope CSE1442) at a sample rate of $f_{\text{BW}} = 80$ MHz. From calibrations of the full detection path, we can then infer the instantaneous optical power in the heterodyne beatnote from the measurement record

$$P_{\text{het}}(t) = \frac{V_{\text{GS}}(t)}{A_r Z_{\text{TI}} G} \tag{2.62}$$

The voltage signal that reaches the computer is entirely classical, but with a noise spectrum amplified from the quantum fluctuations of the operators in Eq. 2.59. The statistics of the recorded heterodyne power can therefore be described by the corresponding symmetrized quantum operators [48], with two-time correlation function

$$R_{\text{het}}(t, t + \tau) = \langle P_{\text{het}}(t)P_{\text{het}}(t + \tau)\rangle = \frac{1}{A_r^2}\langle \text{Re}[\hat{i}_-(t)\hat{i}_-(t + \tau)]\rangle \tag{2.63}$$

from which the optical PSD can be calculated using the Wiener-Khinchin theorem

$$S_{\text{het}}[f] = \int_{-\infty}^{\infty} \langle R_{\text{het}}(t, t + \tau)\rangle_t e^{i2\pi f\tau} d\tau$$

$$\mathcal{S}_{\text{het}}[\omega] = \frac{1}{2\pi}\int_{-\infty}^{\infty} \langle R_{\text{het}}(t, t + \tau)\rangle_t e^{i\omega\tau} d\tau \tag{2.64}$$

in cyclic and angular frequency units, respectively, where $\langle\cdot\rangle_t$ represents a time-average over any non-stationary terms. This angular frequency spectrum has been normalized to satisfy Parseval's theorem

$$\int_{-\infty}^{\infty} df\, S_{\text{het}}[f] = \int_{-\infty}^{\infty} d\omega\,\mathcal{S}_{\text{het}}[\omega] \tag{2.65}$$

implying the conversion $S_{\text{het}}[f] = 2\pi\mathcal{S}_{\text{het}}[2\pi f]$

There are limitations on the features of a quantum state which can be reconstructed from an ultimately classical measurement record [71–73]. The photocurrent 'measurement' operator represents the result of a quantum amplifier, with gain provided by optical multiplication with the LO amplitude, realizing phase-insensitive (sensitive) amplification in the heterodyne (homodyne) configuration. This choice of measurement operator and amplification determines how the quantum fluctuations are reflected in the spectrum of classical noise reaching the computer, after electrical amplification.

Recovering the optodynamical response

For steady-state optodynamics, most information about the optodynamical response can be obtained from the observed heterodyne PSD defined above. However, to extract information about non-stationary, transient or unstable dynamics, we need to interpret the observed signals in the time domain. A measurement record of the optodynamical response $\hat{d}$ in Eq. 2.57 can be recovered from the recorded trace by demodulation. This becomes clear by writing the optical heterodyne power in terms of the real and imaginary components of the measurement operator

$$P_{\text{det}}(t) = \sqrt{\frac{8\epsilon\bar{n}S_{\text{sn}}}{\kappa}} \left[\text{Re}[\hat{d}(t)] \cos(\omega_0 t + \phi_{\text{L}}) + (\kappa + \text{Im}[\hat{d}(t)]) \sin(\omega_0 t + \phi_{\text{L}}) \right] + \sqrt{S_{\text{sn}}}\xi_{sn}(t)$$

$$(2.66)$$

with $\epsilon = \epsilon_{\text{cav}}\epsilon_{\text{path}}\epsilon_{\text{mm}}\epsilon_{\text{Q}}$ defining the total cavity photon detection efficiency, and $\xi_{sn}(t) = \hat{\xi}_d^\dagger + \hat{\xi}_d$ represents the detected shot noise amplitude fluctuations, with $\langle \xi_{sn}(t)\xi_{sn}(t') \rangle = \delta(t - t')$.

Heterodyne demodulation

We demodulate the recorded signal by multiplying with orthogonal sinusoids at the beat frequency, then low-pass filtering, extracting in-phase (amplitude) and quadrature-phase (phase) modulation,

$$P_{\text{I}}(t) = \sqrt{\frac{2\epsilon\bar{n}S_{\text{sn}}}{\kappa}}(\kappa + \text{Im}[\hat{d}(t)]) + \sqrt{\frac{S_{\text{sn}}}{2}}\xi_I(t) \tag{2.67a}$$

$$P_{\text{Q}}(t) = \sqrt{\frac{2\epsilon\bar{n}S_{\text{sn}}}{\kappa}}\, \text{Re}[\hat{d}(t)] + \sqrt{\frac{S_{\text{sn}}}{2}}\xi_Q(t), \tag{2.67b}$$

respectively.

For measurements performed while driving the cavity on resonance $\Delta = 0$, the measurement operator $\hat{d}$ is Hermitian and therefore real, such that the full response appears in the optical phase quadrature as

$$\hat{d}(t) = \frac{\sqrt{2}}{\kappa^2 + \omega_j^2} \sum_j g_j \left(\kappa \hat{X}_j(t) - \epsilon_j \omega_j \hat{P}_j(t) \right), \quad \Delta = 0. \tag{2.68}$$

Alternatively, in the unresolved sideband limit, but at any probe detuning, the measurement operator is approximately

$$\hat{d}(t) \approx \frac{\sqrt{2}\kappa}{\kappa - i\Delta} \sum_j g_j \hat{X}_j(t), \quad \kappa \gg \omega_j, \tag{2.69}$$

which is simply the total displacement, rotated by a phase due to the bare cavity's complex susceptibility. This rotation causes the oscillator position quadrature to modulate both the

optical amplitude and phase, and the instantaneous displacement can be recovered by a linear combination of $P_Q(t)$ and $P_I(t)$

$$P_\phi(t) = P_Q(t) \cos \phi + P_I(t) \sin \phi, \tag{2.70}$$

as if measured by an effective homodyne detector at a rotated quadrature angle ϕ. At the optimal quadrature phase angle $\tan \phi = \Delta/\kappa$, the modulation power is

$$P_\phi(t) = \sqrt{S_\text{sn}} A \sum_j g_j(\hat{a}_j^\dagger(t) + \hat{a}_j(t)) + \sqrt{\frac{S_\text{sn}}{2}} \xi_\phi(t) \tag{2.71}$$

with the optical shot noise $\xi_\phi(t)$ transformed similarly to Eq. 2.70.

This result can be understood as a sequence of unit conversions. The amplitude gain of the Heterodyne detector is $\sqrt{S_\text{sn}}$, in units of $[\text{watts}]/\sqrt{[\text{photon flux}]}$, and describes the detected optical power per unit probe field amplitude. Next, the optodynamical measurement gain is defined as

$$A = \sqrt{\frac{2\epsilon \bar{n} \kappa}{\kappa^2 + \Delta^2}} \tag{2.72}$$

with units $\sqrt{[\text{photon flux}]}/[\text{frequency}]$, describing the change in transmitted probe amplitude, per unit cavity frequency displacement. Finally the optodynamical coupling constants g_j have units of $[\text{frequency}]/[\text{unitless length}]$, quantifying the cavity frequency displacement, per displacement of oscillator j in units of harmonic oscillator lengths.

The optical quadrature signal in Eq. 2.70 contains the sum of displacements of each oscillator and is further considered in Chap. 6, where it is shown that, provided their motion is clearly resolved in frequency, estimates multi-mode oscillator state can be obtained with precision approaching the SQL.

Lost factors of 2π: cyclic vs. angular frequencies

Care must be taken to distinguish cyclic and angular frequencies. All frequency variables defined in the Hamiltonian (Δ, ω_j, and g_j) are in angular units (rad/s), consistent with use of the reduced Plank constant $\hbar$ for conversion to an energy in the Hamiltonians. This puts eigenvalues of the Hamiltonian d_j in convenient units, such that time propagation corresponds to a simple complex exponential $e^{id_j t}$, which is intuitive when d_j is real and describes actual rotation of a phase angle. However, when imaginary components appear in the eigenvalues, reflecting amplification and damping, then these non-cyclic rates are still awkwardly defined in terms of angular frequencies. For consistent theoretical treatment, it is common to describe the decay rates κ and Γ_j in terms of angular frequencies as well, corresponding to their spectral linewidths in the angular frequency PSD. However, the shot noise PSD S_sn as used here is defined in units of W^2/Hz, representing the average power density detected by a spectrum analyzer within a frequency bandwidth measured in cyclic units.

Mean-squared optodynamical displacement

Single-shot measurement traces sampled from Eq. 2.71 are obscured by large amounts of measurement noise. Because of the broad-band nature of measurement shot noise compared to the spectral response of high-Q oscillators, the relative signal-to-noise (S/N) in the temporal signal depends on the sampling bandwidth and can be significantly improved by filtering to remove excess shot noise outside the signal band. However, for typical experimental values ($\Delta = 0$, $\bar{n} = 2$, and $g_j = 2\pi \times 18$ kHz) and assuming a 100 kHz filter bandwidth, the time-domain signal to noise ratio per harmonic oscillator length displacement is still quite small

$$\text{S/N} = \frac{A^2 g_j^2}{f_{\text{BW}}} \approx 10^{-3}. \tag{2.73}$$

Signal filtering can be optimized using knowledge of the oscillator and noise dynamics by application of matched filters, as derived in Chap. 6. However if the system parameters are not well known or a model-independent analysis is needed to evaluate a proposed theoretical description of the system dynamics, then other approaches are necessary to obtain reliable signals.

When possible, it is advantageous to average the results of multiple repetitions of the same measurement to extract statistics of interest with improved signal to noise. The demodulated heterodyne signals in Eqs. 2.67 can be directly averaged to obtain the coherent amplitudes of each oscillator, provided the system is repeatedly prepared and evolves in a state with well-defined absolute phase. This technique was employed for work discussed in Chap. 3 and Chap. 4, observing the evolution of single oscillator and coupled optodynamical systems from an initial state prepared with a coherent excitation pulse. However, if the absolute phase of the oscillators is not initially defined or 'dephases,' for instance due to shot-to-shot fluctuations in oscillator frequency, then the optodynamical response in the heterodyne quadratures also averages away. It is useful, therefore, to construct statistics of the measured signal which are independent of absolute phase. Furthermore, additional information, such as higher-order coherences of the multi-mode state, can be obtained by computing various other statistics of the recorded signals. In principle such higher-order statistics can also be extracted from an ensemble of single-shot matched-filter estimates, as demonstrated in Chap. 6, interpretation of those results requires detailed knowledge of the system dynamics. Time-domain signal analysis, such as the example described below, can provide alternative measures which are not sensitive to the same systematic biases, which can serve as powerful comparisons to confirm the applied models.

One useful signal statistic employed in several works discussed in later chapters is the cycle-averaged mean square displacement

$$\langle |\hat{d}|^2 \rangle_{\text{cyc}} \approx \frac{2\kappa^2}{\kappa^2 + \Delta^2} \left[\sum_i g_i^2 \left(\langle \hat{n}_i \rangle + \frac{1}{2} \right) + \sum_{i \neq j} g_i g_j \langle \hat{Z}_i \hat{Z}_j \rangle_{\text{cyc}} \right] \tag{2.74}$$

Cycle-averaging refers to removal of high-frequency terms in the final product by application of a low-pass filter. For instance, the resulting signal for two (positive mass) oscillators can be written

$$\langle |\hat{d}|^2 \rangle_{\text{cyc}} \approx \frac{2\kappa^2}{\kappa^2 + \Delta^2} \left[g_1^2 \left(\langle \hat{n}_1 \rangle + \frac{1}{2} \right) g_2^2 \left(\langle \hat{n}_2 \rangle + \frac{1}{2} \right) + g_1 g_2 \langle \hat{a}_1^\dagger \hat{a}_2 + \hat{a}_2^\dagger \hat{a}_1 \rangle \right]. \qquad (2.75)$$

Here, the first two terms reflect changes in the occupation of both modes, while the final term captures the amplitude and phase of the second-order coherence between the two oscillators, which evolves at their difference frequency.

The experimental signal-processing sequence used to extract this signal from measured traces is diagrammed in Fig. 2.9, along with simulated spectra and the resulting time trace for realistic experimental parameters. This signal can be understood by analogy to an electronic power detector, such as the input stage of a spectrum analyzer. The raw signal is bandpass filtered, to isolate the signal band containing the optodynamical response, then converted to an RMS power with a non-linear element, such as a diode, and then finally low-pass filtered to remove harmonics produced by the power detector. The same sequence can be applied digitally to the recorded signal, squaring the filtered signal to mimic a non-linear power detector.
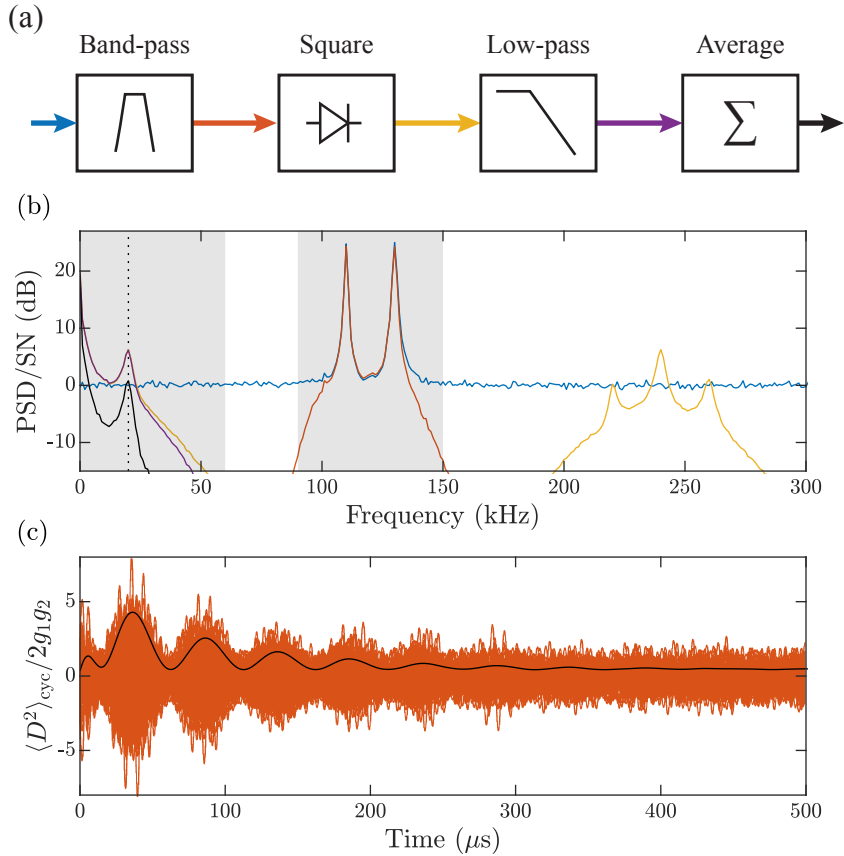
Figure 2.9: (a) Block diagram illustrating the signal processing sequence used to recover the cycle-averaged, mean-squared measurement signal, revealing the coherent beatnote between oscillators. (b) Signal PSD between each stage of processing, for data simulated under similar experimental conditions. (c) Mean squared displacement (black) overlaid on 100 simulated measurement records, illustrating recovery of the beatnote amplitude and phase, independent of the underlying carrier phases.

Chapter 3

Spin optodynamics

The primary experimental results demonstrating cavity spin optodynamics are published in Ref. [24]. In this chapter, I provide a broader theoretical background to the published work, discuss experimental details and complications such as spin dephasing and cavity birefringence, and outline some potential future directions.

Discovery of the quantization of angular momentum played a significant role in the development of quantum mechanics, and quantum spin systems have since become a fundamental model in theoretical and experimental work, representing a basic quantum building block alongside the harmonic oscillator. The interaction of a single mode of the electromagnetic field with a two-level quantum system, described by the optical Bloch equations, forms a basic model for understanding the interaction of light with matter. As considered in Sec. 2.1, this description forms the basic paradigm for cavity QED, in which microwave or optical resonators are used to define and enhance coupling to a single cavity mode relative to decay into the electromagnetic vacuum. The two-level system has also become an essential paradigm for concepts of quantum measurement [48], with spin measurements providing early examples of quantum-limited measurement [21]. The importance of spin systems motivates extending the description of cavity *optodynamics* beyond its conception with harmonic oscillators in the field of optomechanics to also include optical measurement and control of a collective quantum spin degree-of-freedom [23].

In our experiments, we work with ensembles of a few thousand atomic spins trapped within an optical cavity, requiring a more involved theoretical treatment. But, as described in Chap. 2, for atoms symmetrically coupled to the cavity mode, the optical interaction with the total atomic spin is collectively enhanced, while coupling to all other non-symmetric spin modes is negligible. Such collective enhancement has been exploited in free-space optical measurements of polarized ensembles prepared in vapor cells [74] or nitrogen-vacancy centers in diamond. Dispersive optical probing of these ensembles allows observation of Larmor precession at the SQL, through the effect of atomic birefringence, with applications such as atomic magnetometry [22]. In addition to providing sensitivity to external magnetic fields, these systems present a rich platform for exploring quantum measurement and control, with

demonstrations of measurement-based squeezing [75] and entanglement [76], as well as back-action evasion [77] and feedback cooling [78].

Placing the spin ensemble inside a high-finesse cavity further enhances the coherent optical interaction and also facilitates autonomous optodynamical feedback, where fluctuations induced by the spin on the cavity field persist for a finite lifetime and are conditioned by the cavity spectrum, feeding back to the subsequent spin dynamics. This process is autonomous, in that the feedback loop is built into the coherent Hamiltonian dynamics and does not rely on the outcome of any measurement or its detection efficiency. Our work with atomic spin optodynamics has provided early demonstrations of coherent interactions in this unique regime of cavity QED with spin ensembles [24, 29].

Cavity quantum non-demolition measurements

Many experiments in cavity QED are realized with two-level pseudo-spin systems where the energy eigenstates and their coupling to the cavity field are intrinsically determined, for instance on microwave transitions between hyperfine states or optical clock transitions in alkaline-earth atoms. Through dispersive coupling to such systems, the optical cavity provides a sensitive QND measurement of the longitudinal spin component [79]. As introduced in Sec. 2.3 and illustrated in Fig. 3.1, a similar QND measurement configuration is realized in our apparatus by loading the atoms at an anti-node of the probe field, to minimize sensitivity to the atomic position, and applying a magnetic field aligned along the cavity axis.

The effective Hamiltonian for driving only a σ^+-polarized mode of the cavity $\hat{c}$ is given by Eq. 2.14, which can be rewritten as

$$\mathcal{H} = \hbar\omega_{\mathrm{c}}'\hat{c}^\dagger\hat{c} + \hbar\omega_{\mathrm{s}}\hat{F}_z + \hbar\alpha_1 g_{\mathrm{c}}\hat{c}^\dagger\hat{c}\hat{F}_z \tag{3.1}$$

by defining the scalar-shifted cavity resonance $\omega_{\mathrm{c}}' = \omega_{\mathrm{c}} + \alpha_0 g_{\mathrm{c}} N_a$. The interaction term facilitates measurement of the longitudinal spin component as a dispersive shift of the cavity resonance frequency. This realizes a QND measurement because the interaction term commutes with the system Hamiltonian and is therefore a constant of motion, unperturbed by measurement backaction. 'Non-demolition' is, perhaps, a controversial label [80], because any quantum measurement necessarily imparts backaction disturbing the quantum state. Here measurement backaction arises from the intensity-dependent Larmor frequency shift, with photon shot noise fluctuations driving phase diffusion of the transverse spin. This diffusion destroys coherences between the spin eigenstates, yet does not alter their populations, which determine the measurement outcome.

This QND measurement scheme has previously been used on E3 to demonstrate site-resolved, non-destructive spin imaging [33], and is also routinely used to measure the longitudinal spin component for calibration of rf pulses or measurement of intrinsic spin dephasing, described in Sec. 3.4. Similar QND measurements have also been used to prepare conditional population-squeezed spin states [75, 81–84] with potential applications for surpassing the SQL for magnetic field detection [85] or readout of atomic clocks and interferometers
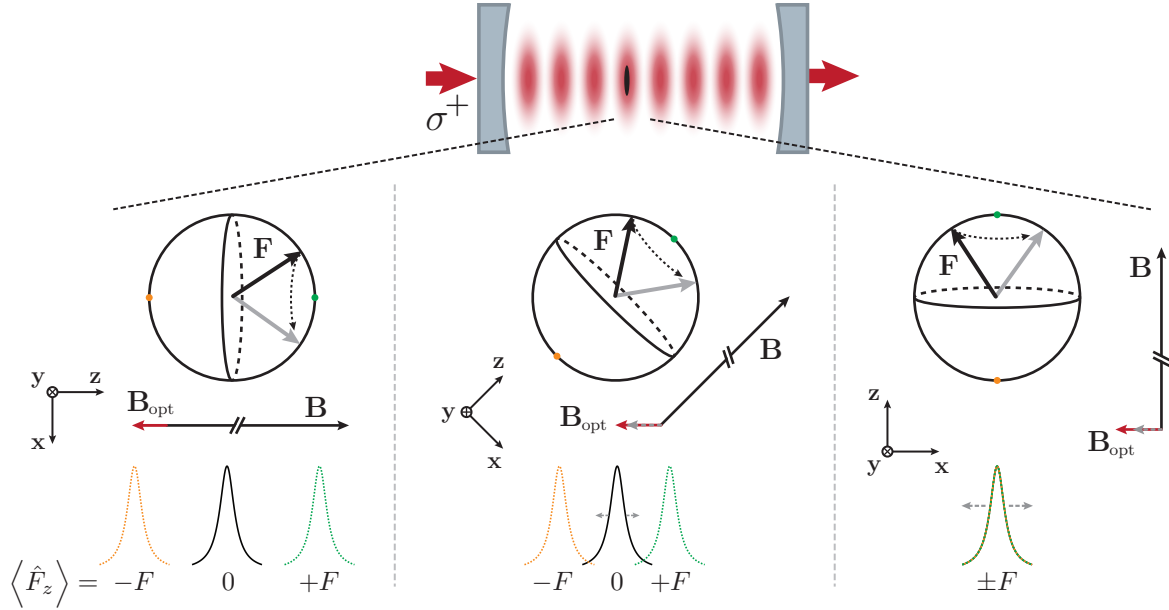
Figure 3.1: Schematic of cavity spin optodynamics configurations. Three distinct configurations can be realized according to the relative angle between the cavity axis **k** and the applied magnetic field along **z**. (left) QND measurement configuration in a magnetic field applied parallel to the cavity axis, providing sensitivity to the static longitudinal spin component. (right) Spin optodynamics configuration in a transverse magnetic field, where Larmor precession modulates the cavity resonance frequency. (center) In between the previous two conditions, the optical cavity is sensitive to both the longitudinal spin and transverse spin components. Optodynamical coupling to the transverse spin mediates energy exchange, which tunes the cycle-averaged cavity resonance frequency, facilitating stabilization of the spin away from the poles, as proposed in Sec. 3.6.

[86]. Related experiments have also demonstrated use of autonomous cavity feedback of the dispersive measurement to generate one-axis twisting dynamics [87] resulting in unconditionally squeezed spin states [88], which do not rely on detection of the cavity output field and are useful for overcoming finite detection efficiency for quantum-limited measurements [89, 90].

Spin optodynamics

In our system, however, we dispersively measure the atomic spin dynamics within a ground-state hyperfine manifold. These spin states are initially degenerate, allowing a choice of quantization axis of their eigenstates relative to the cavity measurement axis by orientation of the applied magnetic field. Varying the angle between the magnetic field and cavity axis allows the cavity-spin interaction to be continuously tuned between two limiting configurations, illustrated in Fig. 3.1 – the QND configuration with the magnetic field along the

Figure 3.2: Larmor precession of the transverse spin modulates the cavity field through the optodynamical interaction, imprinting sidebands on the observed heterodyne PSD spaced by $\omega_s = 2\pi \times 1$ MHz around the heterodyne carrier beat frequency at $\omega_0 = 2\pi \times 10$ MHz. Vibration of the cavity mirrors and electrical radiation add noise peaks near the heterodyne carrier.

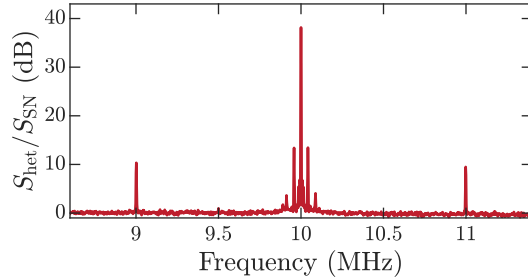cavity axis, and the spin optodynamics configuration, with the field transverse to the cavity axis. With the magnetic field (always along $\mathbf{z}$) applied transverse to the cavity axis ($\mathbf{k} = \mathbf{x}$), the spins precess in a plane parallel to the cavity axis. One component of the precessing transverse spin $\hat{F}_x$ modulates the cavity field at the Larmor frequency, described by the Hamiltonian introduced in Eq. 2.16

$$\mathcal{H} = \hbar\omega_c'\hat{c}^\dagger\hat{c} + \hbar\omega_s\hat{F}_z + \hbar\alpha_1 g_c\hat{c}^\dagger\hat{c}\hat{F}_x, \tag{3.2}$$

having assumed a linear Zeeman shift from a weak magnetic field.

This Hamiltonian conserves the total spin but no longer commutes with $\hat{F}_z$, facilitating energy exchange between the collective spin and the optical field through coupling to the transverse spin $\hat{F}_x = (\hat{F}_+ + \hat{F}_-)/2$. The interaction term can be viewed from two perspectives. As an energy proportional to the photon number, it represents a spin-dependent shift of the cavity frequency, facilitating real-time measurement of the spin precession from modulation of light transmitted through the cavity, as shown in the heterodyne spectrum in Fig. 3.2. Alternatively, as an energy proportional to the spin component $\hat{F}_x$, it represents an effective magnetic field along the cavity axis, defined by the strength of the vector ac Stark shift. This effective field applies an intensity-dependent torque to the precessing spin, which mediates optical feedback onto the spin dynamics. This optical torque also couples backaction into the spin state, from optical shot noise fluctuations driving diffusion of the spin orientation.

Between the two limiting configurations shown in Fig. 3.1, when the magnetic field is applied at an intermediate angle to the cavity axis, the cavity provides sensitivity both to the longitudinal spin component and energy exchange via optodynamical interactions with the transverse spin precession. This configuration should allow feedback stabilization of the spin at a pump-determined polar angle, as proposed in Sec. 3.6.

A note about directions

I have assumed a choice of convention in writing Eq. 3.2, by choosing a positive energy for spin states parallel to the applied magnetic field ("spin up"). The choice of convention here is the relative sign between the unit-less spin vector $\boldsymbol{f}$ and the atomic magnetic moment $\boldsymbol{\mu}$. Taking the same sign convention as Ref. [43], the magnetic moment for a single atom is given by

$$\boldsymbol{\mu} = -g_f \mu_B \hat{\boldsymbol{f}} = \hbar\gamma\hat{\boldsymbol{f}}, \tag{3.3}$$

which implicitly defines the sign of the Landé g-factor g_f and the gyromagnetic ratio $\gamma = -g_f\mu_B/\hbar$.

The rest follows from basic physics and geometry. The Hamiltonian for the action of a magnetic field on an atomic dipole in the low-field limit is $\mathcal{H}_B = -\boldsymbol{\mu}\cdot\boldsymbol{B}$. Under the chosen convention,

$$\mathcal{H}_B = \mathrm{sgn}(g_f)\hbar\omega_{\mathrm{s}}\hat{f}_z, \tag{3.4}$$

with Larmor frequency $\omega_{\mathrm{s}} = |\gamma\boldsymbol{B}| = \mu_B|g_f\boldsymbol{B}|/\hbar$. For the $f = 2$ ground-state manifold of ^{87}Rb, $g_f = 1/2$ and $\gamma/2\pi = -700$ kHz/G under this convention, such that the highest-energy spin state, which the atoms are prepared in prior to magnetic transport into the cavity, is $|f = 2, m = +2\rangle$, labeled by the eigenvalue defined by $\hat{f}_z|f, m\rangle = m|f, m\rangle$.

With the convention fixed, the effective Magnetic field experienced from the vector Stark shift interacting with the cavity is given by

$$\boldsymbol{B}_{\mathrm{opt}} = -\frac{\alpha_1}{\gamma}\frac{g_0^2}{\Delta_{\mathrm{ca}}}\hat{n}_+\mathbf{k} \tag{3.5}$$

and the torque it produces $\boldsymbol{\tau} = \boldsymbol{\mu}\times\boldsymbol{B}$, with $\mathbf{k} = \mathbf{x}$,

$$\boldsymbol{\tau}_{\mathrm{opt}} = -\hbar\alpha_1\frac{g_0^2}{\Delta_{\mathrm{ca}}}\hat{n}_+(\hat{f}_z\mathbf{y} - \hat{f}_y\mathbf{z}) \tag{3.6}$$

3.1 Spin analog of cavity optomechanics

In the transverse-field, spin optodynamics configuration sketched in Fig. 3.1, an exact analog of cavity optomechanics is realized for the Larmor precession of a large collective spin which is nearly parallel or anti-parallel to the applied magnetic field [23]. As illustrated in Fig. 2.5, a large spin precessing near the magnetic pole can be approximately described as a harmonic oscillator rotating in phase space [91], locally approximating the Hilbert space of the spin state on the surface of the sphere by its tangent plane at the pole. In this approximation, the coupled spin-optical dynamics are exactly equivalent to those realized in cavity optomechanics, but with the additional feature of an inverted, high-energy "ground state" [23] and the absence of coupling to an intrinsic thermal bath.

Linearized equations of motion

To derive the spin oscillator version of the linearized, canonical optodynamical Hamiltonian given by Eq. 2.19, I start by linearizing the optical interaction for small modulation of the cavity field around the steady-state photon number $\bar{n}$, following a similar procedure to Sec. 2.4.

Expanding Eq. 3.2 for small fluctuations around the average probe field $\hat{c} \to e^{-i\omega_\mathrm{p}t}(\sqrt{\bar{n}} + \hat{c})$, in a rotating frame defined by the steady-state coherent drive, the Hamiltonian can be approximated to first order as

$$\mathcal{H} = -\hbar\Delta\hat{c}^\dagger\hat{c} + \hbar\omega_\mathrm{s}\hat{F}_z + \hbar\alpha_1\bar{n}g_\mathrm{c}\hat{F}_x + \hbar\alpha_1\sqrt{\bar{n}}g_\mathrm{c}(\hat{c}^\dagger + \hat{c})\hat{F}_x, \tag{3.7}$$

where here $\Delta = \omega_\mathrm{c}' - \omega_\mathrm{p}$ is the probe detuning from the scalar-shifted cavity resonance. The third term, proportional to $\bar{n}$, represents the effective magnetic field produced by the average intracavity intensity, and can be neglected assuming $\alpha_1\bar{n}g_\mathrm{c}/\omega_\mathrm{s} \ll 1$.

This approximation is valid provided the modulation of the cavity frequency by the precessing spin is a small fraction of the cavity linewidth, $\alpha_1 g_\mathrm{c}\langle|\hat{F}_x|\rangle < \kappa$, which is satisfied for a spin precessing sufficiently near its magnetic pole. In this regime, the optodynamical modulation produces amplitude and phase modulation of the cavity field only at the Larmor frequency ω_s, as illustrated in Fig. 2.6. A clear signature of the breakdown of this linear optodynamical approximation is the appearance of higher harmonics of the Larmor frequency in the optical signal, as observed in Fig. 3.5, which arise from the second- and higher-order terms in the expansion, due to the local curvature of the cavity susceptibility represented in Fig. 2.6.

The Heisenberg equations of motion for the Hamiltonian in Eq. 3.7 are

$$\dot{\hat{F}}_x = -\omega_\mathrm{s}\hat{F}_y \qquad\qquad\qquad \dot{\hat{F}}_y = \omega_\mathrm{s}\hat{F}_x - \alpha_1\sqrt{\bar{n}}g_\mathrm{c}(\hat{c}^\dagger + \hat{c})\hat{F}_z$$

$$\dot{\hat{F}}_z = \alpha_1\sqrt{\bar{n}}g_\mathrm{c}(\hat{c}^\dagger + \hat{c})\hat{F}_y \qquad\qquad \dot{\hat{c}} = (i\Delta - \kappa)\hat{c} - i\alpha_1\sqrt{\bar{n}}g_\mathrm{c}\hat{F}_x + \sqrt{2\kappa}\hat{\xi}. \tag{3.8}$$

These equations are still non-linear, however, because the commutator between spin components is not itself a constant, unlike the canonical bosonic commutation for a harmonic oscillator.

Also unlike the optomechanical equations of motion, here I have neglected any non-unitary dissipation of collective spin dynamics, assuming that its intrinsic evolution is fully coherent, entirely constrained within the Hilbert space of a symmetric spin ensemble. The only dissipation channels included in this model are through the cavity mode, allowing measurement of the spin and corresponding diffusion from measurement backaction. This assumption is valid provided the intrinsic spin decay mechanisms, such as longitudinal energy relaxation or transverse dephasing, are negligible on the timescales of interest. Measurements of the relaxation and dephasing rates are reported in Figs. 3.13 and 3.12, respectively, which show negligible relaxation and dephasing on timescales up to a few ms. The nature of the loss dynamics driven by these decay processes cannot be simply described through Langevin

equations, such as for a bath of bosonic modes coupled to a harmonic oscillator, and a rigorous treatment would require description by a master equation.

As described in Ref. [23], for small-amplitude Larmor precession near the magnetic poles Eqs. 3.8 can be approximated by the optomechanical equations of motion by performing a Holstein-Primakoff transformation [91]. Considering excitations away from the highest-energy spin state, represented by bosonic creation and annihilation operators $\hat{a}^\dagger$ and $\hat{a}$, respectively, the collective spin operators can be written as

$$\hat{F}_+ = \sqrt{2F - \hat{a}^\dagger \hat{a}}\,\hat{a}, \qquad \hat{F}_- = \hat{a}^\dagger \sqrt{2F - \hat{a}^\dagger \hat{a}}, \qquad \text{and} \qquad \hat{F}_z = F - \hat{a}^\dagger \hat{a}. \qquad (3.9)$$

This transformation so far is exact, describing the spin in the Hilbert space of a harmonic oscillator, tangent to the high-energy pole but truncated at a maximum excitation $\langle \hat{n}_s \rangle \leq 2F$.

Assuming small excitation numbers $\langle \hat{n}_s \rangle \ll F$, valid for dynamics of a collective spin nearly parallel to the applied field, these transformations can be approximated to first order in $\hat{n}_s$. The position and momentum quadratures of the bosonic operators can then be defined as

$$\hat{X}_\text{s} \cong \frac{1}{\sqrt{F}}\hat{F}_x \qquad\qquad \hat{P}_\text{s} \cong -\frac{\epsilon_s}{\sqrt{F}}\hat{F}_y \qquad\qquad \hat{n}_s = F + \epsilon_s \hat{F}_z \qquad (3.10)$$

where $\epsilon_s = -\,\text{sgn}\langle \hat{F}_z \rangle$ represents the sign of the effective mass of the spin oscillator, performing the Holstein-Primakoff approximation near either magnetic pole.

In terms of these approximations, the linearized Hamiltonian from Eq. 3.7 can be written as

$$\mathcal{H} = -\hbar\Delta \hat{c}^\dagger \hat{c} + \hbar\omega_\text{s}\epsilon_s \hat{a}^\dagger \hat{a} + \hbar\alpha_1 \sqrt{\bar{n}}\,g_\text{c}\frac{\sqrt{F}}{2}(\hat{c}^\dagger + \hat{c})(\hat{a}^\dagger + \hat{a}), \qquad (3.11)$$

having dropped a constant energy term. By comparison to Eq. 2.19, the spin optodynamical coupling rate can directly be identified

$$g_s = \alpha_1 g_\text{c}\sqrt{\frac{F}{2}} \qquad (3.12)$$

where the quantum noise of the coherent spin state $\Delta F_\text{SQL} = \sqrt{F/2}$ plays the role of the oscillator zero-point motion.

Autonomous cavity feedback

This optomechanical analogy was proposed in Ref. [23] and the results of our experimental demonstration are reported in Ref. [24]. In this section, I instead consider solutions to the more general, non-linear equations of motion defined by Eqs. 3.8.

The Hamiltonian assumed in Eq. 3.2 commutes with $|\hat{\boldsymbol{F}}|^2$, conserving the total ensemble spin. This symmetry provides an additional constraint, reducing the dimensionality of the

available Hilbert space, but at the expense of introducing additional non-linearities into the equations of motion. This can be accomplished by transforming the spin vector into spherical coordinates according to

$$\hat{\boldsymbol{F}} = F(\sin\theta\cos\phi,\ \sin\theta\sin\phi,\ \cos\theta), \tag{3.13}$$

defining the polar angle θ between the spin orientation and the high-energy stable state, and the azimuthal angle ϕ relative to the x-axis. To be rigorous, these angles should be defined as operators with non-trivial commutations, but significant difficulties arise in defining a phase operator near the magnetic poles [49], where the optomechanical analogy instead provides a better solution. However, for a large total spin excited far away from the pole, the coherent dynamics dominate the spin evolution, therefore I drop the ˆ from the spin angles for clarity in the following, essentially semi-classical, solution.

In terms of optical quadratures, the equations of motion from Eq. 3.7 after transformation by Eq. 3.13 are

$$\dot{\theta} = -\alpha_1 g_c \sqrt{2\bar{n}}\,\hat{c}^{\mathrm{AM}}\sin\phi \tag{3.14a}$$

$$\dot{\phi} = \omega_s - \alpha_1 g_c \sqrt{2\bar{n}}\,\hat{c}^{\mathrm{AM}}\cot\theta\cos\phi \tag{3.14b}$$

$$\dot{\hat{c}}_{\mathrm{AM}} = -\kappa\hat{c}^{\mathrm{AM}} + \Delta\hat{c}^{\mathrm{PM}} + \sqrt{2\kappa}\,\hat{\xi}^{\mathrm{AM}} \tag{3.14c}$$

$$\dot{\hat{c}}_{\mathrm{PM}} = -\Delta\hat{c}^{\mathrm{AM}} - \kappa\hat{c}^{\mathrm{PM}} + \sqrt{2\bar{n}}\,g_c F\sin\theta\cos\phi + \sqrt{2\kappa}\,\hat{\xi}^{\mathrm{PM}}. \tag{3.14d}$$

These equations already begin to reveal the nature of the optical feedback. The azimuthal spin angle ϕ evolves predominately at the Larmor frequency ω_s and modulates the phase quadrature of the cavity field $\hat{c}^{\mathrm{PM}}$. This modulation rotates into the amplitude quadrature when the probe is detuned ($\Delta \neq 0$) and then couples back into the evolution of both coordinates of the spin orientation. The cavity's finite lifetime causes a phase delay of the amplitude modulation, with the in-phase modulation ($\propto\cos\phi$) inducing an average shift in the precession frequency, and out-of-phase modulation ($\propto\sin\phi$) driving an average nutation of the polar angle.

These effects can be analytically obtained by approximately solving for the state of the cavity field, as in Sec. 2.5, here yielding

$$\hat{c}^{\mathrm{AM}}(t) \approx \alpha_1 g_c \sqrt{\frac{\bar{n}}{2}}\,F\sin\theta(t)\,[\mathrm{Re}\{\alpha[\omega_s']\}\cos\phi(t) + \mathrm{Im}\{\alpha[\omega_s']\}\sin\phi(t)] + \sqrt{\frac{2}{\kappa}}\hat{\xi}_\Delta^{\mathrm{AM}}(t), \tag{3.15}$$

where $\alpha[\omega_s']$ describes the transduction of dispersive modulation at the shifted Larmor frequency $\omega_s' = \omega_s + \delta\omega$ onto intracavity field amplitude, given by Eq. 2.44a.

Substituting Eq. 3.15 into Eqs. 3.14a and performing a rotating-wave approximation, dropping harmonics like $\sin 2\phi$, the reduced equations of motion are approximately

$$\dot{\theta} \approx -\bar{n}g_s{}^2\,\mathrm{Im}\{\alpha[\omega_s']\}\sin\theta - 2\alpha_1 g_c \sqrt{\frac{\bar{n}}{\kappa}}\sin\phi\,\hat{\xi}_\Delta^{\mathrm{AM}} \tag{3.16a}$$

$$\dot{\phi} \approx \omega_s - \bar{n}g_s{}^2\,\mathrm{Re}\{\alpha[\omega_s']\}\cos\theta - 2\alpha_1 g_c \sqrt{\frac{\bar{n}}{\kappa}}\cot\theta\cos\phi\,\hat{\xi}_\Delta^{\mathrm{AM}} \tag{3.16b}$$

These equations capture the optodynamical energy exchange and frequency shift in the first terms and a non-linear coupling to the shot noise fluctuations in the final terms.

Assuming weak optodynamical coupling $g_s \ll \omega_s$, the Larmor frequency shift is small such that $\omega'_s \approx \omega_s$. The equations can then be written in terms of the optodynamical energy damping rate Γ_{opt} and frequency shift $\delta\omega_{opt}$ defined in Eqs. 2.30 for a positive-mass oscillator. Considering only the coherent dynamics, neglecting the shot noise input terms, these equations can be summarized as

$$\dot{\theta} \approx \frac{\Gamma_{opt}}{2} \sin\theta \qquad \text{and} \qquad \delta\omega \approx -\delta\omega_{opt} \cos\theta, \qquad (3.17a)$$

by identifying $\dot{\phi} = \omega'_s$. This result directly gives the optical spring-shift as a function of polar angle, showing that it varies linearly with longitudinal component of the spin.

The non-linear differential equation for the polar angle has an analytic solution, given by

$$\cot\frac{\theta(t)}{2} = e^{-\Gamma_{opt}t/2} \cot\frac{\theta(0)}{2}. \qquad (3.18)$$

Evolution of the longitudinal spin component $\hat{F}_z$ and the magnitude of the transverse spin $\hat{F}_\perp^2 = \hat{F}_x^2 + \hat{F}_y^2$ can be calculated from this solution as

$$\langle\hat{F}_z(t)\rangle = F\cos\theta(t) = F\frac{F_z(0)\cosh\left(\Gamma_{opt}t/2\right) - F\sinh\left(\Gamma_{opt}t/2\right)}{F\cosh\left(\Gamma_{opt}t/2\right) - F_z(0)\sinh\left(\Gamma_{opt}t/2\right)} \qquad (3.19)$$

$$\langle|\hat{\boldsymbol{F}}_\perp(t)|\rangle = F\sin\theta(t) = \frac{F\sqrt{F^2 - F_z(0)^2}}{F\cosh\left(\Gamma_{opt}t/2\right) - F_z(0)\sinh\left(\Gamma_{opt}t/2\right)}, \qquad (3.20)$$

where the initial polar angle is defined by $\langle\cos\theta(0)\rangle = 1 - n_0/F$ in terms of initial excitation number $n_0 = F - \langle\hat{F}_z(0)\rangle$ away from the high-energy pole. These solutions are plotted in Fig. 3.3 for common experimental conditions.
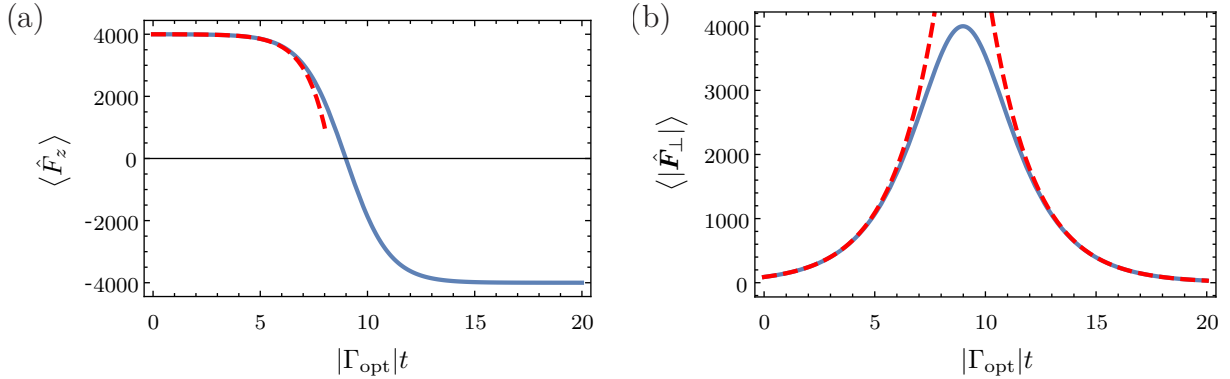
Figure 3.3: Expected optodynamical response of spin $F = 4000$ ensemble, prepared near its high energy state ($\langle \hat{F}_z(0) \rangle = F - 1$), with the cavity driven below resonance. Near the magnetic poles, the longitudinal spin evolves like $\hat{F}_z(t) = F - (F - \hat{F}_z(0))e^{\Gamma_{\text{opt}}t}$ and the magnitude of the transverse spin like $|\hat{\boldsymbol{F}}_\perp(t)| = |\hat{\boldsymbol{F}}_\perp(0)|e^{-\Gamma_{\text{opt}}t/2}$ (dashed lines).

3.2   Experimental demonstration

In the experimental work published in Ref. [24], the optodynamical damping rates and spring shifts were measured by preparing a spin ensemble in equilibrium with a cavity drive detuned by Δ with intracavity photon number $\bar{n}$, then 'kicking' it with short rf pulses and observing the transient response of the transverse spin precession as it evolves back to its equilibrium. The rf pulses were applied to one of the atom chip waveguide wires indicated in Fig. C.1, according to the experimental sequence sketched in Fig. 3.4. The pulses rotate the spin away from the initial state, creating a transverse spin amplitude with a well-defined phase, and the optodynamical interaction coherently drives it back toward the initial pole, determined by the sign of probe detuning Δ.

Amplification & damping

After applying a small $\pi/10$ rotation pulse away from equilibrium, the spin precessing can be observed damping back to the pole, such as displayed in Fig. 3.6a. Alternatively, a near π pulse was used to invert the spin near the opposite pole, but leaving a small displacement to define a coherent initial phase. The transverse spin is then observed amplifying away from the opposite pole, nutating around the equator before damping back to the initial state, as displayed in Fig. 3.5 and Fig. 3.6b.

   The approximate Hamiltonian derived in Eq. 3.7, leading to the solution in Eq. 3.19, is already overly simple to fully describe these experimental results, since it assumes a linear response of the cavity field to the spin precession. This approximation breaks down when the cavity shift induced by the total spin precessing around the equator is not a small fraction of the cavity linewidth $\alpha_1 g_c F \gtrsim \kappa$. When this constraint is exceeded, then the curvature and
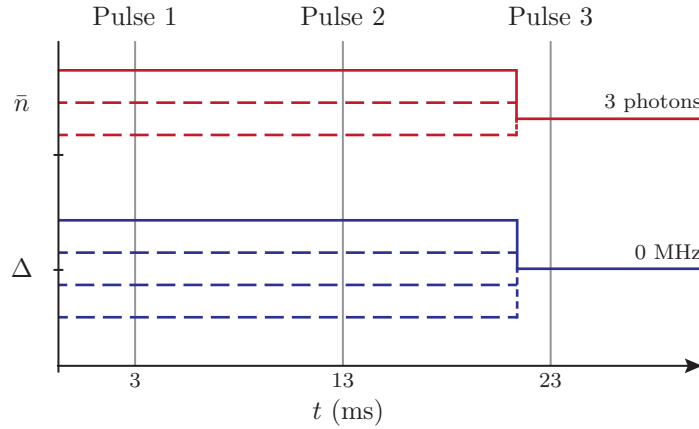
Figure 3.4: Experimental sequence for measuring the optodynamical rates of a spin oscillator. The transient response of the spin to a sequence of 3 applied rf pulses is observed. The first two pulses probe the dynamics of the spin returning to equilibrium with the probe at various calibrated values of probe detuning Δ and intracavity photon number $\bar{n}$. Before the final pulse, the probe is tuned to cavity resonance at a fixed intensity, providing a measurement of the Larmor frequency and cavity-probe detuning for software analysis and feedback to the computer-controlled set points.

higher-order terms of the cavity susceptibility produce optical modulation at harmonics of the Larmor frequency, which can be observed as additional sidebands on the cavity output field, such as displayed in Fig. 3.5.

The optodynamical effects of these harmonics are neglected in the theoretical treatment above, however, to first order, we can consider the time-averaged cavity susceptibility to be broadened and less transmissive, due to the large modulation of the resonance frequency. As observed in Fig. 3.5, the broader 'average' cavity spectrum results in saturation of the fundamental optodynamical response and slower optodynamical energy exchange, with the probe effectively spending a significant fraction of time on the opposite side of cavity resonance. The average intracavity intensity is also reduced, with most of the input power reflected while the cavity is shifted far off resonance.

However, the optical coupling is linear for sufficiently small excitations away from the magnetic poles. Expanding Eqs. 3.17 to leading order, for small rotations away from $\theta = 0$ ($\epsilon_s = -1$) or $\theta = \pi$ ($\epsilon_s = -1$), the transverse spin is exponentially amplified or damped at early times

$$\langle |\hat{\boldsymbol{F}}_\perp(t)|^2 \rangle \approx F^2 \theta^2(t) \approx (F^2 - n_0^2) e^{\Gamma_{\text{opt}} t}. \tag{3.21}$$

Thus the optodynamical rates can be extracted from the initial, small-amplitude dynamics of a spin driven toward or away from the pole, as reported in the published work. The frequency shift can also be qualitatively observed in Fig. 3.5 as a frequency chirp of the observed PSD, as the spin precesses from one pole, over the equator and back to the equilibrium state.
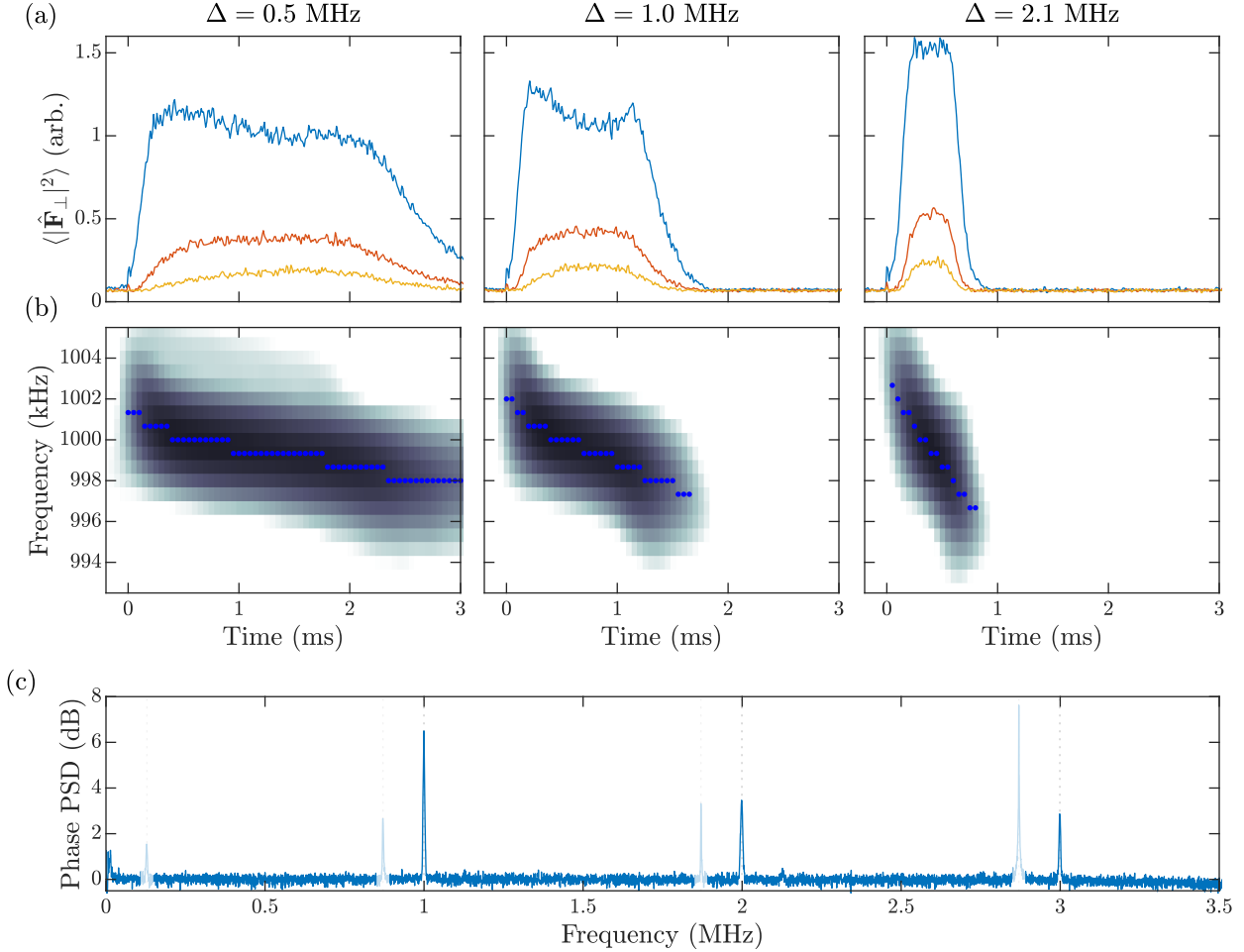
Figure 3.5: Spin optodynamics for an ensemble prepared in the low-energy state, then flipped with a near π pulse at $t = 0$, at increasing probe detuning below cavity resonance Δ. (a) The top row shows the instantaneous modulation power observed within a 100 kHz bandwidth around the Larmor frequency (blue), which is proportional to the square magnitude of the transverse spin for linear optomechanical coupling. The instantaneous power is plotted also from the 2nd (red) and 3rd (yellow) harmonic response. (b) The second row shows the spectral content of the signal as a function of time, calculated within a 0.5 ms Hamming window. This spectrogram demonstrates the optodynamical frequency 'chirp' as the spin is rotated back to the low-energy pole. (c) For large transverse spin, the dispersive shift leads to non-linear modulation of the cavity field, associated with higher harmonics appearing in the spectrum and saturation of the 1st harmonic. To first order, this effectively broadens the average cavity susceptibility, leading to a slow-down in optodynamical interactions, until the spin eventually begins damping back to the opposite pole.
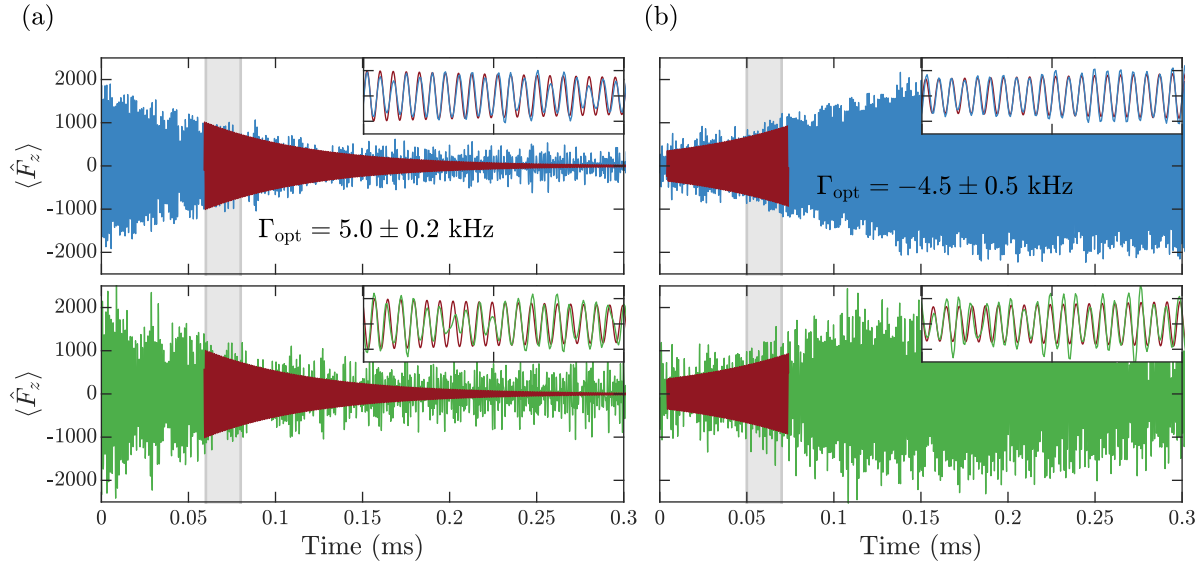
Figure 3.6: Coherent (a) damping and (b) amplification of Larmor precession, observed in the average heterodyne modulation from 30-40 repetitions of the measurement sequence. The observed optical phase modulation (upper row) and amplitude modulation (lower row) are simultaneously fit, with a fixed relative phase, to extract the optodynamical Larmor frequency shift $\delta\omega_{\text{opt}}$ and exponential damping rate Γ_{opt}. The frequency shift $\delta\omega_{\text{opt}}$ is measured relative to the intrinsic Larmor frequency, observed in response to the third rf pulse in the sequence described in Fig. 3.4, also accounting for the frequency difference due to the 60 Hz line phase, displayed in Fig. 3.7.

Coherent signal analysis

The preceding analysis ignores the phase information of Larmor precession recorded in the heterodyne signal. When averaging over an ensemble of measurements for improved signal to noise, considering such a phase-independent signal avoids loss from of uncertainty of the initial phase or ensemble dephasing from shot-to-shot frequency fluctuations. However, the autonomous optodynamical feedback is coherent, preserving the initial phase of the spin, and the phase information in the recorded signals contains additional information, in particular about the optodynamical frequency shift. Backaction from optical shot noise fluctuations does drive diffusion of the spin state, but this is negligible when the spin ensemble has a transverse polarization much larger than the variance of each spin component.

If the spin is prepared with a well-defined initial phase, such as produced by the rf pulse rotating it away from the pole, then the measured spin precession can be directly averaged together, averaging down the measurement noise and backaction diffusion and clearly revealing the coherent part of the optodynamical interaction, as shown in Fig. 3.6. This is performed by averaging the demodulated in-phase and quadrature-phase components of the heterodyne signal, as described by Eqs. 2.67.

For an on-resonance cavity probe, the optodynamical response is entirely contained in the optical phase quadrature. However, when driven off cavity resonance, the optodynamical response is imprinted on both amplitude and phase fluctuations of the light, indicated by the optodynamical measurement operator $\hat{d}$, defined by Eq. 2.57, becoming non-Hermitian. In the unresolved sideband limit, the operator is simply rotated by a complex phase, due to the bare cavity's complex susceptibility. In this case, the full optodynamical measurement can be readily recovered by a linear combination of $P_Q(t)$ and $P_I(t)$ described in Eq. 2.70, as if measured by an effective homodyne detector at a rotated quadrature angle.

However, outside of the unresolved-sideband limit, the finite cavity lifetime is no longer negligible on the timescale of Larmor precession. The cavity amplitude and phase quadratures measure the position of the oscillator with different effective delays, such that no linear combination of the detected quadratures fully captures the measurement operator. This occurs because the operator $\hat{d}$ is no longer a simple complex rotation of a Hermitian operator, due to the optodynamical sidebands sampling significantly different regions of the cavity susceptibility. The measurements captured in the two optical quadratures therefore represent non-collinear combinations of the instantaneous oscillator quadratures $\hat{X}(t)$ and $\hat{P}(t)$. To overcome this complexity, the Larmor precession signals observed in the heterodyne amplitude and phase quadratures, shown in Fig. 3.6, were simultaneously fit to exponentially damped sinusoids, with relative phase fixed to the expected value $\tan\left(\phi_{\mathrm{PM}} - \phi_{\mathrm{AM}}\right) = \omega_{\mathrm{s}}/\kappa$.

Polarization Symmetry

So far in this chapter, I have considered spin optodynamics only for a cavity driven by a single, circularly polarized laser. However, the spin optodynamics is actually independent of probe polarization. In the full Hamiltonian given by Eq. 2.11, the atomic spin couples to the longitudinal Stokes operator of the optical field $\hat{P}_z$, with amplitude dependent on both the intensity and helicity of the total cavity field. When driven with linearly polarized light, the average helicity of the intracavity field is zero, but the spin-dependent dispersive shifts displace the left- and right-circularly polarized cavity resonances in opposite directions, modulating the intracavity helicity. This modulation acts back on the spin through the interaction in Eq. 2.11, generating the same torque as produced by the total intensity modulation in the case of a circularly polarized drive.

In practice, this polarization symmetry is broken by the cavity's linear birefringence, which is considered in Sec. 3.5. The small birefringence of our cavity, however, has a negligible effect when driven with circularly polarized light, and in the published work we demonstrated independence of the measured damping rates and spring shifts on the sign of optical helicity.

Bias coils and magnetic field noise

The magnetic field orientation and Larmor precession frequency are controlled by pairs of (approximately) Helmholtz bias coils surrounding the vacuum chamber along perpendicular axes, as described in Appendix C. The total magnetic field must be sufficiently stable that

variations in the Larmor frequency introduce negligible phase noise to the observed spin precession, with frequency fluctuations well below 1 kHz for experimental timescales of 1 ms.

Frequency fluctuations observed during each measurement are predominantly caused by 60 Hz line-noise, which could largely be mitigated by synchronizing the measurement with the line phase, so that the temporal variations of the Larmor frequency were at least consistent from shot to shot, as seen in Fig. 3.7b. This synchronization is done by re-triggering the experimental sequence to a zero-crossing of the power-line phase immediately prior to the measurement, using the FPGA-based clock generation capability built into the Cicero computer control software [92]. The 60 Hz line noise was also reduced substantially by moving several large power supply transformers further from the vacuum chamber, seen in Fig. 3.7c, with remaining variations of the bias field components below 10 kHz.

The high-current Kepco ATE supplies driving the bias coils during the MOT and transport stages of the experimental sequence, described in Ref. [36], are still too noisy and imprecise for defining a stable Larmor frequency. Therefore, a set of mechanical relays was used to switch the necessary coils to Keithley 2280s precision current sources within 30 ms, between loading the atoms into the ODT and performing the measurement. The Keithley current sources are digitally programmed to ramp up to configured output currents after the, upon receiving triggers from the control computer after the relays switch, and provided improved stability and precision, reflected in Fig. 3.7d.

The residual RMS shot-to-shot fluctuations are typically below 1 kHz, shown in Fig. 3.7e, and slow drifts in the Larmor frequency are stabilized by extracting a Larmor frequency estimate from each shot and feeding back to the set point of the precision current source, as described in Sec. 4.1 and Appendix F. The magnetic fields produced by each of the coils and sources, as a function of driving current, were precisely calibrated by observing relative changes in the Larmor frequency, summarized in Appendix C.

Rf-dressed states and calibration of Rabi frequency

Rf pulses were used to prepare the initial coherent excitations of the collective spin for observation of optodynamical amplification and damping. The spin rotation driven by these pulses can be calibrated by measuring the Rabi frequency Ω_R induced by a resonant rf drive. A steady-state rf signal coupled to one of the nearby atom chip waveguide wires, sketched in Fig. C.1, drives continuous Rabi oscillation of the collective spin from pole to pole, modulating the amplitude of Larmor precession observed in the optodynamical measurement. This modulation produces additional sidebands in optical phase spectrum, at frequencies $\omega_s \pm \Omega_R$ spaced by the Rabi frequency around the Larmor frequency peak, shown in Fig. 3.8a.

These sidebands represent a Mollow triplet of cavity mediated transitions between rf-dressed spin states [93]. For a weak rf drive ($\Omega_R \ll \omega_s$), the energy splitting between the dressed states is linear in the rf coupling strength Ω_R, providing a single-shot calibration of the Rabi frequency for a given drive amplitude. When the rf coupling strength approaches the Larmor frequency, the transverse rf field is no longer a small perturbation and the
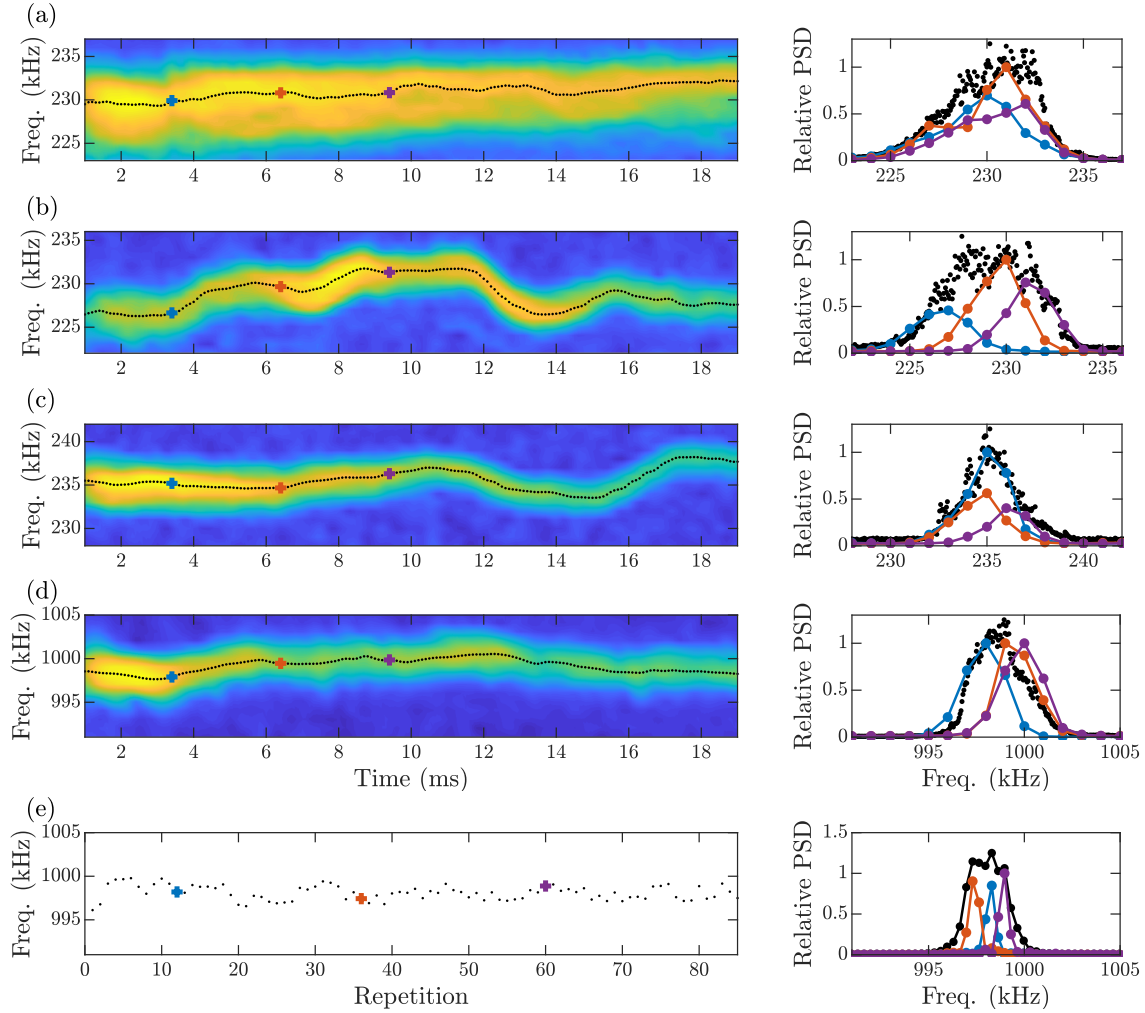
Figure 3.7: Measurement and reduction of Larmor frequency noise. (a-d) Spectrograms computed with a 1 ms Hamming window of the Larmor sideband in the detected optical phase quadrature, averaged over 60–100 repetitions. The right-hand column shows the average PSDs over 20 ms (black) and 1 ms windowed PSDs at the indicated times in the spectrogram (colors). (a) The average response was very broad but stationary in the original experimental configuration, using Kepco current supplies and unsynchronized with the power line phase. (b) Re-triggering the sequence on the 60 Hz power line phase immediately prior to measurement stabilized fluctuations due to magnetic line noise. (c) Moving several large power supplies further from the atoms reduced the amount of magnetic field noise. (d) Driving the magnetic bias coil with a Keithley 2280S precision current source further reduced the absolute frequency fluctuations, even at a much larger Larmor frequency. The Keithley source also exhibits reduced long-term drift and more precise set point control. (e) Larmor frequency from fits to single-shot PSDs of the first 3 ms of data in (d), with the average PSD and selected single-shot PSDs plotted on the right. The average linewidth of single-shot fits is 440 Hz, and the standard deviation of shot-to-shot frequency fluctuations is 830 Hz.
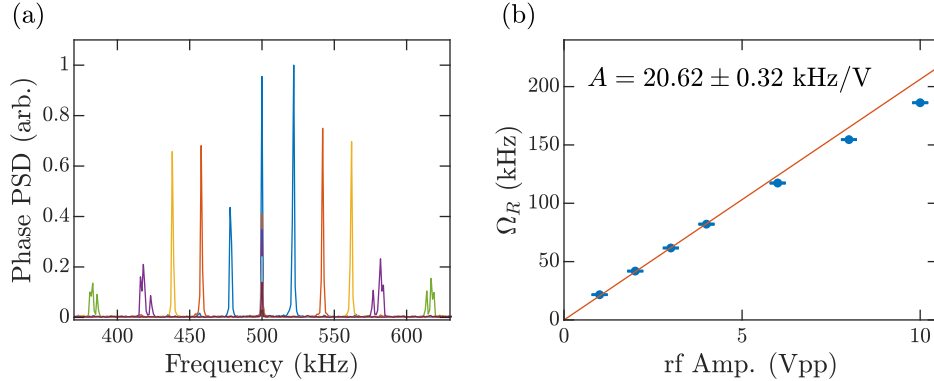
Figure 3.8: Calibration of the Rabi frequency for a steady-state rf drive from observation of the Mollow triplet. (a) Transitions between rf-dressed spin states are observed in the optical phase PSD of a resonantly driven spin, with Larmor frequency $\omega_s = 2\pi \times 500$ kHz, for 5 different continuous rf drive amplitudes. The spectrum of transitions form a Mollow triplet, with sidebands spaced by the Rabi frequency. (b) The Rabi frequency Ω_R is extracted by fitting the spectra observed in (a), providing a measurement of the rf coupling strength for calibrating resonant rf pulses.

system enters the strong-coupling regime, where the usual RWA breaks down, indicated by saturation of the observed splitting for the large drive amplitudes in Fig. 3.8b.

The Rabi frequency measured in this way can be used to determine the amplitude for short rf pulses, such as used to create the initial coherent excitations for the amplification and damping measurements above. However, because of transient effects from the pulse edges, the Rabi frequency calibrated under a continuous drive does not accurately predict the effects of short rf pulses. A more accurate calibration of short pulses was obtained by applying a 2π pulse to a spin ensemble in equilibrium with optodynamical damping and fine-tuning the pulse amplitude to minimize any transient response observed in the optodynamical measurement.

3.3 Equilibrium temperature and sideband thermometry

Under the effect of optodynamical damping and backaction-induced diffusion, the collective spin equilibrates to a steady-state distribution, which can be described by a thermodynamic temperature. Due to the symmetry of the approximate spin optodynamical Hamiltonian which preserves the total atomic spin, we consider only the maximally symmetric Dicke manifold [94], treating the ensemble as a single macroscopic spin F. In a magnetic field applied along $\hat{z}$, the eigenstates of this collective spin have well-defined angular momentum m along this axis. At equilibrium, a thermal distribution of the population P_m of each of

these states satisfies

$$P_{m+1} = P_m \exp(-\hbar\omega_{\rm s}\beta), \tag{3.22}$$

with inverse temperature defined as $\beta^{-1} = k_B T$.

A spin ensemble fully polarized in its highest or lowest energy state, with $\langle \hat{F}_z \rangle = \pm F$, is therefore described by zero temperature $T = 0$, while a maximally mixed state of the ensemble, with equal populations of each eigenstate, has infinite temperature $T \to \pm\infty$. Because of the finite ladder of eigenstates bounded by $-F \leq m \leq F$, any equilibrium state with a positive (negative) longitudinal spin component m therefore corresponds to a negative (positive) temperature distribution, approaching $T \to -\infty$ ($T \to \infty$) for $m \to 0$. The negative temperature states are a result of the finite heat capacity due to the bounded Hilbert space of the spin, in contrast to an ideal harmonic oscillator for which the energy increases without bound as $T \to +\infty$, corresponding to an equal mixture of all Fock states.

The equilibrium spin temperature for a damped spin oscillator is solely determined by the quantum fluctuations of the cavity photon number at the Larmor frequency, assuming negligible intrinsic energy loss. The optodynamical interaction can be rewritten as

$$\mathcal{H}_I = \hbar\frac{\alpha_1 g_{\rm c}}{2}\hat{c}^\dagger\hat{c}(\hat{F}_+ + \hat{F}_-), \tag{3.23}$$

reflecting transitions adding or removing energy from the total spin mediated by photon fluctuations. The transition rate for a collective spin F from state $|m\rangle$ to $|m+1\rangle$ is given by

$$\Gamma_\uparrow = P_m\frac{\alpha_1{}^2 g_{\rm c}{}^2}{4}|\langle m+1|\hat{F}_+|m\rangle|^2 S_{nn}(-\omega_{\rm s}), \tag{3.24}$$

where P_m is the population in state m, and $S_{nn}(\omega)$ is the PSD of photon number fluctuations inside the cavity. The rate of the reverse process is

$$\Gamma_\downarrow = P_{m+1}\frac{\alpha_1{}^2 g_{\rm c}{}^2}{4}|\langle m|\hat{F}_-|m+1\rangle|^2 S_{nn}(\omega_{\rm s}), \tag{3.25}$$

with matrix elements given by $\langle m \pm 1|\hat{F}_\pm|m\rangle = \sqrt{F(F+1) - m(m \pm 1)}$. Assuming these are the only processes mediating energy exchange with the spin ensemble, in equilibrium, detailed balance requires these rates to be equal, which implies

$$\frac{S_{nn}(\omega_{\rm s})}{S_{nn}(-\omega_{\rm s})} = \exp(\hbar\omega_{\rm s}\beta). \tag{3.26}$$

This result is also a statement of the effective temperature of the photon shot-noise fluctuations at the Larmor frequency, shaped by the cavity susceptibility, indicating that the spin equilibrates to the same temperature as this optical bath.

Under optodynamical damping by a single coherent drive, the equilibrium temperature is independent of the intra-cavity intensity. If a single, off-resonant tone damps the spin to

its steady state, the equilibrium temperatures is independent of the intra-cavity intensity since both the energy damping rate and backaction diffusion rate are linear in $\bar{n}$. The spin modulates sidebands on this off-resonant tone, with the total scattered power reflecting the transition rates above. These sidebands represent the total energy exchange with the spin are necessarily symmetrical at equilibrium, equivalent to the statement of detailed balance.

In order to probe the equilibrium temperature, a second, weak probe tone is applied on cavity resonance, adding diffusion which preferentially increases the absolute temperature, reflected in asymmetry of the sidebands modulated on the on-resonance probe, balanced by an asymmetry acquired by the sideband on the off-resonant damping tone (Fig. 3.9).

This two-tone cavity drive is generated from two rf signals, at $f_1 = 80$ MHz and $f_2 = \pm\Delta/2\pi + 80$ MHz, generated by the same direct digital synthesizer (DDS), electronically combined through an rf power splitter, then amplified to drive a single-pass acousto-optical modulator (AOM) in the probe path. The total rf drive power, and therefore first-order diffraction efficiency η, is reduced well below saturation to avoid inter-modulation between the two drive frequencies at f_1 and f_2, resulting in peaks at frequencies $2f_i - f_j$ which arise from non-linear mixing of the rf inputs and scale like η^3. The DDS chip allows precise, digital control of the relative detuning and intensity of the two tones, with the total intensity stabilized at the cavity input and the absolute frequency of one of the tones locked relative to cavity resonance by feedback from the heterodyne signal, as described in Appendix D. The total, time-averaged photon shot-noise spectrum with both tones is given by

$$S_{nn}(\omega) = \frac{2\kappa\bar{n}_{\mathrm{d}}}{(\omega + \Delta)^2 + \kappa^2} + \frac{2\kappa\bar{n}_{\mathrm{p}}}{\omega^2 + \kappa^2}, \tag{3.27}$$

where Δ is the detuning of the damping tone which has mean intra-cavity photon number $\bar{n}_{\mathrm{d}}$, and $\bar{n}_{\mathrm{p}}$ is the corresponding intensity of the probe.

The resulting equilibrium temperature is minimized at detuning $\Delta = -\epsilon\sqrt{\omega_{\mathrm{s}}^2 + \kappa^2}$, with the minimum temperature determined by the balance between the intensity of the two probe tones. For the measurements reported in [24], we chose this balance to achieve a fixed cooperativity for the on-resonance probe, defined by

$$C_s = \frac{4g_{\mathrm{s}}{}^2\bar{n}_{\mathrm{p}}}{\kappa\Gamma_{\mathrm{opt}}}, \tag{3.28}$$

where $\Gamma_{\mathrm{opt}} = \epsilon_s g_{\mathrm{s}}{}^2\big[S_{nn}(\omega_{\mathrm{s}}) - S_{nn}(-\omega_{\mathrm{s}})\big]$ is the optical damping due to the off-resonance tone. Solving Eq. 3.28 for a fixed cooperativity C_s, the necessary ratio of probe to pump power is

$$\frac{\bar{n}_{\mathrm{p}}}{\bar{n}_{\mathrm{d}}} = \frac{\kappa}{2}C_s \,\mathrm{Im}\{\alpha[\epsilon_s\omega_{\mathrm{s}}]\} \tag{3.29}$$

which can be evaluated at the optimal detuning Δ,

$$\frac{\bar{n}_{\mathrm{p}}}{\bar{n}_{\mathrm{d}}} = \frac{C_s\omega_{\mathrm{s}}}{2\sqrt{\omega_{\mathrm{s}}^2 + \kappa^2}}. \tag{3.30}$$
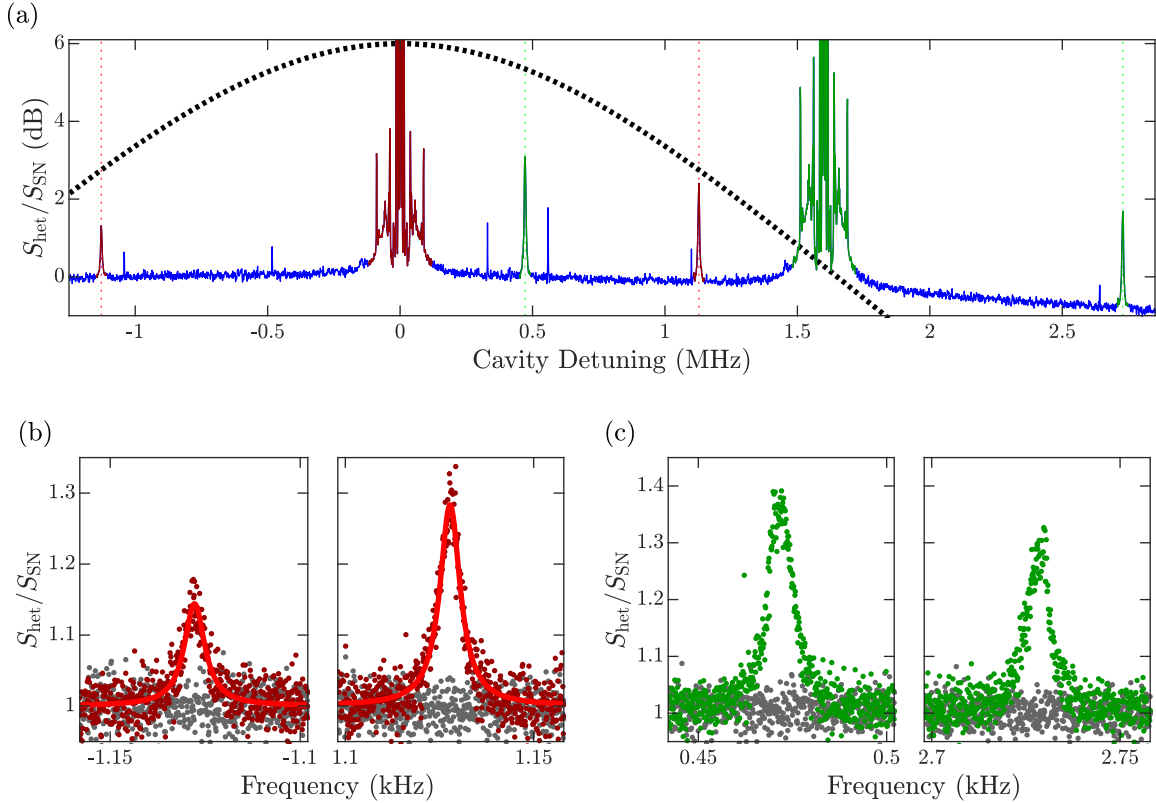
Figure 3.9: Two-tone damping and sideband asymmetry measurement. (a) Raw heterodyne PSD of two-tone cavity drive, normalized by the observed shot noise power density in the vicinity of the on-resonance tone ($\Delta = 0$). the carrier peaks are off scale at 85 dB on resonance (red, $\Delta = 0$) and 92 dB off resonance (green, $\Delta = 2\pi \times 1.6$ MHz) corresponding to 2.0 and 4.1 intracavity photons, respectively. The Stokes and anti-Stokes sidebands corresponding to each drive tone are indicated, and all other spectral features are technical noise peaks present on measurements of an empty cavity. The variation in the observed shot noise power density is due to reduced detector efficiency at higher frequency. The relative cavity transmission spectrum is plotted for reference (dotted black). (b) Sideband asymmetry between Stokes and anti-Stokes scattering from the weak, resonant probe tone, reflecting an absolute temperature $k_B T = -1.5\hbar\omega_{\rm s}$. (c) Sideband asymmetry observed in scattering from the off-resonant damping tone, reflecting damping of the spin to its high energy state. To correct for frequency dependent gain, each sideband in (b-c) is normalized by the locally measured shot noise power density, matching the measured empty-cavity signal (gray).

Driving the cavity in this condition yields a minimum equilibrium temperature given by

$$\exp \hbar\omega_{\mathrm{s}}\beta = 1 + 2\left[\sqrt{1 + \frac{\kappa^2}{\omega_{\mathrm{s}}^2} + \frac{C_s\kappa^2}{\kappa^2 + \omega_{\mathrm{s}}^2}} - 1\right]^{-1}. \tag{3.31}$$

This equilibrium temperature corresponds to an average excitation number away from the poles $\hat{n}_s = F + \epsilon_s \hat{F}_z$, in terms of the longitudinal spin

$$\langle \hat{F}_z \rangle = \frac{1}{Z}\sum_{m=-F}^{F} m\, e^{m\hbar\omega_{\mathrm{s}}\beta} = \frac{(F+1)\sinh F\beta - F\sinh(F+1)\beta}{2\sinh\left(\beta/2\right)\sinh\beta\left(F+1/2\right)}, \tag{3.32}$$

where $Z = \sum_m \exp(m\hbar\omega_{\mathrm{s}}\beta)$ is the partition function. For $\langle \hat{n}_s \rangle \ll F$, this can be approximated by the Bose distribution $n_s \approx (e^{\hbar\omega_{\mathrm{s}}\beta} - 1)^{-1}$ (Fig. 3.10b), reflecting the validity of the Holstein-Primakoff approximation in this regime. The equilibrium occupation for the optodynamically damped spin is analogous to that achieved by optomechanical sideband cooling [95], described by the same equilibrium temperature in the Holstein-Primakoff approximation, however with the absence of a thermal bath.
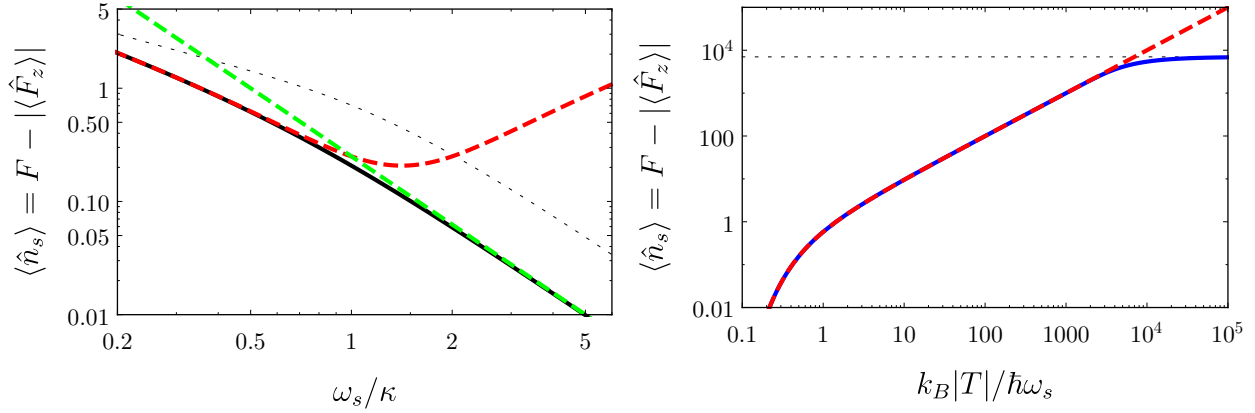
Figure 3.10: (a) Minimum equilibrium spin occupation, as a function of the Larmor frequency, showing the transition between approximations in the unresolved sideband (red dashed) and resolved sideband (green dashed) limits. Measurement of the sideband asymmetry modulated on an additional resonant probe with fixed cooperativity C_s adds a nearly constant offset (dotted line). (b) The average spin excitation $\hat{n}_s$ away from either pole (blue), as a function of the absolute equilibrium temperature. At low temperature, this is well approximated by the Bose distribution (dashed red), while at high temperature it saturates to the maximum thermal excitation $F = 7000$ (dotted gray).

3.4   QND measurements of longitudinal spin

Interaction with the cavity field facilitates sensitive measurements of the collective spin. However, in a transverse magnetic field, as considered above, energy exchange and diffusion driven by the optodynamical interaction introduce backaction, which perturbs the spin state being measured. To measure components of the spin without disturbing them, it is preferable to use the QND configuration in Fig. 3.1, where the dispersive cavity shift can be used as a sensitive, non-destructive probe of the longitudinal spin, both before or after rf pulses. Such QND measurements were used to characterize the intrinsic dynamics of the spin ensemble, such as energy relaxation or dephasing of the transverse spin, using rf pulse sequences applied to an ensemble evolving in the dark, without probe light driving the cavity.

Measurement of cavity shift by probe sweep

In the QND configuration, the applied magnetic field is oriented parallel to the cavity axis $\mathbf{k} = \mathbf{z}$. This configuration results in the effective interaction Hamiltonian given by Eq. 2.14, describing a dispersive cavity frequency shift sensitive to the total atom number and longi-

tudinal spin component according to

$$\Delta_s = g_c N_a \left(\alpha_0 + \alpha_1 \hat{f}_z \right), \qquad (3.33)$$

where $\hat{f}_z$ is the average single-atom longitudinal spin.

This cavity resonance shift is measured by sweeping the probe frequency slowly across a roughly 40 MHz range around the cavity resonance (at about 8 MHz/ms), with a constant drive intensity, and fitting the observed transmission peak. This measurement is then repeated on an empty cavity, immediately after ejecting the atoms, revealing the atom-induced cavity shift as the difference between the probe frequency at the observed peaks, shown in Fig. 3.11a-b.

These cavity shift measurements were used to calibrate the Larmor frequency in the QND field configuration, by observing the effect of short rf pulses on the longitudinal spin projection as a function of drive frequency, with typical results shown in Fig. 3.11c. Then, the rf coupling strength could be calibrated by driving full Rabi oscillations of the longitudinal spin with resonant rf pulses, such as shown in Fig. 3.11d.

Measurement of spin relaxation and dephasing

Describing loss mechanisms for a spin ensemble coupled to the environment are more complicated to model than those for a harmonic oscillator coupled to a thermal bath, with distinct energy relaxation and dephasing mechanisms for the spin oscillator. These decay processes are conventionally parameterized by an exponential energy relaxation rate T_1, describing the longitudinal spin decay, and the transverse spin dephasing rate T_2, which results in loss of spin polarization and doesn't have a direct analog for a single-mode mechanical oscillator. In traditional NMR models, the T_1 time is related to thermal relaxation of an inverted spin population, which at long times equilibrates with spin polarization in the low-energy state, for a sufficiently strong magnetic field or cold environment. The observed dephasing rate T_2^* is typically distinguished between 'inhomogeneous broadening,' due to spatially varying magnetic fields that induce dephasing of the total transverse polarization during Larmor precession, which can be reversed and suppressed with a Hahn-echo pulse sequence, and irreversible dephasing due to interactions between the spins and environment, defining the more intrinsic T_2 dephasing rate. This summary is overwhelmingly simplistic, but captures the basic concepts in the literature.

In order to characterize the loss rates for spin optodynamics experiments discussed in Sec. 3.2, the spin relaxation and dephasing rates were measured in a typical transverse bias field inducing Larmor precession at $\omega_s = 2\pi \times 1$ MHz, with results shown in Fig. 3.12 and 3.13.

With the spin ensemble initially prepared in its highest-energy state, a QND measurement of the initial cavity shift Δ_{S0} provides an estimate of the total atom number, allowing fluctuations in atom number from shot-to-shot to be normalized. The magnetic bias fields were then adiabatically rotated in 20 ms to the spin optodynamics configuration and held
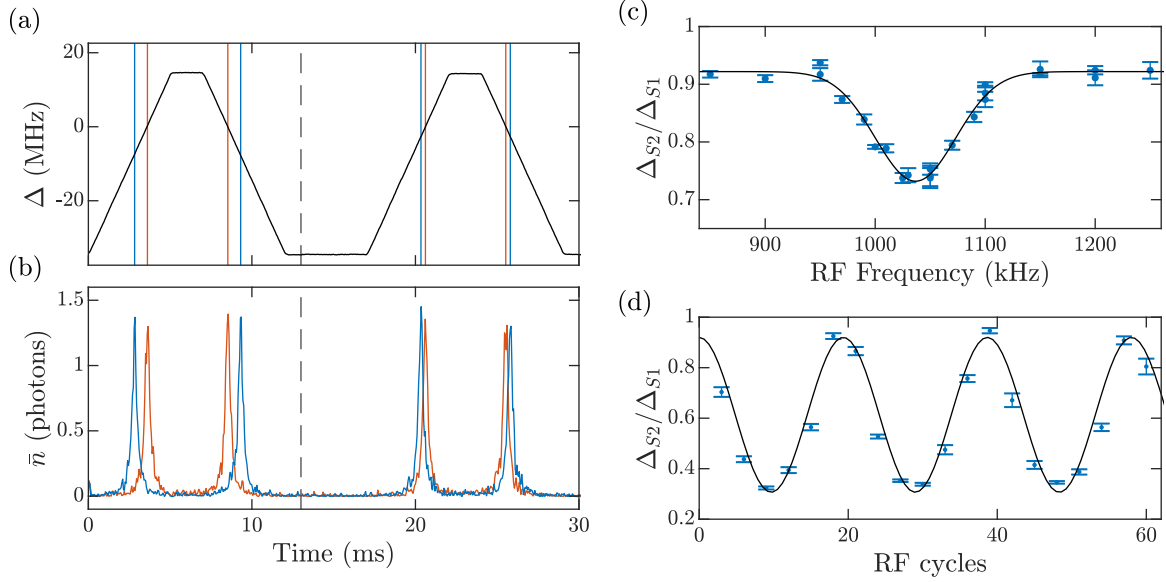
Figure 3.11: Measurement of cavity shift and Rabi frequency calibration in magnetic field parallel to cavity axis. (a) QND measurement of the spin-dependent cavity shift performed by sweeping the probe frequency up and down across the cavity resonance, with detuning Δ here reported relative to the empty-cavity resonance. (b) The atom-induced frequency shift is extracted by fitting the observed cavity transmission peak (blue line), reported here in terms of the corresponding intracavity photon number, and comparing to the empty-cavity frequency measured immediately after ejecting the atoms from the cavity (red line). The rotation produced by an rf pulse applied in between two sets of cavity sweeps (dashed line) can be inferred from the change of the observed cavity shifts. (c) The Larmor frequency in a magnetic field parallel to the cavity axis is calibrated by rf spectroscopy, revealed by a resonance in the ratio of cavity shifts before and after applying a weak rf pulses across a range of frequencies. (d) The Rabi frequency for a fixed pulse amplitude can then be calibrated by applying resonant rf pulses of increasing length, driving complete oscillations of the longitudinal spin. The spins are initially polarized in the highest-energy state, so the ratio of cavity shifts is expected to oscillate between 1 and 1/3. However, as seen for off-resonance pulses in (c), the observed ratios are reduced by almost 10%, likely due to atom loss or heating between sweeps.

Figure 3.12: (a) Timing diagram for QND cavity measurements before and after an rf pulse sequence, applied in a transverse field to characterize loss in the spin optodynamics configuration. The initial cavity shift is measured with probe sweeps to estimate the atom number. The magnetic fields are then adiabatically ram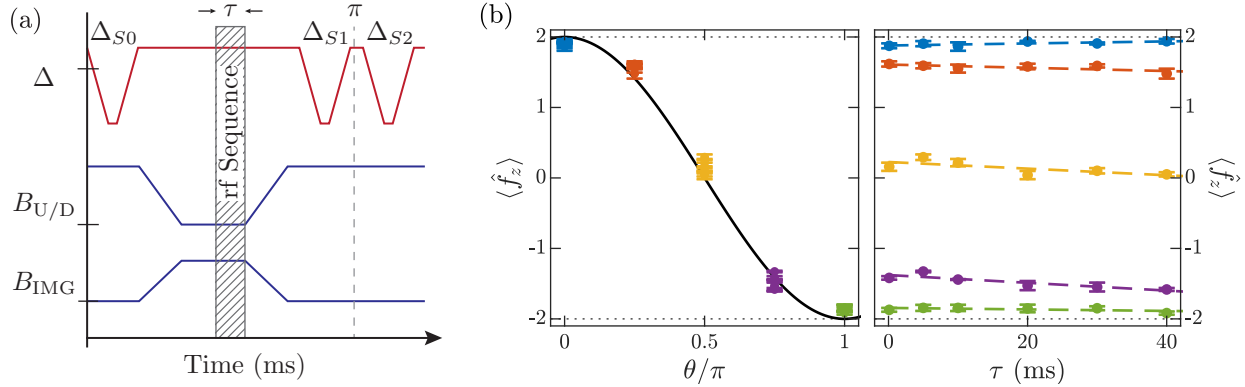ped between the QND and spin optodynamics configuration, preserving the longitudinal spin. After an rf pulse sequence of duration τ, the final spin projection and atom number are independently estimated from two sets of QND measurement sweeps, with a π pulse in between to invert the longitudinal spin component. (b) The spin relaxation rate is measured by rotating the spin to a chosen polar angle θ with a resonant rf pulse, and then holding for time τ in the transverse field. The average spin projection per atom $\hat{f}_z$ plotted vs. both the polar angle and the hold time, show negligible relaxation. States rotated near the equation, with population in multiple Zeeman sublevels, show gradual relaxation, but still negligible on the few ms timescales of experiments reported in this chapter.

for 20 ms more, to allow transients, likely from induced eddy currents, to settle. Then one of the rf pulse sequences described below was performed, to measure either spin relaxation or dephasing. After rotating the field back to the QND configuration, the final longitudinal spin was measured by performing two sets of cavity sweeps, with a π pulse in between to invert the spin population. The same sequence is also on an empty cavity to measure the natural cavity frequency.

The cavity shifts measured before and after the inversion pulse, Δ_{S1} and Δ_{S2} respectively, help disentangle the scalar and vector components of the shift reflected in Eq. 3.33. In particular, the average longitudinal spin per atom $\langle \hat{f}_z \rangle$ can be estimated from the change in cavity shift induced by the spin inversion

$$\langle \hat{f}_z \rangle = \frac{\alpha_0}{\alpha_1} \frac{\Delta_{S1} - \Delta_{S2}}{\Delta_{S1} + \Delta_{S2}}. \tag{3.34}$$

Additionally, comparison of the scalar component of the final shift to the the initial cavity shift Δ_{S0} provides an estimate of the reduction in the scalar interaction, either due to atom

loss or increased thermal width, described by

$$\Delta N_a = \frac{\Delta_{S1} + \Delta_{S2}}{2\alpha_0 \Delta_{S0}}. \tag{3.35}$$

These expressions assume a perfect inversion of the spin population between the final two sets of sweeps, with any error in the final π pulse always resulting in an underestimate of the longitudinal spin component.

Spin relaxation

Energy relaxation of the spin ensemble is mediated by any process that drives incoherent transitions between Zeeman sublevels. For an ensemble of ultracold atoms optically suspended inside an ultra-high vacuum chamber, the lifetimes in the ground-state Zeeman levels is relatively high, with energy relaxation mediated by processes such as inelastic atomic collisions, spin-orbit coupling between the atomic spin and motion (as described in Sec. 5.2), coupling to blackbody radiation, or spontaneous emission. The relaxation rate was measured as a function of polar angle, by rotating the spin with an initial rf pulse, then holding in the transverse field for a variable time τ, before performing the final QND readout, with results displayed in Fig. 3.12b. The observed energy relaxation is negligible after 40 ms, providing a lower bound for the T1 relaxation time.

Spin dephasing

Spin dephasing occurs when individual atoms accumulate a differential phase, leading to depolarization of the total transverse spin, but conserving the total energy. This dephasing can arise from spatial variations of the Larmor frequency, which is not reversible because of thermal motion of the atoms.

The intrinsic spin dephasing rate was measured using a Ramsey pulse sequence, illustrated in Fig. 3.13a. A Hahn-echo pulse is included at the mid-point of the sequence, to suppress the effect of shot-to-shot variations in the Larmor frequency, which would randomize the effective phase of the final Ramsey pulse. The phase of the Ramsey sequence is controlled by inserting a variable time delay of up to one Larmor period before the final $\pi/2$ pulse. This delay allows the transverse spin to accumulate up to one more cycle of rotation, such that the final longitudinal spin after the final $\pi/2$ pulse oscillates from pole to pole, as seen in Fig. 3.13b-c. The amplitude of this oscillation indicates the remaining spin polarization, which is observed to decay for increasing sequence duration in Fig. 3.13c.

The amplitude of the observed Ramsey fringe after each duration τ was determined by a least-squares fit, with results summarized in Fig. 3.13d. The observed fringe contrast shows a fast oscillation, due to collapse and revival of spin polarization caused by the quadratic Zeeman shift, in addition to a slower decay envelope. The quadratic Zeeman shift arises from mixing between the $F = 1$ and $F = 2$ ground state hyperfine manifolds, caused by a magnetic bias field exceeding the small-field limit, and induces beats between vector and
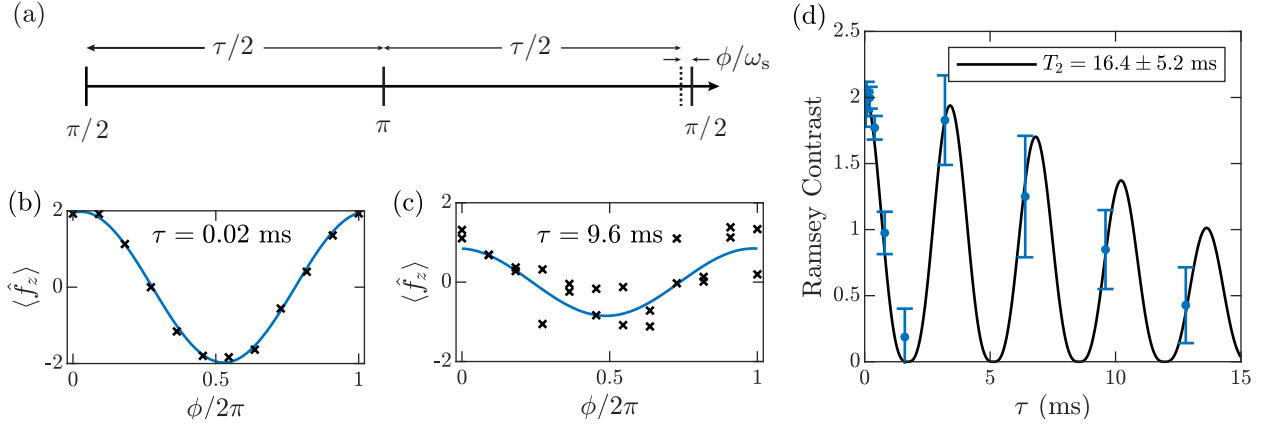
Figure 3.13: (a) Ramsey sequence with Hahn echo pulse, for measuring transverse spin dephasing. The Ramsey phase ϕ is tuned by delaying the final pulse by up to one Larmor period $2\pi/\omega_s$. (b) Ramsey contrast measured in a transverse magnetic field with $\omega_s = 2\pi \times 1$ MHz, after a $\tau = 0.8$ ms total Ramsey sequence duration. (c) Spin dephasing results in a loss of contrast after $\tau = 9.6$ ms of transverse spin precession. (d) Ramsey contrast as a function of the total pulse sequence length, showing the effect of spin dephasing. The fast oscillation is due to polarization collapse and revival from the quadratic Zeeman shift. Although undersampled, the T2 time is estimated by a single-parameter Guassian fit envelope, modulated by the beatnote for the expected quadratic Zeeman shift $|\omega_q| = 2\pi \times 147$ Hz (see Sec. A.1).

tensor components of the $F = 2$ spin manifold. Although the beatnote from the quadratic Zeeman shift is undersampled in Fig. 3.13d, the beat frequency and shape is derived in Appendix A.1 and can be precisely determined according to the Larmor frequency, allowing it to be included in the fit function without additional free parameters. Performing a least squares fit to data in Fig. 3.13d, with an overall Gaussian decay envelope, suggests a e^{-1} dephasing time of $T_2 = 16 \pm 5$ ms, which indicates that intrinsic dephasing is also negligible on the timescale of dynamics considered in this chapter.

3.5 Cavity linear birefringence

Any linear birefringence of the cavity mirrors causes the circular polarization modes to be mixed, breaking the degeneracy between polarization eigenstates. This can be represented by considering an empty cavity with a linear birefringence, which results in slightly different resonance frequencies for the vertical v and horizontal h polarizations.

$$\mathcal{H}_{\mathrm{bi}} = \hbar\omega_h \hat{c}_h^\dagger \hat{c}_h + \hbar\omega_v \hat{c}_v^\dagger \hat{c}_v = \hbar \begin{pmatrix} \hat{c}_h^\dagger & \hat{c}_v^\dagger \end{pmatrix} \begin{pmatrix} \omega_h & 0 \\ 0 & \omega_c \end{pmatrix} \begin{pmatrix} \hat{c}_h \\ \hat{c}_v \end{pmatrix} \tag{3.36}$$

The polarization modes can be transformed into the circular basis using the unitary transformation

$$\begin{pmatrix} \hat{c}_h \\ \hat{c}_v \end{pmatrix} = \frac{1}{\sqrt{2}} \begin{pmatrix} 1 & 1 \\ -i & i \end{pmatrix} \begin{pmatrix} \hat{c}_+ \\ \hat{c}_- \end{pmatrix}, \tag{3.37}$$

which allows writing the birefringent Hamiltonian in terms of circular mode operators

$$\mathcal{H}_{\mathrm{bi}} = \hbar\omega_{\mathrm{c}} \left(\hat{c}_+^\dagger \hat{c}_+ + \hat{c}_-^\dagger \hat{c}_- \right) + \hbar\Delta_b \left(\hat{c}_+^\dagger \hat{c}_- + \hat{c}_-^\dagger \hat{c}_+ \right), \tag{3.38}$$

which is the more natural basis for the atomic interaction, assuming a small linear birefringence. Here, the average of the linear mode frequencies $\omega_{\mathrm{c}} = (\omega_h + \omega_v)/2$ is the cavity 'resonance' frequency for a circularly polarized field, and $\Delta_b = (\omega_h - \omega_v)/2$ is the strength of the linear cavity birefringence which mixes the circular modes.

Measurement of birefringence

The birefringence of our optical cavity was calibrated by measuring the apparent linewidth of the cavity transmission spectrum as a function of input polarization, with results shown in Fig. 3.14a. For a given input polarization, the total transmission spectrum was measured by slowly sweeping the drive frequency across the cavity resonance while recording the transmitted intensity. If the cavity's linear birefringence exceeded its natural linewidth, one would resolve separate resonances for each linear polarization component, with the relative transmitted intensity of each component given by the projection of the input polarization onto the polarization axes of the cavity.

Fortunately, our cavity's birefringence is small, such that the total cavity transmission spectrum is approximately Lorentzian for any input polarization, illustrated in Fig. 3.14b, but with a polarization dependent linewidth. For a linearly polarized input beam aligned with one of the cavity's polarization axes, the input probes the resonance of that polarization mode only, yielding an observed transmission spectrum with a minimal linewidth reflecting the cavity's intrinsic lifetime $\kappa = 2\pi \times 1.8$ MHz. However, if the input polarization is rotated by 45 degrees, then the transmission spectrum is given by the sum of the components transmitted through both linear polarization modes, increasing the apparent linewidth (Fig. 3.14b). Measurements of the polarization-dependent linewidth of our cavity, shown in Fig. 3.14a, are consistent with a linear birefringence of $|\Delta_b| = 2\pi \times 0.6$ MHz.

There is some further subtlety, because the transmitted intensity here was measured by our single-polarization optical heterodyne detector, which introduces an additional polarization dependence into the results. This was controlled by detecting a linear polarization component of the output, with polarization axis rotated to maximize the detected transmission on cavity resonance for each chosen input polarization. Assuming a small birefringence, the output polarization is only slightly perturbed from the input polarization, which might distort the shape of the linewidth modulation observed in Fig. 3.14a, but should not affect the peak-to-peak contrast.
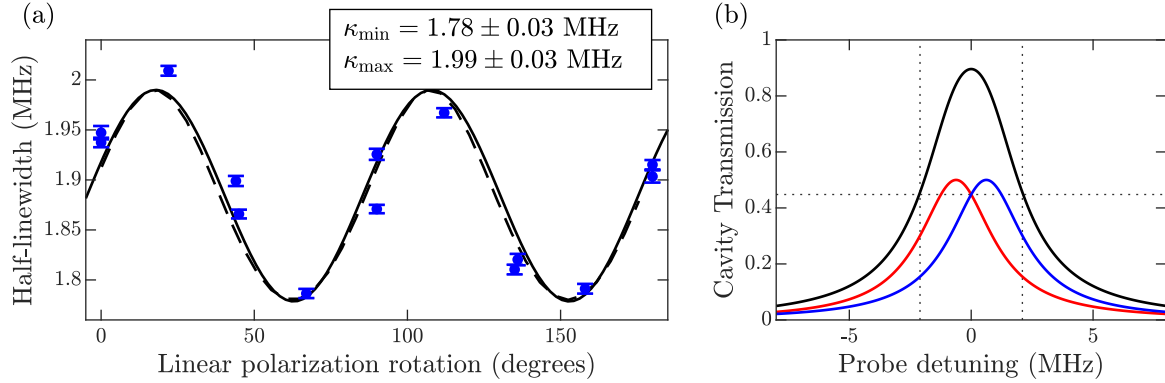
Figure 3.14: (a) Measurement of cavity birefringence from the relative width of the cavity transmission spectrum, as a function of rotation angle of the input linear polarization. (b) The peak-to-peak variation of the linewidths in (a) is consistent with the sum of two Lorentzians with half-linewidth $\kappa = 2\pi \times 1.8$ MHz, separated by $2\Delta_b = 2\pi \times 1.2$ MHz.

Birefringence of an empty cavity

To gain some physical insight into the effects of this birefringence alone, I will solve for the steady state cavity occupation described by the Hamiltonian above. Assuming an amplitude decay of κ for each of the cavity modes, the equations of motion in a rotating frame are,

$$\dot{\hat{c}}_+ = (-i\Delta - \kappa)\hat{c}_+ + \sqrt{2\kappa}\eta_+ - i\Delta_b\hat{c}_- \tag{3.39}$$

$$\dot{\hat{c}}_- = (-i\Delta - \kappa)\hat{c}_- + \sqrt{2\kappa}\eta_- - i\Delta_b\hat{c}_+ \tag{3.40}$$

Where $\eta_\pm$ represent the external cavity drives, with strength parametrized by the maximum intra-cavity photon number $n_{\max}^\pm = \frac{2}{\kappa}\langle|\eta_\pm|^2\rangle$. Assuming a drive with a single, circular polarization ($\eta_- = 0$ and η_+ real), the stationary solutions are

$$\bar{n}_+ = \langle\hat{c}_+^\dagger\hat{c}_+\rangle = n_{\max}^+\frac{\kappa^2(\Delta^2 + \kappa^2)}{\Delta^4 + 2\Delta^2(\kappa^2 - \Delta_b^2) + (\kappa^2 + \Delta_b^2)^2} \tag{3.41}$$

$$\bar{n}_- = \langle\hat{c}_-^\dagger\hat{c}_-\rangle = n_{\max}^+\frac{\kappa^2\Delta_b^2}{\Delta^4 + 2\Delta^2(\kappa^2 - \Delta_b^2) + (\kappa^2 + \Delta_b^2)^2} \tag{3.42}$$

For small birefringence, this can be expanded to first order in the small parameter $\beta = (\Delta_b/\kappa)^2$, giving the leading order corrections to the photon numbers

$$\bar{n}_+ = n_{\max}^+\frac{\kappa^2}{\kappa^2 + \Delta^2}\left(1 - \beta\frac{2\kappa^2(\kappa^2 - \Delta^2)}{(\kappa^2 + \Delta^2)^2}\right) \tag{3.43}$$

$$\bar{n}_- = n_{\max}^+\beta\left(\frac{\kappa^2}{\kappa^2 + \Delta^2}\right)^2 \tag{3.44}$$

By calculating the mean photon number of each polarization modes, I have neglected their relative phase. To better capture the full state of the cavity field, it is helpful to
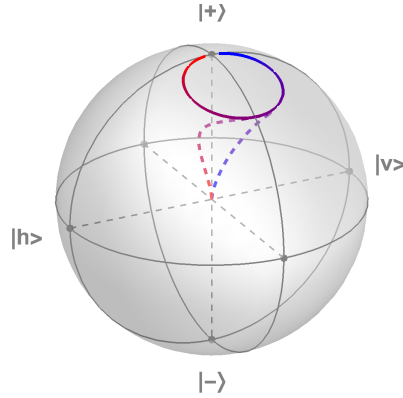
Figure 3.15: Polarization trajectory on the Poincaré sphere for a probe swept across cavity resonance (from red to blue), with a linear birefringent splitting of $\Delta_b = 2\pi \times 0.6$ MHz. The dashed line also reflects the relative transmission across the resonance, with the vector from the origin to each point on the trajectory tracing the solid polarization path on the surface of the sphere.

rewrite these solutions in terms of Stokes operators, defined in Eqs. 2.9.

$$\langle \hat{P}_x \rangle = n_{\max}^+ \frac{1}{4} \left(\frac{\kappa^2}{\kappa^2 + (\Delta + \Delta_b)^2} - \frac{\kappa^2}{\kappa^2 + (\Delta - \Delta_b)^2} \right) \tag{3.45a}$$

$$\langle \hat{P}_y \rangle = n_{\max}^+ \frac{\kappa}{4\Delta} \left(\frac{\kappa^2}{\kappa^2 + (\Delta - \Delta_b)^2} - \frac{\kappa^2}{\kappa^2 + (\Delta + \Delta_b)^2} \right) \tag{3.45b}$$

$$\langle \hat{P}_z \rangle = n_{\max}^+ \frac{1}{2} \frac{\kappa^2 \left(\Delta^2 - \Delta_b^2 + \kappa^2 \right)}{\Delta^4 + 2\Delta^2 \left(\kappa^2 - \Delta_b^2 \right) + \left(\Delta_b^2 + \kappa^2 \right)^2} \tag{3.45c}$$

These can be visualized by plotting a trajectory on the Poincaré sphere, for a probe detuning swept across cavity resonance, from red to blue, as plotted in Fig. 3.15. This demonstrates that the linear birefringence functions as a small, frequency-dependent waveplate, which makes the polarization slightly elliptical near cavity resonance. However, in terms of the occupation of the driven polarization, the leading order correction scales with $(\Delta_b/\kappa)^2 = 0.1$, such that it leads to negligible effects.

Optodynamical effects of birefringence

We can consider the optodynamical effects of the cavity birefringence by combining the spin optodynamical Hamiltonian in Eq. 3.2, but including both polarization modes together with the empty cavity birefringence described by Eq. 3.38. Linearizing the dynamics again around

the average field amplitudes $\alpha_\pm$, the resulting equations of motion are

$$\dot{\hat{Z}}_s = \epsilon_s \omega_s \hat{P}_s \tag{3.46}$$

$$\dot{\hat{P}}_s = -\epsilon_s \omega_s \hat{Z}_s - 2g_s(\alpha_+ \hat{c}_+^\dagger + \alpha_+^* \hat{c}_+ - \alpha_- \hat{c}_-^\dagger - \alpha_-^* \hat{c}_-) \tag{3.47}$$

$$\dot{\hat{c}}_\pm = (i\Delta - \kappa)\hat{c}_\pm \mp ig_s\alpha_\pm \hat{Z}_s + \sqrt{2\kappa}\hat{\xi}_\pm - i\Delta_b \hat{c}_\mp \tag{3.48}$$

A cavity input field of arbitrary polarization, specified on the Poincaré sphere with polar coordinate θ and azimuthal angle ϕ, can be represented as a vector of the circular components $\bar{\boldsymbol{\eta}}$

$$\bar{\boldsymbol{\eta}} = \begin{pmatrix} \bar{\eta}_+ \\ \bar{\eta}_- \end{pmatrix} = P_{\text{in}} \begin{pmatrix} e^{i\phi/2}\cos\theta/2 \\ e^{-i\phi/2}\sin\theta/2 \end{pmatrix} \tag{3.49}$$

In terms of this input, the steady-state cavity field for both polarizations, up to a global phase, is given by the amplitude vector

$$\begin{pmatrix} \alpha_+ \\ \alpha_- \end{pmatrix} = \frac{\sqrt{2\kappa}}{\kappa^2 + \Delta^2 + \Delta_b^2} \begin{pmatrix} \kappa + i\Delta & -i\Delta_b \\ -i\Delta_b & \kappa + i\Delta \end{pmatrix} \bar{\boldsymbol{\eta}} \tag{3.50}$$

An analytic solution of these equations of motion would be tedious, but we can easily recover the susceptibilities of the linear model. Rewriting these equations in terms of a vector of quadratures $\boldsymbol{X} = (\hat{Z}_s, \hat{P}_s, \hat{c}_+^{\text{AM}}, \hat{c}_+^{\text{PM}}, \hat{c}_-^{\text{AM}}, \hat{c}_-^{\text{PM}})^\mathsf{T}$, as in Sec. 2.4, they can be summarized by the matrix equation $\dot{\boldsymbol{X}} = M\boldsymbol{X} + \boldsymbol{v}$, with the coherent response matrix M and input vector $\boldsymbol{v}$ given by

$$M = \begin{pmatrix} 0 & -\omega_s & 0 & 0 & 0 & 0 \\ \omega_s & 0 & -2g_s\alpha_+^{\text{AM}} & 2g_s\alpha_+^{\text{PM}} & 2g_s\alpha_-^{\text{AM}} & -2g_s\alpha_-^{\text{PM}} \\ -g_s\alpha_+^{\text{PM}} & 0 & -\kappa & \Delta & 0 & -\Delta_b \\ g_s\alpha_+^{\text{AM}} & 0 & -\Delta & -\kappa & \Delta_b & 0 \\ g_s\alpha_-^{\text{PM}} & 0 & 0 & -\Delta_b & -\kappa & \Delta \\ -g_s\alpha_-^{\text{AM}} & 0 & \Delta_b & 0 & -\Delta & -\kappa \end{pmatrix} \quad \boldsymbol{v}(t) = \begin{pmatrix} 0 \\ 0 \\ \sqrt{2\kappa}\,\hat{\xi}_+^{\text{AM}} \\ \sqrt{2\kappa}\,\hat{\xi}_+^{\text{PM}} \\ \sqrt{2\kappa}\,\hat{\xi}_-^{\text{AM}} \\ \sqrt{2\kappa}\,\hat{\xi}_-^{\text{PM}} \end{pmatrix} \tag{3.51}$$

This equation is readily solved in Fourier space as $\boldsymbol{X}[\omega] = \Xi[\omega]\boldsymbol{v}[\omega]$, where $\Xi[\omega] = -(M + i\omega\mathbb{I})^{-1}$ represents the susceptibility matrix, with element $\Xi_{ij}[\omega]$ describing the response of coordinate i to input j.

The optodynamical rates can be obtained as $\Gamma_{\text{opt}} = -\operatorname{Im}\{\Xi_{12}[\omega_s]^{-1}\}/\omega_s$ and $\delta\omega_{\text{opt}} = \operatorname{Re}\{\Xi_{12}[\omega_s]^{-1}\}/(2\omega_s)$. This allows straightforward numerical comparison of the effect of cavity birefringence on the optodynamical effects observed, plotted in Fig. 3.16.
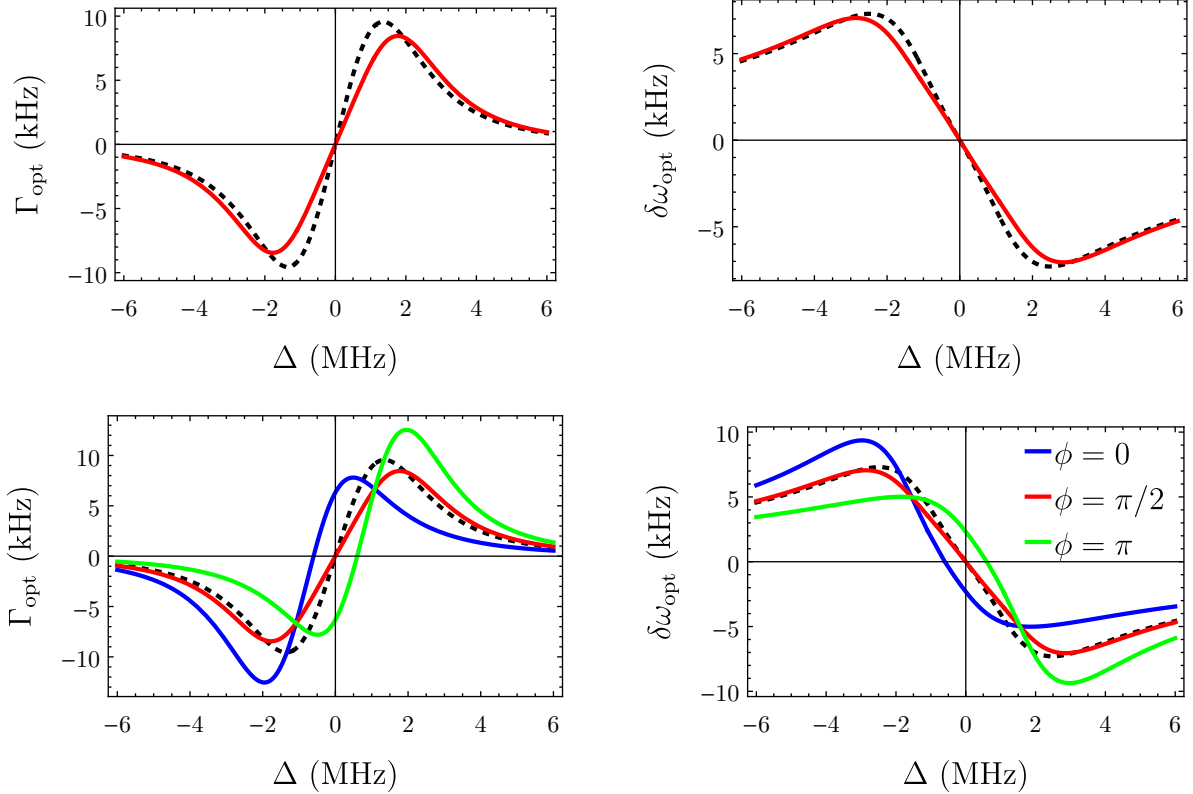
Figure 3.16: Effect of cavity birefringence on optodynamical rates as a function of probe detuning with fixed total intracavity photon number. The top row shows a small perturbation of the optodynamical damping and spring shift for a cavity driven with circularly polarized light ($\theta = 0$), with the measured cavity linear birefringence $\Delta_b = 2\pi \times 0.6$ MHz (red) compared to the non-birefringent theory (black dashed). The bottom row shows the more dramatic effect of birefringence for a cavity driven with linearly polarized light ($\theta = \pi/2$). The horizontal shift of $\pm\Delta_b$ for the zero-crossing of horizontal (green) or vertical (blue) polarization matches the shifted resonance of the fast and slow axis, respectively. The effects of these polarization components add linearly, so the results for a diagonal drive polarization (red) are the average of the corresponding vertical or horizontal polarization rates, identical to the rates for a circular polarization input.

3.6 Open questions and future directions

Conservation of angular momentum

A Gaussian optical mode, as assumed to describe the TEM_{00} mode of our cavity, can only carry intrinsic angular momentum along its propagation axis, with states represented by the circular polarizations of the beam. This raises an embarrassing question about how angular momentum is conserved for the dynamics observed in Fig. 3.5, during which the atomic angular momentum changes by $\Delta F_z = 4N_a \sim 14000$ units of $\hbar$ from beginning to end. The only input and output included in the assumed model are the single polarization cavity mode propagating along $\mathbf{x}$, which cannot carry intrinsic angular momentum along $\mathbf{z}$ as optical polarization. However, conservation of angular momentum for an off-resonant beam transmitted through an atomic vapor polarized along $\mathbf{s}$ results in a birefringent displacement of the circular polarizations of the beam, along the component of $\mathbf{s}$ perpendicular to the propagation axis [21]. This displacement occurs in opposite directions for the two circular polarization components and imparts additional angular momentum along $\mathbf{x} \times \mathbf{s}$ which exactly accounts for the change in atomic angular momentum due to Larmor precession of the spin induced by the vector Stark shift of the light. This displacement creates a small distortion of the cavity mode, breaking its radial symmetry, which must result in a transfer of angular momentum to the cavity mirror through a torque upon reflection. The details of this process have been neglected by assuming a simple Gaussian mode of the cavity, and could possibly be recovered by solving for a self-consistent, spin-dependent cavity mode function. We likely benefit here from the stability of the (not-too-)near-planar cavity geometry, related to the well-resolved transverse modes. A cavity with more nearly degenerate transverse modes, such as confocal or concentric configurations, would likely require a more detailed treatment, which, however, is well beyond the scope of this work.

Feedback-stabilized spin oscillator

The spin QND and optodynamics configurations explored above correspond to two limiting cases of the schematic shown in Fig. 3.1. The intermediate case, with a magnetic field applied at a finite, non-transverse angle from the cavity axis θ_B, is described by the effective Hamiltonian

$$\mathcal{H} = -\hbar\big(\Delta - g_s \hat{F}_z \cos\theta_B\big)\hat{c}^\dagger\hat{c} + \hbar\omega_s \hat{F}_z + \hbar g_s \hat{c}^\dagger\hat{c}\hat{F}_x \sin\theta_B. \tag{3.52}$$

Here, the longitudinal spin component shifts the average cavity frequency, as illustrated in Fig. 3.17, which can be combined into an effective spin-dependent probe detuning $\Delta' = \Delta - g_s \hat{F}_z \cos\theta_B$. At the same time, optodynamical coupling to the transverse spin $\hat{F}_x = \big(\hat{F}_+ + \hat{F}_-\big)/2$ facilitates energy exchange with cavity photons. The relative strength of these two processes can be tuned through the magnetic field angle θ_B.

When the probe is detuned above (below) the effective cavity resonance, with $\Delta' > 0$ ($\Delta' < 0$), the optodynamical interaction will preferentially scatter photons into the red
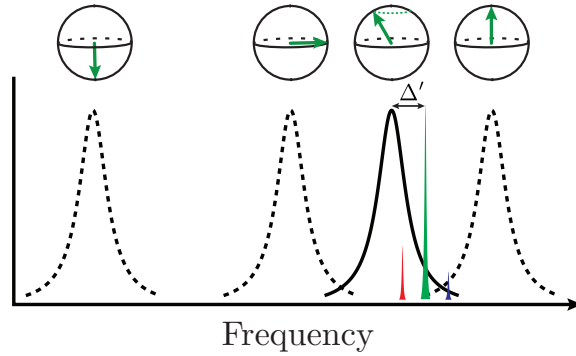
Figure 3.17: Illustration of spin stabilization for non-transverse spin optodynamics.

(blue) Larmor precession sideband, indicated in Fig. 3.17, and drive energy into (out of) the spin ensemble. Like the optodynamical damping and anti-damping observed in Fig. 3.6, this energy exchange rotates the spin toward its high energy (low energy) pole and, therefore, tunes the effective cavity detuning Δ', closing an autonomous feedback loop.

For $g_s \cos \theta_B > 0$, the optodynamical energy exchange drives the spin-shifted cavity resonance toward the probe frequency, realizing a stable negative-feedback configuration. In this condition, the net energy exchange self-terminates with $\Delta' = 0$, stabilizing the spin at a probe-determined longitudinal projection

$$\langle \hat{F}_z \rangle = \frac{\Delta}{g_s \cos \theta_B}, \tag{3.53}$$

in spite of continuous optical measurement and backaction.

The optodynamical measurement also provides simultaneous measurement of the transverse and longitudinal spin dynamics. In the comparison to cavity optomechanics, these interactions are analogous to a tunable linear and quadratic coupling, where measurement of the longitudinal spin represents an effective 'phonon' measurement of the spin oscillator. This tunable coupling might allow observation of backaction-driven quantum jumps under continuous measurement near the QND configuration, following the optomechanical proposal in Ref. [96].

Optodynamical spin locking

For the results published in Ref. [24], which considered dynamics in only the first hundreds of μs when the transverse spin was small, the T2 lifetime observed in Fig. 3.13d was sufficient to justify neglecting loss due to dephasing in the analysis. However, the full dynamics observed in Fig. 3.5 do not clearly reflect loss of polarization after many milliseconds of transverse spin precession, as the spin nutates across the equator. This was further verified by repeating the optodynamical 'spin flip' in each shot, with the second rf pulse indicated in Fig. 3.4, revealing nearly identical Larmor precession amplitude and dynamics the second time around in Fig. 3.18.
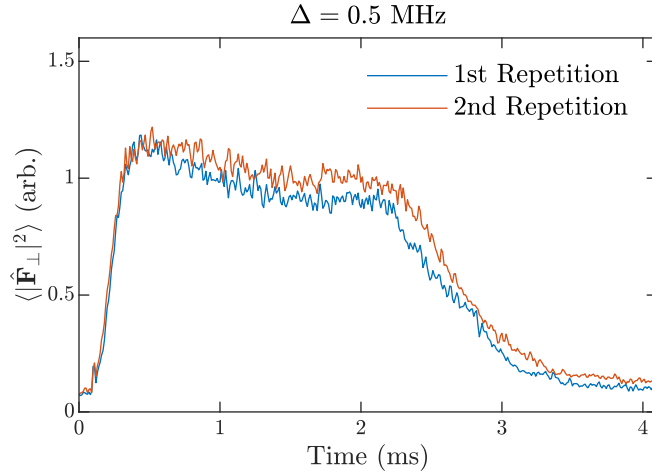
Figure 3.18: Repeated optodynamical driving of a spin from pole to pole shows negligible loss of spin polarization during dynamics over multiple milliseconds. Evolution of the response amplitude is distorted at later times, in part, due to systematic pulling of the probe frequency stabilization. The detuning Δ is measured as a fraction of the cavity linewidth, as described in Appendix D, and is underestimated when large-amplitude modulation of the cavity resonance by the spin precessing near the equator broadens the time-averaged cavity linewidth. Feedback to the probe frequency, derived from this estimate, pulls the probe away from cavity resonance at a timescale of around 1 ms.

The effective absence of spin decay on this timescale is suggestive that the optodynamical interaction may suppress ensemble dephasing through a spin-locking effect. Such spin locking has been demonstrated to suppress complications from the quadratic Zeeman effect in vapor cell magnetometers [97], with a transverse magnetic field modulated in phase with the spin precession. In the rotating frame, this modulation generates an effective magnetic field parallel to the transverse spin, which drives precession of the coherences between neighboring Zeeman sublevels around this axis, suppressing dephasing of the coherences if this drive is stronger than the quadratic shift. Similarly, the same in-phase, optodynamical modulation which produces the observed Larmor frequency shifts may also provide an autonomous spin locking effect when the cavity is driven off resonance, suppressing dephasing due to variations in Larmor frequency across the ensemble.

Planar squeezed states

Considering the reduced equations of motion derived in Eqs. 3.17, it is interesting to note that the shot noise fluctuations decouple from the azimuthal coordinate ϕ, when the spin is on the equator ($\cot\theta = 0$). This condition allows measurement of the Larmor precession phase with arbitrary precision, which is consistent with the spin commutator $[\hat{F}_x, \hat{F}_y] = i\hat{F}_z$ having zero mean when the spin precesses at the equator [98]. In the absence of optodynamical

coupling, measurement backaction primarily increases the variance of the polar angle, which eventually leads to backaction leaking into the spin phase at second order. It could be interesting to consider how adding optodynamical feedback from the cavity might modify the novel squeezed states produced by this QND measurement.

Chapter 4

Coupled mechanical oscillators

This chapter discusses our experimental demonstration of optically mediated coupling between the motion of two distinct atomic ensembles, published in Ref. [35]. I will not review all the experimental results here, but add some experimental details related to the published work, further develop a theoretical model for optodynamically coupled oscillators, and introduce a pulsed coupling and measurement sequence which will be modified for experiments discussed in the next chapter.

After developing the theory of multi-mode optodynamics in Chap. 2 and exploring single-mode optodynamical effects in Chap. 3, now I will start putting these pieces together to consider coupling between two distinct atomic oscillators through the cavity field. Coupled simple harmonic oscillators is a textbook problem in classical physics, and the average results observed here for coherent states of quantum oscillators are well described by the classical dynamics.

However, using the cavity mode to mediate long-range interactions between oscillators introduces an open quantum channel, both leaking information about their motion out to the environment and introducing quantum backaction, driven by photon vacuum fluctuations. This backaction adds diffusive noise to the coherent exchange interaction, placing quantum limits on information exchange mediated by a field of real photons, which can be measured by the environment. In addition, this backaction builds correlations between the two oscillators, proportional to their spectral overlap, because they experience quantum fluctuations of the same cavity field.

4.1 Non-degenerate mechanical oscillators

The atomic optomechanical interaction defined by Eq. 2.5 can be generalized for the axial motion of multiple atomic ensembles, described by the total Hamiltonian

$$\mathcal{H} = -\hbar\Delta\hat{c}^\dagger\hat{c} + \sum_i \hbar\omega_i\hat{a}_i^\dagger\hat{a}_i + \hbar g_\mathrm{c}\hat{c}^\dagger\hat{c}\sum_i \left[k_p\hat{Z}_i\sin(2\phi_p) + k_p^2\cos(2\phi_{p,i})\hat{Z}_i^2\right] \qquad (4.1)$$
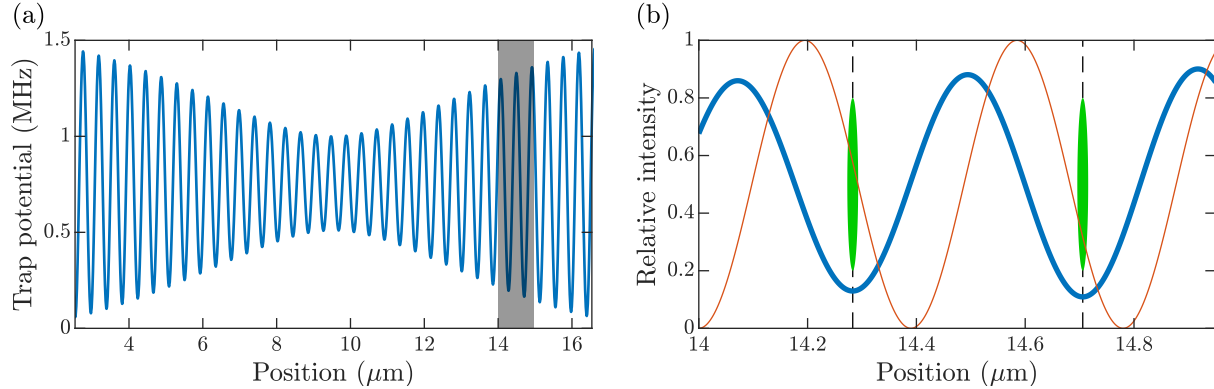
Figure 4.1: (a) Example optical super-lattice potential (blue) formed by the combination of driving a cavity mode at 842 nm and 861 nm. (b) Atomic ensembles (green) loaded in sites within the shaded region of (a) experience different axial trap frequencies, but where both have approximately linear coupling to the cavity probe at wavelength 780 nm (red).

where Δ is the probe detuning from the shifted cavity frequency $\omega_c' = \omega_c + g_c \sum_i N_{a,i} \sin^2(\phi_{p,i})$, $N_{a,i}$ is the atom number in each ensemble, $\phi_{p,i}$ is the probe phase at each ensembles equilibrium position, and $\hat{Z}_i = Z_{\mathrm{ho},i}(\hat{a}_i^\dagger + \hat{a}_i)$ is the center-of-mass displacement of each ensemble from that equilibrium, in terms of harmonic oscillator lengths $Z_{\mathrm{ho},i} = \sqrt{\hbar/2N_{a,i}m_a\omega_i}$.

This Hamiltonian can be mapped onto the canonical optodynamical Hamiltonian in Eq. 2.18 by defining the optomechanical coupling strengths

$$g_i = g_c N_{a,i} k_p Z_{\mathrm{ho},i} \sin(2\phi_{p,i}) \tag{4.2}$$

and absorbing the harmonic probe potential, described by the final term in Eq. 4.1, into a 'static' shift of the corresponding oscillator frequencies, given by Eq. 4.3 and calibrated in Fig. 4.3.

Super-lattice potential

To observe the effects of optical coupling between two ensembles of atoms, their motion needs to be distinguishable in the cavity output, which is sensitive to the total center-of-mass displacement of both ensembles. This can be accomplished by spectrally resolving the oscillators at different frequencies ω_i. Confining the atoms in a super-lattice potential formed by the sum of two ODT lattices, resonant with different modes of the cavity at $\lambda_A = 842$ nm and $\lambda_B = 861$ nm (Fig. 4.1a), neighboring sites of the super-lattice potential have slightly different curvature and, therefore, trap frequencies.

The average trap frequency and frequency difference between neighboring sites is determined by the intensity of each trap lattice and their relative phase. The periodicity of the super-lattice beatnote is $|\lambda_A^{-1} - \lambda_B^{-1}|^{-1}/2 \approx 19$ μm, with the relative phase at a given position determined by the chosen TEM_{00} cavity modes.

Furthermore, the ensembles in both lattice sites must be positioned at a large intensity gradient of the probe field, as illustrated in Fig. 4.1b, in order to experience significant linear optomechanical coupling. The experimentally accessible region of the cavity mode between the mirror and atom chip is a few 10's of μm, therefore satisfying these constraints requires careful choice of all three cavity modes.

The frequency difference between oscillators used in our experimental demonstration was $\delta = \omega_1 - \omega_2 = 2\pi \times 7$ kHz [35]. This choice of detuning was a careful balance between resolving the oscillators relative to their intrinsic linewidth of ~ 1 kHz, while not being too large relative to the achievable optical coupling strength $K = 2\pi \times 2$–4 kHz. In principle, this limitation could be circumvented by dynamically tuning the oscillator frequencies, as performed in Chap. 5 when coupling atomic motion and spin. Although the frequency difference can be dynamically tuned by varying the depth of the second trap beam forming the super-lattice potential, this also has the consequence of shifting the equilibrium position of the atoms, significantly modifying their optomechanical coupling to the probe.

Loading two cold ensembles

The optical lattice was loaded by positioning the final chip-produced magnetic trap within the cavity mode, then adiabatically ramping up the intensity of one ODT before ramping off the magnetic trap. The number of lattice sites filled and the distribution of atoms between sites, therefore, depended on the final width and position of the magnetically trapped cloud.

The width of the cloud was controlled through the atom number and temperature, by varying the final frequency of the rf evaporation ramp. The cloud width was reduced by evaporation until it was small enough to populate only two trap sites, verified by observing the number of optomechanical frequency peaks observed in the heterodyne spectrum. The balance of atoms between sites could then be tuned through small adjustments to the bias field controlling the magnetic trap position. This balance showed the least susceptibility to drift of the trap position when the cloud width was as large as possible, while primarily populating only two sites.

This optimal trap size for reliably loading two sites required applying less rf evaporation than the usual single-site loading conditions, resulting in an increased number and temperature of atoms loaded in the optical trap. To achieve similar temperatures after loading two ensembles, the optically trapped atoms were further evaporatively cooled by lowering the ODT depth to about $U_t/k_B = 7\,\mu$K for 70 ms, before ramping both trap intensities up to their calibrated set points.

Trap frequency drift and stabilization

The frequency of the axial atomic motion is controlled through the intensity of both ODTs, and must be stable to resolve small frequency shifts due to optodynamical coupling and to repeatably observe coherent excitation exchange between the two modes. We actively stabilize the intensity of both optical traps transmitted through the cavity, separated by

dichroic mirrors and independently detected on avalanche photodiodes (APDs) as described in Ref. [37]. The measured photocurrent is stabilized to a computer-controlled set point by feedback to the intensity of the trap laser driving the cavity, controlled by an AOM.

Any change in detection efficiency of the intra-cavity trap light, therefore, results in a change of trap depth for a given stabilization set point. At a constant set point, the trap frequency was observed to drift by many kHz on thermal timescales, of order minutes to hours, as illustrated in Fig. 4.2a. To stabilize the oscillator frequency to 110 ± 1 kHz requires a fractional intensity stability better than 0.3%. Although the APDs are inherently temperature dependent, our detectors have internal temperature compensation circuitry. Additional temperature dependence may also arise along the path from changes in reflection off optical surfaces due to etalon fringes or polarization rotation.
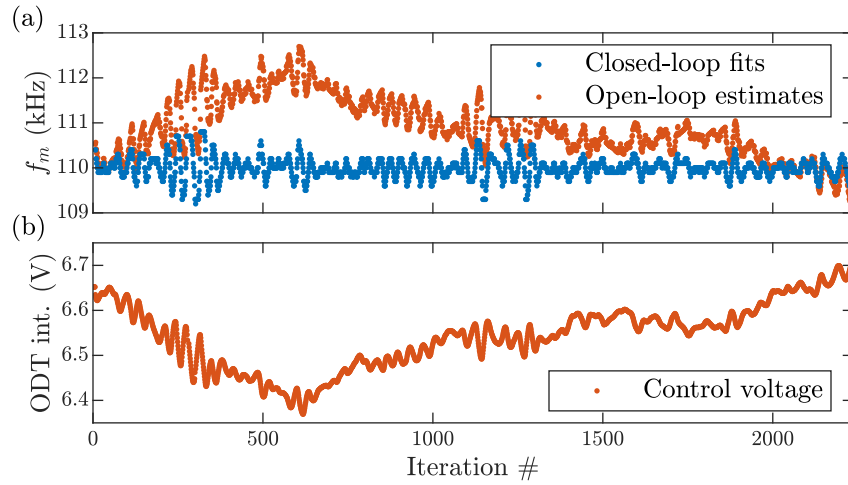
Figure 4.2: Feedback stabilization of mechanical frequency drifts during a typical overnight measurement run. (a) Feedback-stabilized trap frequencies (blue points), measured from fits to a moving-average PSD. Deviations of the estimated frequency from the 110 kHz set point represent the closed-loop feedback error signal, showing residual RMS fluctuations below 1 kHz. The moving-average PSD is used to improve the fit signal to noise, but also introduces a low-pass filter to the feedback response, responsible for the residual oscillations observed in the error signal, with a period of a few iterations. (b) Control voltage for the ODT intensity stabilization, adjusted by the closed-loop feedback output derived from the measured error signal in (a). The open-loop trap frequency (orange points in (a)) can be estimated from variation in the control voltage, suggesting frequency drifts over 2 kHz without feedback control.

The trap frequency was further stabilized against these slow drifts by using information recorded in the heterodyne signal during each experimental iteration to estimate the oscillator frequencies and then to control the set point for the next iteration using digital feedback. Immediately after the particular experimental sequence and measurement in each iteration, the cavity was probed on resonance for about 10 ms with the output field captured in the

recorded heterodyne signal. The phase quadrature PSD was automatically calculated in software after each iteration, and the frequency of one oscillator was estimated by fitting a Lorentzian to the peak observed within a configured frequency band. The estimated trap frequencies were used as an error signal to perform feedback to the computer-generated voltage controlling the intensity of one trap laser, using a digital feedback algorithm detailed in Appendix F. The estimated frequencies and corresponding feedback control voltage from a sequence of over 2000 experimental iterations are shown in Fig. 4.2b.

Calibration of static, probe-induced frequency shift

Both atomic ensembles cannot be precisely positioned at the exact probe phase $\phi_p = \pi/4$ for purely linear optomechanical coupling in Eq. 4.1, where curvature of the probe intensity vanishes. Positioned on either side of the linear phase, each oscillator experiences a small residual curvature of the average probe potential, with opposite sign. This curvature induces a 'static' spring shift of each oscillator frequency, which arises from the average intracavity intensity, not optodynamical modulations. This shift must be calibrated and distinguished from the frequency splitting expected for the optodynamically coupled, hybrid normal modes. Assuming a small curvature which induces a negligible change in the atomic position, the first-order frequency shift described by Eq. 4.1 is

$$\delta\omega_{\text{static},i} \approx \frac{\hbar g_c \bar{n} k_p^2}{m_a} \cos 2\phi_{p,i}. \tag{4.3}$$

This static spring shift was calibrated by a two-part experimental sequence, with the cavity probed on resonance throughout. During the first step of the sequence, the probe intensity was tuned to one of a list of calibrated photon numbers $\bar{n}$, and the shifted oscillator frequencies were observed in the heterodyne phase spectrum at each intracavity power, displayed in Fig. 4.3a. Next, the photon number was adjusted to a fixed intensity $\bar{n} = 2$ for the second step, during which the absolute oscillator frequency was measured and stabilized by feedback, as described in Fig. 4.2 and Appendix F. This measurement sequence is iteratively looped over a list of different probe intensities during the first step, while the absolute oscillator frequencies are stabilized on average across the entire dataset during the second step, allowing precise calibration of the average frequency shifts as a function of the intracavity photon number, as shown in Fig. 4.3b.
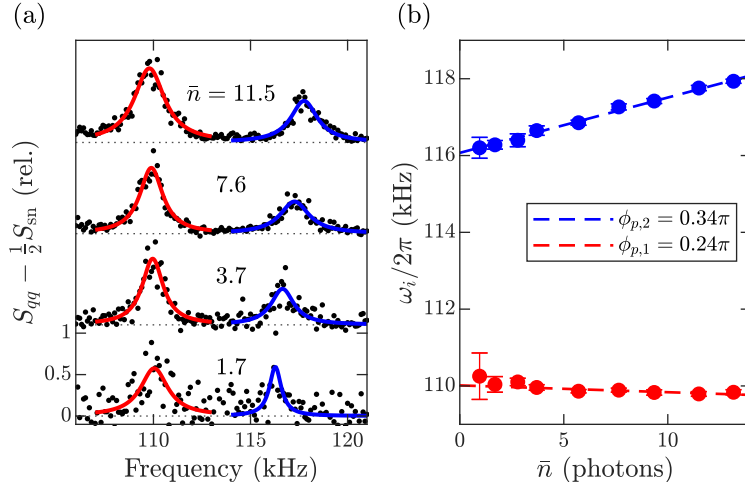
Figure 4.3: Calibration of static probe induced frequency shifts (a) Phase quadrature spectra from two oscillators probed on cavity resonance with increasing intracavity photon number, corresponding to the x-axis of (b). Residual curvature of the probe potential induces frequency shifts of each oscillator. The spectra are normalized by the heterodyne shot noise PSD, with each trace offset above the previous for clarity. (b) The fitted frequencies follow an approximately linear dependence on probe intensity, with the fitted slopes implying trap positions on either side of the linear coupling phase $\phi_p = \pi/4$, with a phase difference consistent with a 430 nm lattice site separation.

4.2 Theory of optodynamically coupled oscillators

The multi-oscillator Hamiltonian in Eq. 4.1 can be mapped onto the canonical optodynamical Hamiltonian from Eq. 2.18. The optically coupled evolution of oscillators can then be described by the reduced equations of motion obtained in Eqs. 2.45, which can be expressed as

$$\dot{\hat{a}}_i = -i\left(\epsilon_i\omega_i' + i\Gamma_i'\right)\hat{a}_i - \frac{i}{2}K_{ii}^*\hat{a}_i^\dagger - \frac{i}{2}\sum_{j\neq i}\left[K_{ij}\hat{a}_j + K_{ij}^*\hat{a}_j^\dagger\right] - i\sqrt{B_i}\hat{\xi}_\Delta^{\mathrm{AM}} + \sqrt{\Gamma_i}\hat{\eta}_i, \qquad (4.4)$$

defining complex coupling constant $K_{ij} = k_{ij} - i\gamma_{ij}$ and optodynamically shifted frequencies $\omega_i' = \omega_i + \epsilon_i k_{ii}/2$ and damping rates $\Gamma_i' = \Gamma_i + \gamma_{ii}$.

These equations can be simplified further by making the rotating-wave approximation. This approximation assumes that only terms which vary slowly with respect to the oscillators intrinsic rotation, at frequency $\epsilon_i\omega_i$, contribute significantly to the state evolution. This is approximately true for $|\omega_i| \gg |K_{ij}|$, assuming the amplitude of the counter-rotating terms are sufficiently small, a constraint which will be revisited in Sec. 5.5 of the next chapter. Transforming the equations of motion into a frame rotating at the average frequency $\bar{\omega} = (\omega_1' + \omega_2')/2$, in a direction defined by the effective mass of each oscillator $\hat{a}_i(t) \to \hat{a}_i(t)e^{-i\epsilon_i\bar{\omega}t}$,

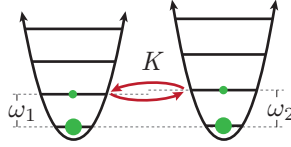Figure 4.4: Illustration of the exchange interaction between two positive-mass harmonic oscillators, facilitating coherent hopping of phonon excitations from one oscillator to the other.

yields

$$\dot{\hat{a}}_i = \left(-i\epsilon_i(\omega_i' - \bar{\omega}) - \frac{\Gamma_i'}{2}\right)\hat{a}_i - \frac{i}{2}K_{ii}^*\hat{a}_i^\dagger e^{2i\epsilon_i\bar{\omega}t} - \frac{i}{2}\sum_{j\neq i}\left[K_{ij}\hat{a}_j e^{i(\epsilon_i-\epsilon_j)\bar{\omega}t} + K_{ij}^*\hat{a}_j^\dagger e^{i(\epsilon_i+\epsilon_j)\bar{\omega}t}\right]$$
$$- i\sqrt{B_i}\hat{\xi}_\Delta^{\mathrm{AM}}e^{i\epsilon_i\bar{\omega}t} + \sqrt{\Gamma_i}\hat{\eta}_i. \quad (4.5)$$

Identifying the counter-rotating terms of the coupled equations, therefore, depends on the relative signs of the effective masses ϵ_i, with only two distinct options for two oscillators–either they have the same signs or different.

Two positive-mass oscillators

In this chapter, I consider the coupled motion of two positive-mass oscillators, realized with the center-of-mass motion of two atomic ensembles in the super-lattice potential illustrated in Fig. 4.1. I return to the positive-/negative-mass configuration in Chap. 5. For nearly degenerate oscillators, with $\omega_1 \approx \omega_2$, the equations of motion after the RWA are

$$\dot{\hat{a}}_1 = \frac{1}{2}(-i\delta' - \Gamma)\hat{a}_1 - \frac{i}{2}K\hat{a}_2 - i\sqrt{B_1}\hat{\xi}_\Delta^{\mathrm{AM}} + \sqrt{\Gamma_1}\hat{\eta}_1 \qquad (4.6)$$

$$\dot{\hat{a}}_2 = \frac{1}{2}(i\delta' - \Gamma)\hat{a}_2 - \frac{i}{2}K\hat{a}_1 - i\sqrt{B_2}\hat{\xi}_\Delta^{\mathrm{AM}} + \sqrt{\Gamma_2}\hat{\eta}_2, \qquad (4.7)$$

defining oscillator detuning $\delta' = \omega_1' - \omega_2' \approx \omega_1 - \omega_2$. The coherent part of these dynamics can be described by the effective Hamiltonian

$$\mathcal{H} = \hbar\omega_1'\hat{a}_1^\dagger\hat{a}_1 + \hbar\omega_2'\hat{a}_2^\dagger\hat{a}_2 - \hbar\frac{K}{2}\left(\hat{a}_1^\dagger\hat{a}_2 + \hat{a}_2^\dagger\hat{a}_1\right) \qquad (4.8)$$

which indicates an exchange interaction between the two modes, illustrated in Fig. 4.4, with exchange rate $K = K_{12} \approx K_{21}$. Furthermore, in the unresolved-sideband regime, γ_{12} is of order ω_2/κ smaller than k_{12} and can be neglected such that K is approximately real.

Because the two mechanical oscillators have similar optodynamical coupling strengths g_i and intrinsic damping rates Γ_i, for simplicity I will approximate them as equal, with
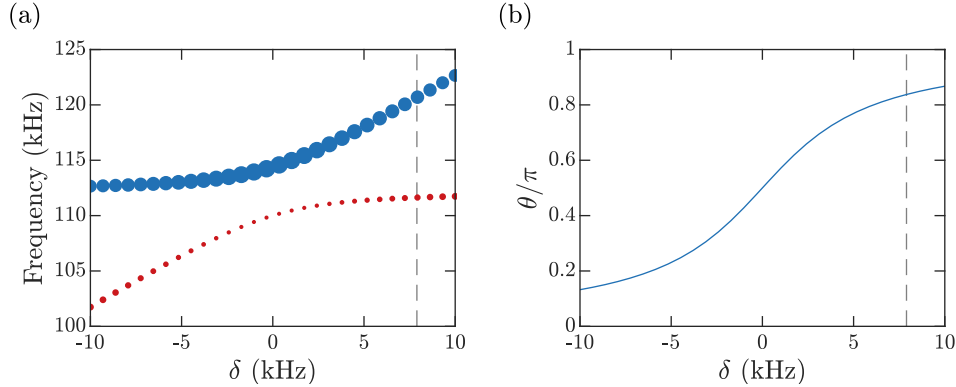
Figure 4.5: Normal mode description of two optodynamically coupled oscillators, with intracavity photon number $\bar{n} = 8$ and probe detuning $\Delta = 2\pi \times 1.2$ MHz, (a) Normal mode frequencies described by the real part of Eq. 4.11, as a function of oscillator detuning δ. The width of each point reflects its overlap with the 'bright' mode of the cavity measurement. (b) Normal mode mixing angle θ, which parametrizes the normal mode transformation matrix in Eq. 4.13. Our experimental demonstration was performed with oscillator frequencies near $\{\omega_1, \omega_2\} = 2\pi \times \{110, 118\}$ kHz (dashed lines), including the static spring shift.

$\Gamma' \approx \Gamma'_1 \approx \Gamma'_2$. The equations of motion in the rotating frame can be summarized by the matrix equation

$$\frac{\partial}{\partial t}\hat{\boldsymbol{a}} = -i\mathrm{M}\hat{\boldsymbol{a}} + \hat{\boldsymbol{v}}, \tag{4.9}$$

in terms of state vector $\hat{\boldsymbol{a}} = (\hat{a}_1, \hat{a}_2)^{\mathsf{T}}$, with dynamical matrix and input noise vector

$$\mathrm{M} = \frac{1}{2}\begin{pmatrix} \delta' - i\Gamma' & K \\ K & -\delta' - i\Gamma' \end{pmatrix} \quad \text{and} \quad \hat{\boldsymbol{v}} = \begin{pmatrix} -i\sqrt{B_1}\hat{\xi}_\Delta^{\mathrm{AM}}e^{i\bar{\omega}t} + \sqrt{\Gamma}\hat{\eta}_1 \\ -i\sqrt{B_2}\hat{\xi}_\Delta^{\mathrm{AM}}e^{i\bar{\omega}t} + \sqrt{\Gamma}\hat{\eta}_2 \end{pmatrix}, \tag{4.10}$$

respectively. The quadrature operator $\hat{\xi}_\Delta^{\mathrm{AM}}$ represents the cavity amplitude fluctuations and is Hermitian, with both co-rotating and counter-rotating components which therefore cannot be simply neglected in this approximation.

The dynamical matrix M has eigenvalues

$$\lambda_\pm = \frac{\pm W - i\Gamma'}{2} \quad \text{with} \quad W = \sqrt{\delta'^2 + K^2} \tag{4.11}$$

which reflect the usual avoided crossing between the coupled normal modes, as displayed in Fig. 4.5a.

The dynamical matrix M can be diagonalized in terms of these eigenvalues

$$\mathrm{M} = \mathrm{E}\begin{pmatrix} \lambda_+ & 0 \\ 0 & \lambda_- \end{pmatrix}\mathrm{E}^{\mathsf{T}} \tag{4.12}$$

by transformation under the unitary eigenvector matrix

$$E = \begin{pmatrix} \cos\theta/2 & \sin\theta/2 \\ -\sin\theta/2 & \cos\theta/2 \end{pmatrix} \tag{4.13}$$

with hybrid mixing angle $\tan\theta/2 = K/(\delta' + W)$, displayed as a function of detuning δ in Fig. 4.5b.

Time evolution of the oscillator coherences can be solved from Eq. 4.9, with no average contribution from the zero-mean input noise. Considering a scenario with an initial coherent displacement of oscillator 2 only and $\langle\hat{a}_1(0)\rangle = 0$, the coupled oscillator coherences evolve as

$$\langle\hat{\boldsymbol{a}}(t)\rangle = \langle\hat{a}_2(0)\rangle e^{-i\Gamma't/2} \begin{pmatrix} i\sin\theta\sin(Wt/2) \\ \cos(Wt/2) + i\cos\theta\sin(Wt/2) \end{pmatrix}, \tag{4.14}$$

which reveals the oscillation of amplitude between the two modes. This interaction realizes a complete exchange after $\tau = \pi/W$ only when $\delta' = 0$, such that the coupled normal modes are completely hybridized with $\theta = \pi/2$.

4.3 Spectral signatures of coupling

The effects of the optically mediated coupling between the two oscillators are visible in the PSD of the shot noise driven mechanical response. This is measured by a two-step experimental sequence, similar to that used for Fig. 4.3. The optodynamical coupling strength is tuned by driving the cavity at a chosen detuning Δ, with a fixed intracavity photon number $\bar{n}$, maintained by adjusting the input power at each detuning. The spectrum of the coupled oscillator's shot noise driven response is observed in the heterodyne phase quadrature during this step, displayed in Fig. 4.6a,c for each value of Δ. By measuring at a fixed photon number, the frequency shifts from the static probe curvature are constant across each dataset, allowing shifts due to optodynamical effects to be clearly resolved. Immediately after the coupling step, the probe is tuned to cavity resonance to observe the natural frequency of each oscillator, which is stabilized by feedback to the trap intensity.

The optically mediated interaction between the two oscillators is revealed by a frequency repulsion, arising from the avoided crossing between their coupled normal modes. There are also individual optodynamical frequency shifts and (anti-)damping acting on each oscillator, but assuming equal optomechanical coupling strengths g_i, the individual optodynamical frequency shifts are equal, and the effect of the optically mediated interaction should be clearly revealed by the frequency difference between the normal modes. Although the strength of the optodynamical coupling $|K|$ is symmetric for a probe detuned above or below cavity resonance, the optodynamical (anti-)damping leads to dramatic differences between the spectra for these two cases, observed in Fig. 4.6a.

For a red-detuned probe, each oscillator experiences optodynamical damping, which broadens the lines observed in the spectrum and obscures measurement of the frequency
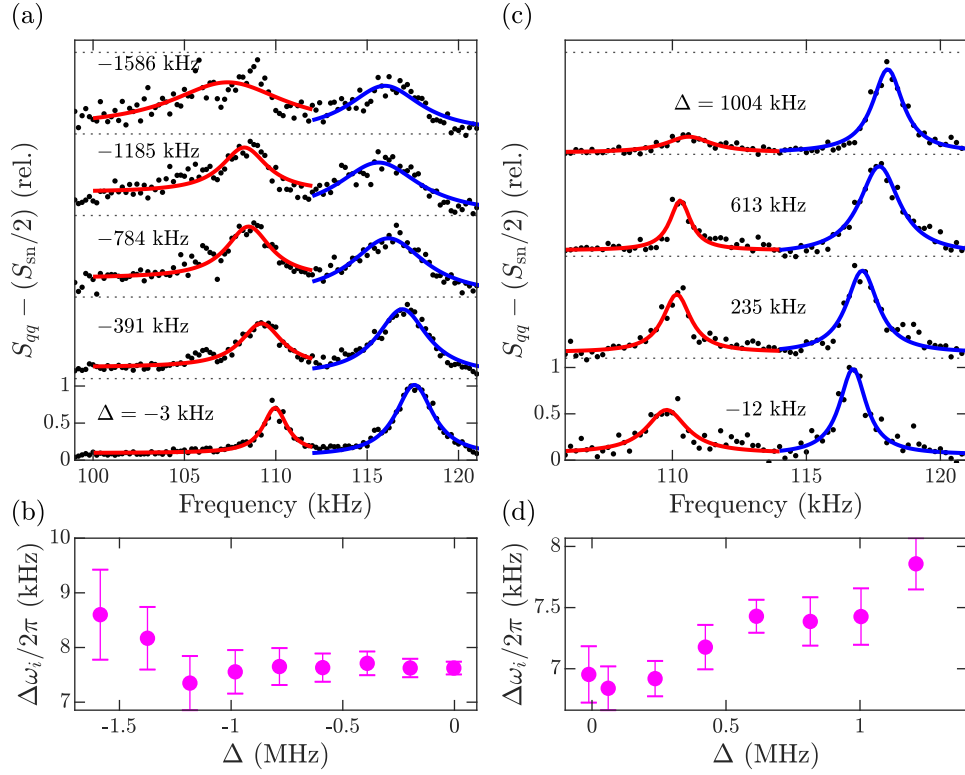
Figure 4.6: Hybridization of coupled normal modes revealed in shot noise driven spectra (a) Optical phase PSD for measurement of two oscillators under increasing optodynamical coupling strength, for a probe detuned below cavity resonance $\Delta < 0$ at a fixed intracavity intensity $\bar{n} = 10$. The frequency splitting between oscillators is obscured by optomechanical damping of each oscillator, which broadens the spectral linewidth. At higher probe intensities, the spectrum may also be distorted by non-linearity of the ODT. (b) Frequency splitting between Lorentzian fits to the peaks observed in (a). (c) Hybridization of the coupled normal modes is more clearly displayed for interactions driven by a probe detuned above cavity resonance $\Delta > 0$, where each oscillator is anti-damped by the optodynamical interaction. For increasing coupling strength, the coupled normal modes evolve toward a bright and dark made of the cavity measurement. (d) The frequency splitting between peaks from fits in (c) more clearly indicates the splitting of normal modes.

difference, as seen in Fig. 4.6a-b. However, driving the cavity to the blue, with an intensity below the self-oscillation threshold [52], the oscillators are anti-damped, maintaining sharp peaks in the spectra and a better resolved measurement of their frequency difference, seen in Fig. 4.6c-d. Here the nature of coupled normal modes are also clearly revealed. As the interaction strength $|K|$ is increased, the normal modes evolve toward a center-of-mass mode and a breathing mode, which correspond to a bright and dark mode of the cavity measurement, respectively, as reflected by the relative height of each mode seen in the optical spectrum.

4.4   Phase-dependent interaction and measurement

The optodynamical coupling facilitates a phase-preserving interaction between the two oscillators. To demonstrate the coherent nature of the interaction, we performed a pulsed excitation, coupling, and measurement sequence to probe the coherent exchange dynamics described by Eq. 4.14.

Mechanical excitation pulse

The oscillator's motion was coherently driven by modulating the intensity of one of the ODT beams. Within the hybrid lattice, this modulation primarily produces a displacement of the trap centers, applying a force to both oscillators. Selective excitation of a single oscillator can be achieved by shaping a resonant trap modulation pulse, such that the pulse spectrum addresses one oscillator, with negligible power at the other oscillator's frequency.

The optodynamically measured response of both oscillators to a broadband excitation pulse, driven by 3 cycle square pulse at 110 kHz, is shown in Fig. 4.7a. With both oscillators coherently excited, there motion interferes in the average measured center-of-mass displacement, producing a beatnote as their motion evolves from in-phase to out-of-phase at their difference frequency.

A single oscillator can be selectively driven using a longer, carefully shaped resonant pulse, as demonstrated in Fig. 4.7b by the single frequency response in the exponential ringdown. This drive pulse must be sufficiently long for its Fourier-limited spectral width to distinguish between the oscillator frequencies $T \gg 1/\delta$, and the pulse amplitude must be windowed to reduce broadband transients from the pulse edges.

Fig. 4.8a shows the PSD for a few common window functions. The Blackman window function [99]

$$W(t) = 0.42 - 0.5\cos(2\pi t/T) + 0.08\cos(4\pi t/T) \tag{4.15}$$

provides concentration of the pulse spectrum in the narrowest bandwidth, minimizing leakage of the coherent drive into the spectrum of the second oscillator's susceptibility. Conveniently, it also begins and ends precisely at 0, rather than asymptotically approaching it as the Gaussian does.
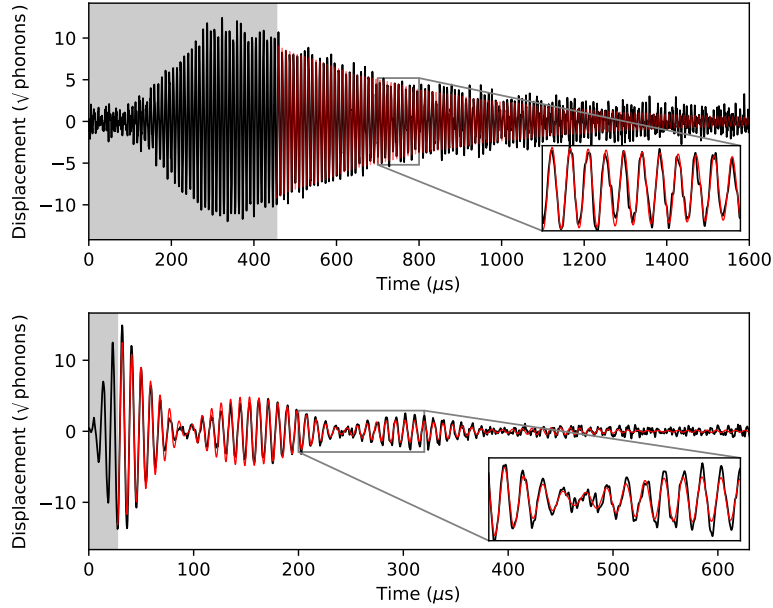
Figure 4.7: Two oscillator mechanical response to (a) a short, 3 cycle square pulse, which equally excites both oscillators and produces a beatnote in the observed center-of-mass displacement. (b) a single-oscillator coherent drive, shaped by the 50-cycle truncated Blackman window, exciting only one frequency component in the observed response.

The envelope of the Blackman pulse, defined above, is shown in Fig. 4.8b, along with its convolution with the oscillator's coherent impulse response, giving the envelope of the expected temporal response. Because of the pulse window's long tail, the peak oscillator response occurs well before the end of the drive pulse, reducing the remaining signal which serves as the input to the coupling sequence. To mitigate this decay, we used a truncated Blackman pulse, stopping the drive after 50 cycles of a 60 cycle pulse window. The spectrum of the truncated pulse maintains a narrow central lobe, at the expense of an increased broadband floor. The drive suppression at the second oscillator's frequency is still -40 dB, reflecting the approximate ratio of coherent phonons added to each oscillator.

Coupling pulse

Once one oscillator was excited by the coherent drive, the coupling interaction was turned on for a variable amount of time, after which the oscillators were uncoupled to observe the free ringdown of their final state. The strength of the optical spring interaction, described by Eq. 2.47, was controlled by varying the probe detuning Δ and the intracavity intensity $\bar{n}$, as shown in Fig. 4.9a. These parameters were tuned by electronically adding pulses, produced by arbitrary waveform generators, to the set point of the probe intensity stabilization and the input of the voltage-controlled oscillator (VCO) controlling the probe frequency.
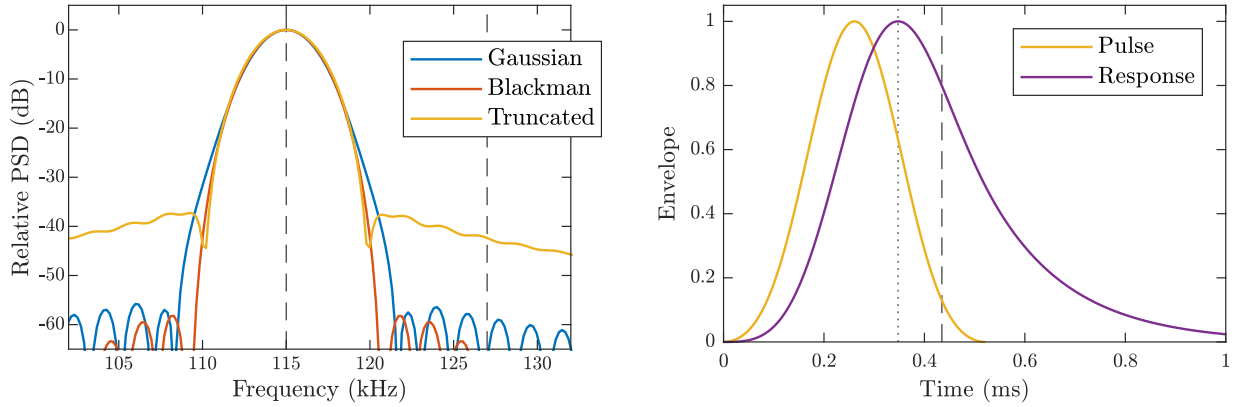
Figure 4.8: (a) PSD of windowed, 60-cycle drive pulses at $f = 115$ kHz. The Gaussian window full-width half-maximum (FWHM) is 1/3 the window length. The Blackman window concentrates the pulse in the narrowest bandwidth, even when truncated after 50 cycles. (b) The Blackman pulse envelope (yellow), and the expected temporal response of the oscillator's amplitude (purple). The peak oscillator response is marked by the dotted line. In practice, the drive pulse was truncated at the dashed line, providing a balance between the response decay and spectral broadening of the pulse.

Because the feedback loop stabilizing the probe detuning (described in Appendix D) has a slow bandwidth of around 1 kHz, the probe frequency was modulated out-of-loop by adding to the probe VCO control voltage directly. This out-of-loop modulation was hidden from the feedback circuit by using a S&H circuit to fix its error signal input for at least twice the modulation pulse length, allowing the error signal to recover after the pulse (it is the demodulation band-pass filters that generate the feedback error signal have a ~ 1 kHz bandwidth, defining the slow response). For long coupling pulses, the VCO modulation pulse was adjusted to correct for a linear drift of the feedback loop, due to an offset introduced by the S&H.

The probe intensity stabilization had sufficient bandwidth, such that the intensity modulation could be applied directly to its set point. Because changes in intracavity intensity also change static radiation pressure forces experienced by the oscillators (described in Sec. 2.4), this coupling interaction must be ramped on adiabatically, with respect to the oscillator frequencies. A coherent response caused by displacement of the oscillators was observed following ramp durations of 10 μs or less. To minimize the transient response from pulse edges, the intensity and detuning were ramped with a half-cycle sinusoidal shape over a 20 μs ramp duration, in which condition no transient excitation could be observed.
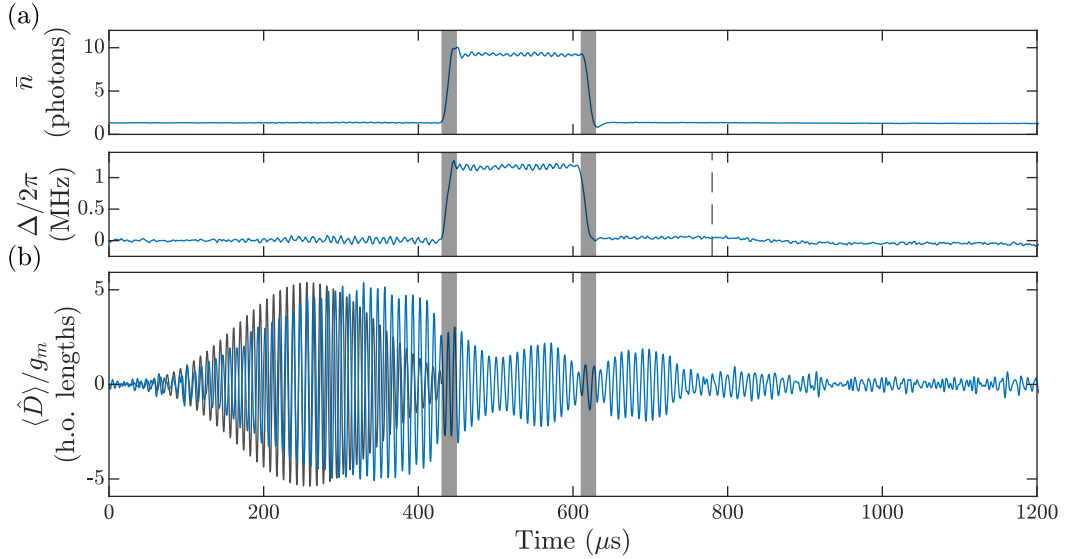
Figure 4.9: Pulse sequence and recorded signal for coherent excitation exchange. (a) Estimated intracavity photon number $\bar{n}$ and probe detuning Δ for a 160 μs coupling pulse. They were ramped over 20 μs with a sinusoidal ramp (grey shading), to reduce transients from the ramp edges. The probe intensity is controlled in-loop, by varying the set point of its intensity stabilization, but the detuning is tuned out-of-loop by direct modulation of the VCO driving an AOM. The detuning pulse was hidden from the low-bandwidth frequency feedback by a sample & hold (S&H) of the error signal, which is held for 350 μs (dashed line), until the low-bandwidth error signal has recovered from the transient pulse. (b) Center-of-mass displacement of both oscillators, recovered from the demodulated heterodyne signal and averaged over 10^4 repetitions. A resonant drive pulse (black, arb. scale) excites the oscillator at $\omega_2 = 2\pi \times 116$ kHz before coupling. The coupling pulse projects the single-oscillator excitation onto the normal mode basis, which interfere in the cavity measurement, producing a beatnote at the normal mode frequency difference. The final state of each oscillator after coupling is revealed in its transient free decay. Transients during the probe ramps cause some distortion of the observed signal (shaded regions).

Optomechanical response

Coherent evolution of the oscillators' final states is revealed in the heterodyne signal $P_\phi(t)$ described by Eq. 2.71, demodulated at the heterodyne quadrature phase $\phi_q = \tan^{-1} \Delta/\kappa$ which is calculated from the time-dependent detuning estimated at each point in the sequence. The total cavity frequency displacement can be recovered from this optical quadrature according to

$$\langle \hat{D}(t) \rangle = \frac{\langle P_\phi(t) \rangle}{A(t)\sqrt{S_{\mathrm{sn}}}} = \sum_i g_i \langle \hat{a}_i^\dagger(t) + \hat{a}_i(t) \rangle, \tag{4.16}$$

scaling by the shot noise PSD S_{sn} and the time-dependent optodynamical measurement gain $A(t)$, calculated from Eq. 2.72. The average results from over 2000 experimental cycles are shown in Fig. 4.9b. The pulse sequence is repeated 5 times during each iteration, spaced by 2 ms to allow the atomic motion to equilibrate with its thermal bath in between each pulse. After the series of pulsed measurements in each iteration, the oscillator frequencies are measured with an on-resonance probe, and stabilized via digital feedback, as described in Sec. 4.1.

The interaction is turned on diabatically with respect to the coupling strength K, projecting the initial single-oscillator excitation onto the coupled normal-mode basis. The coherent amplitudes of each normal mode evolve at different frequencies, producing a beatnote in the measured signal during coupling because the off-resonantly coupled oscillators do not fully hybridize into a completely bright and dark mode of the measurement.

The final amplitude and phase of each oscillator after coupling is revealed by the beatnote observed during their subsequent free evolution, with a longer beatnote period reflecting the smaller frequency difference between uncoupled oscillators. The final state of each oscillator can be extracted by a linear least-squares fit to the sum of damped sinusoids

$$f(t) = \sqrt{2} \sum_i g_i e^{-\Gamma_i t/2} (X_i \cos \omega_i t + P_i \sin \omega_i t), \tag{4.17}$$

extracting the position X_i and momentum P_i quadratures of each oscillator, with the oscillator frequencies and damping rates determined from independent fits to the equilibrium shot-noise–driven PSD.

4.5 Backaction-limited state exchange

A potential application of this optical-spring interaction would be to perform a complete exchange of the quantum states of two oscillators. However, measurement of the coupled oscillator dynamics from light leaking out of the cavity, such as displayed in Fig. 4.9b, necessarily implies backaction noise imparted to the oscillators from vacuum fluctuations of the cavity photons mediating the interaction. This added noise is reflected in the distribution of single-shot quadrature estimates X_i and P_i for each oscillator, which were obtained using

matched filters that provide an analytic solution for the least-squares fit to Eq. 4.17. The number of added thermal phonons is reflected by an increase in the covariance of the resulting phase space distributions, and limits the fidelity of a state exchange interaction.

This matched filter analysis is described in Chap. 6, and the experimental results obtained after various coupling times are reported in the published work [35]. Here, I will develop a basic theoretical model for the added noise and correlations, from the RWA theory derived above.

Time evolution of covariance

It is useful to consider the normally ordered 2nd-moment matrix defined by

$$C = \langle :\hat{\boldsymbol{a}}\hat{\boldsymbol{a}}^\dagger: \rangle = \begin{pmatrix} \langle \hat{a}_1^\dagger \hat{a}_1 \rangle & \langle \hat{a}_1^\dagger \hat{a}_2 \rangle \\ \langle \hat{a}_2^\dagger \hat{a}_1 \rangle & \langle \hat{a}_2^\dagger \hat{a}_2 \rangle \end{pmatrix} \tag{4.18}$$

Evolution of the covariance matrix is perturbed by the covariance of noise added to the oscillators from their thermal baths and measurement backaction. For oscillators in the unresolved-sideband regime, the cavity shot noise fluctuations $\hat{\xi}_\Delta^{\mathrm{AM}}(t)$ driving measurement backaction can be approximated as white noise, with a PSD described by Eq. 2.42.

Therefore, treating all noise inputs as uncorrelated white noise, the covariance matrix evolution can be solved in terms of the initial covariance $C(0)$ according to

$$C(t) = e^{-iMt} C(0) e^{iM^\dagger t} + \int_0^t d\tau\, e^{-iM\tau} N e^{iM^\dagger \tau}, \tag{4.19}$$

in terms of the input noise covariance matrix

$$N = \begin{pmatrix} \Gamma_1 (\nu_1 + \mu_1) & \sqrt{\Gamma_1 \mu_1 \Gamma_2 \mu_2} \\ \sqrt{\Gamma_1 \mu_1 \Gamma_2 \mu_2} & \Gamma_2 (\nu_2 + \mu_2) \end{pmatrix}, \tag{4.20}$$

defined by $\langle :\hat{\boldsymbol{v}}(t)\hat{\boldsymbol{v}}^\dagger(t'): \rangle = N\delta(t - t')$.

This matrix is written in terms of the equilibrium thermal occupation ν_i of each oscillator from its independent bath in addition to the thermal occupation from the common measurement backaction noise

$$\mu_i = \frac{2\bar{n} g_i^2}{\Gamma_i \kappa} \frac{\kappa^2}{\kappa^2 + \Delta^2}, \tag{4.21}$$

which is a product of the optodynamical cooperativity and the cavity's Lorentzian profile.

The integral in Eq. 4.19 can be directly solved by transforming into the normal mode basis, defining the normal mode covariance matrix $C' = E^{-1} C \left(E^{-1}\right)^\dagger$. Carrying out the integration for each component of this matrix yields

$$C'_{nm}(t) = \left(C'_{nm}(0) - \bar{C}'_{nm}\right) e^{i(\lambda_m^* - \lambda_n)t} + \bar{C}'_{nm}, \tag{4.22}$$

where n and m index over the normal modes and corresponding eigenvalues λ_+ and λ_-. I have also defined the steady-state normal mode covariance,

$$\bar{\mathrm{C}}'_{nm} = \frac{\mathrm{N}'_{nm}}{i(\lambda_n - \lambda_m^*)}, \tag{4.23}$$

which describes the equilibrium occupation and correlation for a stable system, where $\mathrm{Im}[\lambda_{\pm}] < 0$. Given this solution, it can be transformed back into the individual-oscillator basis with the reverse transformation

$$\mathrm{C}(t) = \mathrm{E}\mathrm{C}'(t)\mathrm{E}^{\dagger}. \tag{4.24}$$

Added noise occupation

The added noise covariance can be computed according to

$$\delta\mathrm{C}(t) = \mathrm{C}(t) - \mathrm{C}(0). \tag{4.25}$$

Assuming the oscillators begin in equilibrium with their independent thermal baths, with initial covariance matrix

$$\mathrm{C}(0) = \begin{pmatrix} \nu_1 & 0 \\ 0 & \nu_2 \end{pmatrix}, \tag{4.26}$$

Then the noise occupation due to each thermal bath is approximately constant, and the added noise is predominately due to 'measurement' backaction from optical shot noise. The exact solution for time evolution of the covariance matrix is tedious and complicated, with numerical solutions plotted in Fig. 4.10a for experimental parameters similar to the published results [35].

The fidelity of the state exchange interaction can be quantified by the added covariance after one exchange period $T = 2\pi/W$, displayed in Fig. 4.10b, driving a double swap of the oscillator states when $\delta = 0$. We can gain some basic intuition by considering an approximate solution for this added noise after one exchange period. Assuming the total damping is slower than the exchange rate $\Gamma' \ll K$, the added noise can be Taylor expanded to first order in Γ'/K, yielding

$$\delta\mathrm{C}(T) \approx \frac{2\pi\mu\Gamma'}{\sqrt{\delta^2 + K^2}} \begin{pmatrix} 1 + \cos\theta\sin\theta & -\sin^2\theta \\ -\sin^2\theta & 1 - \cos\theta\sin\theta \end{pmatrix}. \tag{4.27}$$

The diagonal components of $\delta\mathrm{C}$ quantify the backaction noise occupation added to each oscillator. For off-resonant coupling, more noise is added to one oscillator than the other, because the oscillators only partially hybridized in the normal modes, with one oscillator forming a larger component of the 'brighter' normal mode that experiences the most measurement backaction. The off-diagonal component of $\delta\mathrm{C}$ represents the correlation of added
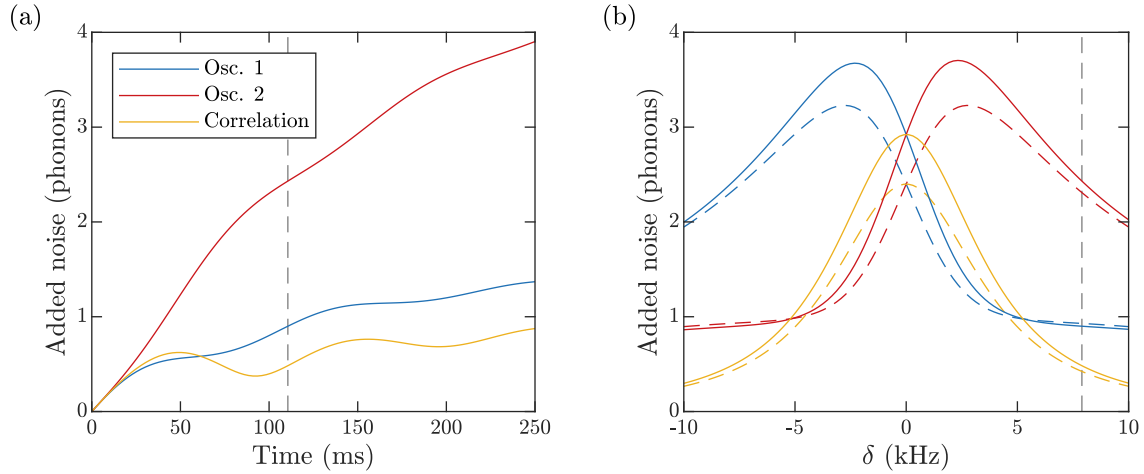
Figure 4.10: Backaction noise and correlations added to each oscillator during coupling by an intracavity photon number $\bar{n} = 8$ and probe detuning $\Delta = 2\pi \times 1.2$ MHz. (a) Time evolution of the added noise occupation of each oscillator and noise correlation $\langle |\hat{a}_1^\dagger \hat{a}_2| \rangle$ between oscillators, numerically calculated from the diagonal and off-diagonal components of Eq. 4.25 at detuning $\delta = 2\pi \times 7.9$ kHz (vertical line in **b**) and with intrinsic damping rate $\Gamma = 2\pi \times 1.5$ kHz. (b) Added noise after one exchange period $T = 2\pi/W$ (vertical line in **a**) as a function of oscillator detuning. A complete state exchange occurs only for $\delta = 0$, where the noise added to each oscillator is perfectly correlated. The approximated solution from Eq. 4.27 qualitatively agrees, with the discrepancy arising from the neglected imaginary component of K.

noise between oscillators. Because each oscillator experiences components of the same backaction fluctuations at each normal mode frequency, the resulting perturbations are correlated. In fact, for resonant coupling, where $\theta = \pi/2$, the cavity field couples only to the center-of-mass normal mode, and the solution in Eq. 4.27 predicts perfect correlation between the backaction perturbing both oscillators, also confirmed by the numerical solutions displayed in Fig. 4.10b.

Qualitatively the approximation agrees well with the full numerical solutions displayed in Fig. 4.10. The discrepancy in amplitude of added noise is due to the neglected imaginary component of K, which reflects the time-delayed nature of the optical coupling. Near $\delta = 0$, this imaginary component adds a differential damping to the eigenvalues in Eq. 4.11, shifting the optodynamical anti-damping entirely to the 'bright' normal mode and reducing decay of the added noise in Fig. 4.10b.

Chapter 5

Negative-mass instability

This chapter discusses our experimental demonstration of optodynamical coupling between the inverted total spin procession and the center of motion of a single atomic ensemble, realizing an effective negative-mass instability. The primary experimental results are reported in Ref. [29], and will be only briefly summarized here. Instead, I provide additional background and detail on the experimental realization and theoretically analyze applications for quantum-limited amplification and two-mode squeezing, accessible with realistic experimental parameters in the absence of incoherent coupling dynamics.

Harmonic oscillators with an effective negative mass, where exciting larger amplitude motion corresponds to a decrease in energy, have received attention in quantum mechanical systems for application as quantum limited amplifiers [100] or to engineer coherent quantum noise cancellation [39]. Beginning in Sec. 5.1, I summarize some proposals and uses of negative-mass dynamics, which motivate the negative-mass instability as a novel optodynamical interaction. In Sec. 5.2, I discuss details of our experimental realization with a single atomic ensemble and technical complications which arise in this system. I derive a theoretical model in Sec. 5.3, which is applied to interpret signals observed during coupling in Sec. 5.4. Information about the full two-mode state is also obtained by observing the free, transient ringdown of both oscillators after a short coupling interaction, using matched filters to extract retrodicted estimates for the final state after coupling, which is discussed in Chap. 6 and related work [29, 101]. Applications of the instability under more ideal conditions are considered in Sec. 5.5, using the theoretical solution to propose generation of two-mode squeezed states or quantum-limited amplification. Finally, Sec. 5.6 discusses some open questions and future directions for the experimental work.

5.1 Background and motivation

Negative-mass backaction cancellation

The total Hamiltonian for a negative-mass oscillator is simply negative that of a normal positive-mass oscillator, with the contributions from both kinetic and potential energy inverted. One consequence for a negative mass is that the oscillator displacement responds by moving *toward* an applied force. Therefore, if the center-of-mass position of a pair of degenerate positive- and negative-mass oscillators is measured by the same optical mode, they experience identical radiation pressure noise from photon vacuum fluctuations, and the induced backaction perturbations are anti-correlated and therefore do not appear in later observations of the center-of-mass motion.

As described in Ref. [30], this situation can be realized in the Hamiltonian for dispersive optical measurement of a negative-mass mode $\hat{a}_1$ and positive-mass mode $\hat{a}_2$

$$\mathcal{H} = -\hbar\omega_1 \hat{a}_1^\dagger \hat{a}_1 + \hbar\omega_2 \hat{a}_2^\dagger \hat{a}_2 + \hbar g \hat{c}^\dagger \hat{c} \left(\hat{X}_1 + \hat{X}_2 \right), \tag{5.1}$$

such as hypothetically performed by the cavity with $\Delta = 0$. For oscillators tuned to the same frequency $\omega_1 = \omega_2$, the normal mode degeneracy is broken only by the measurement operator. Defining hybrid quadrature operators

$$\hat{Q} = \hat{X}_1 + \hat{X}_2 \qquad\qquad \hat{\Pi} = -\hat{P}_1 + \hat{P}_2, \tag{5.2}$$

it can be shown that the equations of motion for these two quadratures form a closed system

$$\dot{\hat{Q}} = \omega\hat{\Pi} \qquad\qquad \dot{\hat{\Pi}} = -\omega\hat{Q}. \tag{5.3}$$

It is significant that no backaction forces associated with the optical measurement appear in the evolution described by Eq. 5.3, in spite of performing a continuous optical measurement of $\hat{Q}$. The optical shot noise instead couples to $\hat{P}_1 + \hat{P}_2$, the canonical momentum quadrature of $\hat{Q}$, and therefore does not show up in later measurements of $\hat{Q}$.

The measurement does, however, induce correlated backaction between the two oscillators and results in a two-mode squeezed state when conditioned on the observed measurement trace [76]. By further adding dissipation to each mode, the measurement induced correlations reach an equilibrium, resulting in deterministic, steady-state entanglement [102]. By making such a measurement of a hybrid spin/mechanical system, this backaction cancellation has been used to demonstrate measurement of the position of a mechanical oscillator with precision below the SQL [31], with application toward beyond-SQL force sensing.

There are two necessary conditions to observe complete backaction cancellation. First, the quadratures of the normal modes that diagonalize the Hamiltonian must form quantum-mechanics-free subspaces, with a trivial commutator like $[\hat{Q}, \hat{\Pi}] = 0$. Second, the normal modes must correspond to a 'bright' and 'dark' mode of the measurement, such that the measured operator is sensitive to only one normal mode, with all the associated backaction perturbing the other mode which is completely 'dark' to the measured result.

Coupled positive and negative masses

However, when the positive- and negative-mass modes are intrinsically coupled by the Hamiltonian, as turns out to be the case for our atomic system described in Sec. 5.2, this interaction defines the normal modes of the system, which may no longer correspond to purely 'bright' and 'dark' modes of the cavity measurement operator. Even though the normal modes realize so-called 'quantum mechanics free' subspaces, derived in Sec. 5.5, their evolution is not backaction free because the optical measurement senses both normal modes, imparting backaction noise to both subspaces. However, the absence of a Heisenberg uncertainty bound between quadratures of each normal mode implies no quantum limit to evolution of the normal mode variances. This condition allows for two-mode squeezing or quantum-limited amplification, as proposed in Sec. 5.5, when optodynamical backaction is suppressed by coupling the oscillators with a far-off-resonance cavity drive $\Delta \gg \kappa$.

This interaction has been proposed for generating two-mode squeezing through coherent, cavity-mediated interaction of positive and negative harmonic modes, approximated by low- and high-energy polarized spin ensembles [103]. Our experimental realization requires a more complicated model, including intrinsic damping and diffusion of the oscillators as well as cavity-conditioned optical backaction. The adiabatic approximation for the cavity field derived in Ref. [103] neglected optodynamical damping/anti-damping, which arises from the finite cavity lifetime and is only negligible for $|\Delta| \gg \kappa, \omega_i$. However, in our experimental demonstration, the optodynamical coupling strength is maximized relative to the intrinsic static-gradient coupling, described in Sec. 5.2, at a probe detuning $|\Delta| = \kappa$. In this condition, the optodynamical damping is not negligible and facilitates optodynamical energy exchange, leading to non-conservative dynamics of the coupled system.

5.2 Experimental realization

As introduced in Sec. 2.3, simultaneous optodynamical coupling to atomic spin and motion can be realized by trapping the atoms at a linear intensity gradient of the probe mode and applying a magnetic field transverse to the cavity axis, illustrated in Fig. 5.1. Considering only a single, circular polarization σ^+ of the cavity mode, the general dispersive Hamiltonian in Eq. 2.12 can be Taylor expanded to first order in the displacement $\hat{z}_i = z_{\text{HO}}(\hat{a}_i + \hat{a}_i^\dagger)$ of each atom away from the trap center, with single-atom harmonic-oscillator length $z_{\text{HO}} = \sqrt{\hbar/2m_a\omega_{\text{m}}}$

$$\mathcal{H} = \hbar\omega_{\text{c}}\hat{c}^\dagger\hat{c} + \sum_i^{N_a} \left[\hbar\omega_{\text{m}}\hat{a}_i^\dagger\hat{a}_i + \hbar\omega_{\text{s}}\hat{f}_z^{(i)} \right] + \hbar g_{\text{c}}\hat{c}^\dagger\hat{c} \sum_i^{N_a} \left(\alpha_0 + \alpha_1\hat{f}_x^{(i)} \right) \left(\frac{1}{2} + k_p\hat{z}_i \right). \qquad (5.4)$$
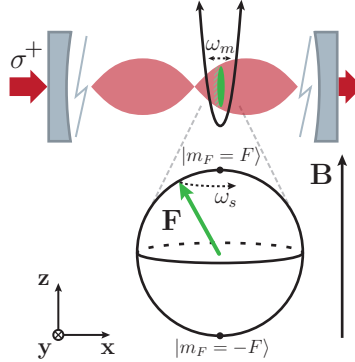
Figure 5.1: Configuration for simultaneous optodynamical spin and position sensitivity. A single ensemble of atoms is confined at the linear probe intensity gradient, and Larmor precession of the spin projection along the cavity axis is induced by an applied magnetic field transverse to the cavity axis. Spatial variation of the vector Stark shift creates an incoherent, 'static-gradient' coupling between the spin and motion of each atom individually. Adapted from Ref. [29], ©2018 American Physical Society.

The simple sums over single atom spin components or displacements can be written in terms of the total atomic spin components $\hat{F}_j = \sum_i \hat{f}_j^{(i)}$ and center-of-mass position $\hat{Z}_m = \sum_i \hat{z}_i / N_a$

$$\mathcal{H} = \hbar\omega_c' \hat{c}^\dagger \hat{c} + \sum_i^{N_a} \hbar\omega_m \hat{a}_i^\dagger \hat{a}_i + \hbar\omega_s \hat{F}_z + \hbar g_c \hat{c}^\dagger \hat{c} \left(\alpha_0 k_p N_a \hat{Z}_m + \frac{\alpha_1}{2}\hat{F}_x + \alpha_1 k_p \sum_i^{N_a} \hat{z}_i \hat{f}_x^{(i)} \right).$$

In this expansion, the interaction separates into a static cavity frequency shift $\omega_c' = \omega_c + \alpha_0 N_a g_c / 2$, independent optodynamical coupling to the center-of-mass position $\hat{Z}_m$ and total transverse spin $\hat{F}_x$, and a direct coupling between each atom's motion and spin in the final term.

This direct spin-orbit interaction arises because of spatial variation of the vector ac Stark shift across the intensity gradient of the probe, which the atoms experience as an effective magnetic field gradient proportional to $\hat{z}_i \hat{f}_x^{(i)}$. This 'static gradient' interaction is present even for a constant cavity intensity, not relying on any dynamical modulation of the cavity field. It is distinct from the optodynamical coupling that drives the negative-mass instability, which is mediated by modulation of the cavity field and interacts only with the collective motion and spin.

The remaining terms describing individual atomic motion can be transformed into the center-of-mass mode $\hat{a}_m = \sum_i \hat{a}_i / \sqrt{N_a}$ and the $N_a - 1$ orthonormal modes $\hat{b}_i$ of residual atomic motion relative to it. The resulting Hamiltonian can be written as the sum of two parts, $\mathcal{H} = \mathcal{H}_c + \mathcal{H}_b$. The 'coherent' Hamiltonian $\mathcal{H}_c$, stated in Eq. 2.17, describes the dynamics and interactions of the collective modes

$$\mathcal{H}_c = \hbar\omega_c' \hat{c}^\dagger \hat{c} + \hbar\omega_m \hat{a}_m^\dagger \hat{a}_m + \hbar\omega_s \hat{F}_z - \hbar g_c \hat{c}^\dagger \hat{c} \left[\alpha_0 N_a k_p \hat{Z}_m - \frac{\alpha_1}{2}\hat{F}_x + \alpha_1 k_p \hat{Z}_m \hat{F}_z \right], \qquad (5.5)$$

and the 'bath' Hamiltonian $\mathcal{H}_b$ contains the thermal energy of the residual atomic motion and a coupling between the spin and this effective mechanical bath,

$$\mathcal{H}_b = \hbar\omega_{\mathrm{m}} \sum_i^{N_a-1} \hat{b}_i^\dagger \hat{b}_i - \hbar\alpha_1 k_{\mathrm{p}} z_{\mathrm{HO}} g_c \hat{c}^\dagger \hat{c} \sum_i^{N_a-1} (\hat{b}_i^\dagger + \hat{b}_i)\hat{f}_z^{(i)}. \tag{5.6}$$

The center-of-mass motion also equilibrates with this bath through its intrinsic damping, likely due to collisions and trap inhomogeneity, which are not included in this model.

Dephasing from static-gradient interaction

This static gradient induces an interaction between the collective spin and motion, in the final term of Eq. 5.5, as well as an equally strong interaction between each of the $N_a - 1$ spin modes and corresponding modes of the thermal bath, described by the interaction term in Eq. 5.6. Developing a rigorous treatment of the dynamics driven by this bath is well beyond the scope of this work. It might not be possible on the level of Heisenberg-Langevin equations or a Lindblad equation for the density matrix, since coupling between the spin of each individual atom and its motion likely does not satisfy the usual approximations of a Markovian bath, linear coupling, or a broadband spectrum.

However, some intuition can be developed by considering the initial dynamics of a spin ensemble polarized in its highest-energy state. Each atom experiences modulation of the effective optical magnetic field at the trap frequency, due to its axial motion across the probe intensity gradient. When the trap frequency is tuned close to the Larmor frequency, this modulation of an effective transverse magnetic field component drives rotation of the individual atomic spins, with the incoherent thermal motion inducing random spin flips within the ensemble, depolarizing the collective atomic spin.

This resonant spin depolarization was observed for a cavity driven on resonance, shown in Fig. 5.2, where there is no optodynamical interaction mediated between the motion and spin. This dephasing can be interpreted as thermalization between the initially negative-temperature collective spin and the positive-temperature thermal motion. As energy flows from the atomic spins into thermal motion, the spin ensemble is driven to increasingly negative temperatures, which diverge to $-\infty$ and then decrease from $+\infty$, because of the spin ensemble's finite heat capacity. Eventually, the spin and motion would equilibrate at a large positive temperature, having added several phonons to the motion of each atom, on average. The effective coupling rate between the spin and thermal bath in Eq. 5.6 is $\alpha_1 k_{\mathrm{p}} z_{\mathrm{HO}} g_c = 2\pi \times 120$ Hz per photon, which is roughly consistent with the observation of one spin-flip per atom after about 5 ms in Fig. 5.2. In the supplement to Ref. [29], we also report evidence for increasing temperature of the atomic motion as the spin depolarized, indicating the finite heat capacity of this mechanical bath, in addition to anomalous diffusion of the collective spin precession observed in the heterodyne signals.
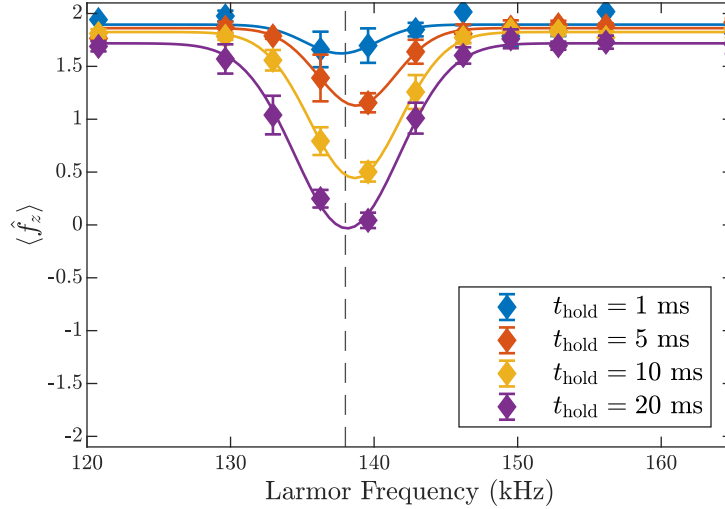
Figure 5.2: Spin depolarization from the static gradient coupling to thermal atomic motion. The cavity is probed on resonance $\Delta = 0$ with intra-cavity photon number $\bar{n} = 2$ for time t_{hold}, and then the final spin projection is measured using QND measurements as in Sec. 3.4. The measurement is repeated for a range of Larmor frequencies, and shows a clear resonance around the mechanical frequency $\omega_m = 2\pi \times 138$ kHz.

Summary of published results

The negative-mass instability was demonstrated in Ref. [29] using a pulsed measurement sequence, summarized in Fig. 5.3a-b. The oscillators were initially prepared near their ground states, with no well-defined phase, such that the amplification driven by the instability occurred at a random absolute phase. The dynamics generated by the instability are revealed through the mean-squared displacement signal $\langle \hat{D}^2 \rangle_{\text{cyc}}$, which is introduced in Sec. 2.6 and described in particular detail here in Sec. 5.4. The amplified normal mode drives correlated growth in the motion of both oscillators, as shown in Fig. 5.3c. Correlations are generated between the oscillators at a fixed relative phase, determined by the normal modes of the interacting system, and is revealed as a beat during their subsequent free ringdown.

The strength of the instability was estimated from the rate of initial exponential growth observed during the interaction, shown in Fig. 5.4. An independent measure of the growth was obtained by estimating the oscillators' final states after a variable coupling time through observation of their subsequent, transient decay, after resolving the oscillators in frequency to distinguish their individual motion. The oscillators' occupations and correlation are described by the two-mode state covariance, which was estimated using matched filters applied to the ringdown signals observed after coupling, as discussed in Chap. 6.
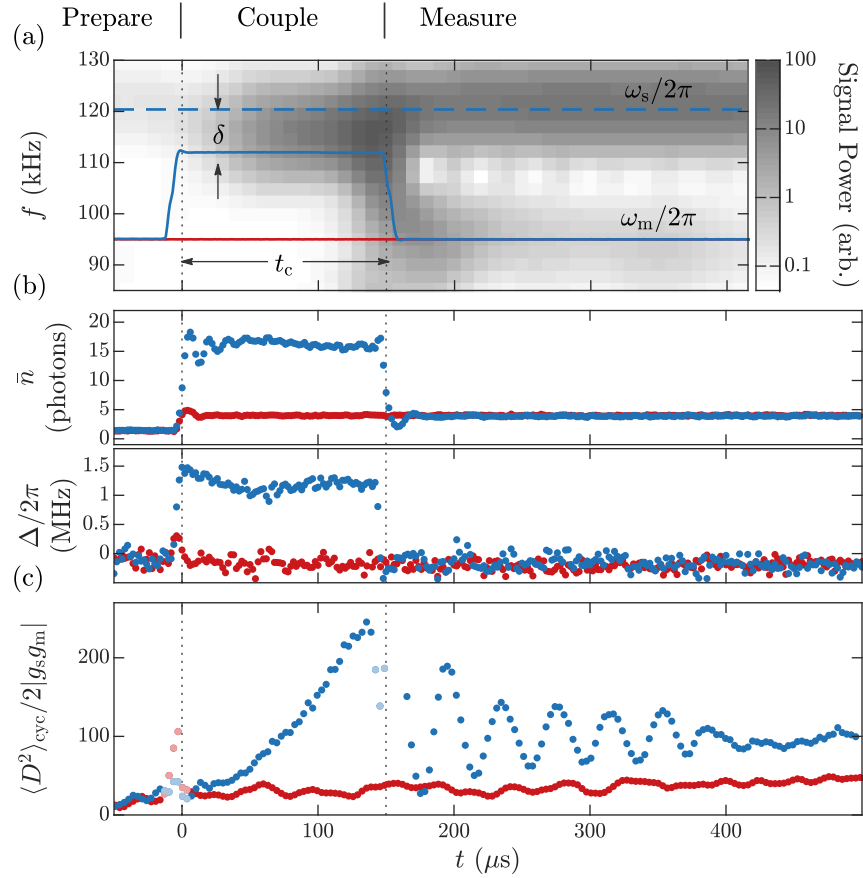
Figure 5.3: Experimental sequence of optodynamical coupling and measurement demonstrating the negative-mass instability, averaged over about 200 iterations. (a) Spectrogram of the observed optodynamical single, with the calibrated Larmor frequency (dashed line) and axial trap frequency (solid line) indicated. The trap frequency was ramped in 15 ms to achieve the desired detuning δ during the $t_c = 150~\mu$s long coupling pulse. (b) The optodynamical interaction was switched on by rapidly detuning the probe frequency to $\Delta = 1.4$ MHz and increasing the intracavity intensity to $\bar{n} = 15$ (blue data), corresponding to an interaction strength $k_{sm} = -8$ kHz. For reference, the experimental sequence was repeated without the coupling pulse (red data). (c) Exponential growth of the coupled dynamics is revealed in the mean-squared displacement of both oscillators $\langle \hat{D}^2 \rangle_{\text{cyc}}$, discussed in Sec. 5.4. After coupling, the correlations generated between the two oscillators are indicated by a stationary beat during their free ringdown. This figure was adapted from Ref. [29], showing data for a different set of experimental parameters.
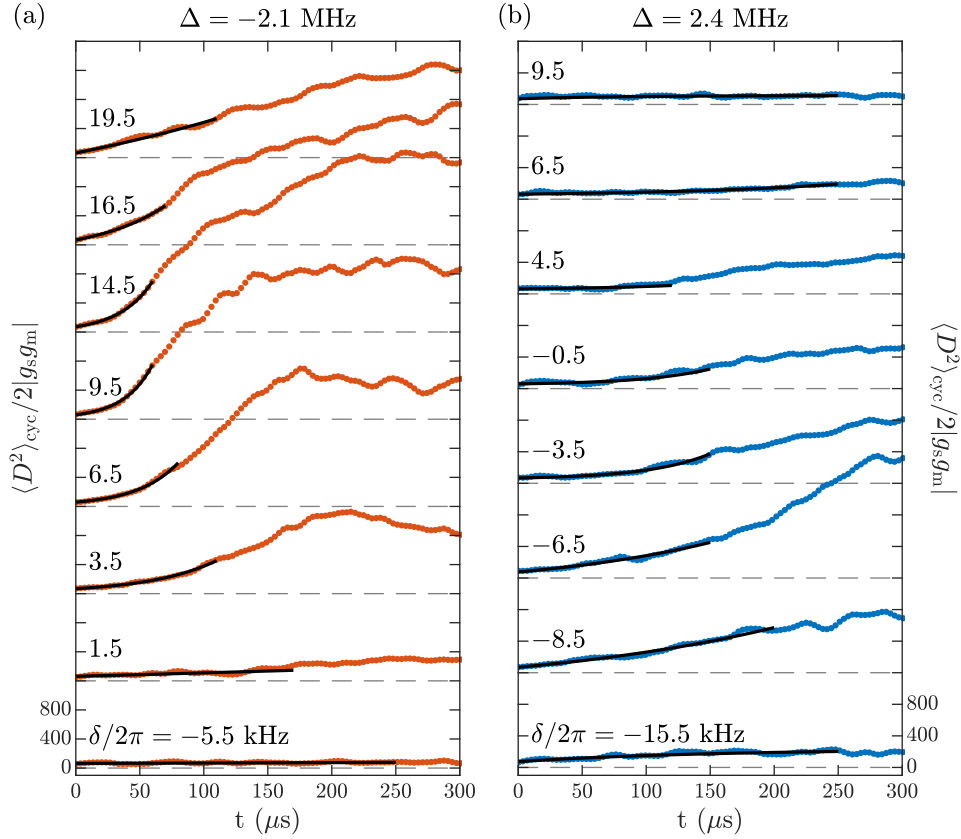
Figure 5.4: Characterization of the instability gain from growth observed in $\langle \hat{D}^2 \rangle_{\mathrm{cyc}}$, for a range of oscillator detunings δ. The optodynamical coupling strength was kept approximately fixed, with an intracavity intensity $\bar{n} = 10$. Each trace (offset for clarity) is the average of around 30 repetitions. (a) The observed growth indicates a peak instability at a finite detuning around $\delta = 9.5$ KHz, due to the optodynamical spring shifts. The exponential amplification rate G_+ was extracted by fits at early time (black lines) described in Sec. 5.4, with results reported in Ref. [29]. (b) For an equal but opposite probe detuning Δ, the sign of the optodynamical coupling strength k_{ms} is inverted, and acts opposite the static-gradient coupling g_{sm} in Eq. 5.8, reducing the total instability gain.

5.3 Theory of negative-mass instability

To describe the small-amplitude dynamics of the coupled system, I start by linearizing the Hamiltonian in Eq. 5.5 for small displacements of each mode around a stable point. As in Sec. 3.1, precession of the collective spin for small excitations away from either its highest- or lowest-energy state can be approximated as the motion of a harmonic oscillator, described by bosonic operator $\hat{a}_s$ according to the Holstein-Primakoff approximation defined by Eqs. 3.10. The dynamics of the cavity field can then be linearized for small modulations about the average photon number $\bar{n}$, in a frame rotating at the probe frequency $\omega_{\rm p}$, by making the transformation $\hat{c} \rightarrow e^{-i\omega_{\rm p}t}(\sqrt{\bar{n}} + \hat{c})$ described in Sec. 2.4.

Keeping terms up to second order for small amplitudes of the operators $\hat{a}_m$, $\hat{a}_s$, and $\hat{c}$, the coherent Hamiltonian is approximately

$$
\begin{aligned}
\mathcal{H}_c = {} & -\hbar\Delta\hat{c}^{\dagger}\hat{c} + \hbar\omega_{\rm m}\hat{a}_m^{\dagger}\hat{a}_m + \epsilon_s\hbar\omega_{\rm s}\hat{a}_s^{\dagger}\hat{a}_s \\
& + \hbar\sqrt{\bar{n}}(\hat{c} + \hat{c}^{\dagger})\left[g_{\rm m}(\hat{a}_m^{\dagger} + \hat{a}_m) + g_{\rm s}(\hat{a}_s^{\dagger} + \hat{a}_s)\right] \\
& + \hbar\bar{n}g_{\rm sm}(\hat{a}_m^{\dagger} + \hat{a}_m)(\hat{a}_s^{\dagger} + \hat{a}_s), \quad (5.7)
\end{aligned}
$$

where $\Delta = \omega_{\rm p} - \omega_{\rm c}'$ is the probe detuning from cavity resonance, $\epsilon_s = -\,{\rm sgn}\langle\hat{F}_x\rangle$ indicates the sign of the spin's effective mass, negative (positive) for a spin near its highest-energy (lowest-energy) state, and defining coupling rates $g_{\rm m} = \alpha_0 N_a g_{\rm c} k_{\rm p} Z_{\rm HO}$, $g_{\rm s} = \alpha_1 g_{\rm c}\sqrt{F/8}$, and $g_{\rm sm} = \alpha_1 g_{\rm c} k_{\rm p} Z_{\rm HO}\sqrt{F/2}$ in terms of the collective harmonic oscillator length $Z_{\rm HO} = z_{\rm HO}/\sqrt{N_a}$.

Equations of motion are derived from this linearized Hamiltonian by including damping and input noise from coupling to the environment, as described in Sec. 2.4. As assumed in Sec. 3.1, the collective spin has negligible dissipation and can be approximated as an undamped harmonic oscillator with $\Gamma_s = 0$. After eliminating the cavity field using the solution from Eq. 2.39, the oscillator equations of motion can be written identically to Eq. 4.4, but now with the complex coupling constant K_{sm} defined to include the static coupling interaction

$$
K_{sm} = k_{sm} + 2\bar{n}g_{sm} - i\gamma_{sm}. \tag{5.8}
$$

Note that the static-gradient coupling g_{sm} adds either constructively or destructively to the optical spring strength k_{sm}, creating an asymmetry in the total interaction strength between oscillators for a cavity driven equally above or below resonance, as seen in Fig. 5.4 and reported in Ref. [29]. Because this static coupling is also associated with the incoherent energy exchange and diffusion of the total spin reflected in Fig. 5.2, which is not included in this theory, for the following theoretical discussion I will assume a more ideal system, with $g_{\rm sm} = 0$.

Unlike the optodynamical interaction between two positive-mass oscillators explored in Chap. 4, here the atomic spin can be prepared near its highest-energy state, where it evolves like an effective negative-mass oscillator ($\epsilon_s = -1$), which is optically coupled with the positive-mass mechanical mode ($\epsilon_m = +1$). The equations of motion can again be transformed into a frame rotating at the average shifted frequency $\bar{\omega} = (\omega_s' + \omega_m')/2$, yielding

Eq. 4.5. Now, making the rotating wave approximation, the equations of motion can be summarized by

$$\dot{\hat{a}}_m = \frac{i}{2}\left[\left(\delta' + i\Gamma'_m\right)\hat{a}_m - K^*_{ms}\hat{a}^\dagger_s\right] - i\sqrt{B_m}\hat{\xi}^{\text{AM}}_\Delta e^{i\bar{\omega}t} + \sqrt{\Gamma_m}\hat{\eta}_m \qquad (5.9\text{a})$$

$$\dot{\hat{a}}^\dagger_s = \frac{i}{2}\left[\left(-\delta' + i\Gamma'_s\right)\hat{a}^\dagger_s + K_{sm}\hat{a}_m\right] + i\sqrt{B_s}\hat{\xi}^{\text{AM}}_\Delta e^{-i\bar{\omega}t} + \sqrt{\Gamma_s}\hat{\eta}^\dagger_s \qquad (5.9\text{b})$$

, defining the oscillator detuning from the optodynamically shifted resonance as $\delta' = \omega'_s - \omega'_m = \delta - (k_{ss} + k_{mm})/2$. This approximation is valid for weak coupling $|\omega_i| \gg |K_{ij}|$ and assuming the amplitude of the neglected counter-rotating terms is sufficiently small. Because of the unstable growth of dynamics from coupling positive- and negative-mass oscillators, this condition is eventually violated, leading to corrections described in Sec. 5.5.

Assuming both oscillators are in the unresolved-sideband regime, the optodynamical coupling is approximately reciprocal and can be summarized by a single complex coupling parameter $K \approx K_{sm} \approx K^*_{ms}$. Defining the state vector $\hat{\boldsymbol{a}} = (\hat{a}^\dagger_s, \hat{a}_m)^\mathsf{T}$, the equations of motion can once again be summarized by the matrix equation

$$\frac{\partial}{\partial t}\hat{\boldsymbol{a}} = -i\text{M}\hat{\boldsymbol{a}} + \hat{\boldsymbol{v}} \qquad (5.10)$$

in terms of a dynamical matrix and noise input vector

$$\text{M} = \frac{1}{2}\begin{pmatrix} D - i\Gamma'_+ & -K \\ K & -D - i\Gamma'_+ \end{pmatrix} \qquad \hat{\boldsymbol{v}} = \begin{pmatrix} i\sqrt{B_s}\hat{\xi}^{\text{AM}}_\Delta e^{-i\bar{\omega}t} + \sqrt{\Gamma_s}\hat{\eta}^\dagger_s \\ -i\sqrt{B_m}\hat{\xi}^{\text{AM}}_\Delta e^{i\bar{\omega}t} + \sqrt{\Gamma_m}\hat{\eta}_m \end{pmatrix}, \qquad (5.11)$$

respectively. Here I have defined a complex detuning parameter $D = \delta' - i\Gamma'_-$ and average and differential damping rates $\Gamma'_\pm = (\Gamma'_s \pm \Gamma'_m)/2$, which account for the significant difference in intrinsic damping rates between the atomic motion and spin. The general solution to this system of equations is given by

$$\hat{\boldsymbol{a}}(t) = e^{-i\text{M}t}\hat{\boldsymbol{a}}(0) + \int_0^t d\tau e^{-i\text{M}(t-\tau)}\hat{\boldsymbol{v}}(\tau). \qquad (5.12)$$

This dynamical matrix M is not generally a normal matrix, with $[\text{M}, \text{M}^\dagger] \neq 0$ unless $\text{Re}[DK] = 0$. By consequence, for a non-normal matrix, the transformation that diagonalizes it, assuming there is one, is not unitary. This condition implies that the transformation to normal mode operators does not preserve the commutator, and the resulting normal modes cannot be described by canonical bosonic operators.

The dynamical matrix M can be diagonalized by eigenvalue decomposition as

$$\text{M} = \text{E}\begin{pmatrix} \lambda_+ & 0 \\ 0 & \lambda_- \end{pmatrix}\text{E}^{-1} \qquad (5.13)$$

where the matrix E is formed by columns of eigenvectors which describe the normal modes of the coupled system. Time evolution of the normal modes is described by the eigenvalues of M

$$\lambda_\pm = \frac{1}{2}\left(\pm W - i\Gamma'_+\right), \qquad \text{with} \qquad W = \sqrt{D^2 - K^2}. \tag{5.14}$$

These eigenvalues are complex, with real and imaginary components plotted in Fig. 5.5a for typical experimental parameters. The real components describe the normal mode frequencies, relative to the rotating frame at $\bar{\omega}$, and the imaginary components define the intrinsic exponential gain. The eigenvalue of the amplified mode λ_+ indicates an instability threshold when $\text{Im}[W] = \Gamma'_+$, below which all amplitudes eventually decay to zero, and above which the amplitude of the amplified normal mode grows without bound.

Normal mode parametrization

The matrix E, formed by columns of eigenvectors of the dynamical matrix M, transforms the state vector $\hat{\boldsymbol{a}}$ from the basis of individual oscillators into the normal mode basis

$$\hat{\boldsymbol{b}} = \begin{pmatrix} \hat{b}_+ \\ \hat{b}_- \end{pmatrix} = \text{E}^{-1}\hat{\boldsymbol{a}}. \tag{5.15}$$

These normal mode amplitudes evolve according to the uncoupled equations

$$\hat{b}_\pm(t) = e^{-i\lambda_\pm t}\hat{b}_\pm(0) + \int_0^t d\tau\, e^{-i\lambda_\pm(t-\tau)}\hat{\eta}_\pm(\tau). \tag{5.16}$$

Normalizing each eigenvector, the transformation matrix can be parametrized as

$$\text{E} = \begin{pmatrix} e^{i\phi}\cos\frac{\theta}{2} & e^{-i\phi}\sin\frac{\theta}{2} \\ \sin\frac{\theta}{2} & \cos\frac{\theta}{2} \end{pmatrix} \tag{5.17}$$

having defined an oscillator mixing angle θ, given by $\tan\frac{\theta}{2} = |K|/|D+W|$, which describes the relative weight of each oscillator in the normal modes, and relative phase of motion $\phi = \angle(D+W)/K$. The inverse transformation is

$$\text{E}^{-1} = \frac{1}{N_E}\begin{pmatrix} \cos\frac{\theta}{2} & -e^{-i\phi}\sin\frac{\theta}{2} \\ -\sin\frac{\theta}{2} & e^{i\phi}\cos\frac{\theta}{2} \end{pmatrix} \tag{5.18}$$

with normalization $N_E = \cos\theta\cos\phi + i\sin\phi$.

The magnitude of this normalization factor is $|N_E|^2 = 1 - \sin^2\theta\cos^2\phi$ and falls in the range $0 \leq |E_n|^2 \leq 1$. It is plotted in Fig. 5.6 for typical experimental parameters. The matrix E is singular when $N_E = 0$, which occurs when $\theta = n\pi/2$ and $\phi = m\pi$ for any integers n, m, representing non-diagonalizable dynamics at a so-called 'exceptional point,' where both the eigenvalues and eigenvectors are indistinguishable.
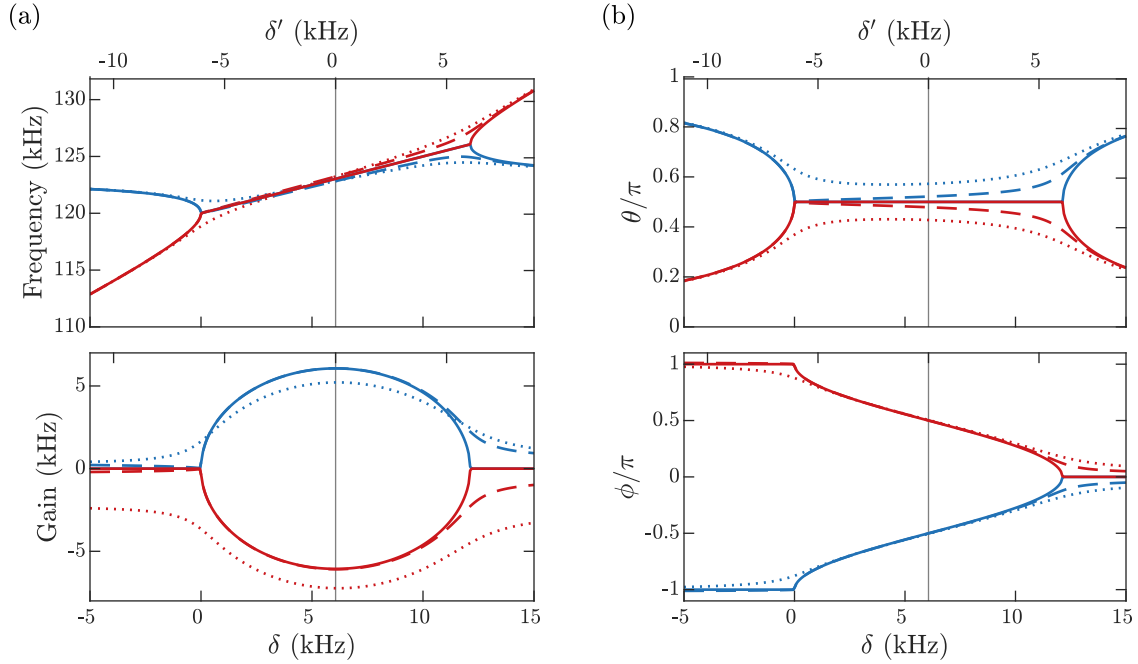
Figure 5.5: Normal mode description of negative-mass instability. (a) The real and imaginary parts of the eigenvalues $\lambda_\pm$ describe the frequency and instability gain, respectively, for the damped (red lines) and amplified (blue lines) modes. (b) The amplified normal mode vector (blue lines) parametrized by mixing angle θ and a relative phase ϕ, defined by Eq. 5.15. The mixing angle and relative phase corresponding to the damped normal mode under the same parametrization is also shown (red lines). Individual optodynamical frequency shifts move the peak instability to a finite detuning (vertical line). Solid lines reflect a system of undamped oscillators, coupled by a far off-resonant optical probe ($\Delta = 100\kappa$ and $\bar{n} = 800$), which produces negligible optodynamical damping. Dashed lines reflect the most efficient optical coupling condition ($\Delta = \kappa$ and $\bar{n} = 8$), achieving the same coupling strength $k_{ms} = 2\pi \times -6$ kHz, but optodynamical damping spoils the mode hybridization away from $\delta = 0$. Finally, the dotted lines show the effect of imbalanced damping, with damping rate $\Gamma_m = 2\pi \times 2$ kHz for the mechanical mode and $\Gamma_s = 0$ for the spin.
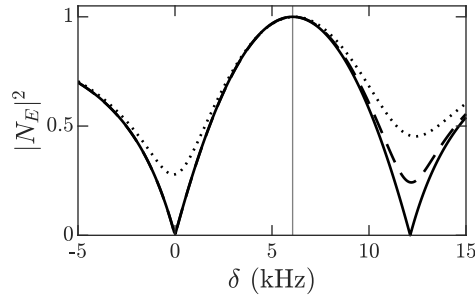
Figure 5.6: Normalization coefficient for the transformation between individual oscillators and the normal modes, defined by Eq. 5.18. The eigenvector matrix E becomes singular as $|N_E|^2 \to 0$, indicating non-diagonalizable interactions. For Γ'_- (solid lines), the transformation to normal modes defined by this matrix is singular at the transitions to the strong coupling region, shown in Fig. 5.5. However, the singularity is softened by unmatched damping rates, either optodynamical (dashed line) or intrinsic (dotted line). On the other hand, $|N_E| = 1$ is a necessary, but not sufficient, condition for the transformation to be unitary, a satisfied when $D = 0$ where $\theta = \pi/2, \phi = -\pi/2$. The sold, dashed, and dotted lines represent the same parameters as represented in Fig. 5.5.

Time evolution of covariance

Time evolution of the two-mode covariance matrix can be computed following the same procedure as used in Sec. 4.5 for coupling between two positive-mass oscillators.

The normally ordered 2nd-moment matrix is defined by

$$C = \langle :\hat{\boldsymbol{a}}\hat{\boldsymbol{a}}^\dagger: \rangle = \begin{pmatrix} \langle \hat{a}_s^\dagger \hat{a}_s \rangle & \langle \hat{a}_s \hat{a}_m \rangle \\ \langle \hat{a}_s^\dagger \hat{a}_m^\dagger \rangle & \langle \hat{a}_m^\dagger \hat{a}_m \rangle \end{pmatrix} \tag{5.19}$$

and evolves in time according to Eq. 4.19 in terms of the input white-noise covariance matrix, which here is

$$N = \begin{pmatrix} \Gamma_s \left(\nu_s + \mu_s \right) & -\sqrt{\Gamma_s \mu_s \Gamma_m \mu_m} \\ -\sqrt{\Gamma_s \mu_s \Gamma_m \mu_m} & \Gamma_m \left(\nu_m + \mu_m \right) \end{pmatrix}. \tag{5.20}$$

This matrix is written in terms of the individual oscillator bath occupations ν_i and the equilibrium backaction occupations μ_i, defined by Eq. 4.21.

Evolution of the covariance matrix can again be solved in the normal mode basis $C' = E^{-1} C \left(E^{-1} \right)^\dagger$, as in Eq. 4.22, and then transformed back into the single-oscillator basis according to Eq. 4.24

Under the effect of strong coupling, the normal mode oscillation frequencies are nearly equal $\mathrm{Re}[\lambda_+] \approx \mathrm{Re}[\lambda_-]$. Therefore, the dominant time evolution of all covariance matrix elements described by Eq. 4.22 is exponential growth or decay, driven by the imaginary part of the eigenvalues $\mathrm{Im}[\lambda_\pm]$. For oscillators initially prepared near their ground states, amplification drives exponential growth of the occupation of each oscillator $\langle \hat{a}_i^\dagger \hat{a}_i \rangle$, as well as their covariance $\langle \hat{a}_s \hat{a}_m \rangle$, at an amplification rate defined by $G_+ = 2 \,\mathrm{Im}[\lambda_+]$.

5.4   Observation of instability gain

The instability gain G_+ is a significant prediction of the theoretical model, and therefore an important parameter to measure experimentally in order to characterize the coherent dynamics of the instability. For initially ground-state oscillators, the instability drives exponential amplification of each oscillators motion at this rate, which can be observed in the optodynamical signals captured by the heterodyne detector. In the unresolved-sideband limit $\omega_i \ll \kappa$, the optodynamical measurement operator $\hat{d}$, defined in Eq. 2.57, simplifies to

$$\hat{d}(t) \approx \sqrt{\frac{\kappa^2}{\kappa^2 + \Delta^2}} e^{i\phi_q} \hat{D}(t), \tag{5.21}$$

in terms of the total dispersive cavity frequency shift $\hat{D}(t)$, a weighted sum of the oscillator displacements

$$\hat{D}(t) = \sqrt{2} \sum_i g_i \hat{X}_i(t), \tag{5.22}$$

which appears as phase and amplitude modulation of the detected optical field, with relative weight determined by the quadrature phase $\tan \phi_q = \Delta/\kappa$.

The signals observed on a single iteration, however, are obscured by measurement noise and diffusion of the oscillators driven by measurement backaction and thermal noise. It would be advantageous to average the result of many iterations of the experiment to suppress stochastic noise, while retaining the deterministic growth in amplitude of each oscillator. But because the oscillators begin near their ground states, with no coherent amplitude, the motion of each oscillator is amplified with a randomly chosen phase on each iteration of the experiment, such that the raw signals observed from many repetitions average to zero $\langle \hat{d}(t) \rangle = 0$.

In order to benefit by averaging the results of multiple iterations of the experiment, we need to construct a statistic which is independent of the absolute oscillator phase. One approach could be to filter the recorded signal from each iteration and extract estimates for the oscillator trajectories; however, constructing any sort of optimal filter for this task is conditioned on assumptions about the underlying signal and noise processes. Because our goal is to experimentally measure parameters of the system Hamiltonian to verify our model, it would not be suitable to use a matched filter analysis such as described in Ch. 6 to form these statistics, since they are constructed from the theoretical model.

Square signal model

Instead, a simpler model-independent statistic which satisfies the requirements is the cycle-averaged mean-square displacement, introduced in Sec. 2.6. Under the unresolved-sideband approximation above, the mean-squared displacement can be written in terms of evolution of the multi-mode covariance matrix as

$$\langle \hat{D}(t)^2 \rangle_{\text{cyc}} = 2\boldsymbol{g}^\mathsf{T} \mathrm{C}(t)\boldsymbol{g} + \boldsymbol{g}^\mathsf{T} \boldsymbol{g}, \tag{5.23}$$

defining an optodynamical coupling vector $\boldsymbol{g} = (g_\mathrm{s}, g_\mathrm{m})^\mathsf{T}$. This signal directly reflects the variance of a linear combination of the two-mode state, defined by the sum of oscillator positions weighted by their corresponding optodynamical coupling strength.

Substituting in the solution for the covariance matrix evolution, this signal can be separated into exponential and sinusoidal terms as

$$\langle \hat{D}^2(t) \rangle_\mathrm{cyc} = e^{-\Gamma_+ t} \left[\mathrm{A}_{11} e^{\mathrm{Im}[W]t} + \mathrm{A}_{22} e^{-\mathrm{Im}[W]t} + 2|\mathrm{A}_{12}| \cos\left(\mathrm{Re}[W]t - \angle\mathrm{A}_{12}\right) \right] + \bar{D}^2 \quad (5.24)$$

with $\tan(\angle\mathrm{A}_{12}) = \mathrm{Im}[\mathrm{A}_{12}]/\mathrm{Re}[\mathrm{A}_{12}]$, in terms of amplitudes

$$\mathrm{A}_{nm} = 2 \left[\mathrm{E}^\dagger \boldsymbol{g}\boldsymbol{g}^\mathsf{T} \mathrm{E} \right]_{nm} \left[\mathrm{C}'(0) - \bar{\mathrm{C}}' \right]_{nm} \quad (5.25)$$

and steady-state value

$$\bar{D}^2 = 2\boldsymbol{g}^\mathsf{T} \bar{\mathrm{C}} \boldsymbol{g} + \boldsymbol{g}^\mathsf{T} \boldsymbol{g}. \quad (5.26)$$

The general form of the solution described by Eqs. 5.24 reflects exponential evolution of the normal mode amplitudes described by the intrinsic gain $G_\pm = \pm\mathrm{Im}[W] - \Gamma'_+$ from Eq. 5.14, in addition to residual oscillations outside of the strong coupling region, seen in Fig. 5.5, from the frequency difference $\mathrm{Re}[W]$ between the coupled normal modes.

The general form of the signal amplitudes A_{nm} in Eq. 5.25 is complicated, but can be directly evaluated for particular system parameters. The predicted trajectories of the squared signal are plotted in Fig. 5.7a for typical experimental parameters as a function of oscillator detuning, revealing the oscillatory nature outside of the strong-coupling region $|\delta'| < G_+$, and the transition to exponential growth near the instability resonance. This prediction reveals an asymmetry in the early time evolution of the square signal, produced by the large oscillatory component at the transition to the unstable region, which adds positive or negative curvature to the signal on either side of the instability seen in Fig. 5.7.

Recovery from heterodyne signal

The optodynamical signal appears in a linear combination of amplitude and phase modulation described by quadrature angle ϕ_q in Eq. 5.21, depending on the cavity probe detuning Δ. The sudden changes in probe detuning at the edges of the coupling pulse, shown in Fig. 5.3, rotate the quadrature angle of the signal and complicate identification of the optical amplitude and phase quadratures of the heterodyne signal, due to an additional detuning-dependent phase shift of the probe from the cavity susceptibility. However, by combining the mean-squared signal observed in both heterodyne quadratures described by Eqs. 2.67, the resulting signal is insensitive to the quadrature phase ϕ_q and only requires calibration of the probe detuning Δ and intensity $\bar{n}$, in addition to the detection efficiency ϵ and shot noise PSD S_sn. Furthermore, the estimated exponential growth rates are insensitive to the absolute scale of the signal amplitude.

The demodulated heterodyne quadratures are band-pass filtered with a typical bandwidth $f_\mathrm{BW} = 65$ kHz, large enough to pass dynamics at both oscillator frequencies, while removing
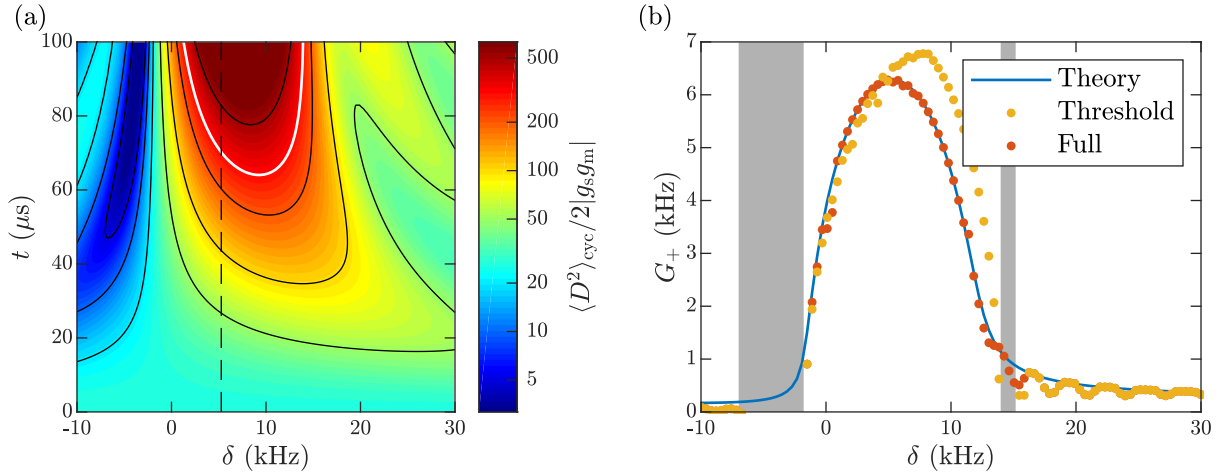
Figure 5.7: (a) Predicted time-evolution (vertical axis) of the mean-square displacement $\langle \hat{D}^2 \rangle_{\mathrm{cyc}}$ as a function of oscillator detuning (horizontal axis) for typical experimental parameters ($\bar{n} = 8$, $\Delta = -\kappa$, $\omega_s = 2\pi \times 120$ kHz, $\Gamma_s = 0$ $\Gamma_m = 2\pi \times 1$ kHz, $\nu_s = 0$, $\nu_m = 1$), but neglecting anomalous diffusion from the static gradient. (b) Estimate of the instability gain G_+ extracted from fits to Eq. 5.29. Fits to the signal below a threshold value of $\langle \hat{D}^2 \rangle_{\mathrm{cyc}} = 300$ (white contour in (a)) are distorted by short-term oscillations at the transition into the strong-coupling region (blue points), while fits to a 300 μs interval of the predicted signal more accurately reflect the exponential gain in the long-term growth (red points).

any dc components, technical noise peaks, and shot noise outside of the signal band. The mean-squared displacement $\langle \hat{D}^2 \rangle_{\mathrm{cyc}}$ can be recovered from the filtered signals quadrature sum, according to

$$\langle P_I(t)^2 + P_Q(t)^2 \rangle_{\mathrm{cyc}} = S_{\mathrm{sn}} A^2 \langle \hat{D}^2(t) \rangle_{\mathrm{cyc}} + S_{\mathrm{sn}} f_{\mathrm{BW}}, \tag{5.27}$$

in terms of the optodynamical measurement gain A defined in Eq. 2.72. Finally, any residual second harmonics, arising from counter-rotating terms in the product of displacements, are removed from the squared signal by 'cycle averaging' with a final low-pass filter with cutoff frequency around ω_i.

Dynamic range of exponential growth

All of the preceding derivations follow from the linearized spin-mechanical Hamiltonian in Eq. 5.7, and rely on the validity of the approximations made in deriving it. The primary assumptions to reach the linearized form were to assume sufficiently small-amplitude dynamics of all three modes—the cavity field, the atomic motion, and the spin precession.

The most restrictive constraint is typically the optical modulation depth. When the atomic dynamics modulate the cavity resonance frequency by a large fraction of κ, the

curvature of the cavity amplitude and phase profile, shown in Fig. 2.6, produces second-order harmonics of the spin and mechanical frequencies in the optical spectrum. In practice, these are observed above a modulation threshold of around $\langle \hat{D}^2 \rangle_{\mathrm{cyc}} < \kappa^2/4$, beyond which the first-order response saturates, and the squared-signal calibration becomes unreliable.

I also have assumed harmonic confinement for the axial atomic motion, which is only approximately true near the bottom of the optical trap potential. Anharmonicity of the ODT decreases the energy separation of each higher eigenstate of atomic motion, observed as additional lower-frequency peaks in the optical spectrum [20]. From investigations of coherent mechanical motion, resonantly driven by a modulated probe intensity, this spectral broadening and the associated dephasing become prominent for center-of-mass phonon occupation $n_m > 100$ with around $N_a = 3500$ atoms.

Finally, the Holstein-Primakoff approximation defined by Eqs. 3.10, used to linearize the spin equations of motion, is valid only for precession near the magnetic poles, when $\hat{n}_s = F - |\hat{F}_z| \ll F$. These constraints define a small dynamic range and the instability quickly drives the system out of the linear regime, resulting in saturation and slower growth. In practice, the interval of exponential growth observed in Fig. 5.4 is of order 100 μs or less, with insufficient structure to constrain a fit to the full theoretical model in Eq. 5.26.

Fit for instability gain

Considering a fit to an arbitrary polynomial, which could be compared to a Taylor expansion of the signal model, one can consider how many coefficients the data could reasonably constrain. For fits to short data traces where $G_+ t$ is small, one might expect to constrain no more than three parameters, related to the mean, slope, and curvature. The curvature of the observed signal is what most clearly distinguishes coherent amplification from linear diffusive growth, and by making a couple simplifying assumptions, a reasonable approximation for the observed gain can be recovered. As reported in Ref. [29], the estimates obtained during the instability also agree well with growth of the estimated final states after increasing coupling times.

Under strong coupling, the observed signal should be dominated by the amplified mode, with a negligible transient from the damped mode. Neglecting the damped mode, we can consider a simplified model for growth of an amplified mode with added noise

$$\dot{\hat{b}}_+ = G_+ \hat{b}_+ + \sqrt{B_T} \eta_+. \tag{5.28}$$

Here, B_T is the total diffusion rate from measurement backaction and thermal baths, also accounting for anomalous diffusion attributed to the spin bath coupling described by Eq. 5.6, which is all assumed to be driven by a total white-noise bath $\langle \eta_+^\dagger(t) \eta_+(t') \rangle = \delta(t - t')$.

Growth of the mean-squared signal is proportional to the occupation of this mode $\langle \hat{b}_+^\dagger \hat{b}_+ \rangle$, suggesting a simplified fit function

$$D_{\mathrm{fit}}(t) = \left(D_0 + \frac{B_T}{G_+} \right) e^{G_+ t} - \frac{B_T}{G_+}, \tag{5.29}$$

with free parameters D_0, G_+, and B_T, where D_0 captures the observed mean-squared displacement of the initial state.

This fit function can be tested against signals predicted by the full model described by Eq. 5.26, and accurately capture the instability gain for long-term dynamics, as shown in Fig. 5.7b. However, fits to the predicted signals within the linear region, below a threshold $\langle \hat{D}^2 \rangle_{\mathrm{cyc}} = 300$, are asymmetrically distorted by curvature from the neglected sinusoidal component, which might contribute to an apparent frequency shift in the published results [29].

5.5 Applications for instability

To develop intuition about the dynamics driven by the negative-mass instability and consider potential applications, here I consider the particular condition with the complex detuning parameter $D = 0$, which can be described by a simplified analytic model. This condition implies two constraints. First, the oscillator frequencies are tuned to realize the peak instability at $\delta' = 0$, accounting for the optodynamical spring shifts. Second, the net damping rate of each oscillator must be precisely matched, satisfying $\Gamma'_- = 0$, defining their common damping rate as $\Gamma = \Gamma'_i = \Gamma'_+$.

In this condition, the eigenfrequencies simplify to

$$\lambda_\pm = \frac{i}{2}\big(\pm K - \Gamma\big), \tag{5.30}$$

and the corresponding eigenmodes become equal parts spin and mechanics

$$\hat{b}_\pm = \frac{1}{\sqrt{2}}\big(\hat{a}_m \mp i\hat{a}_s^\dagger\big), \tag{5.31}$$

which evolve according to Eq. 5.16, with one mode damped and the other amplified, if $\mathrm{Re}[K] > \Gamma$. The normal modes are summarized by the eigenvector matrix E, with $\theta = \pi/2$ and relative phase $\phi = \pi/2$

$$\mathrm{E} = \frac{1}{\sqrt{2}}\begin{pmatrix} i & -i \\ 1 & 1 \end{pmatrix}. \tag{5.32}$$

This transformation is unitary, with inverse $\mathrm{E}^{-1} = \mathrm{E}^\dagger$.

It is important to note that $\hat{b}_-$ is not a canonical bosonic operator. In fact, the commutator vanishes $[\hat{b}_\pm, \hat{b}_\pm^\dagger] = 0$ under these ideal conditions, realizing independent classical subspaces within the system. However, because each normal mode overlaps equally with the 'bright' mode defined by the optodynamical measurement, the coupled positive-/negative-mass system does not satisfy the requirements for quantum noise cancellation described in Sec. 5.1.

The occupations of these normal modes, corresponding to the diagonal elements of the normal-mode second-moment matrix C'_{ii}, evolve according to Eq. 4.22 as

$$\langle \hat{b}_\pm(t)^\dagger \hat{b}_\pm(t) \rangle = \langle \hat{b}_\pm^\dagger(0) \hat{b}_\pm(0) \rangle e^{(\pm\mathcal{G}-1)\Gamma t} \pm V_\pm \big(e^{(\pm\mathcal{G}-1)\Gamma t} - 1\big) \tag{5.33}$$
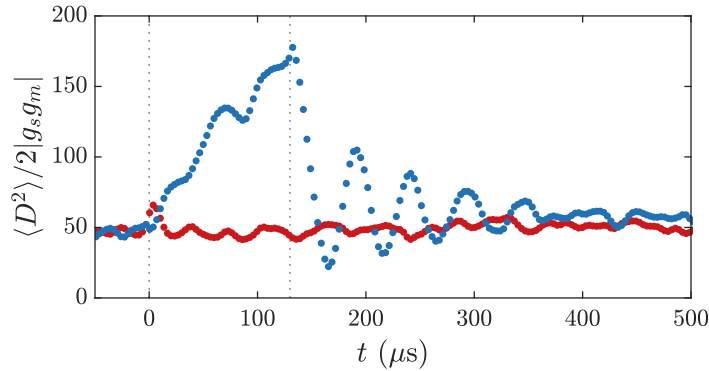
Figure 5.8: Observation of two-mode 'squeezing' of thermal noise, revealed by the correlated beat in the mean-squared signal. The oscillators were prepared in equilibrium with the measurement conditions ($\bar{n} = 2.6$, $\Delta = 2\pi \times 500$ kHz), weakly damping the spin to balance backaction diffusion. A 130 μs coupling pulse (with $\bar{n} = 4.3$ and $\Delta = 2\pi \times 1.5$ MHz) induced correlations between the atomic spin and motion (blue data). After coupling, the oscillator frequencies were ramped to $\omega_s = 2\pi \times 120$ kHz and $\omega_m = 2\pi \times 100$ kHz to observe the induced correlations. The mean-squared signal directly indicates the variance of a hybrid quadrature, with relative phase rotating at the difference frequency. It is observed to dip below the reference signal for the uncoupled thermal state (red data), indicating a reduction of the initial thermal variance.

defining the unitless instability gain $\mathcal{G} = \mathrm{Re}[K]/\Gamma$ and effective variance due to input noise

$$V_{\pm} = \frac{\nu_s + \nu_m + \mu_s + \mu_m + 1}{\mathcal{G} \mp 1}, \tag{5.34}$$

defined to be always positive for $\mathcal{G} > 1$.

Two-mode squeezing

This negative-mass instability, analogous to a non-degenerate parametric amplifier, could be used to produce two-mode squeezing of the damped normal mode, with fluctuations of the hybrid mode reduced below the independent zero-point motion for two ground-state oscillators. Although squeezing below the quantum zero-point level was experimentally obscured by added noise from the static gradient coupling, 'thermal' squeezing by the instability was observed, shown in Fig. 5.8, where the variance of a hybrid quadrature was reduced below its initial thermal state.

The quadratures of the damped hybrid mode are

$$\hat{X}_- = \frac{1}{\sqrt{2}} \left(\hat{b}_-^\dagger + \hat{b}_- \right) = \frac{1}{\sqrt{2}} \left(\hat{P}_s + \hat{X}_m \right) \tag{5.35}$$

$$\hat{P}_- = \frac{i}{\sqrt{2}} \left(\hat{b}_-^\dagger - \hat{b}_- \right) = \frac{1}{\sqrt{2}} \left(\hat{X}_s + \hat{P}_m \right) \tag{5.36}$$

with variances

$$\langle \Delta \hat{X}_-^2(t) \rangle = \langle \hat{b}_-^\dagger(t)\hat{b}_-(t) \rangle + \langle \mathrm{Re}[\hat{b}_-^2(t)] \rangle \tag{5.37}$$

$$\langle \Delta \hat{P}_-^2(t) \rangle = \langle \hat{b}_-^\dagger(t)\hat{b}_-(t) \rangle - \langle \mathrm{Re}[\hat{b}_-^2(t)] \rangle, \tag{5.38}$$

assuming thermal initial states. The 2nd-order coherence $\hat{b}_-^2(t)$ oscillates rapidly, driven by correlated backaction noise

$$\langle \hat{b}_-^2(t) \rangle = \frac{\Gamma}{2} \frac{2\sqrt{\mu_s \mu_m} - i(\mu_s - \mu_m)}{\bar{\omega} + \lambda_-} \left(e^{2i\bar{\omega}t} - e^{-2i\lambda_- t} \right), \tag{5.39}$$

and can be neglected under the RWA for $\bar{\omega} \gg \Gamma$. Therefore the variance of both quadratures of the damped mode are approximately equal, representing an effective thermal state with an occupation that evolves according to Eq. 5.33 as

$$\langle \Delta \hat{X}_-^2(t) \rangle \approx \langle \Delta \hat{P}_-^2(t) \rangle \approx \left(\langle \hat{b}_-^\dagger(0)\hat{b}_-(0) \rangle - V_- \right) e^{-(\mathcal{G}+1)\Gamma t} + V_-. \tag{5.40}$$

At long times, after decay of the initial transient, this solution indicates saturation to a minimum equilibrium variance V_- defined by as Eq. 5.34

$$V_- = \frac{\nu_s + \nu_m + \mu_s + \mu_m + 1}{\mathcal{G} + 1}, \tag{5.41}$$

which reflects a two-mode squeezed state if the unitless gain parameter exceeds the total bath and backaction thermal occupation $\mathcal{G} > \nu_s + \nu_m + \mu_s + \mu_m + 1$.

Comparison to numerical solutions

This approximate solution can be compared against numerical results for evolution of the two-mode covariance matrix $\mathrm{C}(t)$, calculated from the full linear system defined by Eqs. 2.23 according to Eq. 2.36. The squeezing depth can be quantified by how far the minimum variance of a hybrid quadrature is reduced below the zero-point motion of the two-mode ground state. A general hybrid quadrature of the spin and motion at relative phase ϕ can be defined as

$$\hat{Q}(\phi_q) = \frac{1}{\sqrt{2}} \left(\hat{a}_s^\dagger + \hat{a}_s + \hat{a}_m^\dagger e^{i\phi_q} + \hat{a}_m e^{-i\phi_q} \right), \tag{5.42}$$

which has unity variance for the two-mode ground state. The variance of this general hybrid quadrature can be written as

$$\Delta \hat{Q}^2(\phi_q) = n_m + n_s + 2n_c \cos(\phi_q - \phi_c) + 1, \tag{5.43}$$

in terms of the mean oscillator occupations $n_m = \langle \hat{a}_m^\dagger \hat{a}_m \rangle$ and $n_s = \langle \hat{a}_s^\dagger \hat{a}_s \rangle$ and the correlated occupation and phase defined by $n_c e^{i\phi_c} = \langle \hat{a}_s \hat{a}_m \rangle$. The squeezing depth therefore is determined by the minimum variance at quadrature angle $\phi_q = \phi_c + \pi$, given in dB by
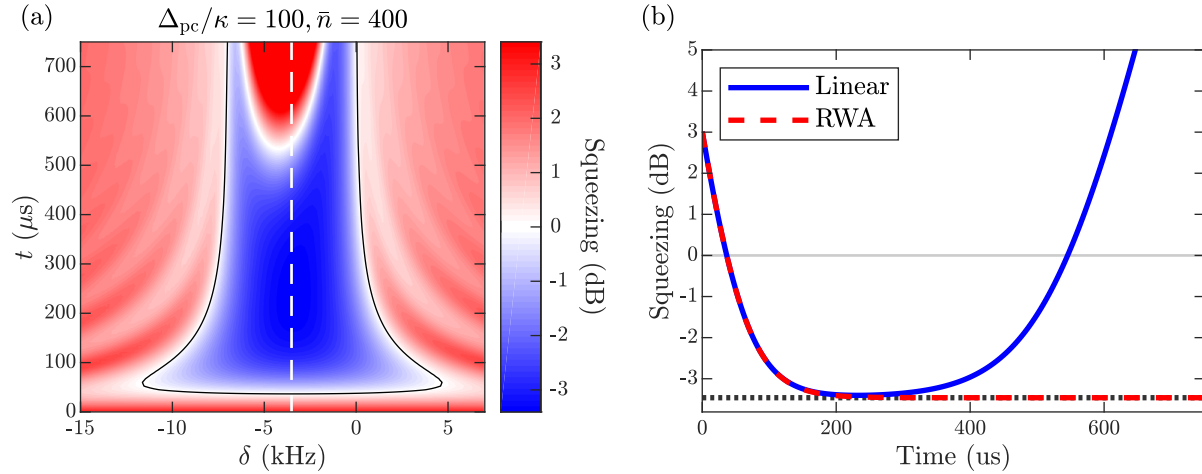
$$S = 10 \log_{10}(n_s + n_m - 2n_c + 1), \tag{5.44}$$

Figure 5.9: (a) Transient two-mode squeezing trajectories as a function of oscillator detuning δ, numerically calculated from the linearized equations of motion. Within the strong-coupling region, fluctuations of the damped quadratures are reduced below the ground-state variance, with the onset of squeezing accurately predicted by the RWA theory (black contour). At long times, the growing counter-rotating term neglected under the RWA,induces a Block-Siegert frequency shift, which spoils the resonance condition and mixes the amplified quadrature into the measurement, overwhelming any observation of squeezing. (b) Trajectory of squeezing for $\delta' = 0$ (dashed line in a), demonstrating the initial agreement between the RWA theory (red dashed line) and the numerical solution (blue line). The maximum squeezing depth is limited by the steady-state normal-mode variance V_- (black dotted line).

which is negative for a squeezed state, reflecting an inseparable entangled state of the oscillators.

Calculating this statistic for evolution of the two-mode state reveals the transient generation of squeezing for various system parameters. Fig. 5.9a shows this evolution as a function of oscillator detuning, for a typical Larmor frequency $\omega_{\rm s} = 2\pi \times 150$ kHz and optodynamical coupling strengths $g_{\rm s} = g_{\rm m} = 2\pi \times 20$ kHz, with no static gradient $g_{\rm sm} = 0$. For all predicted results in this section, the cavity drive is far detuned by $\Delta = 100\,\kappa$, with a large intracavity intensity $\bar{n} = 400$ to produce a typical cavity-mediated coherent interaction strength k_{ms}, while suppressing incoherent backaction from photon shot noise. The oscillators are assumed to begin in equilibrium with their baths at a thermal occupation $\nu_s = \nu_m = 0.5$, demonstrating robustness of the squeezing in the presence of finite temperature thermal baths. Finally, the intrinsic damping rates are chosen to be equal, with $\Gamma'_+ = 2\pi \times 1$ kHz and $\Gamma'_- = 0$.

Bloch-Siegert shift from counter-rotating terms

Numerical time-evolution of the two-mode squeezing depth is shown in Fig. 5.9a, and initially behaves like the RWA solution, exponentially approaching a steady-state variance. The

minimum variance is reduced below zero-point motion within the strong-coupling region, where $|\delta'| < |\operatorname{Re}[K]|$. The maximum squeezing depth is achieved at the optimal detuning $\delta' = 0$, shown in Fig. 5.9b. The numerical solution initially agrees with the RWA theory prediction from Eq. 5.40. However, at later times, the squeezing predicted by numerical solutions blows up, deviating from the steady-state squeezing predicted under the RWA due to the neglected counter-rotating term.

In the analogy to a parametric amplifier, this negative-mass instability is self-driven, with each oscillator appearing like a $2\omega_i$ parametric drive to the other in the rotating frame of Eq. 4.5. These counter-rotating terms grow exponentially with the amplified mode, leading to a break-down of the RWA. The first order correction from this off-resonant drive is a renormalization of the oscillator frequencies, described by the Bloch-Siegert shift [104–106] of oscillator i induced by the motion of oscillator j

$$\delta_{\mathrm{BS,i}} \approx \frac{\mathcal{G}^2\Gamma^2 n_j}{16\omega_j}. \tag{5.45}$$

When the amplitude of the counter-rotating term is sufficient to induce a shift on the order of the instability width $\delta_{\mathrm{BS}} \gtrsim \mathcal{G}\Gamma$, the ideal detuning condition $D = 0$ is broken. The modified normal modes are no longer orthogonal, and a component of the amplified normal mode is mixed into the measurement considered above.

Increasing the instability gain $\mathcal{G}$ drives the system more quickly toward a squeezed state with reduced variance, as predicted by the RWA theory in Eq. 5.41. However, the increased gain also consequently drives faster growth of the counter-rotating terms, which then more rapidly perturbs the RWA conditions. This correction limits the maximum achievable squeezing for oscillator frequencies ω_i, but is suppressed as $1/\omega_i$ for higher-frequency oscillators.

Quantum-limited amplification

Glauber proposed the use of a bath of negative-mass modes as a quantum-limited amplifier [100]. The coupled positive-/negative-mass system considered in this chapter represents the simplest version of this model, with a single negative-mass 'bath' driving amplification of the positive-mass mode. Furthermore, the state of this isolated negative-mass 'bath' can be measured, providing additional information about the amplified mode.

At long times, the amplification is naturally associated with the amplified normal mode $\hat{b}_+ = (\hat{a}_m - i\hat{a}_s^\dagger)/\sqrt{2}$, which evolves according to Eq. 5.16. Assuming the negative-mass mode begins in its ground state, with $\langle \hat{a}_s^\dagger \hat{a}_s \rangle = 0$, evolution of the amplified normal mode describes amplification of the initial coherence of the positive-mass oscillator

$$\langle \hat{b}_+(t) \rangle = \frac{1}{\sqrt{2}} e^{(K-\Gamma)t/2} \langle \hat{a}_m(0) \rangle. \tag{5.46}$$

Measurement of the final state provides an estimate of this initial coherence, amplified by an instantaneous amplification gain

$$\mathfrak{G}(t) = \frac{1}{2}e^{(\text{Re}[K]-\Gamma)t} = \frac{1}{2}e^{(\mathcal{G}-1)\Gamma t}, \tag{5.47}$$

defined as the growth of the square magnitude of the initial state coherent amplitude after amplification for time t.

The amplitude of the initial mechanical state has an equal projection on both the amplified and damped normal modes, resulting in the initial attenuation factor of $1/2$ in Eq. 5.47. An estimator for the initial signal amplitude from later measurement of the amplified normal mode can be defined as

$$\breve{\beta}(t) = \sqrt{2}e^{-(K-\Gamma)t/2}\hat{b}_+(t), \tag{5.48}$$

satisfying $\langle\breve{\beta}(t)\rangle = \langle\hat{a}_m(0)\rangle$.

With sufficient gain, the initial state can be amplified well above measurement noise or zero-point-motion of the final state, such that measurement imprecision of the amplified state is negligible. The amplifier performance can then be described simply in terms of the noise added *during* the amplification process, quantified as the equivalent thermal occupation of the input state necessary to reproduce the same output distribution from an ideal, noiseless amplifier. This added input noise metric corresponds to the increase in variance of the input signal estimator $\breve{\beta}(t)$.

Assuming the oscillators start in uncorrelated states, a necessary condition for phase-insensitive amplification [107], growth of the estimator variance can be calculated from Eq. 5.33, giving

$$\langle|\Delta\breve{\beta}(t)|^2\rangle = \langle\breve{\beta}^\dagger(t)\breve{\beta}(t) + \breve{\beta}(t)\,\breve{\beta}^\dagger(t)\rangle/2 - \langle\breve{\beta}(t)\rangle\langle\breve{\beta}^\dagger(t)\rangle$$

$$= 2|\Delta\hat{b}_+(0)|^2 + 2V_+\left(1 - e^{-(\mathcal{G}-1)\Gamma t}\right) \tag{5.49}$$

$$= |\Delta\hat{a}_1(0)|^2 + |\Delta\hat{a}_2(0)|^2 + 2V_+\left(1 - e^{-(\mathcal{G}-1)\Gamma t}\right), \tag{5.50}$$

where the initial variance of each oscillator is the sum of its thermal occupation and zero-point motion. The amplifier's added noise occupation, plotted in Fig. 5.10, saturates to

$$V_+ = \frac{\nu_s + \nu_m + \mu_s + \mu_m + 1}{\mathcal{G} - 1}, \tag{5.51}$$

which can be made arbitrarily small by increasing the gain to backaction ratio through coupling with far off-resonance probe detuning $|\Delta| \gg \kappa$, as illustrated in Fig. 2.7.

If the negative-mass mode driving the amplification starts in the ground state, with $|\Delta\hat{a}_s(0)|^2 = 1/2$, then the additional zero-point motion it contributes in Eq. 5.50 realizes the high-gain limit $\mathfrak{G} \to \infty$ for the minimum added noise of a quantum-limited amplifier in [107]

$$n_{\text{SQL}} = \frac{1}{2}\left(1 - \frac{1}{\mathfrak{G}^2}\right). \tag{5.52}$$
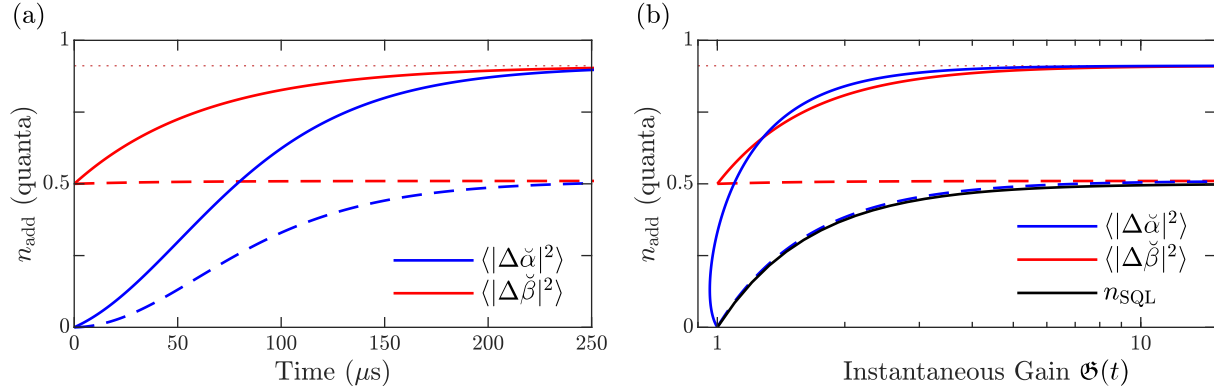
Figure 5.10: Added noise occupation from negative-mass amplification. (a) Variance added to each quadrature estimate, in units of effective noise quanta at the amplifier input, as a function of amplification time. Both oscillator's are assumed to begin in their ground state, with zero-temperature baths and common damping rate $\Gamma = 2\pi \times 1$ kHz. They are optodynamically coupled with probe detuning $\Delta = 100\,\kappa$ and intensity $\bar{n} = 400$. (b) Added noise vs. instantaneous gain for the same calculated results. The final mechanical state typically provides the best amplified estimate $\breve{\alpha}$ for its initial coherence, approaching the amplifier SQL (black line) in the absence of bath dissipation $\Gamma = 0$ (dashed lines), limited only by diffusion from residual backaction during the finite amplification time $1/\operatorname{Re}[K]$.

After amplification both oscillators contain information about the input state $\hat{a}_m(0)$, however there is no advantage to measuring both of them, beyond averaging down measurement noise. Initially, the amplified normal mode contains only half of the input signal, and the other half is uncorrelated zero-point motion of the 'idler' state. This implies that at short times, before the initial transient has decayed, a direct measurement of the signal mode will give a better estimate.

The amplitude of oscillator 2 evolves as

$$\langle \hat{a}_m(t) \rangle = \cosh\left(Kt/2\right) e^{-\Gamma t/2} \langle \hat{a}_m(0) \rangle \tag{5.53}$$

therefore the "instantaneous" amplifier gain at time t is $\mathfrak{G}(t) = \cosh\left(Kt/2\right) e^{-\Gamma t/2}$, and an alternative estimator can be defined

$$\breve{\alpha} = e^{\Gamma t/2} \cosh^{-1}\left(Kt/2\right) \hat{a}_m(t), \tag{5.54}$$

treating the negative-mass oscillator as an 'idler' mode, which drives amplification but is otherwise discarded.

The evolution of this estimator's variance can be calculated numerically, displayed in Fig. 5.10. Before amplification, the 'signal' state can be measured without added noise, and then the variance grows with the gain, saturating to the same added noise limit as Eq. 5.50. As shown in Fig. 5.10b, the added noise for this estimator approaches the quantum-mechanical limit defined by Eq. 5.52 after any duration of amplification, in the coherent optodynamical limit with $\mathcal{G}$ sufficiently large such that $V_+ \to 0$.

5.6 Open questions and future directions

The theoretical analysis above suggests many potential future applications for the negative-mass instability, such as attempting to generate and observe hybrid two-mode squeezing between the atomic motion and spin, or characterizing the performance as an amplifier by measuring correlations between the initial and final states. In our present system, the biggest obstacle to reaching quantum limits in these applications is the 'static' optical coupling between the spin and motion of individual atoms. This limitation could be avoided by coupling positive- and negative-mass modes of spatially separated atomic ensembles, such that only dynamics of the cavity field mediate long-range collective interactions.

This configuration could be realized using the spin of one ensemble and motion of a second ensemble, as long as the remaining motional and spin degrees of freedom can be detuned far off-resonance. The mechanical frequencies can be distinguished by loading ensembles into two sites of the hybrid optical lattice, as demonstrated in Chap. 4. However, the Larmor frequencies of the two ensembles must also be resolved, for instance by applying a magnetic field gradient along the cavity axis.

Provided spin oscillators could be resolved, the instability could also be demonstrated purely between two collective spin degrees of freedom, as proposed in Ref. [103]. The spin commutation also introduces a non-linearity into the equations of motion, as described in Sec. 3.1, which would result in a self-limiting instability, where energy exchange ceases with both spin ensembles on the equator. These non-linear coupled equations of motion might also facilitate generation of non-Gaussian entangled states between two macroscopic spin ensembles.

Multiple non-degenerate spin oscillators

To resolve the Larmor frequencies of neighboring lattice sites by Δf requires creating a gradient of the transverse field component along the cavity axis with strength

$$\left| \frac{\partial B_z}{\partial x} \right| = \frac{2k_p \Delta f}{|\gamma|}. \tag{5.55}$$

Such a gradient can be produced at the location of the atomic cloud by applying co-propagating currents through the atom chip waveguide wires, as illustrated in Fig. 5.11a. However, these wires also produce a large curvature of the field across the approximately 3 μm width of the cloud, shown in Fig. 5.11b-c. Because of the large aspect ratio of the trapped ensemble in the standing-wave ODT, this curvature induces a significant variation of the Larmor frequency across the width of the cloud, inducing rapid dephasing of the collective spin, as observed in Fig. 5.12. Unfortunately, the atom chip does not have sufficient wires to provide enough degrees of freedom to cancel out these higher-order spatial variations.

(a)

(b)

(c)
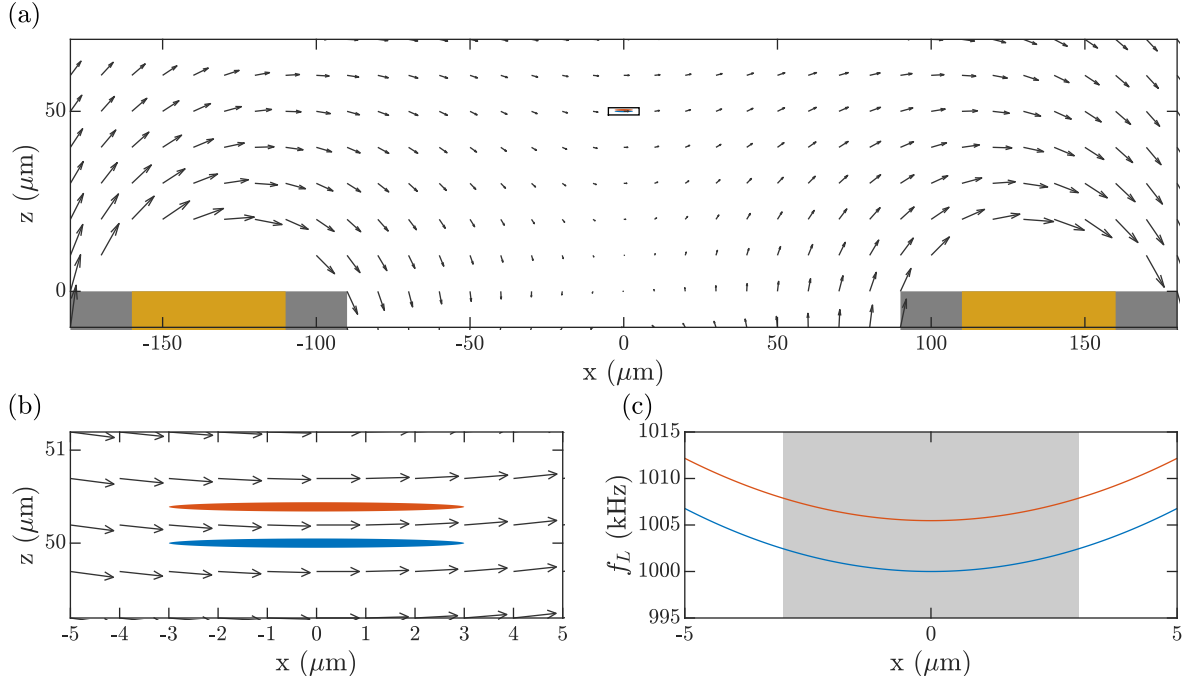
Figure 5.11: Magnetic field gradient, produced by parallel currents in both waveguide wires, for resolving the Larmor precession frequency of neighboring trap sites. (a) Magnetic fields produced by equal parallel currents in both chip waveguide wires. This model assumes the total current flows through the center of the wire, however the spatial size of the wire is significant on the scale of chip and cavity geometry, and must be considered to make more accurate predictions. (b) Expanded view of region of interest (box in a), marking the approximate RMS size of two atomic clouds. (c) Variation of Larmor frequency across the radial dimension of the cloud (ensemble RMS width indicated by shaded region). For a gradient strong enough to achieve a separation of ~ 6 kHz between neighboring sites, the variation of Larmor frequency from the associated field curvature induces rapid dephasing.

(a)

(b)
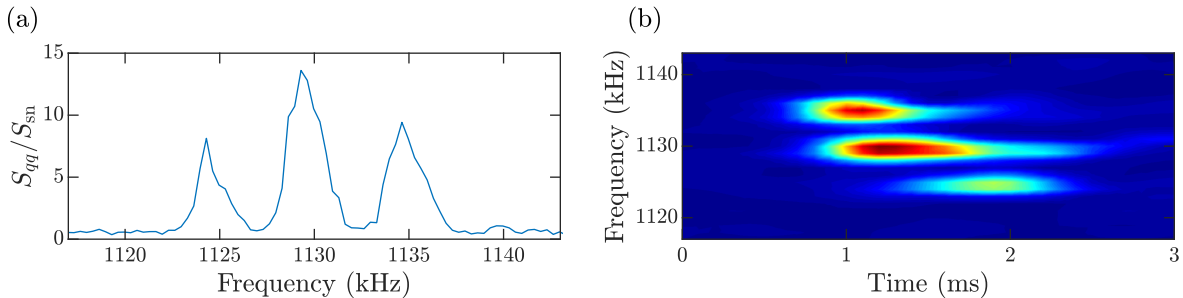
Figure 5.12: Observed (a) phase-quadrature PSD S_{qq} and (b) spectrogram of resolved spin oscillators, loaded in 3 subsequent sites, for a magnetic field configuration similar to Fig. 5.11. These spectra are averaged over 18 repetitions, however all 3 peaks can be observed simultaneously on single iterations.

Chapter 6

Multi-mode state estimation with matched filters

This chapter considers optodynamical state estimation using linear filters, a technique which has been applied in the publications [29, 35] discussed in Chaps. 4 and 5. Here I develop a detailed theoretical model, which facilitates calculation of the systematic effects of noise captured in the optodynamical measurements and describe the derivation of optimal filters. This work provides the context and formalism for a more thorough analysis in our forthcoming manuscript [101].

The state of an oscillator evolving under known dynamics can be estimated from continuous measurement of its position. This becomes clear in a phase space representation, where the oscillator's initial coordinates rotate in time between quadratures, so that a measurement of its position after a quarter cycle yields information about its initial momentum. The reliability of an estimate from such an extended observation, therefore, relies on the oscillator's state remaining undisturbed, subject only to deterministic coherent dynamics. However, quantum mechanics necessarily prevents the oscillator's state from being perfectly reconstructed, because the measurement backaction implied by the Heisenberg uncertainty principle introduces diffusion of the oscillator's state during measurement. This suggests a trade-off between increasing sensitivity with a stronger measurement and reducing measurement backaction, resulting in a standard quantum limit for the minimum uncertainty attainable from a phase-insensitive measurement. Furthermore, diffusion driven by any intrinsic coupling between the oscillator and its environment will contribute additional uncertainty to the estimate.

In this chapter I specifically focus on retrodiction of the initial state of multiple oscillators from optodynamical measurement of their subsequent evolution. Similar matched filtering techniques have been previously demonstrated with optomechanical systems [63, 64] and are related to the concept of temporal mode matching [108–110], which has also been employed in measuring quantum states of microwave fields [111]. Related concepts of optimal state prediction and retrodiction in optomechanical systems from a Bayesian formalism have also

been considered [112–114] and demonstrated [115].

I start in Sec. 6.1 with a simplified model for linear parameter estimation and distinguish between estimators that arise from optimizing different error functions. Then in Sec. 6.2, I develop a model for estimates from a general linear filter applied to optodynamical measurements, and calculate the statistics of state estimates obtained for one class of filters. In Sec. 6.3, I return to the question of optimal filters and apply the generalized least-squares (GLS) method to derive optimal filters for optodynamical estimation. Sec. 6.4 describes numerical simulations of optodynamical signals used to verify the state estimation, and then Sec. 6.5 shows results from application to well-calibrated experimental signals. Finally, in Sec. 6.6 I outline additional experimental corrections that were performed to obtain estimates in Ref. [29].

6.1   Linear parameter estimation

The result of a single iteration of a typical experiment is a recorded trace of the detected optical phase or amplitude modulation, reflecting the coherent evolution of the state of each oscillator, in addition to thermal noise, measurement backaction, and detector shot noise. Although the noise appearing in the signal arises from quantum mechanical fluctuations, the amplified and digitized signal is ultimately classical and the subsequent signal analysis can be performed following standard optimization techniques.

Consider first a simplified toy model for continuous position measurement of a noise-less, damped harmonic oscillator, with frequency ω_1 and damping rate Γ_1. The oscillator's initial state is specified by a vector $\boldsymbol{Q} = (X_1(0), P_1(0))^\mathsf{T}$ of unknown quadratures and undergoes purely coherent evolution, neglecting for now any thermal bath or measurement backaction. Performing a measurement perturbed only by additive, broad-band measurement noise $\xi(t)$, the observed signal $S(t)$ can be modeled as

$$S(t) = \boldsymbol{Q}^\mathsf{T}\boldsymbol{r}(t) + \sqrt{P_\mathrm{SN}}\xi(t), \tag{6.1}$$

defining a vector of quadrature response functions

$$\boldsymbol{r}(t) = e^{-\Gamma_1 t/2} \begin{pmatrix} \cos\omega_1 t \\ \sin\omega_1 t \end{pmatrix}. \tag{6.2}$$

A sample trace from such a signal is displayed in Fig. 6.1a.

A general set of linear estimators, or filters, applied to this signal over the interval $t \in [0, T]$ can be defined as

$$\breve{Q}_i = \int_0^T dt\, S(t)m_i(t), \tag{6.3}$$

where $m_i(t)$ is the weighted contribution of the signal at time t to the filter result. These temporal functions represent vectors in the infinite-dimensional space of the continuous signal
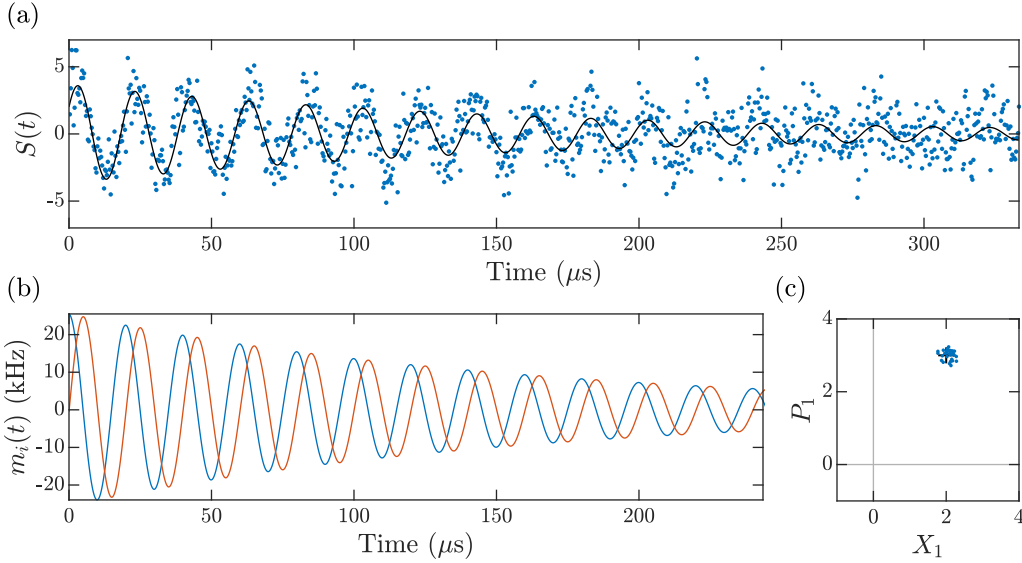
Figure 6.1: Parameter estimation from (a) a signal with broadband measurement noise only. (b) OLS filter functions for retrodiction of both quadratures of the initial oscillator state. (c) Phase space distribution of filter results (blue dots), compared to the initial simulation value (black cross).

$S(t)$, and the filter outputs represent the projection of the observed signal along these vectors. For convenience, I will interchangeably refer to these temporal mode functions as the filter functions from here on.

Ordinary Least Squares

Since the signal described in Eq. 6.1 is linear in the unknown initial amplitudes X_0 and P_0, estimates of these parameters can be obtained by linear least-squares regression. Identical to linear curve fitting, this optimization minimizes the square of residuals between the measured signal $S(t)$ and predicted signal $\breve{S}(t) = \sum_i \breve{Q}_i r_i(t)$

$$\Phi_{\mathrm{LS}} = \int_0^T dt \left(S(t) - \sum_i \breve{Q}_i r_i(t) \right)^2 \tag{6.4}$$

This error function is minimized by the ordinary least-squares (OLS) estimator defined by filter functions

$$m_i(t) = \sum_j [\mathrm{R}^{-1}]_{ij} r_j(t), \tag{6.5}$$

which are normalized by the response function overlap matrix $\mathrm{R}_{ij} = \int_0^T dt\, r_i(t) r_j(t)$.

Example filter functions and simulated results for this toy model are displayed in Fig. 6.1b-c. This estimator represents a projection of the infinite dimensional signal $S(t)$ onto a finite basis of vectors formed by the quadrature response functions $r_i(t)$. The quadrature estimates are obtained after correcting for any non-orthogonality between the basis vectors, captured by the overlap matrix R.

It is easily verified that these estimators are unbiased, satisfying

$$\langle \breve{Q}_i \rangle = \langle Q_i \rangle. \tag{6.6}$$

Further, in the considered case of additive white noise, with $\langle \xi(t) \rangle = 0$ and $\langle \xi(t)\xi(t') \rangle = \delta(t - t')$, the Gauss-Markov theorem proves that this estimator is the minimum-variance unbiased estimator for the initial quadratures [116].

Optimal how?

Any claim of optimality begs the question, optimal with respect to what criteria? Optimizing different figures of merit can yield distinct results, and each can only be proven optimal with respect to a well-defined objective. The first significant choice we have made is to restrict consideration to the set of linear filters, defined by Eq. 6.3.

Next, in the linear regression analysis above, we chose to minimize the variance of residuals between *observations* $S(t)$ and the *predictions* $\breve{S}(t)$ made by the parametrized model. This choice of optimization function results in the OLS estimators defined by Eq. 6.5, only providing a minimum-variance, unbiased estimator of the unknown parameters Q_i when the Gauss-Markov theorem holds, which requires zero-mean, homoscedastic, temporally-uncorrelated noise. These conditions are satisfied for the case of additive white noise, but the optodynamical signals that will be considered also contain narrow-band noise from oscillator diffusion, which requires application of the GLS method, discussed in Sec. 6.3.

Minimum mean-square error

However, already in the simple example considered here, a different choice of error function yields different results, which are more optimal under the chosen criteria. Given a model for the measured signal, parameterized by unknown values Q_i, we can derive a set of filter functions which minimize the mean-square error (MSE) between an ensemble of *estimates* $\breve{Q}_i$ and the underlying *parameters* Q_i.

$$\Phi_{\mathrm{MSE}} = \left\langle \sum_i (Q_i - \breve{Q}_i)^2 \right\rangle. \tag{6.7}$$

Expressing this error function as a functional of the set of filter functions $\{m_i(t)\}$

$$\Phi_{\mathrm{MSE}}[\{m_i(t)\}] = \left\langle \sum_i \left(Q_i - \int_0^T dt S(t) m_i(t)\right)^2 \right\rangle, \tag{6.8}$$

it can be minimized through a variational calculation by setting the functional derivative to zero

$$\frac{\partial \Phi_{\text{MSE}}[\{m_i(t)\}]}{\partial m_i(t)} = \frac{\partial \Phi_{\text{MSE}}[\{m_i(t) + \epsilon \delta_i(t)\}]}{\partial \epsilon} \bigg|_{\epsilon=0} = 0$$

$$= \int_0^T dt \delta_i(t) \left\langle S(t) \int_0^T dt' S(t') m_i(t') - Q_i \right\rangle = 0. \tag{6.9}$$

For the optimal filter $m_i(t)$, therefore, the integrand must be identically zero for any arbitrary functional deviation $\delta_i(t)$, such that the optimal filter $m_i(t)$ for the parameter Q_i is implicitly defined by the integral equation

$$\int_0^T dt' \, \langle S(t)S(t') \rangle \, m_i(t') = \langle Q_i S(t) \rangle . \tag{6.10}$$

This is the defining equation for a minimum MSE estimator [117], and solving it requires prior knowledge of the distribution of the unknown parameters, in addition to a model for the measured signal $S(t)$.

Estimator bias and shrinkage

We can gain some intuition by considering the toy model defined in Eq. 6.1, further simplifying to independent estimation of a single quadrature (for instance if we know *a priori* that $P_1(0) = 0$). The filter definition then reduces to

$$m_1(t) = \frac{\langle X_1^2 \rangle}{P_{\text{SN}}} \left[1 - \int_0^T dt' r_1(t') m_1(t') \right] r_1(t), \tag{6.11}$$

which implies that the optimal filter for X_1 is proportional to the quadrature response function. The filter can be expressed as

$$m_1(t) = \frac{\alpha}{R_{11}} r_1(t) \tag{6.12}$$

in terms of normalization $R_{11} = \int_0^T dt r_1(t)^2$ and unit-less proportionality constant

$$\alpha = \frac{\text{SNR}}{\text{SNR} + 1}, \tag{6.13}$$

which approaches unity for large values of the filtered signal-to-noise ratio $\text{SNR} = R_{11} \langle X_0^2 \rangle / P_{\text{SN}}$.

While this solution does realize the minimum estimator variance, it is biased for finite signal-to-noise ratio (SNR), with mean and 2nd moment

$$\langle \check{X}_1 \rangle = \alpha \langle X_1 \rangle \qquad \text{and} \qquad \langle \check{X}_1^2 \rangle = \alpha \langle X_1^2 \rangle, \tag{6.14}$$
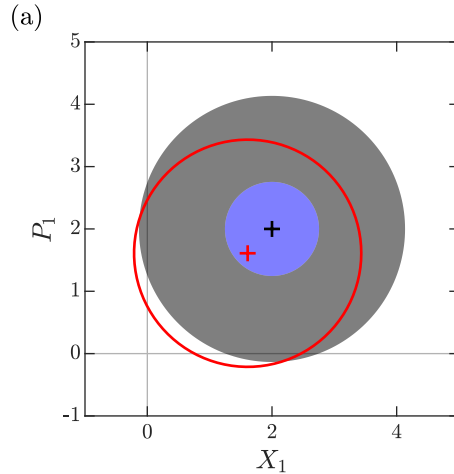
Figure 6.2: Simplified phase space illustration of estimator shrinkage. The minimum MSE estimator covariance (red circle) and mean (red cross) are biased away from the initial state mean (black cross) and covariance (blue disk), due to measurement noise. The optimal *unbiased* estimator realizes the minimum added variance (black annulus) while also preserving the mean.

respectively.

The noise induces diffusion of the distribution of the filter results $\breve{Q}_i$ from the initial distribution of Q_i, and the MSE optimization biases the estimate toward zero to minimize the average error introduced by the noise. This bias is commonly known as shrinkage, and is a typical consequence for minimum-variance estimators. This can be understood by rewriting the MSE error function as

$$\Phi_{\mathrm{MSE}} = \sum_i \left[\mathrm{var}(Q_i) + \mathrm{var}(\breve{Q}_i) - 2\,\mathrm{cov}(Q_i, \breve{Q}_i) + |\langle \breve{Q}_i \rangle - \langle Q_i \rangle|^2 \right], \qquad (6.15)$$

in terms of the variances and covariance of the initial distribution and estimates plus the bias, reflected in the final term. Considering estimates of a particular value X_1 sampled from the initial distribution, the conditional error reduces to

$$\Phi_{\mathrm{MSE}} = \langle \Delta \breve{X}_1^2 \rangle + |\langle \breve{X}_1 \rangle - \langle X_1 \rangle|^2. \qquad (6.16)$$

This expression indicates that the estimator can trade off added bias, penalized by the second term, for a greater reduction of variance in the first term. The error from the variance and bias for each value X_1 is minimized across the entire initial distribution, as illustrated in Fig. 6.2 for estimation of a state in 2-D phase space.

Given prior knowledge of the initial parameter distribution, this MSE estimator does guarantee the closest estimate of the sampled parameters Q_i from each individual iteration of the measurement. However, if one instead wants to obtain estimates of the initial distribution itself, from an ensemble of identical measurements, then a more suitable estimator should

be derived without assuming *a priori* knowledge of the distribution. Considering a uniform *a priori* distribution of the parameter X_1 in this simplified 1-D model, then the *a priori* variance is infinite $\langle \Delta X_1^2 \rangle \to \infty$, in which limit the MSE filter defined by Eq. 6.12 coincides with the OLS estimator in Eq. 6.5.

6.2 Optodynamical signal filtering

The noise added to the optodynamical ringdown signal, however, is not temporally uncorrelated. Diffusion of the oscillators' states, driven by thermal noise and measurement backaction, introduces temporal correlations shaped by the oscillator response functions. By consequence, the optimal filters calculated from Eq. 6.10 are no longer proportional to the response functions $r_i(t)$. Similarly, the OLS filters defined in Eq. 6.5, though still unbiased, no longer satisfy the Gauss-Markov theorem, indicating that a naive curve fitting approach is not optimal for optodynamical state estimation. In this section, I set aside questions of optimality and consider retrodiction of the states of N oscillators using an arbitrary set of linear filters applied to the detected optodynamical signal, evaluating the noise added to the estimates from each signal noise component.

Starting with the balanced photodetector signal described by Eq. 2.66 and specializing to the homodyne configuration, with LO frequency offset $\omega_0 = 0$ and phase $\phi_L = 0$, the recorded optical signal is described by

$$P_{\text{det}}(t) = \sqrt{\frac{8\epsilon \bar{n} S_{\text{sn}}}{\kappa}} \, \text{Re}[\hat{d}(t)] + \sqrt{S_{\text{sn}}} \xi_{sn}(t). \tag{6.17}$$

For optodynamical measurement on cavity resonance $\Delta = 0$, the measurement operator $\hat{d}$ defined in Eq. 2.57 is Hermitian. Further assuming the unresolved-sideband limit $\kappa \gg \omega_i$, this operator is approximately equal to the sum of oscillator displacements weighted by their individual optodynamical coupling strengths

$$\hat{d} \approx \sqrt{2} \sum_i g_i \hat{X}_i, \tag{6.18}$$

which is equal to the total optodynamical frequency shift of the cavity resonance implied by the Hamiltonian in Eq. 2.18.

The recorded signal can be scaled into units of the inferred cavity frequency shift, defining

$$\hat{S}(t) = \sqrt{2} \sum_i g_i \hat{X}_i(t) + \sqrt{P_{\text{SN}}} \hat{\xi}_{\text{sn}}(t). \tag{6.19}$$

with effective shot noise spectral density $P_{\text{SN}} = \kappa/8\epsilon \bar{n}$. An identical expression can be obtained for heterodyne detection by considering only the demodulated phase quadrature, with the usual detection efficiency penalty $\epsilon \to \epsilon/2$.

Oscillator evolution

The oscillator equations of motion from Eqs. 2.46a, after eliminating the cavity field, can be specialized to the measurement condition with an on-resonance probe $\Delta = 0$, summarized as

$$\frac{\partial}{\partial t} \begin{pmatrix} \hat{X}_i \\ \hat{P}_i \end{pmatrix} = \mathrm{A}_i \begin{pmatrix} \hat{X}_i \\ \hat{P}_i \end{pmatrix} + \hat{\boldsymbol{v}}_i. \tag{6.20}$$

in terms of dynamical matrix and input noise vector

$$\mathrm{A}_i = \begin{pmatrix} -\frac{\Gamma_i}{2} & \epsilon_i \omega_i \\ -\epsilon_i \omega_i & -\frac{\Gamma_i}{2} \end{pmatrix} \qquad \text{and} \qquad \hat{\boldsymbol{v}}_i = \begin{pmatrix} \sqrt{\Gamma_i} \hat{\eta}_i^{\mathrm{AM}} \\ \sqrt{\Gamma_i} \hat{\eta}_i^{\mathrm{PM}} - \sqrt{2B_i} \hat{\xi}^{\mathrm{AM}} \end{pmatrix}, \tag{6.21}$$

respectively. Here I have already assumed the unresolved sideband limit, by approximating the cavity amplitude fluctuations by the delta-correlated vacuum input fluctuations $\hat{\xi}_{\Delta=0}^{\mathrm{AM}} \approx \hat{\xi}^{\mathrm{AM}}$.

The matrix equation for each oscillator can be independently solved, in terms of the initial quadrature operators $\hat{\boldsymbol{Q}}_i = (\hat{X}_i(0), \hat{P}_i(0))^{\mathsf{T}}$ and accumulated diffusion

$$\hat{X}_i(t) = \hat{\boldsymbol{Q}}_i^{\mathsf{T}} \boldsymbol{r}_i(t) + \int_0^\infty d\tau \, \hat{\boldsymbol{v}}_i^{\mathsf{T}}(\tau) \boldsymbol{r}_i(t - \tau), \tag{6.22}$$

defining the vector of quadrature response functions

$$\boldsymbol{r}_i(t) = e^{-\Gamma_i t/2} \begin{pmatrix} \cos \epsilon_i \omega_i t \\ \sin \epsilon_i \omega_i t \end{pmatrix} \Theta(t) \tag{6.23}$$

using the Heaviside step function $\Theta(t)$.

The oscillator's average position evolves coherently, unperturbed by the zero-mean noise, and is simply described by

$$\langle \hat{X}_i(t) \rangle = \langle \hat{\boldsymbol{Q}}_i^{\mathsf{T}} \boldsymbol{r}_i(t) \rangle. \tag{6.24}$$

If the response functions $\boldsymbol{r}_i(t)$ are fully deterministic, with stable values of the oscillator frequency and damping, then they can be pulled out of the expectation value, as done below. However, in Sec. 6.6 I consider the effect of shot-to-shot fluctuations of the oscillator frequencies, which introduce additional stochastic fluctuations to the response functions.

It will also be useful to calculate the symmetrized two-time correlation function, which, assuming $\omega_i \gg \Gamma_i$, is approximately

$$\langle \hat{X}_i(t) \hat{X}_j(t') \rangle_s \approx \langle \boldsymbol{r}_i^{\mathsf{T}}(t) \hat{\boldsymbol{Q}}_i \hat{\boldsymbol{Q}}_j^{\mathsf{T}} \boldsymbol{r}_j(t') \rangle_s + \delta_{ij} \Gamma_i \left(\nu_i + \frac{1}{2} \right) R_{ii}(t, t') + \frac{B_{ij}}{2} R_{ij}(t, t') \tag{6.25}$$

defining correlated backaction diffusion rate $B_{ij} = \sqrt{B_i B_j} = 4\bar{n} g_i g_j / \kappa$, where $\langle \hat{A} \rangle_s = \langle \hat{A} + \hat{A}^\dagger \rangle / 2$ is short hand for the symmetrized expectation value.

The backaction-driven diffusion of the different oscillators is correlated, due to the shared bath of cavity amplitude fluctuations and finite spectral overlap assuming a non-zero oscillator linewidth. The two-time correlation between the positions of two oscillators k and l induced by a common, white noise bath with unity variance is given by the integral

$$R_{ij}(t, t') = \int_0^\infty d\tau \langle \boldsymbol{r}_i^\mathsf{T}(t - \tau) \boldsymbol{r}_j(t' - \tau) \rangle. \tag{6.26}$$

Filter definition

Now, the optodynamical signal can be written in terms of the oscillator position solved above as

$$\hat{S}(t) = \sum_i \sqrt{2} g_i \left[\hat{\boldsymbol{Q}}_i^\mathsf{T} \boldsymbol{r}_i(t) + \hat{n}_i(t) \right] + \sqrt{P_{\mathrm{SN}}} \hat{\xi}_{\mathrm{SN}}(t), \tag{6.27}$$

The oscillator dynamics observed in the signal are a sum of the coherent evolution of the initial state and the accumulated diffusion of the oscillator's position, calculated from the convolution

$$\hat{n}_i(t) = \int_0^\infty d\tau \, \hat{\boldsymbol{v}}_i^\mathsf{T}(\tau) \boldsymbol{r}_i(t - \tau). \tag{6.28}$$

Considering a general vector of two real-valued temporal filters $\boldsymbol{m}_i(t)$ for each oscillator, the raw, unnormalized filter outputs are defined as

$$\hat{\boldsymbol{q}}_i \equiv \int_0^T dt \, \boldsymbol{m}_i(t) \hat{S}(t). \tag{6.29}$$

Assuming, for now, that the coherent quadrature response functions $r_i(t)$ are deterministic, the mean of the filter outputs can be evaluated as

$$\langle \hat{\boldsymbol{q}}_i \rangle = \sum_j \mathrm{J}_{ij} \langle \hat{\boldsymbol{Q}}_j(0) \rangle, \tag{6.30}$$

in terms of the overlap matrix between each pair of filters and each oscillator's quadrature response functions, composed of 2×2 blocks for each pair of oscillators

$$\mathrm{J}_{ij} = \sqrt{2} g_j \int_0^T dt \, \boldsymbol{m}_i(t) \boldsymbol{r}_j^\mathsf{T}(t). \tag{6.31}$$

The average quadrature amplitudes can be recovered by inverting the full $2N \times 2N$ overlap matrix J, which serves as a generalization of the normalization matrix appearing in the OLS filters defined in Eq. 6.5. This overlap matrix is invertible as long as the filter functions are linearly independent and span the space of the quadrature response functions $\boldsymbol{r}_i(t)$, providing one filter per quadrature of the multi-oscillator system.
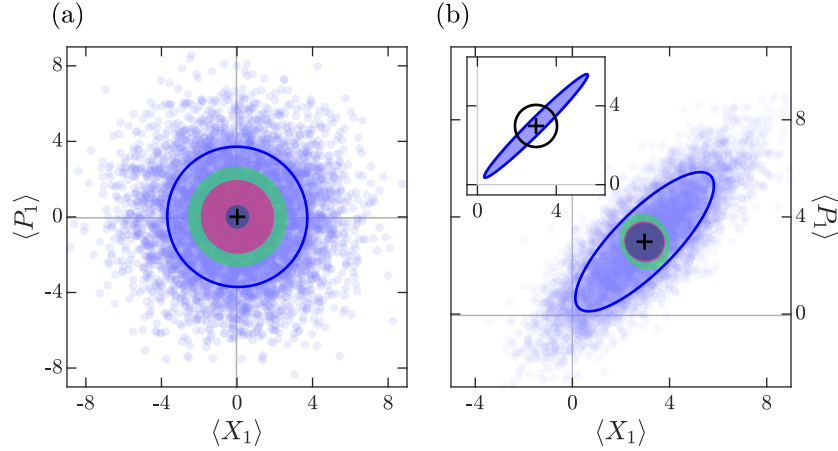
(a)   (b)

Figure 6.3: Phase space distribution of quadratures estimates obtained by filtering simulated signals. (a) Ensemble of estimates (8000 samples) from the OLS filters defined by Eq. 6.5, for measurements of a single, thermal oscillator ($\omega_1 = 2\pi \times 130$ kHz, $\Gamma_1 = 2\pi \times 2$ kHz), in equilibrium with a bath temperature $\nu_1 = 1$ and measurement cooperativity $C_1 = 2.8$. The covariance of the filter outputs define a 1-σ uncertainty ellipse (blue), which is the cumulative sum of the added shot noise covariance (black circle), thermal noise (red annulus), measurement backaction (green annulus), and the retrodicted state covariance. (b) Estimation of simulated measurements of a displaced, squeezed state for the same oscillator, with initial thermal occupation $\langle \hat{a}_1^\dagger \hat{a}_1 \rangle = 0.1$, now with measurement cooperativity $C_1 = 18$ and using the optimal GLS filters defined by Eq. 6.52. Squeezing of the initial state is reflected in the inferred variance (inset, blue ellipse circle) of one quadrature below the zero-point motion (inset, black circle).

The normalized, unbiased quadrature estimator can therefore be defined as

$$\breve{\boldsymbol{Q}} \equiv \mathrm{J}^{-1}\hat{\boldsymbol{q}}. \tag{6.32}$$

This estimator produces a $2N$-component vector of quadrature estimates when applied to each recorded measurement trace, as illustrated in Fig. 6.3 for simulated signals, produced by numerically integrating the stochastic equations of motion as described in Sec. 6.4.

Filtered noise covariance

Fluctuations from each source of noise in the signal enter into the filter outputs, increasing the variance and modifying the covariance of quadrature estimates. The performance of a given set of filter functions $\boldsymbol{m}_i(t)$ can be evaluated for a system with known dynamics and noise spectra, by calculating the effective noise occupation added to the quadrature estimates.

I start by calculating the expected value of the symmetrized second-moments of the raw filter outputs defined in Eq. 6.29, which can be compared to the statistics of estimates obtained from the classical recorded signals. Using the oscillator's two-time correlation function from Eq. 6.25, the result can be separated into a contribution from the initial quantum state, plus systematic biases from the signal noise

$$\langle \hat{\boldsymbol{q}}\hat{\boldsymbol{q}}^\mathsf{T}\rangle_s = \mathrm{J}\langle \hat{\boldsymbol{Q}}\hat{\boldsymbol{Q}}^\mathsf{T}\rangle_s\mathrm{J}^\mathsf{T} + \mathrm{T}' + \mathrm{B}' + \mathrm{S}', \tag{6.33}$$

having separately identified the additive covariance from each noise source – thermal diffusion T', measurement backaction B', and detector shot noise S'.

The shot noise contribution is proportional to the filter overlap matrix

$$\mathrm{S}' = P_{\mathrm{SN}} \int_0^T dt\, \boldsymbol{m}(t)\boldsymbol{m}^\mathsf{T}(t),$$

describing the added variance and covariance between the filter outputs arising from broadband noise and the spectral overlap between pairs of filters, introducing spurious correlations between non-orthogonal filters.

The backaction-driven diffusion of the oscillators is also correlated, due to the shared bath of cavity amplitude fluctuations and the finite spectral overlap of their response functions, assuming a non-zero oscillator linewidth. The backaction covariance added to the un-normalized filter outputs is given by the matrix

$$\mathrm{B}' = \sum_{kl} g_k g_l \sqrt{B_k B_l}\, \mathrm{N}_{kl} \tag{6.34}$$

expressed as a weighted sum over the filter correlations N_{kl} produced by diffusion of each pair of oscillators, k and l, in response to a common, white noise bath with unity variance

$$\mathrm{N}_{kl} = \iint_0^T dt\, dt'\, \boldsymbol{m}(t)R_{kl}(t, t')\boldsymbol{m}^\mathsf{T}(t'), \tag{6.35}$$

expressed in terms of the two-time response function product given by Eq. 6.26.

The thermal contribution to the filter covariance takes a similar form

$$\mathrm{T}' = \sum_k g_k^2 \Gamma_k \left(\nu_k + \frac{1}{2}\right) \mathrm{N}_{kk}, \tag{6.36}$$

given by a simple sum over individual oscillators, because the thermal baths are assumed to be uncorrelated between different oscillators.

The moments of the raw filter outputs given by Eq. 6.30 and Eq. 6.33 can be transformed by the overlap matrix from Eq. 6.31 to determine the covariance of quadrature estimates $\breve{\boldsymbol{Q}}$

$$\mathrm{cov}[\breve{\boldsymbol{Q}}] \equiv \langle \breve{\boldsymbol{Q}}\breve{\boldsymbol{Q}}^\mathsf{T}\rangle_s - \langle \breve{\boldsymbol{Q}}\rangle\langle \breve{\boldsymbol{Q}}\rangle^\mathsf{T} = \mathrm{cov}[\hat{\boldsymbol{Q}}] + \mathrm{T} + \mathrm{B} + \mathrm{S}, \tag{6.37}$$

in terms of the initial state covariance and the normalized noise covariances given by

$$\mathrm{S} = \mathrm{J}^{-1}\mathrm{S}'(\mathrm{J}^{-1})^\mathsf{T} \qquad \mathrm{B} = \mathrm{J}^{-1}\mathrm{B}'(\mathrm{J}^{-1})^\mathsf{T} \qquad \mathrm{T} = \mathrm{J}^{-1}\mathrm{T}'(\mathrm{J}^{-1})^\mathsf{T}, \tag{6.38}$$

which are indicated by the shaded regions in Fig. 6.3

Evaluating noise systematics

Computing the integrals to obtain the diffusive noise covariance matrices N_{kl} is not trivial, even numerically, involving a triple integral over rapidly oscillating products. This computation can be made more tractable by carrying out the integral defining $R_{kl}(t,t')$ in Eq. 6.26. Using the definition of the response functions in Eq. 6.23, it can be shown that $R_{kl}(t,t') = \mathrm{Re}[\tilde{R}_{kl}(t,t')]$ with

$$\tilde{R}_{kl}(t,t') = \frac{1}{(\Gamma_k + \Gamma_l)/2 - i(\omega_k - \omega_l)} \left[\rho_l(t' - t) + \rho_k^*(t - t') - \rho_k^*(t)\rho_l(t') \right] \tag{6.39}$$

in terms of the complex response function $\rho_k(t) = \exp(-i\omega_k t - \Gamma_k t/2)\,\Theta(t)$ for oscillator k. This result can be easily evaluated numerically, allowing efficient calculation of Eq. 6.35 as summations over the discrete filter functions we apply to the digitally sampled signal.

This solution also facilitates obtaining further analytic results. Considering estimation of a single oscillator, the noise matrices T, B, and S can be evaluated for a general exponential set of filters

$$\boldsymbol{m}_{\exp}(t) \equiv e^{-\gamma_1 t/2} \begin{pmatrix} \cos \omega_1 t \\ \sin \omega_1 t \end{pmatrix}. \tag{6.40}$$

Assuming a high-Q oscillator limit $\omega_1 \gg \Gamma_1, \gamma_1$, each noise matrix is proportional to the 2×2 identity matrix I_2, with the filter covariance for diffusive noise

$$N_{11} = \frac{\Gamma_1}{\gamma_1(\gamma_1 + \Gamma_1)^2} I_2 \tag{6.41}$$

and filter normalization matrix

$$J_{11} = \frac{\sqrt{2}g_1}{\gamma_1 + \Gamma_1} I_2 \tag{6.42}$$

from which each systematic bias matrix can be computed

$$T = n_T I_2 \qquad\qquad B = n_B I_2 \qquad\qquad S = n_S I_2, \tag{6.43}$$

representing an equal variance of noise added to each quadrature. These variances are already normalized into units of equivalent thermal occupation, given by

$$n_T = \left(\nu_1 + \frac{1}{2}\right)\frac{\Gamma_1}{\gamma_1} \qquad n_B = \frac{C_1}{2}\frac{\Gamma_1}{\gamma_1} \qquad n_S = \frac{1}{2\epsilon C_1}\frac{(\Gamma_1 + \gamma_1)^2}{4\Gamma_1\gamma_1} \tag{6.44}$$

in terms of the optodynamical cooperativity $C_i = B_i/\Gamma_i$. Minimizing the total of these added noise occupations, therefore, corresponds to a more optimal estimate of the oscillator quadratures from each recorded trace.

Standard error of correlations

For analysis of experimental results, each iteration of the experiment i yields a vector of $d = 2N$ estimated values $\check{\boldsymbol{Q}}_i$ (here i indexes the iteration number, not the components of the vector), which is a vector-valued random variable. For linear filters, having assumed that all input noise is Gaussian, these results are distributed according to the multivariate normal distribution

$$\check{\boldsymbol{Q}}_i \sim N(\boldsymbol{\mu}, \Sigma), \tag{6.45}$$

with population mean vector $\boldsymbol{\mu}$ and covariance matrix Σ.

If we further assume that the results of each of N iterations are sampled from identical, independent distributions, then we can define the sample vector mean and covariance matrix

$$\check{\boldsymbol{\mu}} = \frac{1}{N} \sum_i^N \check{\boldsymbol{Q}}_i \qquad\qquad \check{\Sigma} = \frac{1}{N-1} \sum_i^N (\check{\boldsymbol{Q}}_i - \check{\boldsymbol{\mu}})(\check{\boldsymbol{Q}}_i - \check{\boldsymbol{\mu}})^\mathsf{T} \tag{6.46}$$

which provide unbiased estimates of the population mean $\langle \check{\boldsymbol{\mu}} \rangle = \boldsymbol{\mu}$ and covariance $\langle \check{\Sigma} \rangle = \Sigma$. In practice, variations in experimental parameters cause the iterations not to be identical, and additional stochastic fluctuations, such as shot-to-shot variations in oscillator frequencies, must be included in the model. This is neglected here, but reconsidered in Sec. 6.6.

The sample covariance matrix $\check{\Sigma}$ is therefore a matrix-valued random variable. Correcting for the systematic biases from signal noise, we can form an estimator for the covariance matrix of the multi-mode oscillator state

$$\check{C} = \check{\Sigma} - T - B - S \tag{6.47}$$

with $\langle \check{C} \rangle_s = \mathrm{cov}[\hat{\boldsymbol{Q}}]$.

The systematic bias matrices T, B, and S can be calculated from the filter functions and independent knowledge of the system and noise parameters. Assuming these parameters are known arbitrarily well, then the statistical uncertainty on the estimate of the multi-mode covariance matrix $\check{C}$ is purely determined by the variance of the raw filter covariance estimator $\check{\Sigma}$. This estimator is distributed according to the d-dimensional Wishart distribution, with $N - 1$ degrees of freedom

$$(N-1)\check{\Sigma} \sim W_d(\Sigma, N-1), \tag{6.48}$$

which is the multi-dimensional extension of the χ^2 distribution [118].

The variance of the estimate can then be determined from the properties of the Wishart distribution, with

$$\langle \Delta \check{\Sigma}_{ij}^2 \rangle = \frac{1}{N-1}(\Sigma_{ij}^2 + \Sigma_{ii}\Sigma_{jj}), \tag{6.49}$$

where $\check{\Sigma}_{ij}$ can be used as an estimate for Σ_{ij}. (Thus realizing an estimate of the variance of the multi-mode state covariance estimator. This is getting out of hand...) The diagonal elements Σ_{ii} individually follow χ^2 distributions, however the off-diagonal components do not, and care must therefore be taken when propagating errors for parameters derived from these elements.

6.3 Matched filters

In the presence of temporally correlated noise, such as imparted by the diffusive oscillator dynamics, the optimal linear filters to recover the best estimate of an oscillator's state must be 'matched' to both the coherent response functions $\boldsymbol{r}_i(t)$ and the total noise correlations

$$\Omega(t, t') = \sum_{ij} \langle \hat{n}_i(t) \hat{n}_j(t') \rangle + P_{\mathrm{SN}} \delta(t - t')$$

$$= \sum_i g_i^2 \Gamma_i(\nu_i + 1/2) R_{ii}(t, t') + \sum_{ij} g_i g_j \frac{B_{ij}}{2} R_{ij}(t, t') + P_{\mathrm{SN}} \delta(t - t'), \qquad (6.50)$$

for the optodynamical signal considered above.

The use of such 'matched filters' is a standard signal processing technique [117, 119], and is common in communication or radar systems for detection of signals of a deterministic form in the presence of noise with a well-known spectrum. They have also been used extensively in scientific measurements, such as for detecting black-hole merger events in gravitational wave signals from LIGO [120].

If the signal noise is stationary, with two-time correlation function depending only on the time difference τ, then it can be described by the PSD $S_\Omega[\omega] = \int_{-\infty}^{\infty} e^{i\omega\tau} \Omega(t, t + \tau) d\tau$. The optimal filter function can then be simply stated in Fourier space as [117]

$$m_i[\omega] = \frac{r_i^*[\omega]}{S_\Omega[\omega]}, \qquad (6.51)$$

for known response functions with Fourier transform $r_i[\omega]$. This result illustrates the basic concept of matched filtering, with the observed signal weighted in the estimate by the expected SNR at each component of the spectrum.

However, the application to optodynamical measurements is more complicated, because the motion of the oscillator being estimated is non-deterministic, with inherent diffusion driven by the measurement process itself. While the observed evolution can be separated into a coherent decay of the initial state and additional diffusive noise, this noise is non-stationary and, therefore, cannot be as simply described by a power spectrum.

Generalized least-squares filter

A minimum variance, unbiased estimator can be obtained from the method of Generalized Least Squares [121]. Similar to the OLS method discussed in Sec. 6.1, this method minimizes

the variance of residuals between the observed signal and predicted values. However, first the signal and response model are transformed by the inverted two-time noise correlation, and the optimization is performed to minimize residuals of the resulting temporally uncorrelated signal, once again satisfying the Gauss-Markov theorem.

The solution to the GLS optimization, for application to a signal sampled at discrete times $t_i = i\Delta t$, is obtained with the discretized filter functions

$$\boldsymbol{m}_{\text{GLS}}(t_i) \equiv \sum_j [\Omega^{-1}]_{ij} \boldsymbol{r}(t_j) \Delta t \qquad (6.52)$$

defined in terms of the matrix inverse of the discretized two-time correlation of noise in the measured signal $\Omega_{ij} = \Omega(t_i, t_j)$, with the delta-correlated measurement noise going over to the Kronecker delta function as $\delta(t_i - t_j) \to \Delta t \delta_{ij}$.

6.4 Numerical simulation of stochastic differential equations

In order to validate the derivation and approximations performed to calculate the optimal filters and measurement conditions, it is useful to generate simulated signals with known model parameters. The quantum Langevin equations defined by Eqs. 6.20 can be simulated semi-classically as stochastic differential equations. Their solution can be written in terms of a stochastic integral

$$\boldsymbol{Q}(t) = e^{-\text{A}t} \boldsymbol{Q}(0) + \int_0^t e^{-\text{A}(t-\tau)} \text{B}\, d\boldsymbol{W}_\tau, \qquad (6.53)$$

where $d\boldsymbol{W}_\tau$ is a vector of independent Wiener noise increments at each time τ, with one component for each noise drive, and B is a matrix describing the coupling between each noise source to the corresponding quadrature evolution.

This noise coupling matrix B need not be square. Here it represents coupling between $2N$ quadratures and the $2N + 1$ input quadratures, including thermal noise driving each oscillator and the one shared bath of cavity amplitude fluctuations $\hat{\xi}_\Delta^{\text{AM}}(t)$. For simulating measurement of two oscillators, the noise coupling matrix is

$$\text{B} = \begin{pmatrix} \sqrt{\Gamma_1(\nu_1 + 1/2)} & 0 & 0 & 0 & 0 \\ 0 & \sqrt{\Gamma_1(\nu_1 + 1/2)} & 0 & 0 & -\sqrt{B_1} \\ 0 & 0 & \sqrt{\Gamma_2(\nu_2 + 1/2)} & 0 & 0 \\ 0 & 0 & 0 & \sqrt{\Gamma_2(\nu_2 + 1/2)} & -\sqrt{B_2} \end{pmatrix}$$

Sample trajectories from the distribution solving these equations can be estimated numerically using the stochastic Euler method [122]

$$\boldsymbol{Q}(t + \Delta t) \approx \Delta t\, \text{A}\, \boldsymbol{Q}(t) + \text{B}\, \Delta \boldsymbol{W}_t \qquad (6.54)$$
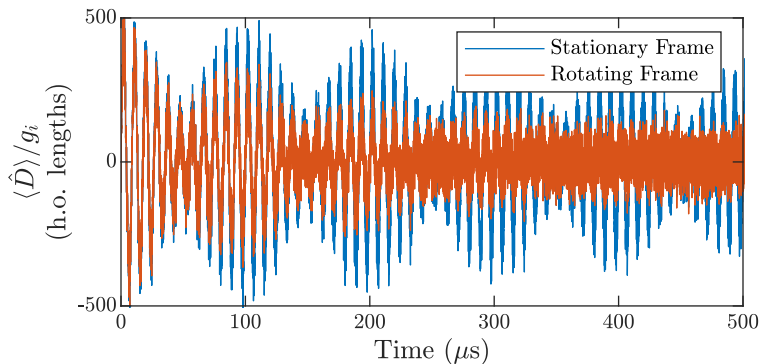
Figure 6.4: A sample trajectory simulating the expected signal from simultaneous measurement of two oscillators (with $\omega_i = 2\pi \times \{120, 110\}$ kHz, $\Gamma_i = 2\pi \times 2$ kHz, $g_i = 2\pi \times 20$ kHz, $\bar{n} = 4$, and $\epsilon = 1$), approximated from the stochastic differential equations by the Euler method defined in Eq. 6.54 with $\Delta t = 20$ ns time steps. Comparing solutions in a rotating frame (red) and in the stationary frame (blue) demonstrates improved stability and accuracy in the rotating frame.

with the vector of discrete, uncorrelated Wiener increments drawn from the multi-variate normal distribution $\Delta \boldsymbol{W}_t \sim N(0, \Delta t \, \mathrm{I}_{2N+1})$, where I_m is the $m \times m$ identity matrix.

The error of the stochastic Euler method scales as $\mathcal{O}(\sqrt{\lambda_{\max}\Delta t})$, where $\lambda_{\max}$ is the fastest system timescale, typically the largest eigenvalue of A. This error scaling is known as the 'strong' order of convergence, corresponding to the accuracy of estimated trajectories compared to exact solutions, and converges more slowly than the deterministic Euler method at $\mathcal{O}(\Delta t)$. This slow convergence presents practical issues of accuracy and stability for simulating equations with rapidly oscillatory dynamics, an example of a so-called 'stiff' integration kernel. However, the issues of numerical stability in this case can be mitigated by estimating the solution in a rotating frame of each oscillator [122], eliminating the largest rate from A and B and allowing the approximation to converge for reasonable time steps, as demonstrated in Fig. 6.4.

6.5 Calibration of matched-filter estimates

Interpretation of the matched filter results requires careful calibration of all system and noise parameters to accurately estimate the oscillator quadratures and account for the variance of added noise. To experimentally verify the accuracy of this process, it is helpful to check the results against a well-calibrated signal. Returning to the temperature measurements of a damped spin oscillator in Sec. 3.3, the equilibrium thermal occupation can be estimated from the distribution of quadrature estimates, obtained from matched filters constructed with the oscillator frequency and linewidth observed in the shot noise–driven PSD, shown in Fig. 6.5a.
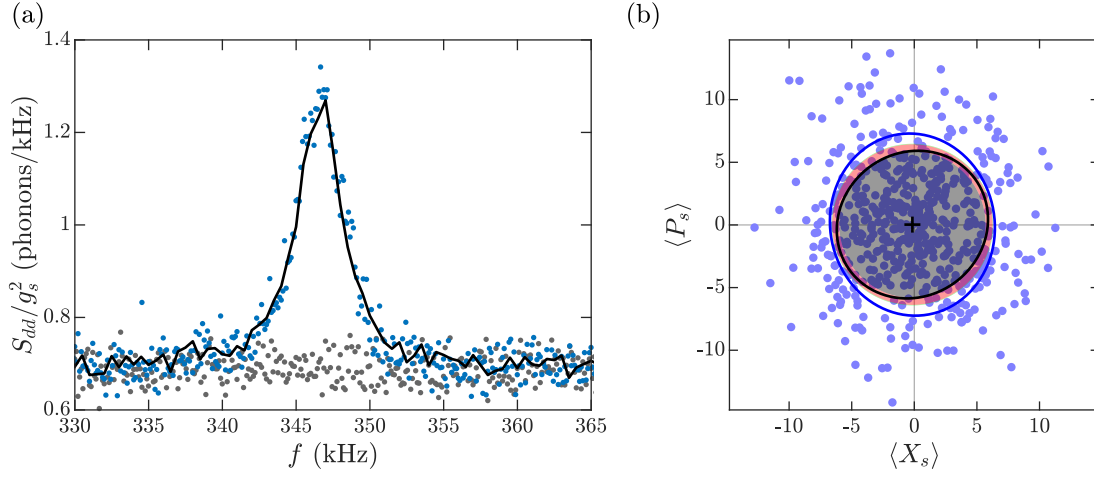
Figure 6.5: Observed phase modulation spectrum for on-resonance probe of damped spin oscillator, as described in Sec. 3.3. (a) The observed spectrum (blue) is compared to a simulated spectrum for an oscillator at the equilibrium occupation $\nu_s = 2.7$ calibrated from the observed sideband asymmetry. (b) Phase space distribution of matched filter estimates (blue dots), with added measurement noise (theory: gray disk, observed: black circle) and thermal noise (red annulus) from the off-resonance damping tone. The inferred equilibrium occupation is $\nu_s = 2.4 \pm 0.5$.

A damped oscillator in equilibrium with its bath and measurement backaction has an average thermal occupation

$$\langle \hat{n}_s \rangle = \nu_s + \frac{C_s}{2} \tag{6.55}$$

The variance of estimates for each quadrature, displayed in Fig. 6.5b, is expected to reflect this occupation, plus the oscillator zero-point motion, and the effective occupation of each optodynamical noise source

$$\langle \breve{X}_s^2 \rangle = \langle \breve{P}_s^2 \rangle = \langle \hat{n}_s \rangle + \frac{1}{2} + n_T + n_B + n_S. \tag{6.56}$$

Using the OLS filters defined by the coherent response functions, the added noise occupation from Eqs. 6.44 are expected to be $n_T = \nu_1 + 1/2$ and $n_B = B_1/2$. The average equilibrium occupation can therefore be estimated from the observed variance according to

$$\breve{n}_s = \frac{\langle \breve{X}_s^2 \rangle + \langle \breve{P}_s^2 \rangle - 2n_S - 2}{4}, \tag{6.57}$$

with the added occupation from measurement noise n_S either calculated or measured from shot noise only signals recorded without atoms in the cavity.

The optodynamical fluctuations observed in the recorded heterodyne signals also provide an intrinsic signature of the absolute temperature, reflected in the asymmetry between the
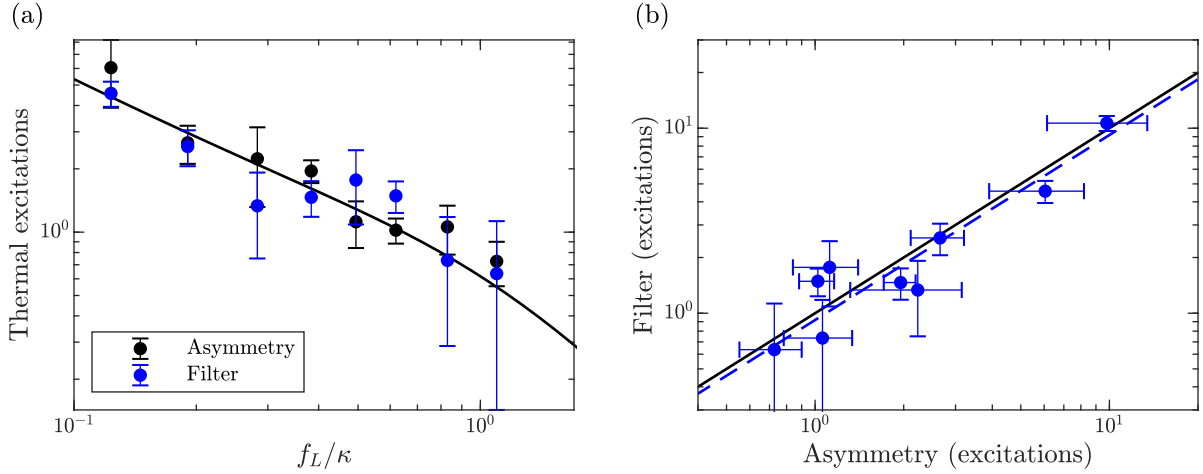
Figure 6.6: Calibration of matched filters from sideband asymmetry of an optodynamically damped spin oscillator. (a) The absolute equilibrium occupation of a damped spin oscillator (black points), measured from the observed sideband asymmetry as described in Sec. 3.3. Independent estimates of the occupation obtained from the distribution of matched filter results (blue points), such as displayed in Fig. 6.5b. The theoretical minimum occupation for optodynamical damping and measurement, with average cooperativity $C_s = 1.6$, is indicated (black line) (b) Comparison of the absolute occupation measured from sideband asymmetry with the filter estimates obtained from the same data show good agreement, with proportionality 0.92 ± 0.10 from a linear fit (dashed blue line).

Stokes and anti-Stokes sidebands. The sideband asymmetry provides an absolute calibration of the thermal occupation of the measured state, independent of coupling strengths, detection efficiency, or measurement noise. The matched-filter estimate of the thermal occupation can be compared to the oscillator occupation measured by sideband asymmetry, demonstrating average agreement between the results in Fig. 6.6.

Correction outside the unresolved sideband regime

The data for Fig. 6.6 include measurements of spin oscillators outside the unresolved sideband regime, and the preceding derivations must be adjusted outside of this limit. When probing the cavity on resonance, modulation of the cavity field at frequencies ω_i is suppressed by the cavity Lorentzian profile, reflected in the optodynamical measurement operator, from Eq. 2.57

$$\hat{d} = \sum_i g_i \sqrt{\frac{2\kappa^2}{\kappa^2 + \omega_i^2}} \hat{X}_i, \tag{6.58}$$

having absorbed the cavity field delay into a phase rotation of $\hat{a}_i$.

Additionally, the cavity spectrum also suppresses the PSD of shot noise fluctuations, defined by Eq. 2.40, at the oscillator frequency by a factor of $\kappa^2/(\kappa^2 + \omega_i^2)$. Both of these effects can be effectively accounted for by using a modified optodynamical coupling strength

$$g_i' = g_i\sqrt{\frac{\kappa^2}{\kappa^2 + \omega_i^2}} \tag{6.59}$$

for both the measurement strength in Eq. 6.19 and the backaction diffusion rate B_i in Eq. 6.21.

6.6   Inhomogeneous broadening

If there are variations in the oscillator dynamics, such as shot-to-shot fluctuations of an oscillator's frequency causing 'inhomogeneous broadening' of the average oscillator spectrum over an ensemble of measurement, then the quadrature response functions $\boldsymbol{r}_i(t)$ are no longer deterministic. The optimal 'average' filter is still implicitly defined by Eq. 6.10, but will now be more complicated to evaluate.

To develop some intuition, consider a simplified case of estimating a single quadrature of an oscillator with no damping or diffusion, described by the response function

$$r_1(t) = \cos\omega_1 t \tag{6.60}$$

However, the frequency is now assumed to be a normally distributed random variable $\omega_1 \sim N(\bar{\omega}_1, \sigma_1^2)$ with mean $\bar{\omega}_1$ and standard deviation σ_1. The average response function has a Gaussian envelope (Fig. 6.7a).

$$\langle r_1(t)\rangle = e^{-\sigma^2 t^2/2}\cos\bar{\omega}t, \tag{6.61}$$

and its response two-time correlation function is

$$\langle r_1(t)r_1(t')\rangle = \frac{1}{2}\left[e^{-\sigma^2(t-t')^2/2}\cos\bar{\omega}(t-t') + e^{-\sigma^2(t+t')^2/2}\cos\bar{\omega}(t+t')\right]. \tag{6.62}$$

Assuming the quadrature amplitude X_1 is independent of the frequency fluctuations, then the MSE filter function is defined by the integral equation

$$\int_0^T dt'\left[2g^2\langle X_1^2\rangle\langle r_1(t)r_1(t')\rangle + P_{\mathrm{SN}}\delta(t-t')\right]m_1(t') = \sqrt{2}g\langle X_1^2\rangle\langle r_1(t)\rangle \tag{6.63}$$

The solution for $m_1(t)$ can be numerically approximated by discretizing this integral, turning it into a finite matrix equation. Sampling at discrete times $t_i = i\Delta t$ and defining the vector $\bar{\boldsymbol{r}}_i = \langle r_1(t_i)\rangle$ and matrix $\mathrm{R}_{ij} = \langle r_1(t_i)r_1(t_j)\rangle$, Eq. 6.63 can be solved for the discrete filter function $m_i = m_1(t_i)$, giving

$$m_i = \frac{1}{\sqrt{2}g\Delta t}\sum_j \bar{r}_j[\mathrm{F}^{-1}]_{ji} \qquad \text{with} \qquad \mathrm{F} = \mathrm{R} + \frac{1}{\mathrm{SNR}}\mathrm{I} \tag{6.64}$$
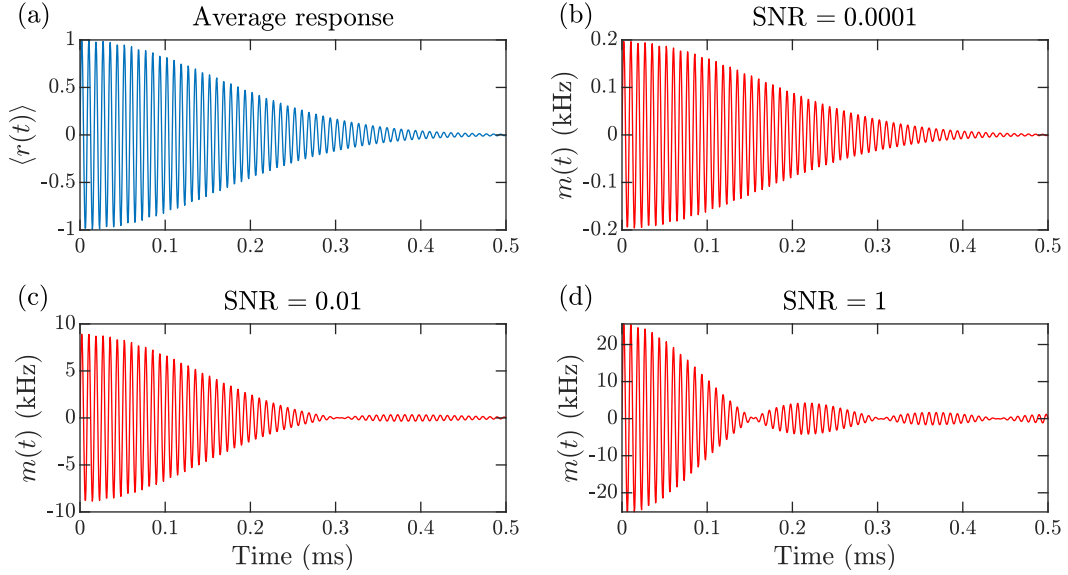
Figure 6.7: Optimal filter for an inhomogeneously broadened signal. (a) The average response for an ensemble of measurements on an undamped oscillator with normally distributed shot-to-shot frequency fluctuations. (b-d) Numerical solutions for the MSE filter defined by Eq. 6.63, proportional to the average response for small SNR values (b), corresponding to typical experimental conditions, while becoming more temporally localized for higher values (d).

having defined signal-to-noise ratio $\mathrm{SNR} = 2g_1^2 \langle X_1^2 \rangle \Delta t / P_{\mathrm{SN}}$.

The relative noise power is $P_{\mathrm{SN}} = \kappa / 8 \epsilon \bar{n}$ for a homodyne measurement, and for weak measurements, with $\kappa \gg g_1$, the SNR therefore is typically small. The implicit filter definition given by Eq. 6.63 is therefore dominated by the delta function, with the discretized solution matrix F approximately proportional to the identity, resulting in an optimal filter that nearly resembles the average response function, as shown in Fig. 6.7b. However, for measurements with larger SNR values, the shape of the optimal filter becomes more localized (Fig. 6.7d), tending toward a delta function in the strong-measurement limit.

Inhomogeneous optodynamical filter systematics

The average coherent response functions are therefore reasonable choices for filter functions

$$\boldsymbol{m}_i(t) = \langle \boldsymbol{r}_i(t) \rangle, \tag{6.65}$$

and I will not worry further about questions of filter optimality. The statistics of the output of these filters applied to optodynamical signals can be computed using the formalism in Sec. 6.2, however expectation values will have to carried out over the response functions $r_i(t)$, which now represent random variables, in addition to the input noise and initial states.

To make the solutions tractable, we assume that the shot-to-shot fluctuations in oscillator frequency are uncorrelated with the initial state $\hat{\boldsymbol{Q}}$ or input noise $\hat{\boldsymbol{v}}_i(t)$, which is perhaps an unrealistic assumption in practice, but a reasonable first approximation.

Returning to the un-normalized filter outputs defined in Eq. 6.29, the mean filter output can then be written

$$\langle \hat{\boldsymbol{q}}_i \rangle = \sum_j \langle \mathrm{J}_{ij} \rangle \langle \hat{\boldsymbol{Q}}_j \rangle, \tag{6.66}$$

which can be solved by inverting the filter overlap matrix with the average response functions,

$$\langle \mathrm{J}_{ij} \rangle = \sqrt{2} g_j \int_0^T dt\, \boldsymbol{m}_i(t) \langle \boldsymbol{r}_j^\mathsf{T}(t) \rangle. \tag{6.67}$$

However, evaluating the 2nd moment of filter outputs to infer the covariance of the actual initial states becomes much more tedious because the overlap matrix J can no longer by pulled out of the expectation as in Eq. 6.33. Expanding the matrix products in terms of indexes over each quadrature (as opposed to the block-matrix indexing used before), the moments can be written as

$$\langle \hat{q}_i \hat{q}_j^\mathsf{T} \rangle_s = \sum_{kl} \langle \mathrm{J}_{ik} \mathrm{J}_{jl} \rangle \langle \hat{Q}_k \hat{Q}_l \rangle_s + \mathrm{T}'_{ij} + \mathrm{B}'_{ij} + \mathrm{S}'_{ij} \tag{6.68}$$

The expectation over the product of overlap matrix elements from Eq. 6.31 is

$$\langle \mathrm{J}_{ik} \mathrm{J}_{jl} \rangle = 2 g_i g_j \iint_0^T dt\, dt'\, m_i(t) \langle r_k(t) r_l(t') \rangle m_j(t') \tag{6.69}$$

which, however, is not separable into independent 1-D integrals, and therefore is more easily evaluated numerically. Once evaluated, these elements can be reindexed as a $4N^2 \times 4N^2$ matrix, which can then be inverted to solve Eq. 6.68 for each element of the multi-mode covariance matrix $\langle \hat{Q}_k \hat{Q}_l \rangle_s$.

The filtered diffusive noise matrices N_{kl} defined by Eq. 6.35 must also be reevaluated as an expectation over the oscillator frequency distributions. This can be simplified by making a further approximation. Assuming the standard deviation of frequency fluctuations σ_i is small relative to the average frequency difference $\bar{\omega}_i - \bar{\omega}_j$, then the expectation of the diffusive noise two-time correlation function $\tilde{R}_{kl}(t, t')$ defined in Eq. 6.39 can be approximated by

$$\langle \tilde{R}_{ij}(t, t') \rangle \approx \frac{1}{(\Gamma_i + \Gamma_j)/2 - i(\bar{\omega}_i - \bar{\omega}_j)} \langle \rho_j(t' - t) + \rho_i^*(t - t') - \rho_i^*(t) \rho_j(t') \rangle, \tag{6.70}$$

which can be directly solved analytically, allowing numerical calculation of T′, B′, and S′, which yield the added noise to the moments of the multi-mode state obtained from inverting Eq. 6.68.

Chapter 7

Conclusion

The preceding chapters provide technical detail and theoretical analysis of our published results [24, 29, 35], demonstrating optodynamical measurement and coupling of the dynamics of collective atomic modes. Atomic ensembles in a high-finesse optical cavity provide a widely tunable platform for studying optically mediated interactions, providing tunable optical coupling, preparation of multiple distinct oscillators with the hybrid lattice, and optical interaction between diverse degrees of freedom, such as the atomic motion and spin.

Each of the different configurations are easily accessible within the same apparatus, as described in Sec. 2.3, requiring only changes in computer-controlled signals. The following sections of Chap. 2 develop a theoretical formalism to analytically describe time-domain dynamics of harmonic modes that are linearly coupled to the optical cavity's field. This formalism provides a flexible framework to understand each of the particular configurations explored in subsequent chapters.

Cavity-assisted optical measurement and control of a single collective atomic degree of freedom is illustrated in Chap. 3, through optodynamical coupling to precession of the collective atomic spin. The collective spin, with negligible intrinsic dissipation, provides a versatile system for demonstrating autonomous optical feedback, in which the cavity conditions optical feedback of the circulating light onto the subsequent atomic dynamics. This feedback was used to demonstrate stabilization of a negative-temperature state of the spin near its inverted 'ground-state,' providing a novel resource for cavity optodynamics. This demonstration of coherent optical interaction with a macroscopic spin ensemble also provides early demonstrations of quantum dynamics related to the emerging field of cavity optomagnonics with solid-state magnetic domains [27, 28].

Chaps. 4 and 5 then discussed demonstrations of two distinct interactions arising from cavity-mediated coupling between distinct atomic oscillators. In Chap. 4, an effective optical spring interaction was mediated by autonomous optical feedback of the motion of one atomic ensemble onto another, facilitating coherent state exchange between the two positive-mass oscillators. A similar optical interaction, described in Chap. 5, between the atomic motion and an inverted collective spin, an effective negative-mass oscillator, realized a negative-mass instability, which spontaneously drives parametric amplification of the two-mode system. As

derived in that chapter, this interaction could theoretically be used to generate entanglement between the atomic motion and spin through generating a two-mode squeezed state, prevented by incoherent noise from the static-gradient coupling between the motion and spin of each atom in our realization.

Having demonstrated proof-of-principle cavity mediated interactions, one future direction for such a system would be to prepare an array of oscillators coupled to the cavity mode [34], and selectively apply state exchange and entanglement interactions among subsets of the oscillators, building a many-body interacting system from the bottom up. Such addressable coupling between non-degenerate oscillators could be performed using time-dependent drives [62], or by addressing ensembles of atoms within the cavity by Stark shifting them into resonance with tightly focused beams, transverse to the cavity mode.

Engineering tunable interactions within a many-body system is itself a challenging and interesting goal, but once having managed to do so, a remaining challenge is to efficiently measure the generated many-body state. The work described in Chap. 6 proposes and demonstrates efficient measurement of multi-mode Gaussian states, spectrally multiplexed in the optodynamical measurement.

Finally, all of the work reported and proposed in this dissertation was carried out in the dispersive limit of optical coupling between the atoms and cavity field. This regime represents a narrow subspace of the accessible cavity QED parameters, leaving an abundance of new frontiers within reach of this venerable apparatus.

Acronyms

AOM acousto-optical modulator. 62, 83, 93

DDS direct digital synthesizer. 62

DMM digital multi-meter. 166

EOM electro-optical modulator. 173, 174, 176

FPGA field-programmable gate array. 173

FWHM full-width half-maximum. 92

GLS generalized least-squares. 125, 127, 133, 138

LO local oscillator. 7, 36, 37, 130, 167, 168, 176

MOT magneto-optical trap. 5, 6, 58, 170

MSE mean-square error. 127–130, 142, 143

ODT optical dipole trap. 6, 7, 17, 23, 58, 81–83, 89, 90, 114, 122

OLS ordinary least-squares. 126, 127, 130, 132, 133, 137, 140

PSD power spectral density. 33, 34, 37–40, 43, 47, 54, 59–61, 63, 83–85, 88–90, 92, 94, 95, 112, 123, 137, 139, 142, 165, 167, 173, 177, 180, 181

QED quantum electrodynamics. 1–3, 5, 7, 12, 20, 44, 45, 146

QND quantum non-demolition. 22, 45, 46, 65–69, 76, 77, 79, 103

RMS root-mean-square. 17, 42, 58, 83, 123, 167, 168

RWA rotating-wave approximation. 14, 60, 86, 95, 117–119

S&H sample & hold. 92, 93

SNR signal-to-noise ratio. 128, 137, 143

SQL standard quantum limit. 2, 4, 18, 40, 44, 45, 99, 121

VCO voltage-controlled oscillator. 91–93

Bibliography

[1] A. Einstein, "Über einen die Erzeugung und Verwandlung des Lichtes betreffenden heuristischen Gesichtspunkt", Annalen der Physik **322**, 132 (1905).

[2] H. J. Kimble, M. Dagenais, and L. Mandel, "Photon antibunching in resonance fluorescence", Phys. Rev. Lett. **39**, 691 (1977).

[3] D. F. Walls, "Evidence for the quantum nature of light", Nature **280**, 451 (1979).

[4] B. P. Abbott et al., "Observation of gravitational waves from a binary black hole merger", Phys. Rev. Lett. **116**, 061102 (2016).

[5] H. J. Metcalf and P. van der Straten, *Laser cooling and trapping* (Springer-Verlag, New York, 1999).

[6] M. Arndt and K. Hornberger, "Testing the limits of quantum mechanical superpositions", Nat. Phys. **10**, 271 (2014).

[7] S. Nimmrichter, K. Hornberger, and K. Hammerer, "Optomechanical sensing of spontaneous wave-function collapse", Phys. Rev. Lett. **113**, 020405 (2014).

[8] H. J. Kimble, "Strong interactions of single atoms and photons in cavity QED", Phys. Scr. **T76**, 127 (1998).

[9] J. M. Raimond, M. Brune, and S. Haroche, "Manipulating quantum entanglement with atoms and photons in a cavity", Rev. Mod. Phys. **73**, 565 (2001).

[10] S. Haroche and J.-M. Raimond, *Exploring the quantum* (Oxford University Press, Oxford, 2006).

[11] K. W. Murch, "Cavity quantum optomechanics with ultracold atoms", PhD thesis (University of California, Berkeley, 2008).

[12] T. J. Kippenberg and K. K. J. Vahala, "Cavity opto-mechanics", Opt. Express **15**, 17172 (2007).

[13] M. Aspelmeyer, T. J. Kippenberg, and F. Marquardt, "Cavity optomechanics", Rev. Mod. Phys. **86**, 1391 (2014).

[14] J.-M. Pirkkalainen, E. Damskägg, M. Brandt, F. Massel, and M. A. Sillanpää, "Squeezing of quantum noise of motion in a micromechanical resonator", Phys. Rev. Lett. **115**, 243601 (2015).

[15] E. E. Wollman, C. U. Lei, A. J. Weinstein, J. Suh, A. Kronwald, F. Marquardt, A. A. Clerk, and K. C. Schwab, "Quantum squeezing of motion in a mechanical resonator", Science **349**, 952 (2015).

[16] R. Riedinger, A. Wallucks, I. Marinković, C. Löschnauer, M. Aspelmeyer, S. Hong, and S. Gröblacher, "Remote quantum entanglement between two micromechanical oscillators", Nature **556**, 473 (2018).

[17] C. F. Ockeloen-Korppi, E. Damskägg, J.-M. Pirkkalainen, M. Asjad, A. A. Clerk, F. Massel, M. J. Woolley, and M. A. Sillanpää, "Stabilized entanglement of massive mechanical oscillators", Nature **556**, 478 (2018).

[18] N. Brahms, T. Botter, S. Schreppler, D. W. C. Brooks, and D. M. Stamper-Kurn, "Optical detection of the quantization of collective atomic motion", Phys. Rev. Lett. **108**, 133601 (2012).

[19] D. W. C. Brooks, T. Botter, S. Schreppler, T. P. Purdy, N. Brahms, and D. M. Stamper-Kurn, "Non-classical light generated by quantum-noise-driven cavity optomechanics", Nature **488**, 476 (2012).

[20] S. Schreppler, N. Spethmann, N. Brahms, T. Botter, M. Barrios, and D. M. Stamper-Kurn, "Optically measuring force near the standard quantum limit", Science **344**, 1486 (2014).

[21] W. Happer and B. S. Mathur, "Off-resonant light as a probe of optically pumped alkali vapors", Phys. Rev. Lett. **18**, 577 (1967).

[22] D. Budker and M. Romalis, "Optical magnetometry", Nat. Phys. **3**, 227 (2007).

[23] N. Brahms and D. M. Stamper-Kurn, "Spin optodynamics analog of cavity optomechanics", Phys. Rev. A **82**, 041804 (2010).

[24] J. Kohler, N. Spethmann, S. Schreppler, and D. M. Stamper-Kurn, "Cavity-assisted measurement and coherent control of collective atomic spin oscillators", Phys. Rev. Lett. **118**, 063604 (2017).

[25] X. Zhang, N. Zhu, C.-L. Zou, and H. X. Tang, "Optomagnonic whispering gallery microresonators", Phys. Rev. Lett. **117**, 123605 (2016).

[26] A. Osada, R. Hisatomi, A. Noguchi, Y. Tabuchi, R. Yamazaki, K. Usami, M. Sadgrove, R. Yalla, M. Nomura, and Y. Nakamura, "Cavity optomagnonics with spin-orbit coupled photons", Phys. Rev. Lett. **116**, 223601 (2016).

[27] T. Liu, X. Zhang, H. X. Tang, and M. E. Flatté, "Optomagnonics in magnetic solids", Phys. Rev. B **94**, 060405 (2016).

[28] S. Viola Kusminskiy, H. X. Tang, and F. Marquardt, "Coupled spin-light dynamics in cavity optomagnonics", Phys. Rev. A **94**, 033821 (2016).

[29] J. Kohler, J. A. Gerber, E. Dowd, and D. M. Stamper-Kurn, "Negative-mass instability of the spin and motion of an atomic gas driven by optical cavity backaction", Phys. Rev. Lett. **120**, 013601 (2018).

[30] M. Tsang and C. M. Caves, "Evading quantum mechanics: engineering a classical subsystem within a quantum environment", Phys. Rev. X **2**, 031016 (2012).

[31] C. B. Møller, R. A. Thomas, G. Vasilakis, E. Zeuthen, Y. Tsaturyan, M. Balabas, K. Jensen, A. Schliesser, K. Hammerer, and E. S. Polzik, "Quantum back-action-evading measurement of motion in a negative mass reference frame", Nature **547**, 191 (2017).

[32] T. P. Purdy, D. W. C. Brooks, T. Botter, N. Brahms, Z.-Y. Ma, and D. M. Stamper-Kurn, "Tunable cavity optomechanics with ultracold atoms", Phys. Rev. Lett. **105**, 133602 (2010).

[33] N. Brahms, T. P. Purdy, D. Brooks, T. Botter, and D. M. Stamper-Kurn, "Cavity-aided magnetic resonance microscopy of atomic transport in optical lattices", Nat. Phys. **7**, 604 (2011).

[34] T. Botter, D. W. C. Brooks, S. Schreppler, N. Brahms, and D. M. Stamper-Kurn, "Optical readout of the quantum collective motion of an array of atomic ensembles", Phys. Rev. Lett. **110**, 153001 (2013).

[35] N. Spethmann, J. Kohler, S. Schreppler, L. Buchmann, and D. M. Stamper-Kurn, "Cavity-mediated coupling of mechanical oscillators limited by quantum back-action", Nat. Phys. **12**, 27 (2016).

[36] T. P. Purdy, "Cavity QED with ultracold atoms on an atom chip", Doctoral (University of California, Berkeley, 2009).

[37] T. C. M. Botter, "Cavity optomechanics in the quantum regime", PhD thesis (University of California, Berkeley, 2013).

[38] S. F. Schreppler, "Quantum measurement with atomic cavity optomechanics", PhD thesis (University of California, Berkeley, 2016).

[39] M. Tsang and C. M. Caves, "Coherent quantum-noise cancellation for optomechanical sensors", Phys. Rev. Lett. **105**, 123601 (2010).

[40] J. Kohler, *skaffold2*, (2018) `https://bitbucket.org/amoberkeley/skaffold2`.

[41] D. M. Stamper-Kurn, in *Cavity optomech.* (Springer Berlin Heidelberg, Berlin, Heidelberg, 2014), p. 43.

[42] M. Tavis and F. W. Cummings, "Exact solution for an N-molecule—radiation-field Hamiltonian", Phys. Rev. **170**, 379 (1968).

[43] D. A. Steck, "Rubidium 87 D line data", 2010.

[44] S. Leslie, N. Shenvi, K. R. Brown, D. M. Stamper-Kurn, and K. B. Whaley, "Transmission spectrum of an optical cavity containing N atoms", Phys. Rev. A **69**, 043805 (2004).

[45] B. Julsgaard, "Entanglement and quantum interactions with macroscopic gas samples", PhD thesis (University of Aarhus, 2003).

[46] S. Gupta, K. L. Moore, K. W. Murch, and D. M. Stamper-Kurn, "Cavity nonlinear optics at low photon numbers from collective atomic motion", Phys. Rev. Lett. **99**, 213601 (2007).

[47] C. Gardiner and M. Collett, "Input and output in damped quantum systems: quantum stochastic differential equations and the master equation", Phys. Rev. A **31**, 3761 (1985).

[48] A. A. Clerk, M. H. Devoret, S. M. Girvin, F. Marquardt, and R. J. Schoelkopf, "Introduction to quantum noise, measurement, and amplification", Rev. Mod. Phys. **82**, 1155 (2010).

[49] D. F. Walls and G. J. Milburn, *Quantum optics*, 2nd (Springer-Verlag Berlin Heidelberg, Berlin, 2008).

[50] T. Botter, D. Brooks, N. Brahms, S. Schreppler, and D. M. Stamper-Kurn, "Linear amplifier model for optomechanical systems", Phys. Rev. A **85**, 013812 (2012).

[51] T. J. Kippenberg, H. Rokhsari, T. Carmon, A. Scherer, and K. J. Vahala, "Analysis of radiation-pressure induced mechanical oscillation of an optical microcavity", Phys. Rev. Lett. **95**, 033901 (2005).

[52] O. Arcizet, P.-F. Cohadon, T. Briant, M. Pinard, and A. Heidmann, "Radiation-pressure cooling and optomechanical instability of a micromirror", Nature (London) **444**, 71 (2006).

[53] S. Gigan, H. R. Böhm, M. Paternostro, F. Blaser, G. Langer, J. B. Hertzberg, K. C. Schwab, D. Bäuerle, M. Aspelmeyer, and A. Zeilinger, "Self-cooling of a micromirror by radiation pressure", Nature (London) **444**, 67 (2006).

[54] A. Schliesser, P. Del'Haye, N. Nooshi, K. J. Vahala, and T. J. Kippenberg, "Radiation pressure cooling of a micromechanical oscillator using dynamical backaction", Phys. Rev. Lett. **97**, 243905 (2006).

[55] T. P. Purdy, P.-L. Yu, R. W. Peterson, N. S. Kampel, and C. A. Regal, "Strong optomechanical squeezing of light", Phys. Rev. X **3**, 031012 (2013).

[56] S. Weis, R. Riviere, S. Deleglise, E. Gavartin, O. Arcizet, A. Schliesser, and T. J. Kippenberg, "Optomechanically induced transparency", Science **330**, 1520 (2010).

[57] G. S. Agarwal and S. Huang, "Electromagnetically induced transparency in mechanical effects of light", Phys. Rev. A **81**, 041803 (2010).

[58] A. H. Safavi-Naeini, T. P. M. Alegre, J. Chan, M. Eichenfield, M. Winger, Q. Lin, J. T. Hill, D. E. Chang, and O. Painter, "Electromagnetically induced transparency and slow light with optomechanics", Nature **472**, 69 (2011).

[59] J. D. Teufel, T. Donner, M. a. Castellanos-Beltran, J. W. Harlow, and K. W. Lehnert, "Nanomechanical motion measured with an imprecision below that at the standard quantum limit", Nat. Nanotechnol. **4**, 820 (2009).

[60] A. B. Shkarin, N. E. Flowers-Jacobs, S. W. Hoch, A. D. Kashkanova, C. Deutsch, J. Reichel, and J. G. E. Harris, "Optically mediated hybridization between two mechanical modes", Phys. Rev. Lett. **112**, 013602 (2014).

[61] R. Rossignoli and A. M. Kowalski, "Complex modes in unstable quadratic bosonic forms", Phys. Rev. A **72**, 032101 (2005).

[62] L. Buchmann and D. M. Stamper-Kurn, "Nondegenerate multimode optomechanics", Phys. Rev. A **92**, 013851 (2015).

[63] T. A. Palomaki, J. W. Harlow, J. D. Teufel, R. W. Simmonds, and K. W. Lehnert, "Coherent state transfer between itinerant microwave fields and a mechanical oscillator", Nature **495**, 210 (2013).

[64] T. A. Palomaki, J. D. Teufel, R. W. Simmonds, and K. W. Lehnert, "Entangling mechanical motion with microwave fields", Science **342**, 710 (2013).

[65] A. H. Safavi-Naeini, J. Chan, J. T. Hill, T. P. M. Alegre, A. Krause, and O. Painter, "Observation of quantum motion of a nanomechanical resonator", Phys. Rev. Lett. **108**, 033602 (2012).

[66] A. H. Safavi-Naeini, J. Chan, J. T. Hill, S. Gröblacher, H. Miao, Y. Chen, M. Aspelmeyer, and O. Painter, "Laser noise in cavity-optomechanical cooling and thermometry", en, New J. Phys. **15**, 035007 (2013).

[67] M. Collett, R. Loudon, and C. Gardiner, "Quantum theory of optical homodyne and heterodyne detection", J. Mod. Opt. **34**, 881 (1987).

[68] G. J. Milburn, "Quantum measurement theory of optical heterodyne detection", Phys. Rev. A **36**, 5271 (1987).

[69] H. R. Carleton and W. T. Maloney, "A balanced optical heterodyne detector", Appl. Opt. **7**, 1241 (1968).

[70] H. P. Yuen and V. W. S. Chan, "Noise in homodyne and heterodyne detection", Opt. Lett. **8**, 177 (1983).

[71] C. M. Caves, "Quantum limits on noise in linear amplifiers", Phys. Rev. D **26**, 1817 (1982).

[72] A. A. Clerk, "Quantum-limited position detection and amplification: A linear response perspective", Phys. Rev. B - Condens. Matter Mater. Phys. **70**, 1 (2004).

[73] H. Nha, G. J. Milburn, and H. J. Carmichael, "Linear amplification and quantum cloning for non-Gaussian continuous variables", New J. Phys. **12**, 103010 (2010).

[74] K. Hammerer, A. S. Sørensen, and E. S. Polzik, "Quantum interface between light and atomic ensembles", Rev. Mod. Phys. **82**, 1041 (2010).

[75] A. Kuzmich, L. Mandel, and N. P. Bigelow, "Generation of spin squeezing via continuous quantum nondemolition measurement", Phys. Rev. Lett. **85**, 1594 (2000).

[76] B. Julsgaard, A. Kozhekin, and E. S. Polzik, "Experimental long-lived entanglement of two macroscopic objects", Nature (London) **413**, 400 (2001).

[77] G. Vasilakis, V. Shah, and M. V. Romalis, "Stroboscopic backaction evasion in a dense alkali-metal vapor", Phys. Rev. Lett. **106**, 143601 (2011).

[78] N. Behbood, G. Colangelo, F. Martin Ciurana, M. Napolitano, R. J. Sewell, and M. W. Mitchell, "Feedback cooling of an atomic spin ensemble", Phys. Rev. Lett. **111**, 103601 (2013).

[79] V. B. Braginsky, Y. I. Vorontsov, and K. S. Thorne, "Quantum nondemolition measurements", Science **209**, 547 (1980).

[80] C. Monroe, "Demolishing quantum nondemolition", Phys. Today **64**, 8 (2011).

[81] M. H. Schleier-Smith, I. D. Leroux, and V. Vuletić, "States of an ensemble of two-level atoms with reduced quantum uncertainty", Phys. Rev. Lett. **104**, 073604 (2010).

[82] Z. Chen, J. G. Bohnet, S. R. Sankar, J. Dai, and J. K. Thompson, "Conditional spin squeezing of a large ensemble via the vacuum Rabi splitting", Phys. Rev. Lett. **106**, 133601 (2011).

[83] J. G. Bohnet, K. C. Cox, M. A. Norcia, J. M. Weiner, Z. Chen, and J. K. Thompson, "Reduced spin measurement back-action for a phase sensitivity ten times beyond the standard quantum limit", Nat. Photonics **8**, 731 (2014).

[84] O. Hosten, N. J. Engelsen, R. Krishnakumar, and M. A. Kasevich, "Measurement noise 100 times lower than the quantum-projection limit using entangled atoms", Nature (London) **529**, 505 (2016).

[85] R. J. Sewell, M. Koschorreck, M. Napolitano, B. Dubost, N. Behbood, and M. W. Mitchell, "Magnetic sensitivity beyond the projection noise limit by spin squeezing", Phys. Rev. Lett. **109**, 253605 (2012).

[86] A. Kuzmich, N. P. Bigelow, and L. Mandel, "Atomic quantum non-demolition measurements and squeezing", Europhys. Lett. **42**, 481 (1998).

[87] M. H. Schleier-Smith, I. D. Leroux, and V. Vuletić, "Squeezing the collective spin of a dilute atomic ensemble by cavity feedback", Phys. Rev. A **81**, 021804 (2010).

[88] I. D. Leroux, M. H. Schleier-Smith, and V. Vuletić, "Implementation of cavity squeezing of a collective atomic spin", Phys. Rev. Lett. **104**, 073602 (2010).

[89] E. Davis, G. Bentsen, and M. Schleier-Smith, "Approaching the Heisenberg limit without single-particle detection", Phys. Rev. Lett. **116**, 053601 (2016).

[90] O. Hosten, R. Krishnakumar, N. J. Engelsen, and M. A. Kasevich, "Quantum phase magnification", Science **352**, 1552 (2016).

[91] T. Holstein and H. Primakoff, "Field dependence of the intrinsic domain magnetization of a ferromagnet", Phys. Rev. **58**, 1098 (1940).

[92] A. Keshet and W. Ketterle, "A distributed, graphical user interface based, computer control system for atomic physics experiments", Rev. Sci. Instrum. **84**, 015105 (2013).

[93] B. R. Mollow, "Power spectrum of light scattered by two-level systems", Phys. Rev. **188**, 1969 (1969).

[94] R. H. Dicke, "Coherence in spontaneous radiation processes", Phys. Rev. **93**, 99 (1954).

[95] F. Marquardt, J. P. Chen, A. A. Clerk, and S. M. Girvin, "Quantum theory of cavity-assisted sideband cooling of mechanical motion", Phys. Rev. Lett. **99**, 093902 (2007).

[96] L. Dellantonio, O. Kyriienko, F. Marquardt, and A. S. Sørensen, "Quantum nondemolition measurement of mechanical motion quanta", (2018).

[97] G. Bao, A. Wickenbrock, S. Rochester, W. Zhang, and D. Budker, "Suppression of the nonlinear Zeeman effect and heading error in earth-field-range alkali-vapor magnetometers", Phys. Rev. Lett. **120**, 033202 (2018).

[98] G. Colangelo, F. M. Ciurana, L. C. Bianchet, R. J. Sewell, and M. W. Mitchell, "Simultaneous tracking of spin angle and amplitude beyond classical limits", Nat. Publ. Gr. **543**, 525 (2017).

[99] R. B. Blackman and J. W. Tukey, "The measurement of power spectra from the point of view of communications engineering - part II", Bell Syst. Tech. J. **37**, 485 (1958).

[100] R. J. Glauber, "Amplifiers, attenuators, and Schrödinger's cat", Ann. N. Y. Acad. Sci. **480**, 336 (1986).

[101] J. Kohler, J. A. Gerber, E. Dowd, and D. M. Stamper-Kurn, "Simultaneous multimode optodynamical state estimation with linear filters", forthcoming, 2018.

[102] H. Krauter, C. A. Muschik, K. Jensen, W. Wasilewski, J. M. Petersen, J. I. Cirac, and E. S. Polzik, "Entanglement generated by dissipation and steady state entanglement of two macroscopic objects", Phys. Rev. Lett. **107**, 080503 (2011).

[103] C. K. Andersen and K. Mølmer, "Squeezing of collective excitations in spin ensembles", Phys. Rev. A **86**, 043831 (2012).

[104] F. Bloch and A. Siegert, "Magnetic resonance for nonrotating fields", Phys. Rev. **57**, 522 (1940).

[105] J. H. Shirley, "Solution of the Schrödinger equation with a Hamiltonian periodic in time", Phys. Rev. **138**, B979 (1965).

[106] Y. Yan, Z. Lü, and H. Zheng, "Bloch-Siegert shift of the Rabi model", Phys. Rev. A **91**, 053834 (2015).

[107] C. M. Caves, J. Combes, Z. Jiang, and S. Pandey, "Quantum limits on phase-preserving linear amplifiers", Phys. Rev. A **86**, 063802 (2012).

[108] W. Wasilewski, K. Jensen, H. Krauter, J. J. Renema, M. V. Balabas, and E. S. Polzik, "Quantum noise limited and entanglement-assisted magnetometry", Phys. Rev. Lett. **104**, 133601 (2010).

[109] G. Vasilakis, H. Shen, K. Jensen, M. Balabas, D. Salart, B. Chen, and E. S. Polzik, "Generation of a squeezed state of an oscillator by stroboscopic back-action-evading measurement", Nat. Phys. **11**, 389 (2015).

[110] A. P. Reed, K. H. Mayer, J. D. Teufel, L. D. Burkhart, W. Pfaff, M. Reagor, L. Sletten, X. Ma, R. J. Schoelkopf, E. Knill, and K. W. Lehnert, "Faithful conversion of propagating quantum information to mechanical motion", Nat. Phys. **13**, 1163 (2017).

[111] C. Eichler, D. Bozyigit, C. Lang, L. Steffen, J. Fink, and A. Wallraff, "Experimental state tomography of itinerant single microwave photons", Phys. Rev. Lett. **106**, 220503 (2011).

[112] S. Gammelmark, B. Julsgaard, and K. Mølmer, "Past quantum states of a monitored system", Phys. Rev. Lett. **111**, 160401 (2013).

[113] J. Zhang and K. Mølmer, "Prediction and retrodiction with continuously monitored Gaussian states", Phys. Rev. A **96**, 062131 (2017).

[114] Z. Huang and M. Sarovar, "Smoothing of Gaussian quantum dynamics for force detection", Phys. Rev. A **97**, 042106 (2018).

[115] W. Wieczorek, S. G. Hofer, J. Hoelscher-Obermaier, R. Riedinger, K. Hammerer, and M. Aspelmeyer, "Optimal state estimation for cavity optomechanical systems", Phys. Rev. Lett. **114**, 12 (2015).

[116] F. W. McElroy, "A necessary and sufficient condition that ordinary least-squares estimators be best linear unbiased", J. Am. Stat. Assoc. **62**, 1302 (1967).

[117] L. A. Wainstein and V. D. Zubakov, *Extraction of signals from noise*, trans. by R. A. Silverman (Dover Publ., Incorporated, New York, 1970).

[118] C. Chatfield and A. J. Collins, *Introduction to multivariate analysis* (Springer US, Boston, MA, 1980).

[119] C. W. Helstrom, *Statistical theory of signal detection*, 2nd (Pergamon Press, London, 1968).

[120] B. P. Abbott et al., "Analysis of LIGO data for gravitational waves from binary neutron stars", Phys. Rev. D **69**, 122001 (2004).

[121] A. C. Aitken, "IV.–On least squares and linear combination of observations", Proc. R. Soc. Edinburgh **55**, 42 (1936).

[122] C. W. Gardiner, *Handbook of stochastic methods*, 3rd (Springer-Verlag Berlin Heidelberg, Berlin, 2004).

[123] E. Brion, L. H. Pedersen, and K. Mølmer, "Adiabatic elimination in a lambda system", J. Phys. A Math. Theor. **40**, 1033 (2007).

[124] G. Breit and I. I. Rabi, "Measurement of nuclear spin", Phys. Rev. **38**, 2082 (1931).

[125] The HDF Group, *Hierarchical Data Format, version 5*, (1997-2018) `http://www.hdfgroup.org/HDF5/`.

Appendix A

Generalized Tavis-Cummings model and tensor corrections

Here I present a derivation of the spin-dependent dispersive interaction Hamiltonian stated in Eq. 2.7, starting from the generalized Tavis-Cummings models given by Eqs. 2.6. I closely follow the method used in Ref. [45], first finding approximate equations of motion for the atomic ground-state density operators after eliminating the excited-state manifolds, then postulating an effective Hamiltonian that gives rise to the same equations of motion. In retrospect, there is likely a much more elegant solution described by second-order perturbation theory [123], however the following brute-force approach does help demonstrate some features of the approximation. In this derivation, I neglect the spatial variation of the cavity mode $|U(\hat{\boldsymbol{r}})|^2$ for clarity, since it can be factored out of the original Hamiltonian. The equations of motion for the the atomic density operators can be evaluated with the help of the commutation relation

$$\left[\hat{\sigma}^{(i)}_{\alpha;\beta}, \hat{\sigma}^{(j)}_{\mu;\nu}\right] = \left(\hat{\sigma}^{(i)}_{\alpha;\nu}\delta_{\beta\mu} - \hat{\sigma}^{(i)}_{\mu;\beta}\delta_{\alpha\nu}\right)\delta_{ij}, \tag{A.1}$$

where α, β, μ, ν each represent full sets of atomic quantum numbers.

Evolution of the ground-state populations and coherences $\hat{\sigma}^{(i)}_{g,f,m+n;g,f,m}$ is given by

$$\frac{\partial}{\partial t}\hat{\sigma}^{(i)}_{g,f,m+n;g,f,m} = i\sum_{f'}\Big\{g^{+}_{f,m+n;f',m+n+1}\hat{c}_{+}\hat{\sigma}^{(i)}_{e,f',m+n+1;g,f,m}+g^{-}_{f,m+n;f',m+n-1}\hat{c}_{-}\hat{\sigma}^{(i)}_{e,f',m+n-1;g,f,m}$$

$$- g^{+}_{f,m;f',m+1}\hat{\sigma}^{(i)}_{g,f,m+n;e,f',m+1}\hat{c}^{\dagger}_{+} - g^{-}_{f,m;f',m-1}\hat{\sigma}^{(i)}_{g,f,m+n;e,f',m-1}\hat{c}^{\dagger}_{-}\Big\}, \quad (A.2)$$

describing dynamics induced by optical coupling on all possible transitions to the excited state manifolds.

Next, in order to eliminate the excited states from these equations of motion, I need to find approximate expressions for the ground-state/excited-state coherences $\hat{\sigma}^{(i)}_{g,f,m+n;e,f',m}$. The first approximation is made here, assuming that, in the dispersive limit, all populations

and coherences involving only excited states are negligible

$$\hat{\sigma}^{(i)}_{e,f',m';e,f'',m''} \approx 0. \tag{A.3}$$

Under this approximation, the equations of motion for the ground-state/excited-state coherences simplify to

$$\frac{\partial}{\partial t}\hat{\sigma}^{(i)}_{g,f,m+n;e,f',m} = -i(\omega_{\mathrm{a}} + \Delta_{f'})\hat{\sigma}^{(i)}_{g,f,m+n;e,f',m}$$
$$- ig^{+}_{f,m-1;f',m}\hat{c}_{+}\hat{\sigma}^{(i)}_{g,f,m+n;g,f,m-1} - ig^{-}_{f,m+1;f',m}\hat{c}_{-}\hat{\sigma}^{(i)}_{g,f,m+n;g,f,m+1}, \tag{A.4}$$

with the optical field inducing coherences between the ground-states and excited-states depending on the ground-state only density operators.

Next, because the cavity modes $\hat{c}_{\pm}$ and the atomic coherences $\hat{\sigma}^{(i)}_{g,f,m+n;e,f',m}$ rapidly oscillate, with frequencies ω_{c} and about ω_{a} respectively, which are fast relative to all other time scales, it is helpful to transform into a frame rotating at the cavity frequency to remove the fastest of these dynamics

$$\hat{\sigma}^{(i)}_{g,f,m+n;e,f',m} \rightarrow \hat{\sigma}^{(i)}_{g,f,m+n;e,f',m}e^{-i\omega_{\mathrm{c}}t} \qquad \text{and} \qquad \hat{c}_{\pm} \rightarrow \hat{c}_{\pm}e^{-i\omega_{\mathrm{c}}t}. \tag{A.5}$$

The transformed equations of motion, in the rotating frame, are

$$\frac{\partial}{\partial t}\hat{\sigma}^{(i)}_{g,f,m+n;e,f',m} = i(\Delta_{\mathrm{ca}} + \Delta_{f'})\hat{\sigma}^{(i)}_{g,f,m+n;e,f',m}$$
$$- ig^{+}_{f,m-1;f',m}\hat{c}_{+}\hat{\sigma}^{(i)}_{g,f,m+n;g,f,m-1} - ig^{-}_{f,m+1;f',m}\hat{c}_{-}\hat{\sigma}^{(i)}_{g,f,m+n;g,f,m+1}. \tag{A.6}$$

Now the ground-state/excited-state coherences rotate at the cavity detuning frequency $\Delta_{\mathrm{ca}} + \Delta_{f'}$, which is still fast relative to the final two source terms, which are products between the slowly varying cavity field in the rotating frame and the ground-state populations and coherences. This clear separation of timescales allows adiabatic elimination of the remaining fast excited-state dynamics, since only slow evolution of these coherences contribute to the ground-state equations of motion in Eq. A.2. Here, in practice, the approximate solution can be obtained by finding stationary solutions to the ground-state/excited-state coherences, given by

$$\frac{\partial}{\partial t}\hat{\sigma}^{(i)}_{g,f,m+n;e,f',m} \approx 0. \tag{A.7}$$

However, this shortcut can be more rigorously justified by solving the Fourier transform of Eq. A.6 and then assuming that only frequencies $\omega \ll \Delta_{\mathrm{ca}} + \Delta_{f'}$ are significant in computing the inverse transform, yielding

$$\hat{\sigma}^{(i)}_{g,f,m+n;e,f',m} = \frac{1}{\Delta_{\mathrm{ca}} + \Delta_{f'}}\left(g^{+}_{f,m-1;f',m}\hat{c}_{+}\hat{\sigma}^{(i)}_{g,f,m+n;g,f,m-1}\right.$$
$$\left. + g^{-}_{f,m+1;f',m}\hat{c}_{-}\hat{\sigma}^{(i)}_{g,f,m+n;g,f,m+1}\right) \tag{A.8}$$

This result can be substituted into the ground-state equations of motion in Eq. A.2, yielding expressions which involve only ground-state density operators, and therefore I will drop the indices g, f from the density operators for clarity. Taking care of photon operator commutators and grouping sums of dipole coefficients, the remaining equations of motion can be written

$$\partial_t \hat{\sigma}^{(i)}_{m+n,m} = i\big[a_+(m+n) - a_+(m)\big]\hat{c}^\dagger_+\hat{c}_+\hat{\sigma}^{(i)}_{m+n,m} + i\big[a_-(m+n) - a_-(m)\big]\hat{c}^\dagger_-\hat{c}_-\hat{\sigma}^{(i)}_{m+n,m}$$
$$+ i\,b(m+n+1)\,\hat{c}^\dagger_-\hat{c}_+\hat{\sigma}^{(i)}_{m+n+2,m} - i\,b(m-1)\,\hat{c}^\dagger_-\hat{c}_+\hat{\sigma}^{(i)}_{m+n,m-2}$$
$$+ i\,b(m+n-1)\,\hat{c}^\dagger_+\hat{c}_-\hat{\sigma}^{(i)}_{m+n-2,m} - i\,b(m+1)\,\hat{c}^\dagger_+\hat{c}_-\hat{\sigma}^{(i)}_{m+n,m+2}, \quad (A.9)$$

having defined

$$a_\pm(m) = \sum_{f'} \frac{(g^\pm_{f,m;f',m\pm1})^2}{\Delta_{\mathrm{ca}} + \Delta_{f'}} \quad (A.10)$$

$$b(m) = \sum_{f'} \frac{(g^+_{f,m-1;f',m})(g^-_{f,m+1;f',m})}{\Delta_{\mathrm{ca}} + \Delta_{f'}} \quad (A.11)$$

Now, postulating the effective Hamiltonian

$$\mathcal{H}^{(i)}_I \approx \hbar \sum_m \left\{ \left(a_+(m)\hat{c}^\dagger_+\hat{c}_+ + a_-(m)\hat{c}^\dagger_-\hat{c}_-\right)\hat{\sigma}^{(i)}_{m,m} \right.$$
$$\left. + b(m)\left(\hat{c}^\dagger_-\hat{c}_+\hat{\sigma}^{(i)}_{m+1,m-1} + \hat{c}^\dagger_+\hat{c}_-\hat{\sigma}^{(i)}_{m-1,m+1}\right)\right\}, \quad (A.12)$$

it can be shown to reproduce the same equations of motion. This effective Hamiltonian describes the approximate dynamics in dispersive limit, where the cavity detuning from the excited state hyperfine levels is sufficiently large, such that the excited state populations are negligible and the ground-state/excited-state coherences adiabatically follow the cavity field.

QED coupling constants

The cavity-enhanced dipole coupling strengths $g^\pm_{f,m;f',m'}$ are spin-state and polarization dependent, described for each available transition in terms of the dipole matrix element for circular unit polarization vectors $\mathbf{e}_\pm = \mp(\mathbf{x} \pm i\mathbf{y})/\sqrt{2}$

$$g^\pm_{f,m;f',m'} = \sqrt{\frac{\omega_0}{2\hbar\epsilon_0 V_m}}\,\big\langle fm|\mathbf{e}^*_{\pm1} \cdot e\boldsymbol{r}|f'm'\big\rangle \quad (A.13)$$

These matrix elements can be decomposed into a product of the reduced dipole matrix element for the D_2 transition, Clebsch-Gordon coefficients, and a Wigner 6-J symbol [43, 45], summarizing the selection rules and coupling strengths for the various angular momentum states. In terms of these elements, the coupling strengths can be expressed as

$$g^\pm_{f,m;f',m'} = 2\,(-1)^{f'+m'-m}\,\sqrt{2f+1}\,\langle fm;1\pm1|f'm'\rangle \begin{Bmatrix} f & f' & 1 \\ j' & j & I \end{Bmatrix} g_0, \quad (A.14)$$

relative to the familiar cycling-transition coupling strength g_0 defined in Eq. 2.3. For the ^{87}Rb D$_2$ transition, with $j = 1/2$, $j' = 3/2$, and $I = 3/2$, and assuming the $f = 2$ ground state manifold, this expression reduces to the Clebsch-Gordon coefficients

$$g^{\pm}_{2,m;f',m'} = \frac{1}{\sqrt{2}} \langle 2m; 1 \pm 1 | f'm' \rangle g_0 \tag{A.15}$$

The coupling constants defined by Eqs. A.10 and A.11 can be written in terms of products of these Clebsch-Gordon coefficients, expanded in powers of m as

$$a_{\pm}(m) = \frac{g_0^2}{\Delta_{ca}} \left(\alpha_0 \pm \alpha_1 m + \alpha_2 m^2 \right) \tag{A.16}$$

$$b(m) = \frac{g_0^2}{\Delta_{ca}} \alpha_2 \sqrt{(2+m)(3+m)(3-m)(2-m)} \tag{A.17}$$

defining the unitless scalar, vector, and tensor coupling constants α_0, α_1, and α_2, respectively, given for the $f = 2$ ground-state manifold by Eqs. 2.8.

Now the effective Hamiltonian from Eq. A.12 can be written as

$$\mathcal{H}_I^{(i)} \approx \hbar \frac{g_0^2}{\Delta_{ca}} \sum_m \Big\{ \left[\alpha_0 \left(\hat{n}_+ + \hat{n}_- \right) + \alpha_1 \left(\hat{n}_+ - \hat{n}_- \right) m + \alpha_2 \left(\hat{n}_+ + \hat{n}_- \right) m^2 \right] \hat{\sigma}^{(i)}_{m,m}$$

$$- \alpha_2 \sqrt{(2+m)(3+m)(3-m)(2-m)} \left[\hat{c}^{\dagger}_- \hat{c}_+ \hat{\sigma}^{(i)}_{m+1,m-1} + \hat{c}^{\dagger}_+ \hat{c}_- \hat{\sigma}^{(i)}_{m-1,m+1} \right] \Big\}. \tag{A.18}$$

The sums over ground-state density operators can be recognized as moments of the spin operators

$$\hat{f}_k^{(i)} = \sum_m m \, \hat{\sigma}^{(i)}_{m,m}$$

$$\left(\hat{f}_k^{(i)} \right)^2 = \sum_m m^2 \hat{\sigma}^{(i)}_{m,m}$$

$$\left(\hat{f}_{\pm}^{(i)} \right)^2 = \sum_m \sqrt{(f-m)(f+m)(f+m+1)(f-m+1)} \, \hat{\sigma}^{(i)}_{m\pm1,m\mp1},$$

where $\hat{f}_{\pm}^{(i)}$ adds or removes a unit of angular momentum along $\mathbf{k}$, satisfying $[\hat{f}_k^{(i)}, \hat{f}_{\pm}^{(i)}] = \pm \hat{f}_{\pm}^{(i)}$, resulting in dispersive Hamiltonian stated in Eq. 2.7.

A.1   Quadratic Zeeman shift

There are also tensor corrections to the atomic spin dynamics induced by a large magnetic field. The Hamiltonian taken in Eq. 3.2 to describe the influence of the applied magnetic field on the atomic states already assumes a Zeeman energy shift linear in the magnetic

field magnitude. This approximation is valid only in the weak field limit, with the second-order correction described by the quadratic Zeeman shift. For Alkali atoms, with $j = 1/2$ electronic ground states from one valance electron with $l = 0$, the Zeeman energy splitting of the ground-state hyperfine sublevels, labeled by m, can be solved exactly by the Breit-Rabi formula [124]

$$\Delta E = -\frac{\hbar\omega_{\text{hfs}}}{2(2I+1)} + \mu_B g_I |\boldsymbol{B}| m \pm \frac{\hbar\omega_{\text{hfs}}}{2}\sqrt{1 + \frac{2xm}{I+1/2} + x^2} \tag{A.19}$$

$$= -\frac{\hbar\omega_{\text{hfs}}}{2(2I+1)} + \hbar\omega_{\text{s}}\frac{g_I}{g_f}m \pm \frac{\hbar\omega_{\text{hfs}}}{2}\sqrt{1 + \frac{2xm}{I+1/2} + x^2} \tag{A.20}$$

in terms of the ground-state hyperfine splitting ω_{hfs} and defining field-strength parameter

$$x = \frac{\mu_B|\boldsymbol{B}|(g_j - g_I)}{\hbar\omega_{\text{hfs}}} \tag{A.21}$$

$$= \frac{g_j - g_I}{f}\frac{\omega_{\text{s}}}{\omega_{\text{hfs}}}, \tag{A.22}$$

alternately written in terms of the small-field Larmor frequency, $\omega_{\text{s}} = \mu_B g_f |\boldsymbol{B}|/\hbar$.

For a small B-field ($\omega_{\text{s}} \ll \omega_{\text{hfs}}$) along $\mathbf{z}$, the Zeeman splitting can be approximated by a Taylor expansion to second order, yielding

$$\Delta E \approx \frac{\pm(2I+1)-1}{2(2I+1)}\hbar\omega_{\text{hfs}} + \frac{(4\mp1)g_I \pm g_j}{4g_f}\hbar\omega_{\text{s}}m \mp \frac{(g_j - g_I)^2}{16g_f^2}\hbar\frac{\omega_{\text{s}}^2}{\omega_{\text{hfs}}}m^2. \tag{A.23}$$

For the electronic ground-state of ^{87}Rb, the nuclear angular momentum is $I = 3/2$ with g-factor $g_I \approx 0$, and the electronic g-factor is $g_j \approx 2$. Within the $f = 2$ hyperfine manifold, the total atomic spin g-factor is $g_f = 1/2$, resulting in magnetic Zeeman shifts

$$\Delta E \approx \frac{3}{8}\hbar\omega_{\text{hfs}} + \hbar\omega_{\text{s}}m - \hbar\frac{\omega_{\text{s}}^2}{\omega_{\text{hfs}}}m^2, \tag{A.24}$$

while for $f = 1$, $g_f = -1/2$ and the shifts are given by

$$\Delta E \approx -\frac{5}{8}\hbar\omega_{\text{hfs}} + \hbar\omega_{\text{s}}m + \hbar\frac{\omega_{\text{s}}^2}{\omega_{\text{hfs}}}m^2. \tag{A.25}$$

The effective Hamiltonian for a single hyperfine manifold can then be written

$$\mathcal{H} = \hbar\omega_{\text{s}}\hat{f}_z + \hbar\omega_q\hat{f}_z^2 \tag{A.26}$$

where ω_q is the quadratic Zeeman shift, given for $f = 2$ (or $f = 1$ with plus sign) by

$$\omega_q = \mp\frac{\omega_{\text{s}}^2}{\omega_{\text{hfs}}} \tag{A.27}$$

This quadratic term couples the vector and tensor components of the spin states, resulting in an oscillation between the transverse spin components and nematic spin components, with a collapse and rival time of the transverse polarization given by $\tau = \pi/\omega_q$, such as observed in Fig. 3.13d.

The transverse spin component for a single atom $\hat{f}_x$ can be written in terms of the first-order coherences

$$\hat{f}_x = \sum_{m=-f}^{f-1} \sqrt{f(f+1) - m(m+1)} \, \mathrm{Re}[\hat{\sigma}_{m+1,m}] \tag{A.28}$$

with $\hat{\sigma}_{m+1,m} = |m+1\rangle \langle m|$. Its time evolution, in a frame rotating at the Larmor frequency, is given by the density-matrix components evolving under the quadratic shift

$$\hat{f}_x(t) = \sum_{m=-f}^{f-1} \sqrt{f(f+1) - m(m+1)} \, \mathrm{Re}[\hat{\sigma}_{m+1,m}(0)e^{-i(2m+1)\omega_q t}]. \tag{A.29}$$

For a spin prepared along $\boldsymbol{x}$, the resulting evolution of of the transverse spin magnitude for $f = 2$ is

$$\langle |\hat{\boldsymbol{f}}_\perp(t)| \rangle = \frac{1}{4} \left| 3\cos\omega_q t + \cos 3\,\omega_q t \right|, \tag{A.30}$$

displayed in Fig. A.1 along with analogous results for $f = 1$.

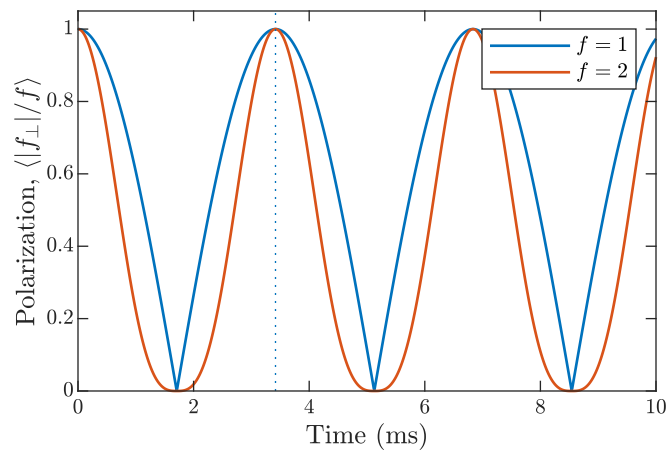Figure A.1: Collapse and revival of spin polarization from induced by the quadratic Zeeman shift, for a Rb-87 atom in a 1.4 gauss magnetic field, inducing a Larmor frequency of $\omega_s = 2\pi \times 1$ MHz and quadratic Zeeman shift $|\omega_q| = 2\pi \times 147$ Hz, for both $f = 1$ and $f = 2$ manifolds. The longer collapse time for $f = 2$ reflects the larger number of frequency components in the evolution of coherences.

Appendix B

Heterodyne signal calibrations

B.1 Photon number calibration

Considering a driven, empty cavity, the average intracavity photon number $\bar{n} = \langle \hat{c}^\dagger \hat{c} \rangle$ can be determined from the transmitted probe power $P_p = 2\kappa\epsilon_{\mathrm{cav}}\bar{n}\hbar\omega_{\mathrm{p}}$. Assuming the cavity mode is in a coherent state, with amplitude $\langle \hat{c} \rangle = \sqrt{\bar{n}}$, and calculating the autocorrelation of the output field given by Eq. 2.55, the inferred optical PSD $S_{\mathrm{het}}(f) = S_{ii}[f]/A_r^2$ is

$$S_{\mathrm{het}}[f] = \epsilon_{\mathrm{mm}}P_p P_{LO}\left(\delta(f - f_0) + \delta(f + f_0)\right) + \frac{P_{LO}\hbar\omega_{\mathrm{p}}}{\epsilon_{\mathrm{Q}}} \tag{B.1}$$

The optical power transmitted through the output mirror of the cavity is $P_{\mathrm{out}} = 2\kappa\epsilon_{\mathrm{cav}}\bar{n}\hbar\omega_{\mathrm{p}}$, and, given a path efficiency ϵ_{path}, the inferred optical PSD is

$$S_{\mathrm{het}}[f] = 2\kappa\epsilon_{\mathrm{cav}}\epsilon_{\mathrm{path}}\epsilon_{\mathrm{mm}}\bar{n}P_{LO}\hbar\omega_{\mathrm{p}}\left(\delta(f - f_0) + \delta(f + f_0)\right) + \frac{P_{LO}\hbar\omega_{\mathrm{p}}}{\epsilon_{\mathrm{Q}}} \tag{B.2}$$

Defining the heterodyne shot noise PSD as

$$S_{\mathrm{SN}} = S_{\mathrm{het}}[f \neq f_0] = \frac{P_{LO}\hbar\omega_{\mathrm{p}}}{\epsilon_{\mathrm{Q}}} \tag{B.3}$$

then the photon number can be determined from the total power in a small band around f_0,

$$P_{\mathrm{car}} = \int_{-\delta f/2}^{\delta f/2} df\, S_{\mathrm{het}}[f_0 + f] = 2\kappa\epsilon\bar{n}S_{\mathrm{SN}} + S_{\mathrm{SN}}\delta f \tag{B.4}$$

where $\epsilon = \epsilon_{\mathrm{cav}}\epsilon_{\mathrm{path}}\epsilon_{\mathrm{mm}}\epsilon_{\mathrm{Q}}$ is the total cavity photon detection efficiency.

For a discrete spectrum, if the sample frequency is not exactly commensurate with the heterodyne frequency, then the carrier power is spread between at least two discrete frequencies, such that the spectrum must be integrated across a sufficient frequency band δf to capture the full carrier power, yielding

$$\bar{n} = \frac{P_{\mathrm{car}} - S_{\mathrm{SN}}\delta f}{4S_{\mathrm{SN}}\kappa\epsilon_{\mathrm{het}}}, \tag{B.5}$$

in terms of the effective heterodyne detection efficiency $\epsilon_{\text{het}} = \epsilon/2$ and noting that κ is the angular-frequency cavity half-linewidth.

B.2 Photodetector gain

There are many stages in the probe detection chain, each of which must be calibrated in order to accurately interpret the recorded signals. Our Newport 1807-FS balanced photodetector has a built-in transimpedance amplifier, with an output voltage given by the total detector gain

$$G_{\text{TI}}^{\infty} = Z_{\text{TI}}A_r = 29 \text{ V/mW}, \tag{B.6}$$

a product of the photodiode responsivity $A_r = e\epsilon_{\text{Q}}/\hbar\omega_{\text{p}}$ and the transimpedance Z_{TI}, defined in Sec. 2.6.

We cannot easily measure these parameters individually, since the sealed detector does not give direct access to the photocurrent. However, the product was calibrated by measuring the average output voltage (with a high-impedance digital multi-meter (DMM)) over a range of incident optical power. Fig. B.1 shows the results, measured with two independent calibrated power meters.
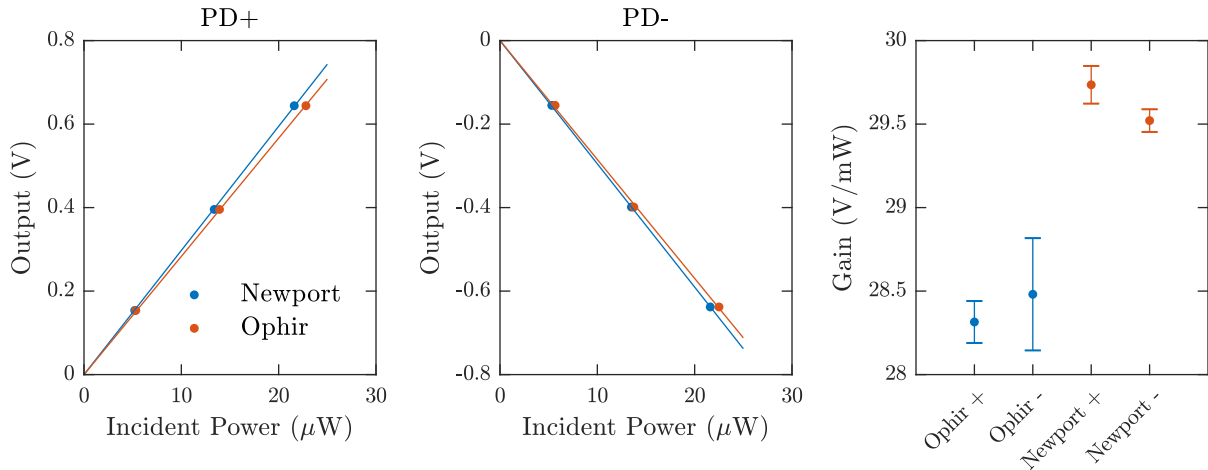

Figure B.1: Balanced photodetector calibration under constant illumination of each individual photodiode with a incident power measured with two commercial power meters.

B.3   Quantum efficiency

The rated quantum efficiency of our photodetector, $\epsilon_Q = 0.8$, can be inferred from the responsivity $A_r = 0.5$ A/W read off of the manufacturer's datasheet. However, the actual efficiency might differ or could be effectively reduced by poor alignment onto the photodiode or other optical losses.

For a shot noise limited optical detection, the effective quantum efficiency can be inferred from the observed shot noise PSD of the output voltage.

$$S_{VV} = (G_{\mathrm{TI}}^{\infty})^2 S_{\mathrm{sn}} = (G_{\mathrm{TI}}^{\infty})^2 \frac{P_{\mathrm{LO}} \hbar \omega_{\mathrm{p}}}{\epsilon_Q} \tag{B.7}$$

For a known detector gain G_{TI}^{∞}, the observed RMS shot noise voltage is inversely proportional to ϵ_Q, because a reduced quantum efficiency implies a correspondingly greater transimpedance Z_{TI}, representing greater classical amplification of the detected optical shot noise fluctuations.

Illuminating the balanced photodetector with the LO only, the shot noise spectrum was measured on a spectrum analyzer at a range of incident LO power, summarized in Fig. B.2. The linear scaling of the observed PSD confirms shot noise limited detection, and the fitted slope implies an actual quantum efficiency of about $\epsilon_Q = 0.6$.

The smaller measured value of ϵ_Q implies a larger intra-cavity photon number $\bar{n}$, compared to estimates formerly obtained using the rated value. However, other than calibrating the photon numbers used for comparison to theory, this has surprisingly few practical consequences. The detection efficiency is scaled away in most derived optodynamical signals, with the relevant information contained in the effective modulation depth, not the absolute intensities.
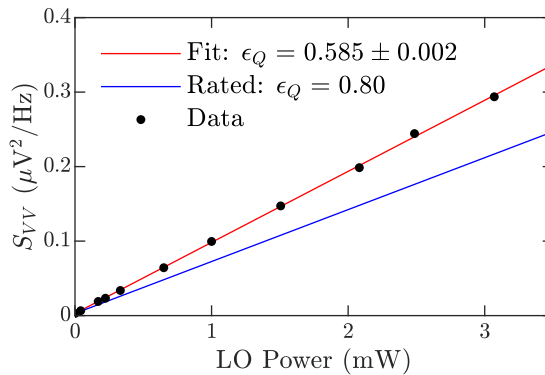

Figure B.2: Calibration of quantum efficiency from the observed shot noise PSD at the photodetector output.

B.4   Mode matching

The mode-matching efficiency describes the spatial overlap of the probe and LO modes. It is calibrated by measuring the incident probe and LO powers, P_p and P_{LO} respectively, then recording the RMS voltage V_{beat} of the heterodyne beatnote with a spectrum analyzer, given by

$$V_{\mathrm{beat}} = \frac{1}{2} G_{\mathrm{TI}}^{\infty} \sqrt{\epsilon_{\mathrm{mm}}} \sqrt{2 P_{\mathrm{LO}} P_p}. \tag{B.8}$$

Since the output impedance of the photo-diode and input impedance of the spectrum analyzer are both 50 Ω, the measured voltage is attenuated by a factor of 2. Therefore, the mode-matching efficiency can be inferred from the measured values according to

$$\epsilon_{\mathrm{mm}} = \frac{2(V_{\mathrm{beat}}/G_{\mathrm{TI}}^{\infty})^2}{P_p P_{\mathrm{LO}}} \tag{B.9}$$

B.5   Detection chain

The photodetector's output voltage passes through a bias-T, a 20 MHz low-pass filter, and then a +33 dB power amplifier. The amplifier's input impedance is nominally 50 Ω, attenuating the photodiode output by about 2 (assuming the nominal 50 Ω output impedance is accurate).

After the amplifier, the signal is split, with one half sent to Gagescope for recording and the other half to an analog lock box for real-time feedback. All together, the total gain of the electrical path from the photodiode output to GageScope input is $G_{\mathrm{amp}} = +29.6$ dB (measured at 10 MHz with a 50 Ω network analyzer). In terms of all the detection chain calibrations, the final output voltage as seen by GageScope, with input impedance Z_{GS}, is

$$V_{\mathrm{GS}}(t) = \frac{Z_{\mathrm{GS}}}{50 \ \Omega + Z_{\mathrm{GS}}} (10^{G_{\mathrm{amp}}/20}) G_{TI}^{\infty} P_{\mathrm{het}}(t) \tag{B.10}$$

in terms of the inferred optical power $P_{\mathrm{het}}(t)$, in units of W, which corresponds to the raw signal calculated in our analysis code.

Appendix C

Magnetic field calibrations

There are approximate Helmholtz configuration magnetic bias coils wrapped around the vacuum chamber along 3 different axes, illustrated in Fig. C.1. Each axis has a 'big' and a 'small' coil, defined according to the relative number of turns. Unless noted below, all calibrated bias fields are produced by currents supplied to the 'big' set of bias coils in each direction. In addition, there is a third 'ribbon' cable bias coil added in the up-down direction.

The magnetic fields produced by each bias coil can be accurately calibrated by fitting the Larmor precession frequency observed in the heterodyne output. To observe modulation of the cavity field from a precessing spin, there must be a significant component of the total magnetic field perpendicular to the cavity axis, such that the precessing transverse spin component is optodynamically driven by backaction from probe shot noise and modulates the cavity field, which can be observed in the transmitted heterodyne spectrum as discussed in Chap. 3. The field produced by any individual coil can then be calibrated by measuring the change in Larmor frequency it induces on top of a large background field transverse to the cavity axis. For an arbitrary background field $\boldsymbol{B}$, the total magnetic field magnitude can be decomposed into a component parallel to the field produced by the chosen coil and the remaining perpendicular field $\boldsymbol{B}_\perp$. These components add in quadrature to determine the Larmor frequency according to

$$f_L(I)^2 = \left(\frac{\gamma|\boldsymbol{B}_\perp|}{2\pi}\right)^2 + A_I^2(I - I_0)^2, \tag{C.1}$$

where A_I is the Larmor frequency per unit current supplied to the coil and I_0 is the current which minimizes the Larmor frequency, corresponding to the zero-field condition parallel to the coil axis.

Calibrations for the low-noise Keithley 2280S power supplies, used to supply coils for spin optodynamics experiments in Chs. 3 and 5, are plotted in Fig. C.2 along with fits to Eq. C.1. The fit results are summarized in Table C.1.

During atomic cooling and transport, most coils are supplied by Kepco ATE current sources, as described in Ref. [36]. The current output by the Kepco supplies is controlled by an analog voltage, which is output from the computer control system. Calibration of the
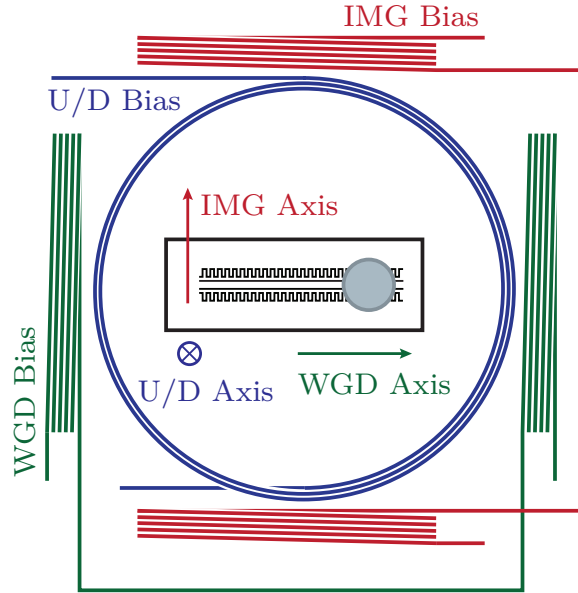
Figure C.1: Schematic of Helmholtz bias coils along axes defined according to the atom chip orientation, viewed from below with the cavity mirrors on the right (not to scale). The 'waveguide' (WGD) axis runs east-west, defined parallel to the atom chip waveguide wires which guide the magnetic transport of atoms from the MOT into the cavity. The 'imaging' (IMG) axis runs north-south, defined by the direction of absorption imaging of atoms in the MOT and cavity. The 'up-down' (U/D) axis is vertical, parallel to the longitudinal axis of the optical cavity.

field strengths produced by each coil are shown in Fig. C.3, in units of Larmor frequency per volt of the computer control output, and is fit to

$$f_L(V)^2 = \left(\frac{\gamma|\boldsymbol{B}_\perp|}{2\pi}\right)^2 + A_V^2(V - V_0)^2, \tag{C.2}$$

in terms of the Larmor frequency per unit control voltage A_V and the zero-field control voltage V_0. After transport, the IMG bias coil is switched to the low-noise Keithley source using a set of four mechanical relays.
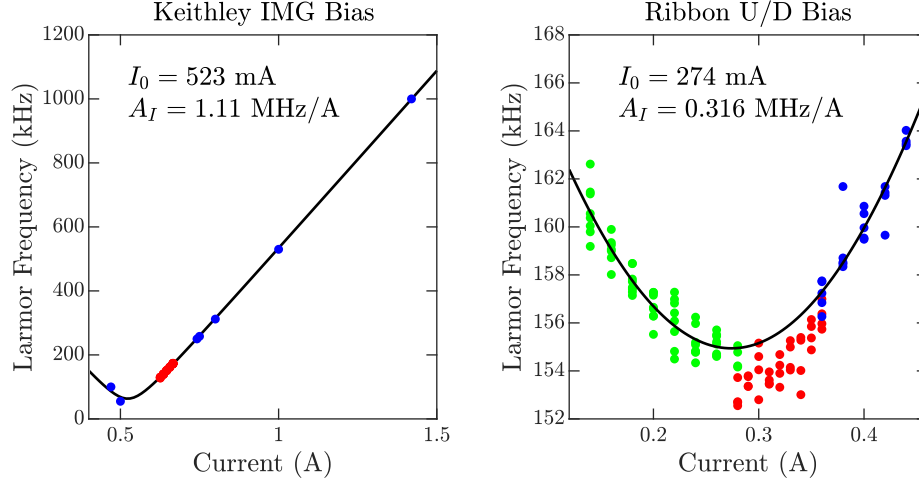
Figure C.2: Bias field calibration for Keithley current sources, fit to Eq. C.1. In these calibrations, current is driven through the IMG bias coil in the same direction as the Kepco current source, calibrated below, and the ribbon coil polarity creates a field *parallel* to the Big U/D coil driven by its Kepco supply.

	Slope		Offset		
Kepco Supplies	MHz/V	G/V	mV	kHz	mG
Big U/D	4.95 ± 0.22	7.08 ± 0.31	13.5 ± 0.3		
Small U/D	0.557 ± 0.002	0.795 ± 0.003	-145 ± 1		
IMG	3.15 ± 0.02	4.5 ± 0.02	158 ± 0.41		
WGD	1.97 ± 0.01	2.82 ± 0.02	338 ± 1		
Keithley Supplies	MHz/A	G/A	mA	kHz	mG
IMG	1.11 ± 0.004	1.59 ± 0.01	523 ± 1	582 ± 2	831 ± 2
Ribbon U/D	0.316 ± 0.006	0.451 ± 0.008	274 ± 2	86.5 ± 1.2	124 ± 2

Table C.1: Fit parameters, in cyclic frequency units, for each current source used to drive each coil. The parameters for Kepco current supplies are stated in units of the corresponding computer control voltage.
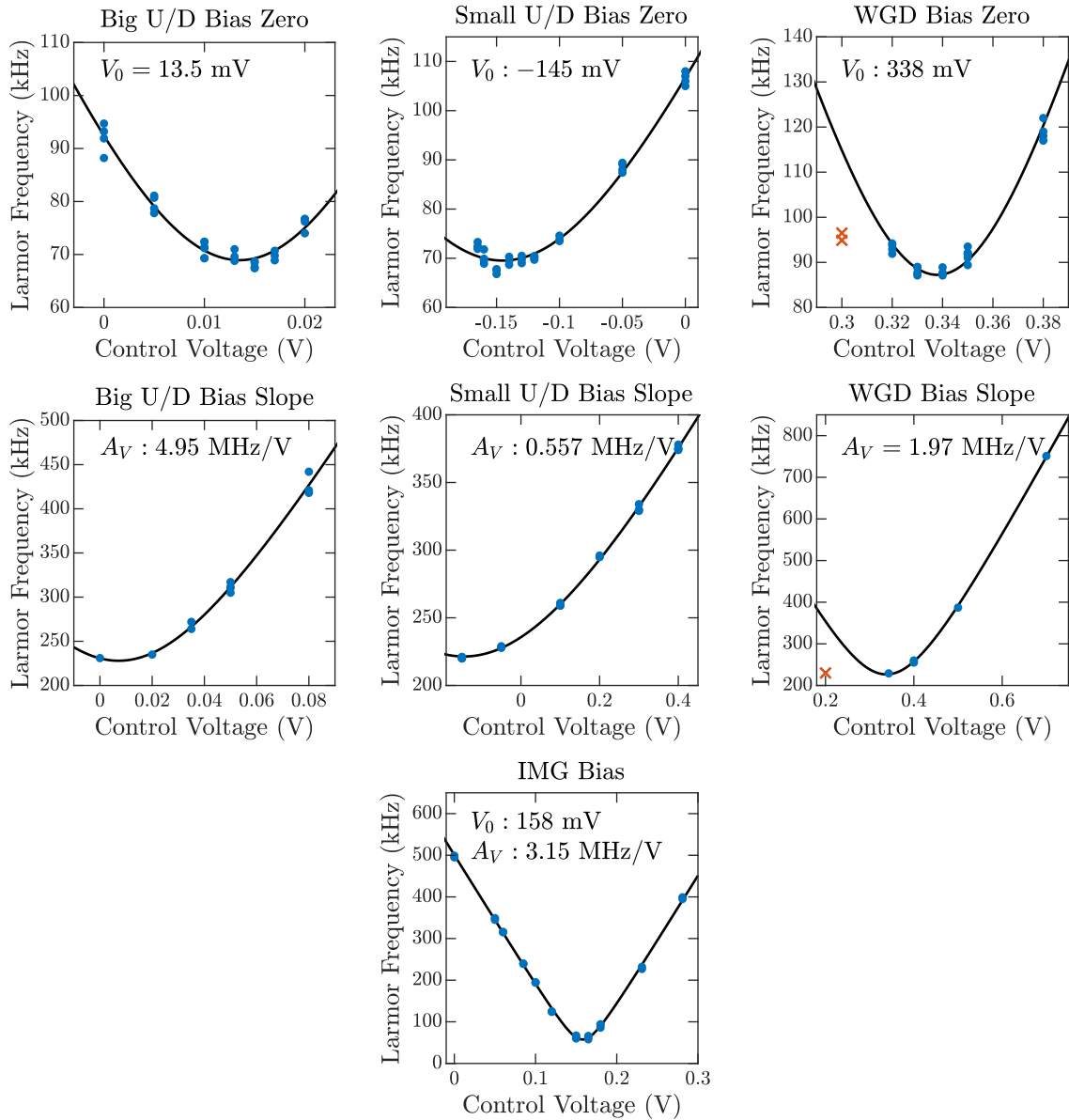
Figure C.3: Bias field calibration for Kepco current sources, fit to C.2. The slope and zero-field condition for most coils are determined by separate fits to different ranges of control voltages.

Appendix D

Probe detuning measurement and feedback stabilization

During most experiments, the probe detuning from cavity resonance is measured in real time by measuring the relative power transmitted through the cavity from sidebands phase-modulated onto the cavity probe laser with an electro-optical modulator (EOM), as displayed in Fig. D.1. These 'marker' sidebands conveniently encode information about the probe detuning into the recorded heterodyne signals, while being weak enough that their optodynamical effects can be neglected. In addition to providing a record for subsequent analysis, this information is used to provide real-time feedback to stabilize the probe frequency relative to the atom-shifted cavity resonance by deriving an analog error signal, as described in Ref. [38]. Here I will derive an analytic model for estimating this probe-cavity detuning from the recorded signals, and suggest an improved estimator derived from the heterodyne signal, analogous to a Pound-Drever-Hall error signal, which could be implemented in real-time with an field-programmable gate array (FPGA).
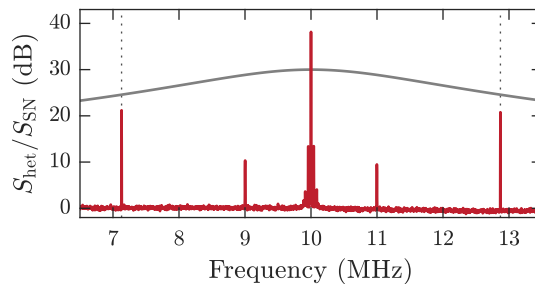

Figure D.1: Broadband heterodyne signal PSD, showing the EOM marker sidebands at $\omega_{\mathrm{m}} = 2\pi \times 2.87$ MHz around the carrier (dotted lines), in addition to the Larmor precession sidebands at $\omega_{\mathrm{s}} = 2\pi \times 1$ MHz. The cavity transmission profile is superimposed for reference.

Modulated cavity drive

Assuming the cavity input field is in a coherent state, it can be represented in a frame rotating at the probe frequency ω_p by a real number

$$\alpha_{\mathrm{p}} = \sqrt{\frac{P_{\mathrm{p}}}{\hbar\omega_p}}, \tag{D.1}$$

which is fully general, amounting to a definition of when $t = 0$ We phase-modulate sidebands onto this coherent state with an EOM at modulation frequency $\pm\omega_{\mathrm{m}}$. For small modulation depth ($A_{\mathrm{m}} \ll 1$) the coherent cavity drive amplitude is approximately

$$\eta(t) = \alpha_{\mathrm{p}}\left[1 + \frac{A_{\mathrm{m}}}{2}\left(e^{i(\omega_{\mathrm{m}}t+\phi_{\mathrm{m}})} - e^{-i(\omega_{\mathrm{m}}t+\phi_{\mathrm{m}})}\right)\right] \tag{D.2}$$

Or in frequency space, after a Fourier transform

$$\eta[\omega] = \sqrt{2\pi}\alpha_{\mathrm{p}}\left[\delta(\omega) + \frac{A_{\mathrm{m}}}{2}\left(e^{i\phi_{\mathrm{m}}}\delta(\omega + \omega_{\mathrm{m}}) - e^{-i\phi_{\mathrm{m}}}\delta(\omega - \omega_{\mathrm{m}})\right)\right] \tag{D.3}$$

Cavity transfer function

The cavity's transfer function is defined by

$$T[\omega] = \frac{\langle \hat{c}_{\mathrm{out}}[\omega]\rangle}{\langle \eta[\omega]\rangle} = \frac{2\kappa}{\kappa - i(\Delta + \omega)}$$
$$= \frac{2\kappa}{\sqrt{\kappa^2 + (\Delta + \omega)^2}}e^{i\phi_T}, \quad \text{with} \quad \tan\phi_T = \frac{\kappa}{\Delta + \omega}. \tag{D.4}$$

Therefore, the total cavity output field can be expressed in the time domain, using the inverse Fourier transform

$$\hat{c}_{\mathrm{out}}(t) = \frac{1}{\sqrt{2\pi}}\int_{-\infty}^{\infty} d\omega\, e^{-i\omega t} T[\omega]\eta[\omega] \tag{D.5}$$
$$= \alpha_{\mathrm{p}}\left[T[0] + \frac{A_{\mathrm{m}}}{2}e^{i\phi_{\mathrm{m}}}T[-\omega_{\mathrm{m}}]e^{i\omega_{\mathrm{m}}t} - \frac{A_{\mathrm{m}}}{2}e^{-i\phi_{\mathrm{m}}}T[\omega_{\mathrm{m}}]e^{-i\omega_{\mathrm{m}}t}\right] \tag{D.6}$$

Heterodyne signal

In terms of the total cavity photon detection efficiency ϵ, the detected heterodyne power calculated from Eq. 2.59 is

$$\langle P_{\mathrm{het}}(t)\rangle = 2\sqrt{\epsilon S_{\mathrm{sn}}}\langle \mathrm{Im}[\hat{c}_{\mathrm{out}}(t)e^{-i(\omega_0 t+\phi_{\mathrm{L}})}]\rangle, \tag{D.7}$$

assuming the local-oscillator in a coherent state with initial amplitude and phase $\alpha_L = \sqrt{P_{\mathrm{LO}}/\hbar\omega_{\mathrm{p}}}e^{i\phi_{\mathrm{L}}}$. Inserting the cavity output field from Eq. D.6, the detected signal can be written as the sum of three harmonic terms

$$\langle P_{\mathrm{het}}(t)\rangle = 2\sqrt{\epsilon S_{\mathrm{sn}}}\,\mathrm{Im}[\alpha_c e^{-i\omega_0 t} + \alpha_b e^{-i(\omega_0+\omega_{\mathrm{m}})t} + \alpha_r e^{-i(\omega_0-\omega_{\mathrm{m}})t}], \tag{D.8}$$

having defined complex amplitudes for the carrier, red, and blue sidebands

$$\alpha_c = e^{-i\phi_{\mathrm{L}}}T[0]\alpha_{\mathrm{p}} \quad \alpha_r = \frac{A_{\mathrm{m}}}{2}e^{-i(\phi_{\mathrm{L}}-\phi_{\mathrm{m}})}T[-\omega_{\mathrm{m}}]\alpha_{\mathrm{p}} \quad \alpha_b = -\frac{A_{\mathrm{m}}}{2}e^{-i(\phi_{\mathrm{L}}+\phi_{\mathrm{m}})}T[\omega_{\mathrm{m}}]\alpha_{\mathrm{p}}, \tag{D.9}$$

respectively. These amplitudes can be extracted by demodulation of the detected signal at the respective frequencies, for instance the carrier's complex amplitude can be recovered according to

$$\alpha_c = \frac{i}{\sqrt{\epsilon S_{\mathrm{sn}}}}\mathcal{L}\{e^{i\omega_0 t}P_{\mathrm{het}}(t)\} \tag{D.10}$$

where $\mathcal{L}\{\cdot\}$ represents a low-pass filter operation with suitable cut-off frequency to remove the 2nd-order harmonics.

Sideband power analysis

Our traditional method for estimating the detuning from the recorded spectra considers only the total sideband power observed in the heterodyne spectrum

$$P_r = \hbar\omega_{\mathrm{p}}|\alpha_r|^2 = \frac{A_{\mathrm{m}}^2}{4}|T[-\omega_{\mathrm{m}}]|^2 P_{\mathrm{p}} \tag{D.11}$$

$$P_b = \hbar\omega_{\mathrm{p}}|\alpha_b|^2 = \frac{A_{\mathrm{m}}^2}{4}|T[\omega_{\mathrm{m}}]|^2 P_{\mathrm{p}}. \tag{D.12}$$

From Eq. D.4 it follows that the relative sideband imbalance is related to the detuning by

$$r_p = \frac{P_r - P_b}{P_r + P_b} = \frac{2\Delta\omega_{\mathrm{m}}}{\Delta^2 + \kappa^2 + \omega_{\mathrm{m}}^2}. \tag{D.13}$$

Solving for Δ, there are two solution branches

$$\Delta = \frac{\omega_{\mathrm{m}}}{r_p} \pm \sqrt{\left(\frac{\omega_{\mathrm{m}}}{r_p}\right)^2 - (\omega_{\mathrm{m}}^2 + \kappa^2)}, \tag{D.14}$$

one for large detuning $\Delta > \omega_{\mathrm{m}}$ and one for small detuning $\Delta < \omega_{\mathrm{m}}$.

Though always bounded by $-1 \le r_p \le 1$, the ratio r_p only corresponds to a real detuning for $r_p \le (1 + \kappa^2/\omega_{\mathrm{m}}^2)^{-1/2}$. Noise in the measurement of the sideband powers introduces fluctuations into the estimate of r_p, which can result in unrealistic values and systematic biases of the non-linear estimate. It is therefore best, when possible, to compute the average

sideband powers across a dataset first, averaging down noise before computing the average detuning from Eq. D.14.

We also perform real-time feedback to stabilize the probe frequency relative to the cavity resonance by calculating the sideband power imbalance electronically and generating an error signal, as described in Ref. [38]. This process, however, suffers from differential delays in the separate power detection paths for the red and blue sideband, limiting the effective feedback bandwidth to less than 1 kHz and introducing a susceptibility to changes in the probe intensity. This issue could be mitigated by directly sampling the heterodyne signal and digitally calculating an improved error signal, described below.

Complex sideband analysis

There is additional phase information in the detected EOM modulation, which is discarded in the previous analysis. However, if the complex sideband amplitudes are extract, then information about the cavity and probe can be recovered from these values. In principle, there are three measured complex values, which give six unique independent relations. The unknowns are nominally the probe intensity α_p, the probe detuning Δ, the cavity linewidth κ, the initial LO phase relative to the probe ϕ_L, the initial modulation phase ϕ_m, and the modulation depth A_m. The problem now reduces to finding a combination of the three complex amplitudes that yields Δ, the primary value of interest.

For the special case $\phi_m = 0$, it can be conveniently shown that a normalized ratio of the complex sideband imbalance satisfies

$$\frac{\alpha_r - \alpha_b}{\alpha_r + \alpha_b} = \frac{\Delta}{\omega_m} + i\frac{\kappa}{\omega_m}, \tag{D.15}$$

providing a measurement of the probe detuning and cavity linewidth. Because the LO phase ϕ_L introduces a common rotation to all detected amplitudes, it cancels out of this ratio. The modulation phase ϕ_m produces a differential rotation of each sideband's phase, which cannot be uniquely distinguished from the cavity-induced phase shift, but provided the modulation phase is known, it can be rotated out, effectively ensuring $\phi_m = 0$. In practice, one could simply measure or control this phase (for instance by syncing the experimental sequence with the modulation function generator).

This formula for the complex imbalance is simpler than the preceding power analysis in that it can always be inverted to uniquely determine the detuning. This could be useful for application in real-time feedback, providing an unlimited lock range for the error signal, constrained only by decreasing signal-to-noise at very large detuning. The demodulation and complex error signal calculation could be performed digitally with an FPGA connected to a high-speed ADC, directly sampling the heterodyne signal.

Appendix E

Efficient analysis of large datasets

Most experimental data in E3 is extracted from the digitally recorded heterodyne signal, which requires several stages of computationally intensive signal processing to extract meaningful results, such as computing Fast Fourier Transforms, and filtering. Unlike the absorption or florescence images common to many other cold atoms experiments, the 10 MHz heterodyne signal is not comprehensible at a glance. Therefore, it has been essential to develop flexible tools for automated analysis, which provide rapid visualization of the recorded traces from each experiment, facilitating faster diagnosis and iteration in experiment design and allowing careful monitoring during unattended data taking.

Early in my E3 career, I undertook a top-down redevelopment of our standard analysis code, resulting in an object-oriented library of Matlab code named 'skaffold2.' This analysis library was designed to meet the following goals:

- A modular structure of standardized analysis tasks,
- Flexible, self-documenting analysis files for each dataset,
- A dictionary-based data model storing results at each analysis stage,
- Intermediate result caching for efficient data re-analysis, and
- Rapid visualization of recorded data

The library code is available in a public repository at Ref. [40], where it is more thoroughly documented and full example scripts are provided. Here I summarize the high-level structure and features implemented.

A modular structure of standardized analysis tasks

Each analysis task is implemented as a state-less `Analyzer` object, which is configured with 'source' and 'target' fields, followed by a list of parameter name/value pairs. Once created, the analyzer object's `run` method is called on a `DataModel` object, from which the input data is retrieved from 'source' fields and the analysis results are saved back to 'target' fields. For instance, the PSD of the 'raw' signal can be computed and stored in 'rawFft' with the following analyzer:

```
analyze.FFT('raw', 'rawFft', 'range', [tLockStart, tLockStop],...
    'type', 'powerDensity')
```

Flexible, self-documenting analysis files for each dataset

Each dataset has a master 'skaffold' analysis script, which assembles a tree of state-less `Analyzer` objects, specifying the data model source and target fields, in addition to all analysis parameters for each particular calculation. The following code is the beginning of a typical experimental analysis procedure:

```
gsl = loader.Gagescope(pathname, filenumber, 'dataRate', 80e6,...
    'defaultRange', [0, tStop + 1e-3], 'triggerPattern', [32,1]);
    ahet = analyze.Block({...
    analyze.Load(gsl, {'raw', 'source', 'timestamp'}, {'channel', 1}),...
    analyze.RescaleHeterodyne('raw', 'transimpedance', 28.8e3,...
        'gain', 30.1, 'impedance',1e6),...
    analyze.Heterodyne('raw', {'iQuad','qQuad','hetMag','hetPhase'},...
        'carrierFreq', 10e6, 'filterBw', 10e3),...
    analyze.Load(gsl, {'vco', 'vcoSource'}, {'channel', 2}, 'increment', true),...
    analyze.RescaleVco('vco', 'bw', 20e3, 'scaleFun', @(x) -255.2-396*x),...
    analyze.Mean('vco', 'vcoBar', 'range', [tLockStart, tLockStart]),...
    analyze.FFT('raw', 'rawFft', 'range', [tLockStart, tLockStop],...
        'type', 'powerDensity'),...
    ...
});
```

This analyzer tree is handed off to the `Scanner`, which orchestrates a loop of loading, analyzing, and saving the results for each iteration of the experiment.

The sequence of calculations should be transparent from within this single file, tracing the flow of data, from loading the raw traces through the input and output of each analyzer, and also records the particular parameter values and calibrations used in each stage of the analysis. This master analysis file therefore also serves as a form of documentation, with all relevant timing and calibrated parameters used to analyze and visualize the signals summarized in this single file.

A dictionary-based data model storing results at each analysis stage

The analysis tree typically starts with an `analyze.Load` analyzer, which loads raw data into the data model from the configured `Loader` source. The data model is then passed through each subsequent analyzer, which loads data from its 'source' fields and then saves results back to 'target' fields. All analysis results are stored in the `DataModel`, with the `Analyzer` object representing an immutable calculation, which acts on the contents of the `DataModel` only.

Intermediate result caching for efficient data re-analysis

The output of all analyzers for each individual iteration is collected in the `DataModel`, and then saved into an HDF5 storage database, accessed through the `DataScan` object. These intermediate analysis results are stored along with unique signatures for each analyzer used. These signatures maintain consistent data integrity as the sequence of analyzers applied to the data is changed, and also facilitate efficient reanalysis, only recalculating results affected by modified analysis parameters or source fields.

The HDF5 file format [125] allows building arbitrary, multi-dimensional arrays of fixed data types, arranged in a file-system like hierarchy, and offers several significant advantages. Arrays can be resized in place by fragmentation, with a configurable chunk size, allowing the database to dynamically grow as data comes in. The standard code library handles tunable memory caching, allowing efficient read/write access of arbitrary data elements selected out of large datasets. The file format works efficiently over standard network file sharing protocols, like CIFS/SMB, allowing easy access from multiple workstations (although writing to the database from two locations can lead to file corruption).

Rapid visualization of recorded data

The power of this flexible and automated analysis can be applied to visualize data recorded from the experiment quickly, which provides interpretation and diagnosis of results obtained from the experiment in real time. This capability is implemented through a series of plot `Reporter` objects, which provide data visualization for the analysis results, traces, and spectra recovered from the measurements.

```
plotAgg = report.Figure('Aggregated plots', {...
    report.Axes({...
        report.Plot('empty_rawFft','lineProperties',{'Color','r'})...
        report.Plot('rawFft'),...
    },'xLabel','Frequency (Hz)','yLabel','Het PSD (W^2/Hz)',...
        'YLim',[0 2e-20], 'XLim', 10e6 + [-250e3, 250e3]),...
    report.LoopPlot('deltaPc', 'YLim', 1000e3*[-1,1]),...
    report.LoopPlot('nBar', 'YLim', [0,5]),...
    report.LoopPlot('deltaN', 'YLim', [-15,0]),...
}, 'save', e3.get_fig_files(runname, 'agg'));
```

These `Reporter` objects, such as created by the example above, generate plots directly from fields of the `DataModel`, either showing results from single iterations or aggregated across multiple repeated iterations in the data set.

Appendix F

Automated sideband fitting and Cicero feedback

The heterodyne signal recorded in E3 has a rich record of information about each measurement. In addition to the optodynamical signals for atomic spin and motion, it also encodes the intracavity intensity $\bar{n}$ in the carrier peak and the cavity-probe detuning Δ, reflected in the transmitted phase-modulation sidebands described in Appendix D.

One capability enabled by the flexible, automated data analysis described in Appendix E is to extract information from each iteration of the experiment and use it to adjust parameters in subsequent repetitions. We have primarily used this automation to perform slow feedback, stabilizing the mechanical trap frequency, the Larmor frequency, as well as the cavity probe detuning, all of which are observed to drift on the timescale of minutes to hours. Stable and accurate control of the oscillator frequencies was essential in order to perform the coherent excitation and coupling experiments described in previous chapters. In addition, this automated feedback has improved the long-term experiment stability, facilitating a record 48 hours of unattended data collection, during which the lab computers were only remotely accessed to configure new measurement parameters.

Passive stability is always preferable, and some improvements were made to the stability of both the mechanical frequency (Sec. 4.1) and Larmor frequency (Sec. 3.2). However, there are still residual fluctuations and drifts which limit the accuracy and long-term consistency of experiments. After extracting estimates for parameters of interest from the heterodyne signal, a digital feedback algorithm was used to adjust signals output from the computer through the control software Cicero [92]. The probe detuning Δ is estimated from the sideband imbalance, as described in Appendix D, and the difference from the desired set point is used as an error signal for digital feedback described below.

Automated sideband fits

Stabilizing the oscillator frequencies requires more complicated analysis routines, fitting a Lorentzian function to the observed heterodyne PSD. The non-linear fit routine may not

provide a reliable fit, so a goodness-of-fit parameter is monitored to decide whether to use the information gained from a particular iteration or not. A useful statistic for evaluating the goodness-of-fit between observed values y_i and fit predictions f_i is the coefficient of determination

$$r^2 = 1 - \frac{\sum_i (y_i - f_i)^2}{\sum_i (y_i - \bar{y})^2},$$

(F.1)

where $\bar{y}$ is the mean observed value. This statistic reflects the fraction of the variance of the observed data accounted for by the fit, and falls in the range $0 \leq r^2 \leq 1$. In practice, fits were typically accepted when $r^2 > 1/4$, which provided a good balance between filtering out spurious fits to shot noise fluctuations and accepting reasonable fits to small signals.

The spin sideband can readily be resolved on a single iteration, provided it is not opto-dynamically damped. After the measurement of interest has been performed, an rf pulse is typically applied to kick the spin and observe its Larmor frequency in the heterodyne signal. The optomechanical signals, however, are much weaker, due to the intrinsic damping of the center of mass motion. It is often necessary to average multiple iterations together before a clear peak is visible in the average PSD. This averaging adds an additional low-pass filter to the feedback loop, reducing the achievable bandwidth. To achieve the optimal feedback bandwidth for the observed signals, an adaptive averaging algorithm is used, sequentially averaging in one more past spectrum and performing the Lorentzian fit, until an acceptable fit result is obtained.

Digital feedback control

A digital PID feedback loop can be easily implemented using a simple recursive formula. Given an error signal $e(t)$, a generic PID controller output $h(t)$ can be expressed as

$$O(t) = K_p e(t) + K_i \int_0^t d\tau e(\tau) + K_d \frac{de(t)}{dt}$$

(F.2)

defining the proportional, integral, and differential gains K_p, K_i, and K_d, respectively. For a sequence of discrete samples from an error signal e_i, with sampling interval Δ_t, the output sequence h_i can be approximated as

$$h_i = K_p e_i + K_i \Delta_t \sum_j = 1^i e_j + \frac{K_d}{\Delta_t} (e_i - e_{i-1})$$

(F.3)

This series can also be re-written in a recursive form

$$h_i = h_{i-1} + K_p(e_i - e_{i-1}) + K_i \Delta_t e_i + \frac{K_d}{\Delta_t} (e_i - 2e_{i-1} + e_{i-2})$$

(F.4)

This format is more useful in practice, because the history of the feedback loop is entirely contained within the previous output value, and only a few recent samples of the error

signal must be stored in memory. Furthermore, this simplifies the 'start-up' problem for the integrator, allowing one to simply choose an initial condition for the output h_0, and then perform feedback from there. In our implementation we only use proportional and integral feedback (PI), with $K_d = 0$, providing a more stable feedback loop.